ENVIRONMENTAL TRANSFORMATIONS OF NEXT-GENERATION CARBON NANOMATERIALS

By

Benjamin P. Frank

A dissertation submitted to Johns Hopkins University in conformity with the requirements for the degree of Doctor of Philosophy

Baltimore, Maryland

June 2020

Abstract

Carbon nanomaterials represent a populous family of nanoparticles that have been increasingly utilized over the past decade in a range of commercial products, a trend which is projected to progress beyond 2020. This widespread use in various fields has spurred swift and ever-advancing research into new carbon nanomaterials. Perhaps unsurprisingly, the rapid advancement and application of carbon nanomaterials have outpaced a comprehensive understanding of their potential environmental impact. Such an understanding is crucial to minimize the environmental risk of these new technologies. A range of studies seeking to elucidate the microbial and photolytic environmental transformations of various carbon nanomaterials is outlined herein. The carbon nanomaterials evaluated in this work are (i) carbon nanotubes incorporated into polymer nanocomposites, (ii) nanocellulose treated with various surface modifications, and (iii) organic acid-based carbon dots whose environmental transformations are largely unknown due to their recent discovery. The goal in all of these studies was to obtain an understanding of the factors, parameters, and conditions that outline the environmental transformation of these carbon nanomaterials. This understanding can then be leveraged for the sustainable design of carbon nanomaterials with minimal impact after environmental release.

The first system investigated in this work involves the biodegradation of carbon nanotube/polymer nanocomposites (CNT/PNCs). The goal of this study was to identify the influence of polymer type, CNT dispersion, and microbial culture on the biodegradation of CNT/PNCs. It was found that a gradual polymer biodegradation process exacerbated the effect of CNT incorporation on polymer loss.

Next, two different efforts to describe the biodegradation of surface-modified nanocellulose are described. One study involves the effect of silanization on the biodegradation of nanocellulose, and the next details the impact of covalent functionalization. It was found that more extensive surface modification of nanocellulose decreases its biodegradability

Finally, carbon dots (CDs) synthesized from organic acids and ethylene diamine were examined for their phototransformations via direct and indirect photolysis. After release into the environment, CDs were found to transform primarily via indirect photolysis over many decades into CO_2 and nitrate ions.

Committee Members

Advisor: Dr. D. Howard Fairbrother

Reader: Dr. Sara Thoi

Reader: Dr. Arthur Bragg

Acknowledgements

During my Ph.D. research at Johns Hopkins University, I have been extremely fortunate to be surrounded by lab mates and collaborators who have contributed to my growth, edification, and maturation as a researcher and scientist. My interaction with the many great people I have met during my graduate research has shaped me as a person and will leave me with memories which will not be forgotten.

First, I need to thank my wonderful wife, Anna. I said as much in my vows, but without your constant support, reassurance, comfort, and patience (not to mention editing) I would not be at the stage of preparing to defend my Ph.D. thesis right now. The knowledge that every day I could return home to your love and smiling face got me through so many hard days, and her seemingly endless platters of comfort food which were ever the envy of my colleagues. Maybe now I will think of myself as Dr. Frank as you have been insisting on for the past year. Thank you, Anna, I love you, and cannot wait to begin our future together.

My family has also been there for me every step of the way, from childhood to Ph.D. Thank you to my Mom and Dad, both chemists when I was growing up, who instilled in me the sense of wonder and curiosity which has driven me to this point. Your love and care have shaped me into the person I am, and the selflessness that has characterized you both has allowed me to flourish as I continue to grow.

I also want to thank my siblings: first my sister, Andi, for the laughs whenever we chat, always getting my super outdated references, and not bragging (too much…) about doing *her* graduate work in San Diego. I'm so proud of you and can't wait to see what you do with your degree, any help you need with grad school, always let me know, from Dr. to (eventual) Dr. Looking forward to more DnD sessions with my DM, and maybe DotR remake?? Thank you to my brother Rob for always being there for me and putting up with my constant rehashing of the same games and music (robotic…), I've always been thankful that you have the same video game history as I do so I can release my nostalgia at any given moment. More importantly, thank you for being my Best Man, and being an amazing brother. I cannot wait to keep growing together and it's nice to have a match in rice cake

consumption. Thank you to my sister Leah, for continuing the Pitt representation (H2P) and letting some small part of my undergraduate self live on. I have always been in awe of your persistent upbeat and social nature, traits that are less pervasive in the other Franks. Thank you for always being excited to see Anna and I during our short visits home, it always helped me recover during some busy weekends. I know I can always count on you for a Disney sing-along and for keeping up with the new lingo the kids are using. Thank you to all three of you, I love you and it has been such a treat to see you all grow into adults (you all will be old too someday).

Now onto the actual researchers who have supported me during the long days in lab which were legion. First, thank you to my advisor, Howard Fairbrother. Upon taking me into your research group, I was a raw, but motivated student who needed to be shown how scientific research was performed. Thank you for the mentorship, patience, and direction which has helped me get to this point. Your philosophy has shown me that the sweat, repetition, and frustration which goes into good research is rewarded by clear, impactful, and valuable results. The lessons I have learned during my time in your group will guide how I conduct research throughout my career. I would also like to thank Professor Sara Thoi and Professor Art Bragg for being on my thesis committee. Your input and advice from the time of my graduate board orals until my defense have been incredibly helpful, and I am thankful for the time you have invested in my scientific growth.

Next, I have to acknowledge the ranks of lab mates who have been indispensable in my journey through graduate school. While there are too many to all detail here, I appreciate all the help and support through the years. First, I need to thank Dr. Ron Lankone, although our lines of research didn't intersect until the final few years of my

degree (in a somewhat explosive manner), having you as a close friend through all the trials and tribulations of graduate school was invaluable in keeping my spirits up and getting papers done. Here's looking forward to our next iBar trip together. Dr. Dave Goodwin deserves thanks for being my mentor upon joining the Fairbrother group. Thanks, Dave, for being patient with my learning process and teaching me the biodegradation skills and tests which have shaped the vast majority of my thesis. Still need to share that glass of scotch, let's make it happen. I also must thank Dr. Dave Durkin, from the time we both joined the group, you are likely the lab mate who I've been most closely tied to. From classes, to my first authorship on one of your papers, to your support on *my* first paper, including the frequent visits to Annapolis, I truly could not have had such a successful graduate school experience without your help, so thank you. A thank you is in order for Michael Barclay as well. Thank you for always being around to repair instrumentation and clean up (non-literal) fires that your lab mates cause. Your mechanical knowledge has fed into my confidence in repairing high vacuum instrumentation and has allowed me to hold that role in the twilight of my graduate school years. My current lab mates I owe considerable thanks as well. Thank you to Dr. Alyssa Deline for your remarkable efforts in getting the carbon dot paper to publication and assembling the monumental Chem Review article from our lab, bringing your enthusiasm for research to the lab, and the valuable discussions about various projects. I respect your drive and scientific sense immensely and apologize for all the venting I aimed towards you during the more frustrating times of my degree. Next, I need to thank Casey Smith for being the only lab mate in my graduate school career for matching my enthusiasm for cellulose. Thank you for putting up with my sometimes fickle directions, changing research goals, and long days.

Your penchant for crafting publication-worthy figures have also been a huge boon for me and the group, so thank you for your tireless efforts in that area. I need to thank Lexi for being my first Levvy Wednesday partner (never forget Tracey and Jefferey), and always being in a good mood and being there to help relieve stress during the day in lab. I also want to thank my closest collaborators, Dr. Emily Caudill and Joel Pedersen for their tireless work and help with running NMR for my nanocellulose work, without it the materials we made would still be a mystery, so thank you to you both.

I also need to thank my friends from outside of lab. Jim and Josh, thank you for always being there to chat with me and making me laugh whenever I got the chance to visit you in NYC. Thank you for being my closest friends for most of my life, I have always been so grateful to count on you both through everything. And you can just say you're not going to visit me in Maryland, its fine. Lee, thank you for having the exact same sense of humor as I do, and always being there for some SMITE, I know I can always look to you to make me laugh. Rich and Lisa, thank you for being the best escape room partners Anna and I could have, we are already looking forward to visiting Mark again with you two once we are released from COVID quarantine…At this point I think I have padded my thesis length enough with this section, but I'd also like to thank Jake, Collin, Jack, Alana, Emma, Dave, Gene, Diamond, Donald, and the many others who have been friends, colleagues, and family during this journey.

Table of Contents

List of Tables

List of Figures

Chapter 1. Introduction

1.1 Nanomaterials

A particle is considered a nanoparticle or nanomaterial when it possesses a dimension smaller than 100 nm in size.[1] Nanomaterials have been used for centuries, even before their scientific classification (e.g., carbon nanotubes in Damascus steel),[2] and can be both naturally produced (e.g., alumina, iron oxide) or engineered (e.g., carbon nanotubes, quantum dots).[1, 3] Nanoparticles offer a range of impressive properties such as the high tensile strength of carbon nanotubes (CNTs), the strong fluorescence of quantum dots, and the antimicrobial properties of silver nanoparticles.[1, 4-5] The nanoscale dimensions of nanomaterials give rise to a high surface area-to-volume ratio which renders them highly effective at imparting these impressive properties to products, thereby garnering considerable interest for their utilization in a variety of applications.[1, 6-7] Nanomaterials can be utilized both via direct application (e.g., *in vivo* bioimaging using quantum dots) and via incorporation into composite materials (e.g., reinforcing polymer matrices with CNTs). Applications of nanomaterials include sensing, antimicrobials, polymer reinforcement, medical devices, drug delivery, and environmental remediation.[1, 4-9] The myriad uses of nanomaterials have led to an increase in the research and production of nano-enabled systems over the previous few decades, with the market for such technology projected to reach $7.3 billion by 2022.[10] While the potential applications enabled by nanomaterials are exciting, it is crucial to assess their environmental risk before their extensive use. As nanoparticles will inevitably be released during the production, use, and disposal of nano-enabled products, a portion of these nanomaterials will make their way into the environment via runoff, incinerator ash, and disposal in landfills.[11-13] Unfortunately, the

widespread production and application of nanomaterials has tended to outpace the measured assessment of their potential environmental risk. Thus, it is critical to attain a better understanding of this risk before further increasing implementation of such technology, lest an environmentally devastating effect manifest analogous to the weakening of bald eagle eggs caused by dichlorodiphenyltrichloroethane (DDT).[14] The environmental risk of a nanomaterial can be understood as the hazard of such materials (e.g., toxicity) combined with their opportunity for exposure to organisms (e.g., concentration, persistence, and transport in the environment).[15] Because the properties of materials can be altered or enhanced upon conversion to the nanoscale, risk assessments made at the macroscale cannot necessarily be translated to a nanomaterial. Additionally, many nanomaterials such as carbon nanotubes and carbon dots (CD) do not have analogous macroscale forms, and thus their environmental risk must be considered in isolation.

1.1 Carbon Nanomaterials

Carbon nanomaterials (CNMs) represent a structurally diverse group of materials, each of which is composed of a carbon-rich backbone. This class of nanomaterial is incredibly varied due to the multitude of stable carbon-based structures which exist.[16-17] While the terminology of "CNM" typically refers to the class of nanomaterials encompassing CNTs, graphene/graphene oxide (GO), and fullerenes, this dissertation uses a broader definition which includes all carbon-based nanoallotropes. This classification includes CNMs composed of graphenic carbon (e.g., CNTs, graphene, GO), sp^2- and sp^3-hybridized carbon (e.g., fullerenes, nanodiamond), or polymerized carbon backbones (e.g., carbon dots (CD), nanocellulose).[17-20] The morphology of CNMs ranges from high aspect ratio thread-like structures (e.g., CNTs, nanocellulose) to flat 2D sheets (e.g., graphene,

GO), to 0D spheres or clusters of organic-acid polymer (e.g., fullerenes, CDs). The variety of carbon nanomaterials speaks to their vast range of applications. This thesis will exclusively focus on carbon nanotubes, nanocellulose, and carbon dots, which are described in greater detail below.

CNTs are synthesized via chemical vapor deposition (CVD), arc discharge, or laser ablation, and they consist of either a single layer (single wall CNTs) or multiple concentric layers (multi wall CNTs) of cylindrical graphene sheets.[21-22] CNT diameters are typically on the order of nanometers and CNT lengths are generally on order of microns.[21] Due to their unique sp^2-hybridized carbon lattice structure, CNTs possess incredible tensile strength, thermal stability, and conductivity.[1] CNTs have been reported as having tensile strengths up to 150 GPa and Young's modulus up to 1800 GPa: properties which are dependent on CNT diameter, chiral structure, and number of lattice defects.[23-25] The thermal conductivity of CNTs is also impressive and tunable, with a reported range from 0.1 W/mK (insulating) to 6600 W/mK (conductive).[26] The electrical conductivity of CNTs is apparent in the low resistivity of single wall CNTs (SWCNTs; 1 μΩ/cm) and multi wall CNTs (MWCNTs; 5 μΩ/cm) as well as the high current density of 10^{10} A/cm^2.[27] These properties have resulted in CNTs being used in biomedical devices,[28] in batteries as anode materials,[29] and as thermal stability additives.[30] One of the most common applications of CNTs is in the reinforcement of polymer materials.[31-34] The reinforcement capacity of CNTs is especially important for increasing the utility of naturally sourced biopolymers such as polyhydroxyalkanoates (PHA), polylactic acid (PLA), and natural rubber which typically possess inherently weak mechanical properties.[35-39] Although the environmental transience of biopolymer materials is important for the reduction of waste, the application

of these materials is strongly limited by their fragility.[40] Incorporation of CNTs into PHA at 0.5% w/w has been shown to improve secant elastic modulus by a factor of 7, and 0.7% w/w in PLA can improve tensile strength from 59.9 MPa to 72.2 MPa and toughness from 93.9 MPa% to 114.7 MPa%.[41-42] The wide range of applications for CNTs have seen their production and use rise over the past decade, and this trend is expected to increase beyond 2020.

Nanocellulose, a carbon nanomaterial with a similar thread-like morphology to CNTs.[19] Nanocellulose is derived from naturally the occurring macrocellulose, that serves as a structural component of plants and certain animals.[43] Macrocellulose and nanocellulose are both comprised of hierarchical cellulose chains which consist of β-1-4 linked D-glucose units.[44] The carbons in each glucose subunit are numbered 1-6 beginning at the β-glycosidic linkage (C1) and ending at the carbon outside of the sugar ring (C6) that protrudes out of the plane of the molecule (Figure 1.1). Cellulose is characterized by an extensive hydrogen bonding network, which dictates the formation of several different polymorphs known as Cellulose I, II, III, and IV.[19] Of these, only Cellulose I and II are

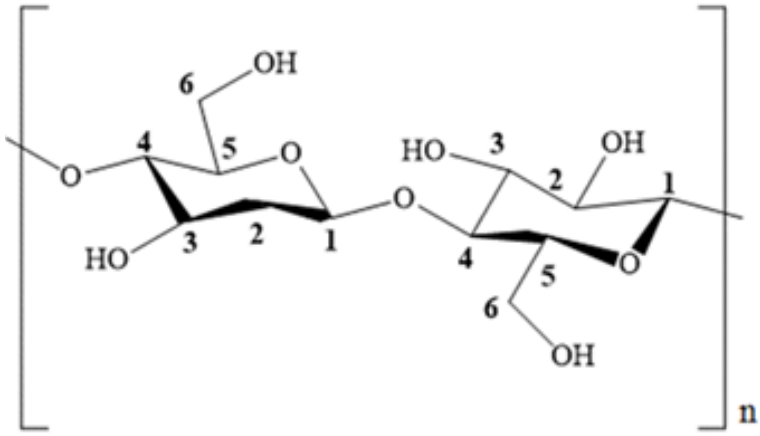

Figure 1.1 Cellobiose repeat unit of nanocellulose with carbon atoms 1-6 labeled.

found naturally. Cellulose I, which consists of parallel chains of cellulose, is the most common in nature. Cellulose II, which consists of antiparallel chains of cellulose, is more thermodynamically stable and is typically recovered after the dissolution of cellulose in solvent. Cellulose II is the form of nanocellulose used in this thesis due to its applicability as an eco-friendly biodegradable polymer material.[19, 45]

By treating macrocellulose (e.g., wood pulp) with mechanical milling, acid treatments, or enzymatic digestion, nanocellulose can be isolated as cellulose nanofibrils (CNF).[19, 46-50] CNFs feature the same molecular structure as macrocellulose, and lengths on the order of hundreds of nanometers and <100 nm widths. Upon isolation from macrocellulose, particularly by acid hydrolysis, CNFs are stable in aqueous media due to the abundance of hydroxyl groups that pattern its surface. The removal of water from the system yields a fluffy, white solid consisting of highly aggregated nanofibrils which is the typical form of nanocellulose used in manufacturing and research.

By further treating CNFs with strong acids or bases, amorphous regions in the nanofibril can be dissolved to yield highly crystalline cellulose nanocrystals (CNC).[43] In addition to the top-down methods of nanocellulose synthesis that yield CNFs and CNCs, bottom-up pathways are utilized by certain types of bacteria (e.g., genus *Gluconacetobacter*) to produce bacterial cellulose (BC), which is also highly crystalline.[51] The multiple structural forms of nanocellulose make it a fairly versatile material useful in polymer reinforcement as well as biomedical, food, and cosmetic applications.[19, 51]

Carbon dots are fluorescent carbon nanomaterials with dimensions typically <10 nm. CDs have arisen as intriguing alternatives to quantum dots since their identification by Sun et al. in 2006.[52] Since then, publications involving CDs have increased each year, reaching

5700 in 2019, with nearly 2,000 already published in 2020 according to Web of Science (See Figure 1.2). While quantum dots feature heavy metal cores which can leach toxic ions into the environment, carbon dots are characterized by a carbon-rich structure. The popularity of carbon dots can be attributed to their strong, tunable fluorescence coupled with their biocompatibility, thus making them incredibly useful as sensors, in drug

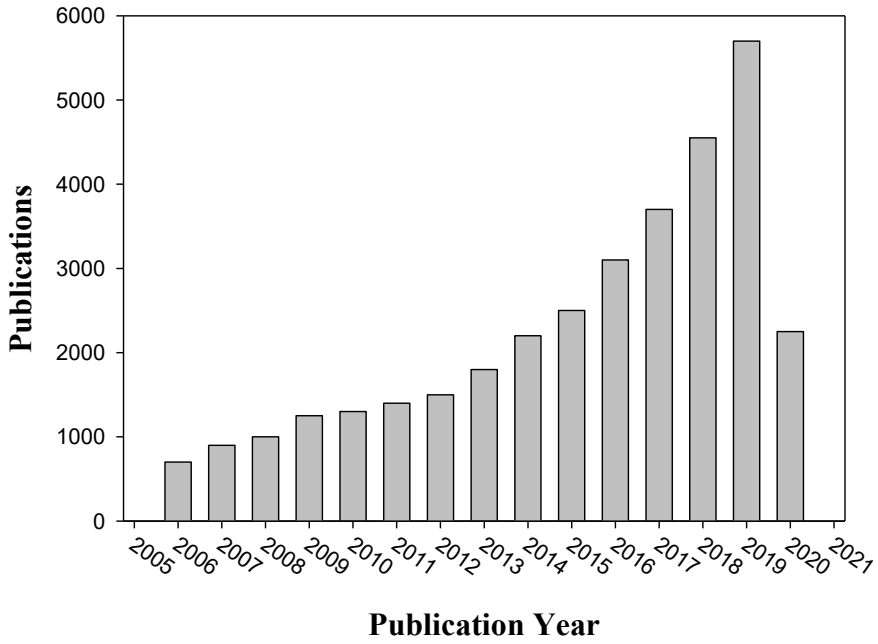

Figure 1.2 Web of Science data outlining the number of publications, books, articles, etc. with the word "Carbon Dot" mentioned per year since 2006.

delivery, and as bioimaging agents.[53-54] Carbon dots can be synthesized via a variety of bottom-up and top-down methods.[55] Bottom-up methods involve polymerizing small molecular precursors such as organic acids (e.g., citric acid, malic acid) and nitrogen-based crosslinking agents (e.g., ethylene diamine, urea) using microwave or hydrothermal treatments.[55] Top-down methods involve the digestion of carbon materials such as graphene oxide, carbon fibers, and activated carbon in acid or other oxidants using microwave or hydrothermal methods.[55] The fluorescence of carbon dots can be adjusted

by tuning their size or excitation wavelength, which makes them extremely valuable in a range of imaging applications.[54-55]

1.2 Environmental Risk and Persistence of Carbon Nanomaterials

Due to the wide variety of structures that exist for CNMs, environmental risk should generally be considered on a case-by-case basis. Although carbon itself is typically a relatively inert substance, the chemistry of CNMs that arises from their unique structures and nanoscale dimensions presents the opportunity for risk. The risk of a material can be understood by its inherent toxicity coupled with its concentration and persistence in the environment. For example, ultrafine carbon nanoparticles have been shown to be cytotoxic towards mice, however, the risk of the manifestation of such toxicity is dictated by the odds that a mouse will encounter these nanoparticles.[56] For a given environmental contaminant, increased production will lead to a concomitant increase in environmental presence such has been seen for various pesticides in recent years.[57] The risk of a contaminant once released to the environment will be strongly influenced by its resistance to degradation, as a persistent contaminant is more likely to accumulate and exhibit prolonged environmental impact compared to more transient species.[58] Thus, a contaminant is most detrimental when it possesses high inherent toxicity, is widely released into the environment, and is recalcitrant to degradation after release. Through this lens, the environmental risk of CNMs can be understood.

CNTs are cytotoxic to a range of organisms including bacteria, fungi, and animals due to their needle-like morphology and aromatic structure. For example, Hartono et al., showed that MWCNTs decreased the viability of *E. coli* due to membrane damage (e.g., piercing) in a variety of biological media.[59] While membrane damage is one route of

cytotoxicity for CNTs, the exact mechanism of their overall toxicity is still unclear, as several CNT properties and behaviors have been shown to play a role. CNT toxicity has been shown to depend on factors including CNT size, oxidation, and purity (i.e., presence of residual metal catalysts), thus requiring careful control of CNT properties to determine the underlying cause of a toxic response.[60-67] One route of CNT toxicity stems from the ability of CNTs to physically damage cellular membranes via direct interaction or piercing due to their nanoscale needle-like morphology.[59, 62, 68-69] Another route of CNT toxicity is the cellular uptake of CNTs, followed by the internal disruption of cellular components and processes as well as driving internal reactive oxygen species (ROS) production.[70-72] These mechanisms are observed to a greater extent for oxidized CNTs, as oxidation can improve CNT dispersibility in solution, increasing uptake. In addition to their observed cytotoxicity, CNTs are generally recalcitrant to environmental degradation processes, thus increasing the likelihood of their exposure to vulnerable species and increasing environmental risk. For example, Parks et al., showed that radiolabeled SWCNTs failed to biodegrade after 6 months of exposure to selected microbial species.[73] Due to the cytotoxicity and environmental persistence of CNTs coupled with their increasing commercial use, their potential for environmental risk is quite high.

As described previously, CNTs are often used to reinforce polymer materials to improve properties such as tensile strength, Young's modulus, and conductivity.[74] Therefore, the potential environmental risk of carbon nanotube/polymer nanocomposites (CNT/PNCs) must be accounted for as well. This environmental risk will primarily be dictated by the rate of polymer degradation in the environment. Because CNTs are recalcitrant and cytotoxic, their incorporation into polymer may have adverse effects on

the rate of microbe-driven polymer loss. The extent of this inhibition will be dependent on a variety of factors including CNT type, CNT dispersion state, polymer type, and biodegrading culture. Thus, it is important to attain an understanding of the factors that control the rate of polymer loss after CNT incorporation in order to fully characterize the environmental fate of such materials.

Unlike CNTs, nanocellulose is biocompatible, biodegradable, and nontoxic in nearly all vectors, generally only posing risk upon inhalation.[19, 75] The retention of these properties upon conversion of cellulose to the nanoscale is perhaps unsurprising due to its polysaccharine molecular structure. Indeed, nanocellulose readily biodegrades in both aerobic and anaerobic microbial environments (e.g., compost, waste water, landfills, soil).[76-80] However, commercial forms of nanocellulose are typically chemically modified before utilization. This is necessary because the hydrogen bonding network within nanocellulose is strong enough to preclude its dispersion in water or organic media. Options for addressing this severe homoaggregation include the modification of the surface of nanocellulose using hydrophobic coatings or functionalizations with different chemical groups (i.e., carboxyl, ether, ester, urethane). These grafted chemical groups occupy hydrogen bonding sites on nanocellulose and thus interfere with the network that forms in native materials. Oxidation of nanocellulose with 2,2,6,6-tetramethylpiperidine-1-oxyl radical (TEMPO) is the most widely utilized functionalization option as it replaces the C6 hydroxyl group with a carboxylic acid moiety, at once reducing homoaggregation and improving aqueous dispersibility by imparting negative charge to the CNF surface.[19, 81] TEMPO oxidation is additionally valuable as the carboxyl character added to nanocellulose

can be used as the substrate for the grafting of a wide range of additional chemical groups such as polymers, surfactants, and drugs.[19, 81-82]

However, in addition to reducing homoaggregation, many applications of nanocellulose require hydrophobic modification strategies to improve its dispersion in nonpolar media including solvents and polymers.[19, 83] For example, in order to use nanocellulose in the reinforcement of a hydrophobic polymer (e.g., polystyrene, polypropylene), it must first be made hydrophobic to improve energetic interactions with the surrounding polymer matrix. Chemical functionalization enables modification of hydroxyl groups on the nanocellulose surface without forming a coating.[19, 83] A range of different chemical properties can be achieved via functionalization because a variety of carboxylic acid, alkyl halide, and alcohol reagents can be used with multiple R-group chemistries. As environmental interactions strongly depend on surface chemistry, the incredible range of nanocellulose surface modifications that exist can potentially alter its environmental impact. Thus, while the environmental degradation of unmodified cellulose is known with confidence, the environmental risk of modified nanocellulose remains unclear. While some studies on the toxicity of certain functionalized nanocellulose exist,[75, 84-85] investigations involving the environmental persistence of such nanomaterials are scant. As prolonged environmental lifetime leads to increased odds of exposure to potentially vulnerable organisms, an understanding of and ability to control the environmental transformations of functionalized nanocellulose is valuable to obtain.

As CDs have only recently emerged as a popular and useful nanomaterial, much of their environmental behavior is unknown. In terms of their environmental risk, CDs are largely considered to be nontoxic at environmental concentrations, though this depends on

the precursors used in their synthesis and surface chemistry (e.g., positive charge more toxic).[86-90] Unknown, however, is the fate of CDs after their environmental release and their subsequent likelihood of exposure to environmental organisms. The most commonly used CDs are hydrophilic by virtue of their synthesis from organic acids (e.g., citric acid, malic acid) which impart high densities of carboxylic acid and hydroxyl groups to their surface.[91-92] The high negative charge at the surface of CDs gives rise to considerable electrostatic repulsion between individual CDs which keeps them stable in aqueous solution as predicted by Derjaguin-Landau-Vervey-Overbeek (DLVO) theory.[93-94] This stability keeps CDs suspended in water under environmental conditions, at which point they are available for transport through aqueous systems and soil (modeled by column transport studies).[95-99] This high mobility suggests that CDs released into the environment are prone to find their way into rainwater, wastewater, or agricultural runoff, which can transport these nanoparticles to natural water systems. Once there, CDs will remain stable in the water column for extended periods of time, increasing the odds of their exposure to aqueous organisms as well as those drinking from waterways. However, the outlined route of exposure to organisms necessitates a high level of environmental stability, as degradation before such extensive transport will nullify any potential risks. Furthermore, this extended transport scenario offers the potential for CDs to undergo environmental transformations (e.g., decarboxylation, chemical changes) which could alter their chemistry compared to the starting material. Due to their recent development, little is known about the environmental degradation and transformations of CDs, but this knowledge must be achieved in order to understand the true environmental risk of CDs.

1.3 Environmental Transformations of Carbon Nanomaterials

The environmental transformations of CNMs primarily occur at their surface. Environmental properties of CNMs such as aqueous stability, environmental transport, contaminant adsorption, biodegradation, and photostability stem from their surface chemistry.[100-106] Thus, it is in the surface region of carbon nanomaterials where environmental transformations will have the greatest impact, necessitating techniques which allow for the accurate assessment of surface chemistry.

1.3.1 Surface Analysis

X-ray photoelectron spectroscopy (XPS) is a technique which provides information on the chemical composition and bonding environment at the first ca. 10 nm of a materials surface. XPS involves irradiating samples with X-ray photons which are typically generated via a magnesium (photon energy 1253.6 eV) or aluminum (photon energy 1486.6 eV) anode. The energy of these X-rays is on the order of the binding energies of atomic core-level electrons. By absorbing photons, core-level electrons are ejected from atoms within a sample with a kinetic energy which depends on the orbital from which they escape. The kinetic energy of these photoelectrons is equal to the difference between the energy of the photon (hν) and its binding energy within the orbital. Because each orbital (e.g., 1s, 2s, 2p…) within each element (e.g., C, O, N…) has a characteristic energy, electrons occupying each orbital have their own distinct binding energy as well. As such, when photoelectrons are emitted from a sample, they possess a characteristic kinetic energy which can be isolated using an energy analyzer (e.g., hemispherical analyzer) to identify the element and orbital from which an electron originated. XPS is surface sensitive because the inelastic mean free path (IMFP) for an electron is roughly 10 nm in the energy regime

covered by XPS. This means that while X-rays can penetrate into samples (depending on material) to the depths of microns before being fully absorbed, electrons—being massive particles—can typically only travel roughly 10 nm before colliding with another particle (e.g., electron, proton). The remarkable surface sensitivity of XPS makes it an invaluable tool for assessing and tracking the surface chemistry of nanoparticles as they undergo environmental transformations.

1.3.2 Microbial Transformations

As previously described, the environmental transformations of carbon nanomaterials are important to consider as alterations to their toxicological, transport, stability, and structural properties can drastically impact environmental risk. Environmental transformations can be initiated via a variety of mechanisms including interactions with microbes, sunlight, and reactive oxygen species (ROS). Examples of microbially-induced transformations of nanoparticles include the surface oxidation of CNTs upon exposure to bacteria, the mineralization of nanocellulose, and the biodegradation of the graphene lattice of graphene oxide (GO).[76, 107] Microbial interactions such as biofilm formation and biodegradation generally require surface colonization, a foundation that is sensitive to the morphology and chemistry of the material surface.[108-109] Various methods exist to assess the biodegradation of materials and nanomaterials. After colonization of microbes at a material's surface, biodegradation proceeds via the microbially-driven degradation of chemical structure, depolymerization or degradation into low molecular weight species, and culminates in complete mineralization into biogas.[110] Assessments of biodegradation can be performed using a variety of microbes (bacteria, fungi, archaea), populations (single, mixed), conditions (pH, nutrients) and environments (aerobic, anaerobic).

Biodegradation tests are usually performed by burying samples in soil or compost, or via exposure to microbial media. Because biodegradation can occur to different extents with different end products, its quantification is a multi-faceted approach. The detection of initial subtle structural changes typically requires spectroscopic techniques such as Fourier transform infrared spectroscopy (FTIR) or scanning electron microscopy (SEM).[111-112] Assessment of further biodegradation to soluble low molecular weight species typically necessitates more sensitive identification techniques such as high-performance liquid chromatography (HPLC), gas chromatography (GC), or mass spectrometry (MS).[113-114] Biodegradation at this stage can also be determined by tracking mass loss, as soluble species are prone to diffuse away from the bulk material, reducing the final mass as compared to the initial mass. Complete mineralization of materials into biogas is the ultimate goal of biodegradable products to ensures that no residual byproduct with unintended environmental impact remains.[115-116] Unfortunately, the tracking of mineralization is difficult, as it typically requires advanced experimental set-ups or materials. Typically, these tests are performed by monitoring the evolution of biogas during biodegradation of a material.[117-118] The composition of this biogas from hydrocarbon materials and most carbon nanomaterials either consists of CO_2 and H_2O (aerobic) or CO_2 and CH_4 (anaerobic).[119] By scrubbing evolved CO_2 or using radiolabeled samples (e.g., ^{14}C), the degree of biogas production can be used to relate the extent of biodegradation of CNMs.[120] Instead of quantifying a single byproduct, total biogas production can be measured using a sealed system. Anaerobically, this is relatively easy to accomplish if an anoxic media can be ensured and maintained. One method of this experimental setup is known as the biomethane potential (BMP) test, first outlined by Owen et al. in 1979 and

Table 1.1 Biomethane potential (BMP) test stock solutions S1-S7. BMP media consists of 1.8 mL S2, 5.4 mL S3, 27 mL S4, 1.8 mL S5, 1.8 mL S6, and 18mL S7 per liter of MilliQ water.

Solution	Compound	Concentration, g/L
S1	Sample	<2 g/L degradable COD in assay liquid (estimated)
S2	Resazurin (oxidation-reduction indicator)	1
S3	$(NH_4)_2HPO_4$	26.7
S4	$CaCl_2 \cdot 2H_2O$	16.7
	NH_4CI	26.6
	$MgCl_2 \cdot 6H_2O$	120
	KCl	86.7
	$MnCl_2 \cdot 4H_2O$	1.33
	$CoCl_2 \cdot 6H_2O$	2
	H_3BO_3	0.38
	$CuCl_2 \cdot 2H_2O$	0.18
	$Na_2MoO_4 \cdot 2H_2O$	0.17
	$ZnCl_2$	0.14
S5	$FeCl_2 \cdot 4H_2O$	370
S6	$Na_2S \cdot 9H_2O$	500
S7	Biotin	0.002
	Folic acid	0.002
	Pyridoxine hydrochloride	0.01
	Riboflavin	0.005
	Thiamine	0.005
	Nicotinic acid	0.005
	Pantothenic acid	0.005
	B12	0.0001
	p-aminobenzoic acid	0.005
	Thioctic acid	0.005

modified by Angelidaki et al. who outlined nutritional media consisting of seven stock solutions (Table 1.1) to promote the degradation of macropollutants in wastewater.[117-118] BMP media consists of the sample to be mineralized (Stock 1), resazurin which serves as an indicator of redox reactions to signal the loss of anoxic conditions (Stock 2), diammonium phosphate (Stock 3), various metal salts (Stock 4), iron chloride (Stock 5), sodium sulfide acts as an oxygen scavenger to keep the media anoxic (Stock 6), and a cocktail of vitamins to promote bacterial growth (Stock 7). In BMP tests, samples are sealed in vessels containing anaerobic wastewater obtained from an anaerobic digestor, a culture awash with a diverse and environmentally relevant microbial community. As

materials are mineralized by this community, biogas production is quantified via volume measurements using a septum in the cap of the vessel. Aerobically, the need for an oxygenated environment poses an obstacle for the use of sealed systems as aerobic microbes require a sufficient partial pressure of oxygen to survive.[121-122] Thus, tests seeking to use aerobic biodegradation setups typically require a more complex sealed system or make use of CO_2-scrubbing analysis. Importantly, biogas production can be used to describe biodegradation kinetics in addition to ultimate biodegradability. This can be done using kinetic models such as the first order rate model, pseudo parallel first order rate model, Logistic model, and modified Gompertz model.[123-126] The latter two models are more suitable for fitting data that feature a lag phase (i.e., delay in biogas production after beginning incubation).

1.3.3 Phototransformations

Photolytic transformations of CNMs involve processes that initiate via the absorption of photons by the material in question (direct photolysis) or by natural constituents of water (e.g., nitrate, natural organic matter) to produce ROS which drive subsequent photochemistry (indirect photolysis).[127] Such phototransformations include the photofragmentation of graphene oxide and the mineralization of fullerenes (direct photolysis) under natural sunlight.[104, 106] Indirect photolysis has also been shown to fragment the structure of GO as modeled with hydroxyl radicals as well as degrade pesticide contaminants in the environment.[128-129] Direct photolysis experiments can be performed either using laboratory lamps (e.g., simulated sunlight, UV lamps) or under natural sunlight via outdoor exposure. Since these changes are typically structural in nature, assessment of photodegradation can be made using spectroscopic techniques such as X-ray

photoelectron spectroscopy (XPS) or FTIR to assess changes in chemical bonding or photoluminescence spectroscopy (PL) to measure changes in emissive properties. Indirect photolysis, however, in addition to structural degradation, often leads to mineralization of carbon nanomaterials into CO_2, which volatilizes out of aqueous solution.[104, 106, 130] Thus, in addition to spectroscopic techniques, the degradation of CNMs via indirect photolysis can be assessed by quantifying CO_2 production, assessing total organic carbon (TOC) content in solution, or measuring mass loss. Indirect photolysis is modeled either via the addition of ROS-producing constituents of water (e.g., NOM, nitrate) or via the direct addition of ROS-producing molecules (e.g., H_2O_2 forms hydroxyl radicals) to aqueous samples; both methods are followed by irradiation with sunlight or a wavelength of light that causes ROS production.[103, 105, 131]

1.3.4 Transformations of CNTs

As with most CNMs, the behavior of CNTs after environmental release is largely dictated by their surface chemistry. CNTs are known to be stable in natural waters if they possess a negatively charged surface, which is typically imparted by oxygen-containing functional groups.[132] A negatively charged surface enables CNTs to transport in the environment and highly increases their chance of encountering organisms.[133] As previously mentioned, well-dispersed CNTs are more prone to interaction and uptake by environmental organisms and microbes, severely increasing their risk due to the inherent toxicity of CNTs and oxidized CNTs. Once this surface charge is lost, however, CNTs lose their aqueous stability and begin to aggregate and sediment out of solution, decreasing their capacity for environmental transport considerably.[134] Furthermore, the adsorption of environmental contaminants such as pharmaceuticals, pesticides, and heavy metals to

CNTs increases their potential exposure to different organisms, and the extent of this adsorption depends on CNT oxidation state.[64-65, 135-137] As surface oxygen groups enable most environmental interactions for CNTs, they are perhaps the most important facet of CNT chemistry.[138] In addition, different CNT surface chemistry imparts different levels of dispersion within polymer nanocomposites,[139] which has the potential to alter the environmental interactions of such CNT-enabled materials.

1.3.5 Transformations of Modified Nanocellulose

A major advantage for the production and use of nanocellulose is its biocompatibility and biodegradability; thus, understanding microbial interactions with nanocellulose is crucial for determination of its environmental persistence and ultimate risk. In the case of nanocellulose, surface modification is often required to enable its use in the widespread applications that are being researched.[83, 140] While the need for surface modification of nanocellulose is generally unavoidable, such treatments have the potential to drastically alter the environmental interactions (e.g., biodegradation) of nanocellulose. As cellulose has existed for centuries as plant matter, microbial species have extensively developed robust, highly specific enzymatic pathways to degrade cellulosic material.[119, 141] This has permitted the relatively facile and extensive biodegradation of cellulose to occur in a variety of microbial environments. In aerobic environments, cellulose is generally degraded by cellulase and β-glucosidase enzymes excreted from bacteria and fungi. Cellulases initiate degradation of the cellulose structure by hydrolyzing internal bonds (endoglucanases) and chain-ends (cellobiohydrolases) to yield cellobiose molecules.[119] β-glucosidase then concludes the biodegradation process by converting cellobiose into glucose that environmental microbes can aerobically mineralize into CO_2 and water.[119] In

contrast, anaerobic microbes utilize cellulosome or multiprotein complexes of enzymes to mineralize cellulose into water and CO_2 and CH_4 biogas.[119, 141-142] Moreover, while a single aerobic microbe specie is sufficient to fully mineralize cellulose (e.g., *Trichoderma reesei*), multiple anaerobe species are required to work in concert to produce the enzymes necessary for conversion of cellulose to biogas.[141] These highly specific enzymatic pathways have lent themselves to the biodegradation of native cellulose but offer limited adaptability to new substrates. Thus, modification of the surface of nanocellulose offers the very real possibility to render the material less, if not wholly, unbiodegradable, negating one of its primary merits. An understanding of the environmental persistence of modified nanocellulose is crucial as such materials are often marketed as fully biodegradable by virtue of being sourced from cellulose. If these materials are not biodegradable as advertised, they may have disproportionate environmental impact if used with impunity. In addition to understanding the environmental transformations of modified nanocellulose, strategies to control their environmental fate are valuable to inform their sustainable production by balancing commercial viability and environmental impact.

1.3.6 Transformations of CDs

Despite the recent development of CDs as a valuable and interesting nanomaterial, little is known about their potential environmental transformations. In practice, they are most similar to quantum dots (fluorescent, nano-sized particles), although chemically they are quite different. Thus, other carbon nanomaterials serve as a better basis for comparison to predict environmental behavior. CDs are highly oxygenated, perhaps only matched by GO and nanocellulose among CNMs. The small size of CDs suggests that they may behave more similarly to GO than nanocellulose, but their polymeric structure suggests a unique

behavior. While CDs consist of organic acids that should, in theory, be prone to microbial degradation, the small size and incredible dispersibility and aqueous stability of these nanodots suggest that microbial interactions may be difficult to achieve.[143-147] It is more likely that, after release, the primary environmental transformations of CDs upon release will be driven by photolytic processes while they remain suspended in the water column where they are prone to irradiation by sunlight and interactions with ROS. Slow photodegradation increases the potential for interaction of environmental organisms with CDs and their photoproducts, thereby increasing their risk. Thus, the photochemical transformations of CDs are the most crucial degradation pathway to identify and understand as the primary predictor of their environmental fate, risk, and impact after release.

1.4 Carbon Nanomaterials Examined in this Thesis

Of the wide-ranging family of carbon nanomaterials, three primary nanoparticles will be discussed in this thesis: CNTs, nanocellulose, and CDs. In this section, the specific nanomaterial systems relevant to this thesis will be outlined in greater detail. CNTs will be considered in the context of their incorporation into polymer nanocomposites and the effects of the combination on polymer biodegradation. Nanocellulose will be considered in terms of its biodegradation under both aerobic and anaerobic conditions after chemical modification of its surface. Finally, CDs will be assessed for their phototransformations under direct irradiation by natural sunlight as well as indirect photolysis by hydroxyl radicals produced via the irradiation of hydrogen peroxide.

CNTs are commonly used to reinforce polymer materials due to their impressive inherent material properties. Incorporation into polymer matrices is typically accomplished

via solution blending or melt mixing techniques. In PNCs, the initial environmental impact of CNTs is largely mitigated due to localization and shielding within a polymer matrix until the polymer is degraded in the environment. The process of polymer loss is largely driven by microbial interactions and has implications for waste management as the cytotoxicity and recalcitrance of CNTs has been shown to slow the rate of polymer loss.[148-150] While ultimately the polymer biodegrades irrespective of CNT inclusion, the already lengthy timescales required for polymer biodegradation in the environment are further extended with CNT incorporation. Thus, independent of the environmental risk of CNTs themselves, the effect of their incorporation into polymers must be understood in order to predict the behavior of CNT/PNCs after release. While CNT incorporation into polymers has consistently reduced the rate of polymer loss, a systematic analysis of the different factors that influence this rate has not been carried out. In Chapter 2 of this thesis, a study will be outlined that sought to identify the critical factors that influence the effect of CNT incorporation into polymer nanocomposites. Specifically, the effects of polymer type (i.e., rapid or gradual biodegradation), CNT type (i.e., pristine or oxidized), and biodegrading population (i.e., single or community culture, aerobic or anaerobic) were assessed. MWCNTs were incorporated into polycaprolactone (PCL) or polyhydroxyalkanoates (PHA) nanocomposites at a range of loadings to assess the impact of polymer on CNT/PNC biodegradation. CNT type was probed by loading PHA with pristine and oxidized MWCNTs at different loadings, with the primary effect of CNT surface oxidation being improved dispersion of the nanomaterial throughout the polymer matrix. Biodegradation was assessed via volumetric biogas measurements produced during polymer mineralization by an anaerobic community. Comparison to past studies that utilized single and aerobic

cultures to biodegrade CNT/PNCs facilitated assessment of the effect of the biodegrading community.

Research seeking to identify the impact of chemical modification on the biodegradation of nanocellulose will be outlined in Chapters 3 and 4. In Chapter 3, nanocellulose modified with different hydrophobic silanes will be assessed for both dispersibility and biodegradation. Silane reagents are commonly used to modify the surface of nanocellulose to improve their dispersion and interfacial adhesion in polymer nanocomposites. Here, methyl-, propyl-, and aminopropyl-trimethoxysilanes were used to modify the surface of CNFs with a coating of siloxane polymer. The impact of siloxane coatings on the dispersion of nanocellulose is evaluated in both solvent casting media (i.e., chloroform) and hydrophobic biopolymer (i.e., PHA). Both are critical systems to analyze as a well-dispersed filler is required to effectively reinforce a polymer matrix, and this dispersion is strongly related to the stability of the nanofiller in organic media. Coupled with determination of the dispersibility of modified nanocellulose is an assessment of its biodegradability. CNFs modified with different amounts of each silane reagent were exposed to an anaerobic microbial community with biodegradation determined via measurement of biogas production resulting from mineralization of each nanocellulose material.

Chapter 4 also involves modified nanocellulose but focuses on the effect of chemical functionalizations, rather than coatings, on the biodegradation of nanocellulose. By directly grafting different functional groups onto the surface of nanocellulose, surface chemistry is able to be tuned while avoiding the formation of an extensive coating as described in Chapter 3. Here, chemical functionalization of nanocellulose using different ester, ether,

and carboxylic acid groups was achieved. The extent of functionalization is reported as the degree of substitution (DS), or the average number of successfully substituted hydroxyl groups in each glucose subunit (0-3). The effect of these functionalizations on the biodegradation of CNFs in both aerobic and anaerobic wastewater was assessed and compared to existing literature involving the biodegradation of functionalized macrocellulose. The effects of chemical linkage (e.g., ester vs. ether) as well as overall DS and surface DS on CNF biodegradation were studied. Surface DS is rarely reported in functionalized cellulose literature, which is perhaps understandable as the importance of this region is minimized in macrocellulose. With the advent of nanocellulose, the surface takes on increased importance, and thus surface DS is a crucial parameter to assess. Surface DS was examined here using XPS to measure changes in carbon character as aliphatic functional groups were added to the nanocellulose surface. In this context, the mineralization of esterified CNF with a range of surface DS values by an anaerobic microbial community was evaluated in order to determine the parameter that dictates the biodegradation of functionalized nanocellulose.

The phototransformations of CDs are explored in Chapter 5 of this thesis. In particular, CDs were synthesized via the bottom-up approach, polymerizing citric or malic acid with ethylene diamine. These are some of the most commonly used CDs in both research and (projected) commercial applications. As such, they were chosen as model CDs to demonstrate the photolytic transformations CDs may experience after environmental release. Citric acid (CACD) and malic acid (MACD) CDs were assessed for phototransformations during both direct and indirect photolysis. Transformations of CDs during direct photolysis by exposure to natural sunlight was assessed using PL, ATR, and

XPS spectroscopies as well as TOC. Similarly, the transformations initiated via indirect photolysis by hydroxyl radicals were examined using ATR, XPS, and TOC as well as ion chromatography. The environmental relevance of such hydroxyl radical-driven transformations was understood via relation of hydroxyl radical concentration to the natural steady-state concentration of hydroxyl radicals in the environment. As such, general environmental timescales for CD phototransformations were modeled to predict the real-time phototransformations of CDs after release into the environment.

1.5 References

1. Khan, I.; Saeed, K.; Khan, I., Nanoparticles: Properties, applications and toxicities. *Arabian Journal of Chemistry* **2019,** *12* (7), 908-931.
2. Reibold, M.; Paufler, P.; Levin, A. A.; Kochmann, W.; Pätzke, N.; Meyer, D. C., Carbon nanotubes in an ancient Damascus sabre. *Nature* **2006,** *444* (7117), 286-286.
3. Griffin, S.; Masood, M. I.; Nasim, M. J.; Sarfraz, M.; Ebokaiwe, A. P.; Schäfer, K.-H.; Keck, C. M.; Jacob, C., Natural Nanoparticles: A Particular Matter Inspired by Nature. *Antioxidants (Basel)* **2017,** *7* (1), 3.
4. Bera, D.; Qian, L.; Tseng, T.-K.; Holloway, P. H., Quantum Dots and Their Multimodal Applications: A Review. *Materials* **2010,** *3* (4), 2260-2345.
5. Syafiuddin, A.; Salmiati; Salim, M. R.; Beng Hong Kueh, A.; Hadibarata, T.; Nur, H., A Review of Silver Nanoparticles: Research Trends, Global Consumption, Synthesis, Properties, and Future Challenges. *Journal of the Chinese Chemical Society* **2017,** *64* (7), 732-756.
6. Alsaba, M. T.; Al Dushaishi, M. F.; Abbas, A. K., A comprehensive review of nanoparticles applications in the oil and gas industry. *Journal of Petroleum Exploration and Production Technology* **2020,** *10* (4), 1389-1399.
7. Salata, O. V., Applications of nanoparticles in biology and medicine. *Journal of Nanobiotechnology* **2004,** *2* (1), 3.
8. Tuerhong, M.; Xu, Y.; Yin, X.-B., Review on Carbon Dots and Their Applications. *Chinese Journal of Analytical Chemistry* **2017,** *45* (1), 139-150.
9. Guerra, F. D.; Attia, M. F.; Whitehead, D. C.; Alexis, F., Nanotechnology for Environmental Remediation: Materials and Applications. *Molecules* **2018,** *23* (7), 1760.
10. McWilliams, A., Nanocomposites, Nanoparticles, Nanoclays and Nanotubes: Global Markets to 2022. *BCC Research* **2018**.
11. Bundschuh, M.; Filser, J.; Lüderwald, S.; McKee, M. S.; Metreveli, G.; Schaumann, G. E.; Schulz, R.; Wagner, S., Nanoparticles in the environment: where do we come from, where do we go to? *Environmental sciences Europe* **2018,** *30* (1), 6-6.
12. Petersen, E. J.; Zhang, L.; Mattison, N. T.; O'Carroll, D. M.; Whelton, A. J.; Uddin, N.; Nguyen, T.; Huang, Q.; Henry, T. B.; Holbrook, R. D.; Chen, K. L., Potential Release

Pathways, Environmental Fate, And Ecological Risks of Carbon Nanotubes. *Environ. Sci. Technol.* **2011,** *45* (23), 9837-9856.
13. Giese, B.; Klaessig, F.; Park, B.; Kaegi, R.; Steinfeldt, M.; Wigger, H.; von Gleich, A.; Gottschalk, F., Risks, Release and Concentrations of Engineered Nanomaterial in the Environment. *Sci. Rep.* **2018,** *8* (1), 1565.
14. Bowerman, W. W.; Giesy, J. P.; Best, D. A.; Kramer, V. J., A review of factors affecting productivity of bald eagles in the Great Lakes region: implications for recovery. *Environ. Health Perspect.* **1995,** *103 Suppl 4* (Suppl 4), 51-59.
15. Muralikrishna, I. V.; Manickam, V., Chapter Eight - Environmental Risk Assessment. In *Environmental Management*, Muralikrishna, I. V.; Manickam, V., Eds. Butterworth-Heinemann: 2017; pp 135-152.
16. Choudhary, N.; Hwang, S.; Choi, W., Carbon Nanomaterials: A Review. In *Handbook of Nanomaterials Properties*, Bhushan, B.; Luo, D.; Schricker, S. R.; Sigmund, W.; Zauscher, S., Eds. Springer Berlin Heidelberg: Berlin, Heidelberg, 2014; pp 709-769.
17. Patel, K. D.; Singh, R. K.; Kim, H.-W., Carbon-based nanomaterials as an emerging platform for theranostics. *Materials Horizons* **2019,** *6* (3), 434-469.
18. Georgakilas, V.; Perman, J. A.; Tucek, J.; Zboril, R., Broad Family of Carbon Nanoallotropes: Classification, Chemistry, and Applications of Fullerenes, Carbon Dots, Nanotubes, Graphene, Nanodiamonds, and Combined Superstructures. *Chem. Rev.* **2015,** *115* (11), 4744-4822.
19. Dufresne, A., *Nanocellulose: From Nature to High Performance Tailored Materials*. Walter de Gruyter: Berlin, Germany, 2012.
20. Turcheniuk, K.; Mochalin, V. N., Biomedical applications of nanodiamond (Review). *Nanotechnology* **2017,** *28* (25), 252001.
21. Iijima, S., Helical microtubules of graphitic carbon. *Nature* **1991,** *354* (6348), 56-58.
22. Saifuddin, N.; Raziah, A. Z.; Junizah, A. R., Carbon Nanotubes: A Review on Structure and Their Interaction with Proteins. *Journal of Chemistry* **2013,** *2013*, 676815.
23. Loos, M. R.; Schulte, K., Is It Worth the Effort to Reinforce Polymers With Carbon Nanotubes? *Macromolecular Theory and Simulations* **2011,** *20* (5), 350-362.
24. Takakura, A.; Beppu, K.; Nishihara, T.; Fukui, A.; Kozeki, T.; Namazu, T.; Miyauchi, Y.; Itami, K., Strength of carbon nanotubes depends on their chemical structures. *Nature Communications* **2019,** *10* (1), 3040.
25. Rahimian-Koloor, S. M.; Hashemianzadeh, S. M.; Shokrieh, M. M., Effect of CNT structural defects on the mechanical properties of CNT/Epoxy nanocomposite. *Physica B: Condensed Matter* **2018,** *540*, 16-25.
26. Kumanek, B.; Janas, D., Thermal conductivity of carbon nanotube networks: a review. *Journal of Materials Science* **2019,** *54* (10), 7397-7427.
27. Lekawa-Raus, A.; Patmore, J.; Kurzepa, L.; Bulmer, J.; Koziol, K., Electrical Properties of Carbon Nanotube Based Fibers and Their Future Use in Electrical Wiring. *Advanced Functional Materials* **2014,** *24* (24), 3661-3682.
28. He, H.; Pham-Huy, L. A.; Dramou, P.; Xiao, D.; Zuo, P.; Pham-Huy, C., Carbon Nanotubes: Applications in Pharmacy and Medicine. *BioMed Research International* **2013,** *2013*, 578290.
29. Li, L.; Yang, H.; Zhou, D.; Zhou, Y., Progress in Application of CNTs in Lithium-Ion Batteries. *Journal of Nanomaterials* **2014,** *2014*.

30. Durkin, D. P.; Gallagher, M. J.; Frank, B. P.; Knowlton, E. D.; Trulove, P. C.; Fairbrother, D. H.; Fox, D. M., Phosphorus-functionalized multi-wall carbon nanotubes as flame-retardant additives for polystyrene and poly (methyl methacrylate). *Journal of Thermal Analysis and Calorimetry* **2017,** *130* (2), 735-753.
31. Arash, B.; Wang, Q.; Varadan, V. K., Mechanical properties of carbon nanotube/polymer composites. *Sci. Rep.* **2014,** *4* (1), 6479.
32. Spitalsky, Z.; Tasis, D.; Papagelis, K.; Galiotis, C., Carbon nanotube–polymer composites: Chemistry, processing, mechanical and electrical properties. *Progress in Polymer Science* **2010,** *35* (3), 357-401.
33. Chang, T. E.; Jensen, L. R.; Kisliuk, A.; Pipes, R. B.; Pyrz, R.; Sokolov, A. P., Microscopic mechanism of reinforcement in single-wall carbon nanotube/polypropylene nanocomposite. *Polymer* **2005,** *46* (2), 439-444.
34. Safadi, B.; Andrews, R.; Grulke, E. A., Multiwalled carbon nanotube polymer composites: Synthesis and characterization of thin films. *J. Appl. Polym. Sci.* **2002,** *84* (14), 2660-2669.
35. Plank, J., Applications of biopolymers and other biotechnological products in building materials. *Applied Microbiology and Biotechnology* **2004,** *66* (1), 1-9.
36. Tang, X. Z.; Kumar, P.; Alavi, S.; Sandeep, K. P., Recent Advances in Biopolymers and Biopolymer-Based Nanocomposites for Food Packaging Materials. *Critical Reviews in Food Science and Nutrition* **2012,** *52* (5), 426-442.
37. Yadav, P.; Yadav, H.; Shah, V. G.; Shah, G.; Dhaka, G., Biomedical Biopolymers, their Origin and Evolution in Biomedical Sciences: A Systematic Review. *J Clin Diagn Res* **2015,** *9* (9), ZE21-ZE25.
38. Zhao, X.; Cornish, K.; Vodovotz, Y., Narrowing the Gap for Bioplastic Use in Food Packaging: An Update. *Environ. Sci. Technol.* **2020,** *54* (8), 4712-4732.
39. Steinbüchel, A., Production of rubber-like polymers by microorganisms. *Current Opinion in Microbiology* **2003,** *6* (3), 261-270.
40. Sun, J.; Shen, J.; Chen, S.; Cooper, M. A.; Fu, H.; Wu, D.; Yang, Z., Nanofiller Reinforced Biodegradable PLA/PHA Composites: Current Status and Future Trends. *Polymers* **2018,** *10* (5), 505.
41. Vallejo-Giraldo, C.; Pugliese, E.; Larrañaga, A.; Fernandez-Yague, M. A.; Britton, J. J.; Trotier, A.; Tadayyon, G.; Kelly, A.; Rago, I.; Sarasua, J.-R.; Dowd, E.; Quinlan, L. R.; Pandit, A.; Biggs, M. J., Polyhydroxyalkanoate/carbon nanotube nanocomposites: flexible electrically conducting elastomers for neural applications. *Nanomedicine* **2016,** *11* (19), 2547-2563.
42. Pinto, V. C.; Ramos, T.; Alves, S.; Xavier, J.; Tavares, P.; Moreira, P. M. G. P.; Guedes, R. M., Comparative Failure Analysis of PLA, PLA/GNP and PLA/CNT-COOH Biodegradable Nanocomposites thin Films. *Procedia Engineering* **2015,** *114*, 635-642.
43. Thomas, B.; Raj, M. C.; B, A. K.; H, R. M.; Joy, J.; Moores, A.; Drisko, G. L.; Sanchez, C., Nanocellulose, a Versatile Green Platform: From Biosources to Materials and Their Applications. *Chem. Rev.* **2018,** *118* (24), 11575-11625.
44. Chinga-Carrasco, G., Cellulose fibres, nanofibrils and microfibrils: The morphological sequence of MFC components from a plant physiology and fibre technology point of view. *Nanoscale Res. Lett.* **2011,** *6* (1), 417-417.

45. Nunes, R. C. R., 13 - Rubber nanocomposites with nanocellulose. In *Progress in Rubber Nanocomposites*, Thomas, S.; Maria, H. J., Eds. Woodhead Publishing: 2017; pp 463-494.
46. Feng, Y.-H.; Cheng, T.-Y.; Yang, W.-G.; Ma, P.-T.; He, H.-Z.; Yin, X.-C.; Yu, X.-X., Characteristics and Environmentally Friendly Extraction of Cellulose Nanofibrils from Sugarcane Bagasse. *Ind. Crops. Prod.* **2018,** *111* (Supplement C), 285-291.
47. Hamid, S. B. A.; Zain, S. K.; Das, R.; Centi, G., Synergic Effect of Tungstophosphoric Acid and Sonication for Rapid Synthesis of Crystalline Nanocellulose. *Carbohydr. Polym.* **2016,** *138*, 349-355.
48. Henriksson, M.; Henriksson, G.; Berglund, L. A.; Lindström, T., An Environmentally Friendly Method for Enzyme-Assisted Preparation of Microfibrillated Cellulose (MFC) Nanofibers. *Eur. Polym. J.* **2007,** *43* (8), 3434-3441.
49. Phanthong, P.; Karnjanakom, S.; Reubroycharoen, P.; Hao, X.; Abudula, A.; Guan, G., A Facile One-Step Way for Extraction of Nanocellulose with High Yield by Ball Milling with Ionic Liquid. *Cellulose* **2017,** *24* (5), 2083-2093.
50. Yadav, C.; Saini, A.; Maji, P. K., Energy Efficient Facile Extraction Process of Cellulose Nanofibres and their Dimensional Characterization using Light Scattering Techniques. *Carbohydr. Polym.* **2017,** *165* (Supplement C), 276-284.
51. de Amorim, J. D. P.; de Souza, K. C.; Duarte, C. R.; da Silva Duarte, I.; de Assis Sales Ribeiro, F.; Silva, G. S.; de Farias, P. M. A.; Stingl, A.; Costa, A. F. S.; Vinhas, G. M.; Sarubbo, L. A., Plant and bacterial nanocellulose: production, properties and applications in medicine, food, cosmetics, electronics and engineering. A review. *Environmental Chemistry Letters* **2020,** *18* (3), 851-869.
52. Sun, Y.-P.; Zhou, B.; Lin, Y.; Wang, W.; Fernando, K. A. S.; Pathak, P.; Meziani, M. J.; Harruff, B. A.; Wang, X.; Wang, H.; Luo, P. G.; Yang, H.; Kose, M. E.; Chen, B.; Veca, L. M.; Xie, S.-Y., Quantum-Sized Carbon Dots for Bright and Colorful Photoluminescence. *Journal of the American Chemical Society* **2006,** *128* (24), 7756-7757.
53. Tuerhong, M.; Xu, Y.; Yin, X.-B., Review on Carbon Dots and Their Applications. *Chinese Journal of Analytical Chemistry* **2017,** *45*, 139-150.
54. Zhi, B.; Cui, Y.; Wang, S.; Frank, B. P.; Williams, D. N.; Brown, R. P.; Melby, E. S.; Hamers, R. J.; Rosenzweig, Z.; Fairbrother, D. H.; Orr, G.; Haynes, C. L., Malic Acid Carbon Dots: From Super-resolution Live-Cell Imaging to Highly Efficient Separation. *ACS Nano* **2018,** *12* (6), 5741-5752.
55. Liu, M. L.; Chen, B. B.; Li, C. M.; Huang, C. Z., Carbon dots: synthesis, formation mechanism, fluorescence origin and sensing applications. *Green Chem.* **2019,** *21* (3), 449-471.
56. Silva, V. M.; Corson, N.; Elder, A.; Oberdörster, G., The Rat Ear Vein Model for Investigating In Vivo Thrombogenicity of Ultrafine Particles (UFP). *Toxicological Sciences* **2005,** *85* (2), 983-989.
57. Ozkara, A.; Akyil, D.; Konuk, M., *Pesticides, Environmental Pollution, and Health, Environmental Health Risk-Hazardous Factors to Living Species*. IntechOpen: 2016.
58. Cousins, I. T.; Ng, C. A.; Wang, Z.; Scheringer, M., Why is high persistence alone a major cause of concern? *Environ. Sci. Proc. Imp.* **2019,** *21* (5), 781-792.

59. Hartono, M. R.; Kushmaro, A.; Chen, X.; Marks, R. S., Probing the toxicity mechanism of multiwalled carbon nanotubes on bacteria. *Environmental Science and Pollution Research* **2018,** *25* (5), 5003-5012.
60. Allegri, M.; Perivoliotis, D. K.; Bianchi, M. G.; Chiu, M.; Pagliaro, A.; Koklioti, M. A.; Trompeta, A.-F. A.; Bergamaschi, E.; Bussolati, O.; Charitidis, C. A., Toxicity determinants of multi-walled carbon nanotubes: The relationship between functionalization and agglomeration. *Toxicology Reports* **2016,** *3*, 230-243.
61. Di Cristo, L.; Bianchi, M. G.; Chiu, M.; Taurino, G.; Donato, F.; Garzaro, G.; Bussolati, O.; Bergamaschi, E., Comparative in Vitro Cytotoxicity of Realistic Doses of Benchmark Multi-Walled Carbon Nanotubes towards Macrophages and Airway Epithelial Cells. *Nanomaterials* **2019,** *9* (7), 982.
62. Kang, S.; Herzberg, M.; Rodrigues, D. F.; Elimelech, M., Antibacterial Effects of Carbon Nanotubes: Size Does Matter! *Langmuir* **2008,** *24* (13), 6409-6413.
63. Kobayashi, N.; Izumi, H.; Morimoto, Y., Review of toxicity studies of carbon nanotubes. *J Occup Health* **2017,** *59* (5), 394-407.
64. Liu, X.; Guo, L.; Morris, D.; Kane, A. B.; Hurt, R. H., Targeted removal of bioavailable metal as a detoxification strategy for carbon nanotubes. *Carbon* **2008,** *46* (3), 489-500.
65. Liu, X.; Gurel, V.; Morris, D.; Murray, D. W.; Zhitkovich, A.; Kane, A. B.; Hurt, R. H., Bioavailability of Nickel in Single-Wall Carbon Nanotubes. *Advanced Materials* **2007,** *19* (19), 2790-2796.
66. Poulsen, S. S.; Jackson, P.; Kling, K.; Knudsen, K. B.; Skaug, V.; Kyjovska, Z. O.; Thomsen, B. L.; Clausen, P. A.; Atluri, R.; Berthing, T.; Bengtson, S.; Wolff, H.; Jensen, K. A.; Wallin, H.; Vogel, U., Multi-walled carbon nanotube physicochemical properties predict pulmonary inflammation and genotoxicity. *Nanotoxicology* **2016,** *10* (9), 1263-1275.
67. Wick, P.; Manser, P.; Limbach, L. K.; Dettlaff-Weglikowska, U.; Krumeich, F.; Roth, S.; Stark, W. J.; Bruinink, A., The degree and kind of agglomeration affect carbon nanotube cytotoxicity. *Toxicology Letters* **2007,** *168* (2), 121-131.
68. Patlolla, A. K.; Hussain, S. M.; Schlager, J. J.; Patlolla, S.; Tchounwou, P. B., Comparative study of the clastogenicity of functionalized and nonfunctionalized multiwalled carbon nanotubes in bone marrow cells of Swiss-Webster mice. *Environ Toxicol* **2010,** *25* (6), 608-621.
69. Ursini, C. L.; Cavallo, D.; Fresegna, A. M.; Ciervo, A.; Maiello, R.; Casciardi, S.; Tombolini, F.; Buresti, G.; Iavicoli, S., Study of Cytotoxic and Genotoxic Effects of Hydroxyl-Functionalized Multiwalled Carbon Nanotubes on Human Pulmonary Cells. *Journal of Nanomaterials* **2012,** *2012*, 9.
70. Kennedy, Alan J.; Hull, M. S.; Steevens, J. A.; Dontsova, K. M.; Chappell, M. A.; Gunter, J. C.; Weiss, J., Charles A., Factors influencing the partitioning and toxicity of nanotubes in the aquatic environment. *Environmental Toxicology and Chemistry* **2008,** *27* (9), 1932-1941.
71. Kennedy, A. J.; Gunter, J. C.; Chappell, M. A.; Goss, J. D.; Hull, M. S.; Kirgan, R. A.; Steevens, J. A., Influence of nanotube preparation in Aquatic Bioassays. *Environmental Toxicology and Chemistry* **2009,** *28* (9), 1930-1938.

72. Zheng, X.; Su, Y.; Chen, Y.; Wan, R.; Li, M.; Wei, Y.; Huang, H., Carboxyl-modified single-walled carbon nanotubes negatively affect bacterial growth and denitrification activity. *Sci. Rep.* **2014,** *4* (1), 5653.
73. Parks, A. N.; Chandler, G. T.; Ho, K. T.; Burgess, R. M.; Ferguson, P. L., Environmental biodegradability of [14C] single-walled carbon nanotubes by Trametes versicolor and natural microbial cultures found in New Bedford Harbor sediment and aerated wastewater treatment plant sludge. *Environmental Toxicology and Chemistry* **2015,** *34* (2), 247-251.
74. Kausar, A.; Rafique, I.; Muhammad, B., Review of Applications of Polymer/Carbon Nanotubes and Epoxy/CNT Composites. *Polym. Plast. Technol. Eng.* **2016,** *55* (11), 1167-1191.
75. Endes, C.; Camarero-Espinosa, S.; Mueller, S.; Foster, E. J.; Petri-Fink, A.; Rothen-Rutishauser, B.; Weder, C.; Clift, M. J. D., A critical review of the current knowledge regarding the biological impact of nanocellulose. *Journal of Nanobiotechnology* **2016,** *14* (1), 78.
76. Frank, B. P.; Durkin, D. P.; Caudill, E. R.; Zhu, L.; White, D. H.; Curry, M. L.; Pedersen, J. A.; Fairbrother, D. H., Impact of Silanization on the Structure, Dispersion Properties, and Biodegradability of Nanocellulose as a Nanocomposite Filler. *ACS Applied Nano Materials* **2018,** *1* (12), 7025-7038.
77. Hofsten, B. V.; Edberg, N., Estimating the Rate of Degradation of Cellulose Fibers in Water. *Oikos* **1972,** *23* (1), 29-34.
78. Ruka, D. R.; Sangwan, P.; Garvey, C. J.; Simon, G. P.; Dean, K. M., Biodegradability of Poly-3-hydroxybutyrate/Bacterial Cellulose Composites under Aerobic Conditions, Measured via Evolution of Carbon Dioxide and Spectroscopic and Diffraction Methods. *Environ. Sci. Technol.* **2015,** *49* (16), 9979-9986.
79. Wang, S.; Lydon, K. A.; White, E. M.; Grubbs, J. B.; Lipp, E. K.; Locklin, J.; Jambeck, J. R., Biodegradation of Poly(3-hydroxybutyrate-co-3-hydroxyhexanoate) Plastic under Anaerobic Sludge and Aerobic Seawater Conditions: Gas Evolution and Microbial Diversity. *Environ. Sci. Technol.* **2018,** *52* (10), 5700-5709.
80. Singh, G.; Chandoha-Lee, C.; Zhang, W.; Renneckar, S.; Vikesland, P. J.; Pruden, A., Biodegradation of Nanocrystalline Cellulose by Two Environmentally-Relevant Consortia. *Water Res.* **2016,** *104*, 137-146.
81. Isogai, A.; Saito, T.; Fukuzumi, H., TEMPO-oxidized cellulose nanofibers. *Nanoscale* **2011,** *3* (1), 71-85.
82. Lin, N.; Dufresne, A., Nanocellulose in biomedicine: Current status and future prospect. *Eur. Polym. J.* **2014,** *59*, 302-325.
83. Abushammala, H.; Mao, J., A Review of the Surface Modification of Cellulose and Nanocellulose Using Aliphatic and Aromatic Mono- and Di-Isocyanates. *Molecules* **2019,** *24* (15), 2782.
84. Kovacs, T.; Naish, V.; O'Connor, B.; Blaise, C.; Gagné, F.; Hall, L.; Trudeau, V.; Martel, P., An ecotoxicological characterization of nanocrystalline cellulose (NCC). *Nanotoxicology* **2010,** *4* (3), 255-270.
85. Harper, B. J.; Clendaniel, A.; Sinche, F.; Way, D.; Hughes, M.; Schardt, J.; Simonsen, J.; Stefaniak, A. B.; Harper, S. L., Impacts of chemical modification on the toxicity of diverse nanocellulose materials to developing zebrafish. *Cellulose (London, England)* **2016,** *23* (3), 1763-1775.

86. Havrdova, M.; Hola, K.; Skopalik, J.; Tomankova, K.; Petr, M.; Cepe, K.; Polakova, K.; Tucek, J.; Bourlinos, A. B.; Zboril, R., Toxicity of carbon dots – Effect of surface functionalization on the cell viability, reactive oxygen species generation and cell cycle. *Carbon* **2016,** *99*, 238-248.
87. Liu, J.-H.; Wang, Y.; Yan, G.-H.; Yang, F.; Gao, H.; Huang, Y.; Wang, H.; Wang, P.; Yang, L.; Tang, Y.; Teisl, L. R.; Sun, Y.-P., Systematic Toxicity Evaluations of High-Performance Carbon "Quantum" Dots. *Journal of Nanoscience and Nanotechnology* **2019,** *19* (4), 2130-2137.
88. Bagheri, Z.; Ehtesabi, H.; Hallaji, Z.; Latifi, H.; Behroodi, E., Investigation the cytotoxicity and photo-induced toxicity of carbon dot on yeast cell. *Ecotoxicology and Environmental Safety* **2018,** *161*, 245-250.
89. Yao, K.; Lv, X.; Zheng, G.; Chen, Z.; Jiang, Y.; Zhu, X.; Wang, Z.; Cai, Z., Effects of Carbon Quantum Dots on Aquatic Environments: Comparison of Toxicity to Organisms at Different Trophic Levels. *Environ. Sci. Technol.* **2018,** *52* (24), 14445-14451.
90. Belkahla, H.; Boudjemaa, R.; Caorsi, V.; Pineau, D.; Curcio, A.; Lomas, J. S.; Decorse, P.; Chevillot-Biraud, A.; Azaïs, T.; Wilhelm, C.; Randriamahazaka, H.; Hémadi, M., Carbon dots, a powerful non-toxic support for bioimaging by fluorescence nanoscopy and eradication of bacteria by photothermia. *Nanoscale Advances* **2019,** *1* (7), 2571-2579.
91. Semeniuk, M.; Yi, Z.; Poursorkhabi, V.; Tjong, J.; Jaffer, S.; Lu, Z.-H.; Sain, M., Future Perspectives and Review on Organic Carbon Dots in Electronic Applications. *ACS Nano* **2019,** *13* (6), 6224-6255.
92. Sharma, A.; Das, J., Small molecules derived carbon dots: synthesis and applications in sensing, catalysis, imaging, and biomedicine. *Journal of Nanobiotechnology* **2019,** *17* (1), 92.
93. Derjaguin, B.; Landau, L., Theory of the stability of strongly charged lyophobic sols and of the adhesion of strongly charged particles in solutions of electrolytes. *Progress in Surface Science* **1993,** *43* (1), 30-59.
94. Verwey, E. J. W., Theory of the Stability of Lyophobic Colloids. *The Journal of Physical and Colloid Chemistry* **1947,** *51* (3), 631-636.
95. Bayati, M.; Dai, J.; Zambrana, A.; Rees, C.; Fidalgo de Cortalezzi, M., Effect of water chemistry on the aggregation and photoluminescence behavior of carbon dots. *J. Environ. Sci.* **2018,** *65*, 223-235.
96. Dager, A.; Uchida, T.; Maekawa, T.; Tachibana, M., Synthesis and characterization of mono-disperse carbon quantum dots from fennel seeds: photoluminescence analysis using machine learning. *Sci. Rep.* **2019,** *9* (1), 14004.
97. Kamrani, S.; Rezaei, M.; Kord, M.; Baalousha, M., Transport and retention of carbon dots (CDs) in saturated and unsaturated porous media: role of ionic strength, pH, and collector grain size. *Water Res.* **2018,** *133*, 338-347.
98. Li, Q.; Chen, B.; Xing, B., Aggregation kinetics and self-assembly mechanisms of graphene quantum dots in aqueous solutions: cooperative effects of pH and electrolytes. *Environ. Sci. Technol.* **2017,** *51* (3), 1364-1376.
99. Liu, X.; Li, J.; Huang, Y.; Wang, X.; Zhang, X.; Wang, X., Adsorption, aggregation, and deposition behaviors of carbon dots on minerals. *Environ. Sci. Technol.* **2017,** *51* (11), 6156-6164.

100. Pasquini, L. M.; Hashmi, S. M.; Sommer, T. J.; Elimelech, M.; Zimmerman, J. B., Impact of Surface Functionalization on Bacterial Cytotoxicity of Single-Walled Carbon Nanotubes. *Environ. Sci. Technol.* **2012,** *46* (11), 6297-6305.
101. Sumaraj; Padhye, L. P., Influence of surface chemistry of carbon materials on their interactions with inorganic nitrogen contaminants in soil and water. *Chemosphere* **2017,** *184*, 532-547.
102. Zhang, S.; Shao, T.; Bekaroglu, S. S. K.; Karanfil, T., The Impacts of Aggregation and Surface Chemistry of Carbon Nanotubes on the Adsorption of Synthetic Organic Compounds. *Environ. Sci. Technol.* **2009,** *43* (15), 5719-5725.
103. Hou, W.-C.; BeigzadehMilani, S.; Jafvert, C. T.; Zepp, R. G., Photoreactivity of unfunctionalized single-wall carbon nanotubes involving hydroxyl radical: chiral dependency and surface coating effect. *Environ. Sci. Technol.* **2014,** *48* (7), 3875-3882.
104. Hou, W.-C.; Chowdhury, I.; Goodwin, D. G.; Henderson, W. M.; Fairbrother, D. H.; Bouchard, D.; Zepp, R. G., Photochemical transformation of graphene oxide in sunlight. *Environ. Sci. Technol.* **2015,** *49* (6), 3435-3443.
105. Hou, W.-C.; Henderson, W. M.; Chowdhury, I.; Goodwin, D. G.; Chang, X.; Martin, S.; Fairbrother, D. H.; Bouchard, D.; Zepp, R. G., The contribution of indirect photolysis to the degradation of graphene oxide in sunlight. *Carbon* **2016,** *110*, 426-437.
106. Hou, W.-C.; Jafvert, C. T., Photochemical transformation of aqueous C60 clusters in sunlight. *Environ. Sci. Technol.* **2009,** *43* (2), 362-367.
107. Liu, L.; Zhu, C.; Fan, M.; Chen, C.; Huang, Y.; Hao, Q.; Yang, J.; Wang, H.; Sun, D., Oxidation and degradation of graphitic materials by naphthalene-degrading bacteria. *Nanoscale* **2015,** *7* (32), 13619-13628.
108. Dang, H.; Lovell, C. R., Microbial Surface Colonization and Biofilm Development in Marine Environments. *Microbiol. Mol. Biol. Rev.* **2016,** *80* (1), 91-138.
109. Dussud, C.; Hudec, C.; George, M.; Fabre, P.; Higgs, P.; Bruzaud, S.; Delort, A.-M.; Eyheraguibel, B.; Meistertzheim, A.-L.; Jacquin, J.; Cheng, J.; Callac, N.; Odobel, C.; Rabouille, S.; Ghiglione, J.-F., Colonization of Non-biodegradable and Biodegradable Plastics by Marine Microorganisms. *Front Microbiol* **2018,** *9*, 1571-1571.
110. Siracusa, V., Microbial Degradation of Synthetic Biopolymers Waste. *Polymers* **2019,** *11* (6), 1066.
111. Wu, C.-S., Preparation, characterization, and biodegradability of renewable resource-based composites from recycled polylactide bioplastic and sisal fibers. *J. Appl. Polym. Sci.* **2012,** *123* (1), 347-355.
112. Das, M. P.; Kumar, S., An approach to low-density polyethylene biodegradation by Bacillus amyloliquefaciens. *3 Biotech* **2015,** *5* (1), 81-86.
113. Rizzarelli, P.; Carroccio, S., Modern mass spectrometry in the characterization and degradation of biodegradable polymers. *Analytica Chimica Acta* **2014,** *808*, 18-43.
114. Zhang, J.; Wang, X.; Gong, J.; Gu, Z., A study on the biodegradability of polyethylene terephthalate fiber and diethylene glycol terephthalate. *J. Appl. Polym. Sci.* **2004,** *93* (3), 1089-1096.
115. Zumstein, M. T.; Narayan, R.; Kohler, H.-P. E.; McNeill, K.; Sander, M., Dos and Do Nots When Assessing the Biodegradation of Plastics. *Environ. Sci. Technol.* **2019,** *53* (17), 9967-9969.
116. Zumstein, M. T.; Schintlmeister, A.; Nelson, T. F.; Baumgartner, R.; Woebken, D.; Wagner, M.; Kohler, H.-P. E.; McNeill, K.; Sander, M., Biodegradation of synthetic

polymers in soils: Tracking carbon into CO(2) and microbial biomass. *Sci Adv* **2018,** *4* (7), eaas9024-eaas9024.
117. Angelidaki, I.; Sanders, W., Assessment of the Anaerobic Biodegradability of Macropollutants. *Rev. Environ. Sci. Biotechnol.* **2004,** *3* (2), 117-129.
118. Owen, W. F.; Stuckey, D. C.; Healy, J. B.; Young, L. Y.; McCarty, P. L., Bioassay for Monitoring Biochemical Methane Potential and Anaerobic Toxicity. *Water Res.* **1979,** *13* (6), 485-492.
119. Pérez, J.; Muñoz-Dorado, J.; de la Rubia, T.; Martínez, J., Biodegradation and biological treatments of cellulose, hemicellulose and lignin: an overview. *International Microbiology* **2002,** *5* (2), 53-63.
120. Komarek, R. J.; Gardner, R. M.; Buchanan, C. M.; Gedon, S., Biodegradation of radiolabeled cellulose acetate and cellulose propionate. *J. Appl. Polym. Sci.* **1993,** *50* (10), 1739-1746.
121. Onken, U.; Liefke, E. In *Effect of total and partial pressure (oxygen and carbon dioxide) on aerobic microbial processes*, Berlin, Heidelberg, Springer Berlin Heidelberg: Berlin, Heidelberg, 1989; pp 137-169.
122. Singh, A. K., Chapter 8 - Nanoparticle Ecotoxicology. In *Engineered Nanoparticles*, Singh, A. K., Ed. Academic Press: Boston, 2016; pp 343-450.
123. Bohutskyi, P.; Betenbaugh, M. J.; Bouwer, E. J., The effects of alternative pretreatment strategies on anaerobic digestion and methane production from different algal strains. *Bioresource Technology* **2014,** *155*, 366-372.
124. Bohutskyi, P.; Keller, T. A.; Phan, D.; Parris, M. L.; Li, M.; Richardson, L.; Kopachevsky, A. M., Co-digestion of Wastewater-Grown Filamentous Algae With Sewage Sludge Improves Biomethane Production and Energy Balance Compared to Thermal, Chemical, or Thermochemical Pretreatments. *Frontiers in Energy Research* **2019,** *7* (47).
125. Li, P.; Li, W.; Sun, M.; Xu, X.; Zhang, B.; Sun, Y., Evaluation of Biochemical Methane Potential and Kinetics on the Anaerobic Digestion of Vegetable Crop Residues. *Energies* **2019,** *12* (1), 26.
126. Morales, G.; Llorente, I.; Montesinos, E.; Moragrega, C., A model for predicting Xanthomonas arboricola pv. pruni growth as a function of temperature. *PLOS ONE* **2017,** *12* (5), e0177583.
127. Wang, Y.; Roddick, F. A.; Fan, L., Direct and indirect photolysis of seven micropollutants in secondary effluent from a wastewater lagoon. *Chemosphere* **2017,** *185*, 297-308.
128. Duan, L.; Zhang, T.; Song, W.; Jiang, C.; Hou, Y.; Zhao, W.; Chen, W.; Alvarez, P. J. J., Photolysis of graphene oxide in the presence of nitrate: implications for graphene oxide integrity in water and wastewater treatment. *Environ. Sci.: Nano* **2019,** *6* (1), 136-145.
129. Remucal, C. K., The role of indirect photochemical degradation in the environmental fate of pesticides: a review. *Environ. Sci. Proc. Imp.* **2014,** *16* (4), 628-653.
130. Gligorovski, S.; Strekowski, R.; Barbati, S.; Vione, D., Environmental implications of hydroxyl radicals (•OH). *Chem. Rev.* **2015,** *115* (24), 13051-13092.
131. Zepp, R. G.; Faust, B. C.; Hoigne, J., Hydroxyl radical formation in aqueous reactions (pH 3-8) of iron(II) with hydrogen peroxide: the photo-Fenton reaction. *Environ. Sci. Technol.* **1992,** *26* (2), 313-319.

132. Schierz, A.; Zänker, H., Aqueous suspensions of carbon nanotubes: Surface oxidation, colloidal stability and uranium sorption. *Environmental Pollution* **2009,** *157* (4), 1088-1094.
133. Yang, J.; Bitter, J. L.; Smith, B. A.; Fairbrother, D. H.; Ball, W. P., Transport of Oxidized Multi-Walled Carbon Nanotubes through Silica Based Porous Media: Influences of Aquatic Chemistry, Surface Chemistry, and Natural Organic Matter. *Environ. Sci. Technol.* **2013,** *47* (24), 14034-14043.
134. Bitter, J. L.; Yang, J.; Beigzadeh Milani, S.; Jafvert, C. T.; Fairbrother, D. H., Transformations of oxidized multiwalled carbon nanotubes exposed to UVC (254 nm) irradiation. *Environ. Sci.: Nano* **2014,** *1* (4), 324-337.
135. Li, J.; Chen, C.; Zhang, S.; Wang, X., Surface functional groups and defects on carbon nanotubes affect adsorption–desorption hysteresis of metal cations and oxoanions in water. *Environ. Sci.: Nano* **2014,** *1* (5), 488-495.
136. Naasz, S.; Altenburger, R.; Kühnel, D., Environmental mixtures of nanomaterials and chemicals: The Trojan-horse phenomenon and its relevance for ecotoxicity. *Science of The Total Environment* **2018,** *635*, 1170-1181.
137. Song, M.; Wang, F.; Zeng, L.; Yin, J.; Wang, H.; Jiang, G., Co-exposure of Carboxyl-Functionalized Single-Walled Carbon Nanotubes and 17α-Ethinylestradiol in Cultured Cells: Effects on Bioactivity and Cytotoxicity. *Environ. Sci. Technol.* **2014,** *48* (23), 13978-13984.
138. Deline, A. R.; Frank, B. P.; Smith, C.; Wallace, A.; Sigmon, L. R.; Durkin, D. P.; Goodwin, D. G., Jr.; Gallagher, M. J.; Fairbrother, D. H., Influence of Oxygen-Containing Functional Groups on the Environmental Properties, Transformations, and Toxicity of Carbon Nanotubes. *Chem. Rev.* **Submitted**.
139. Zhao, B.; Wang, J.; Li, Z.; Liu, P.; Chen, D.; Zhang, Y., Mechanical strength improvement of polypropylene threads modified by PVA/CNT composite coatings. *Mater. Lett.* **2008,** *62* (28), 4380-4382.
140. Daud, J. B.; Lee, K.-Y., Surface Modification of Nanocellulose. In *Handbook of Nanocellulose and Cellulose Nanocomposites*, 2017; pp 101-122.
141. Leschine, S. B., Cellulose Degradation in Anaerobic Environments. *Annu. Rev. Microbiol.* **1995,** *49* (1), 399-426.
142. Béguin, P.; Aubert, J.-P., The biological degradation of cellulose. *FEMS Microbiology Reviews* **1994,** *13* (1), 25-58.
143. Fiuza, T.; Gomide, G.; Campos, A. F. C.; Messina, F.; Depeyrot, J., On the Colloidal Stability of Nitrogen-Rich Carbon Nanodots Aqueous Dispersions. *C — Journal of Carbon Research* **2019,** *5* (4), 74.
144. Wang, W.; Damm, C.; Walter, J.; Nacken, T. J.; Peukert, W., Photobleaching and stabilization of carbon nanodots produced by solvothermal synthesis. *Physical Chemistry Chemical Physics* **2016,** *18* (1), 466-475.
145. Xu, M.; Xu, S.; Yang, Z.; Shu, M.; He, G.; Huang, D.; Zhang, L.; Li, L.; Cui, D.; Zhang, Y., Hydrophilic and blue fluorescent N-doped carbon dots from tartaric acid and various alkylol amines under microwave irradiation. *Nanoscale* **2015,** *7* (38), 15915-15923.
146. Zhang, B.; Liu, C.-y.; Liu, Y., A Novel One-Step Approach to Synthesize Fluorescent Carbon Nanoparticles. *European Journal of Inorganic Chemistry* **2010,** *2010* (28), 4411-4414.

147. Zhao, P.; Zhu, L., Dispersibility of carbon dots in aqueous and/or organic solvents. *Chemical Communications* **2018,** *54* (43), 5401-5406.
148. Goodwin, D. G.; Boyer, I.; Devahif, T.; Gao, C.; Frank, B. P.; Lu, X.; Kuwama, L.; Gordon, T. B.; Wang, J.; Ranville, J. F.; Bouwer, E. J.; Fairbrother, D. H., Biodegradation of Carbon Nanotube/Polymer Nanocomposites using a Monoculture. *Environ. Sci. Technol.* **2018,** *52* (1), 40-51.
149. Goodwin, D. G.; Marsh, K. M.; Sosa, I. B.; Payne, J. B.; Gorham, J. M.; Bouwer, E. J.; Fairbrother, D. H., Interactions of Microorganisms with Polymer Nanocomposite Surfaces Containing Oxidized Carbon Nanotubes. *Environ. Sci. Technol.* **2015,** *49* (9), 5484-5492.
150. Goodwin, D. G.; Xia, Z.; Gordon, T. B.; Gao, C.; Bouwer, E. J.; Fairbrother, D. H., Biofilm development on carbon nanotube/polymer nanocomposites. *Environ. Sci.: Nano* **2016,** *3* (3), 545-558.

Chapter 2. Influence of Polymer Type and Carbon Nanotube Properties on Carbon Nanotube/Polymer Nanocomposite Biodegradation

Reproduced from

Frank, B.P.; Goodwin, D.G., Jr.; Bohutskyi, P.; Lu, X.; Kuwama, L.; Bouwer, E. J.; Fairbrother, D. H., Influence of Polymer Type and Carbon Nanotube Properties on Carbon Nanotube/Polymer Nanocomposite Biodegradation. *Science of the Total Environment*. **Submitted 2020**.

2.1 Abstract

The interaction of anaerobic microorganisms with carbon nanotube/polymer nanocomposites (CNT/PNC) will play a major role in determining their persistence and environmental fate at the end of consumer use when these nano-enabled materials enter landfills and encounter wastewater. Motivated by the need to understand how different parameters (*i.e.,* polymer type, microbial phenotype, CNT characteristics) influence CNT/PNC biodegradation rates, we have used volumetric biogas measurements and kinetic modeling to study biodegradation as a function of polymer type and CNT properties. In one set of experiments, oxidized multiwall carbon nanotubes (O-MWCNTs) with a range of CNT loadings 0 – 5% w/w were incorporated into poly-ε-caprolactone (PCL) and polyhydroxyalkanoates (PHA) matrices and subjected to biodegradation by an anaerobic microbial community. For each CNT/PNC, complete polymer biodegradation was ultimately observed, although the rate of biodegradation was inhibited above certain

critical CNT loadings dependent upon the polymer type. Higher loadings of pristine MWCNTs were needed to decrease the rate of polymer biodegradation compared to O-MWCNTs, an effect ascribed principally to differences in CNT dispersion within the polymer matrices. Above certain CNT loadings, a CNT mat of similar shape to the initial PNC was formed after polymer biodegradation, while below this threshold, CNT aggregates fragmented in the media. In situations where biodegradation was rapid, methanogen growth was disproportionately inhibited compared to the overall microbial community. Analysis of the results obtained from this study indicates that the inhibitory effect of CNTs on polymer biodegradation rate is greatest under conditions (*i.e.,* polymer type, microbial phenotype, CNT dispersion) where biodegradation of the neat polymer is slowest. This new insight provides a means to predict the environmental fate, persistence and transformations of CNT-enabled polymer materials.

2.2 Introduction

Bio-derived polymers are appealing for commercial applications by virtue of being both cheap and environmentally transient as they are sourced from renewable precursors such as plants, algae, and bacteria.[1-2] Examples of biopolymers include poly(butylene succinate) (PBS), polylactic acid (PLA), cellulose, starch, and polyhydroxyalkanoates (PHA). However, these biopolymers often possess poor mechanical properties which severely restrict their range of application.[3-5] One way to overcome this issue is to use fillers such as multiwall carbon nanotubes (MWCNTs) whose high mechanical strength, electrical conductivity, and thermal properties can be imparted to a polymer.[6-10] For example, MWCNTs have been shown to significantly improve the mechanical strength and electrical conductivity of PLA nanocomposites[10] as well as the tensile strength of PHA.[7]

CNT loadings in carbon nanotube/polymer nanocomposites (CNT/PNCs) are typically in the range of 1-10% w/w, with the ideal loading depending on application (*e.g.,* material reinforcement vs. thermal stability), polymer type, and CNT dispersion.[11-15]

After the disposal of CNT/PNCs at the end of their consumer lifetime, a primary route of degradation will stem from interactions with anaerobic microorganisms in landfills, surface waters, soils, and wastewater treatment plants.[16-17] Biopolymers are typically biodegradable on the timescales of months to a few years due to their enzymatically labile chemical linkages, in marked contrast to many petroleum-based polymers which are more stable to bacterial degradation.[18-20] CNTs have previously been shown to impact the biodegradation of polymers[21] due to their inherent cytotoxicity and recalcitrance.[22] After biodegrading surface polymer of CNT/PNCs, bacteria are exposed to a cytotoxic CNT surface which impedes bacterial growth and the formation of an active biofilm. Additionally, a high loading of CNTs may lead to the formation of an extensive CNT surface which can inhibit access of microorganisms to underlying polymer. Thus, it is important to understand how, under what conditions, and to what extent the inclusion of CNTs influences the biodegradation of polymer-based nanocomposites.

We have previously shown that the rate of polycaprolactone (PCL) loss from pristine MWCNT/PCL and oxidized-MWCNT (O-MWCNT)/PCL nanocomposites in the presence of axenic *Pseudomonas aeruginosa*, an aerobic culture, decreased significantly and systematically with increasing CNT loading between 0.1-10% w/w.[21] A related study, however, found that the biodegradation of MWCNT/PHA PNCs across the same range of loadings occurred at rates unaffected by the presence of CNTs, suggesting that the effect of CNT incorporation on PNC biodegradation is sensitive to the conditions under which

biodegradation occurs.[19] Examples of such conditions include the source and phenotype of the culture used, polymer type, oxidation-reduction potential of the environment, and CNT characteristics (*e.g.,* surface oxidation state, dispersion).

In previous studies, different combinations of polymers (PHA *vs.* PCL) and microbial inocula (axenic/consortia, aerobic/anaerobic) were utilized, so the comparative influence of each variable on the biodegradation of CNT/PNCs was obscured.[19, 21] The impact of CNT surface oxidation on the biodegradation of CNT/PNCs is also a relevant factor to consider due to the widespread use of both oxidized and pristine MWCNTs in polymeric materials.[8-9, 23-24] To systematically evaluate how CNTs inhibit biodegradation rates across different PNC types, this work compares the effect of O-MWCNT inclusion on the biodegradation of a highly biodegradable bio-polymer (PHA) compared to a polymer with a slower biodegradation profile (PCL) under the same environmental conditions and inoculum source. Furthermore, PNCs prepared using PHA and either pristine or oxidized MWCNTs were assayed to isolate the effect of CNT type and dispersion on PNC biodegradation. These experiments were designed to develop a holistic understanding of how the biodegradation rate of CNT/PNCs is influenced by the polymer, CNT type, and nature of the microbial community.

Solution blended CNT/PCL and CNT/PHA nanocomposites loaded with either pristine or oxidized MWCNTs were exposed to an anaerobic microbial community under conditions representative of those that CNT/PNCs will be exposed to in landfills, soils, sediments, and sewage sludge at wastewater treatment plants.[25-28] The biodegradability of CNT/PNCs was monitored by volumetric production of biogas as the polymer component was mineralized into a mixture of CO_2 and CH_4 under anaerobic conditions. To assess the

attainment of ultimate polymer biodegradation, biogas production for each CNT/PNC was compared to the theoretically estimated maximum volume expected for each polymer type. The effect of CNT inhibition was evaluated by comparing the ability of four kinetic models to fit the rate of biogas production. Methane production was tracked to measure the impact of CNTs on methanogenic microorganisms, the most sensitive members of the anaerobic consortia.[29-30] The range of CNT loadings was selected based on typical values used to prepare CNT/PNCs.[11-15]

2.3 Experimental

2.3.1 O-MWCNT/PCL Nanocomposite Preparation

Neat PCL and O-MWCNT/PCL nanocomposites were prepared using solution blending. Full details of PNC synthesis can be found in the Appendix (Chapter 6). All % w/w values refer to the mass loading with respect to the polymer mass, unless otherwise stated. For example, 20 mg of CNTs added to 400 mg of polymer would be referred to as 5% w/w.

O-MWCNTs were prepared by refluxing Nanocyl MWCNTs (Nanocyl NC7000, outer diameter 9.5 nm, 1.5 μm length, 90% purity) in 0.3 M HNO_3 for 5 h at 110 °C. The resulting O-MWCNTs were washed with deionized water continuously until the pH of the filtrate reached 7 and then dried in an oven overnight at 80 °C. These O-MWCNTs had an oxygen content of 4.1% as measured with X-ray photoelectron spectroscopy (XPS).

O-MWCNT/PCL nanocomposites were prepared by adding 16 mg (5% w/w) of ethyl cellulose (EC) and a particular mass of CNTs (0.1, 0.5, or 2% w/w) to 40 mL of dichloromethane (DCM) and sonicating in an ice water bath for 1 h to optimize dispersion quality. The EC macromolecules were used to stabilize the CNTs in DCM. PCL (400 mg)

was then added to each CNT suspension and sonicated for an additional 3 h to create a casting solution. To cast PNCs, 5 mL aliquots of the casting solutions were added to aluminum dishes and dried overnight. Neat PCL films containing 5% w/w EC without CNTs were also prepared as controls using the same conditions. PCL and CNT/PCL nanocomposites were recovered and trimmed to a uniform size (~30 mm in diameter) and mass (27 ± 3 mg). Composite characterization using differential scanning calorimetry (DSC), thermal gravimetric analysis (TGA), and energy dispersive X-ray spectroscopy (EDS) can be found in Goodwin et al.[21]

2.3.2 O-MWCNT/PHA and Pristine MWCNT/PHA Nanocomposite Preparation

Both oxidized and pristine MWCNT were used to prepare CNT/PHA nanocomposites using solution blending. The same O-MWCNTs used with PCL were also used with PHA. Pristine MWCNTs were obtained from NanoLab Inc. (outer diameter 15 ± 5 nm, length 5-20 μm). To prepare each PHA nanocomposite, a particular mass of O-MWCNTs (0.1, 2, or 5% w/w) or pristine MWCNTs (0.1, 2, 5, or 10% w/w) and 80 mg (5% w/w) EC were added to 160 mL chloroform and sonicated for 3 h. After sonication, 1600 mg of polyhydroxyalkanoates (PHA), a copolymer of poly-3-hydroxybutyrate (P3HB) and poly-4-hydroxybutyrate (P4HB), was added before sonicating for an additional 2 h to prepare a casting solution. A previously determined volume of this casting suspension, discussed further in Phan et al.,[19] was then poured into aluminum dishes and allowed to sit overnight to enable solvent evaporation. Neat PHA films containing 5% w/w EC without CNT fillers were also prepared as controls. The nanocomposites and neat PHA were then peeled from the aluminum dishes and trimmed around the edges to have similar physical dimensions (~30 mm diameter) and masses (31.1 ± 2.1 mg). Further composite

characterization including DSC, TGA, and EDS can be found in Phan et al.[19]

2.3.3 Biogas and Biomethane Potential Test of CNT/PNCs

The biomethane potential (BMP) test was used to evaluate the biodegradation of both neat polymers and CNT/PNCs containing different mass loadings of CNTs by tracking the amount of biogas and methane produced by anaerobic microorganisms. The procedure for the BMP test follows that from Owen et al.,[31] with minor modifications as described previously.[32] Triplicate bottles containing PHA or CNT/PHA samples were incubated for 60 d while triplicate bottles containing PCL or CNT/PCL samples were incubated for 395 d or longer. Blank samples without PNCs added were also incubated to account for biogas and methane production (<40 mL) from the inoculum. Sampling details are described in the SI.

Theoretical maximum biogas volume and composition were calculated using the Buswell equation:[33]

$$C_cH_hO_oN_n + y(H_2O) \rightarrow x(CH_4) + (c-x)CO_2 + n(NH_3) \quad (1)$$

where: $x = (4c + h - 2o - 3n)/8$ and $y = (4c - h - 2o + 3n)/4$

It should be noted that the theoretical yield for PHA is based on $[C_4H_6O_2]_n$ which is an approximation of the molecular structure, while PCL has a well-defined monomer unit. Thus, the Buswell equation is slightly more accurate for PCL than PHA.

2.3.4 Scanning Electron Microscopy (SEM) of PCL and O-MWCNT/PCL Nanocomposites

SEM (SEM, JEOL JSM-IT100, 20 kV, 11 mm working distance) was used to characterize the surface morphology and CNT accumulation at the surface of O-

MWCNT/PCL nanocomposites at the highest CNT loading, 2% w/w, before and after biodegradation. Prior to analysis, samples were first cut into 1 cm^2 pieces and sputter-coated with a layer of Au (MicroNano Tools MNT-JS1600 Plasma Sputtering Coater, 10 mA plasma current, 1 min) to improve sample conductivity.

2.3.5 Stereo Microscopy of CNT/PHA Nanocomposites

Stereo microscopy was used to optically image O-MWCNT/PHA and pristine MWCNT/PHA nanocomposites to qualitatively assess differences in CNT dispersion quality. A Leica Wilde M420 stereo microscope with a 150 W halogen lamp and a Nikon Digital Sight U3 camera were used. 5% w/w O-MWCNT/PHA nanocomposites and 5% w/w MWCNT/PHA nanocomposites were each imaged in duplicate. A neat PHA control was imaged under the same conditions.

2.3.6 Raman Microscopy of CNT/PHA Nanocomposites

Raman microscopy was used to assess dispersion quality and identify regions of CNT aggregation in 5% w/w O-MWCNT/PHA and 5% w/w pristine MWCNT/PHA nanocomposites. For each PNC type, five different spots (2 μm diameter) on two different specimens were used for analysis. Raman spectra were measured using a micro-Raman setup (Horiba JY T64000 spectrometer) with a liquid nitrogen-cooled charge coupled device (CCD). Raman spectra were acquired using the 514.5 nm line of an Ar^+/Kr^+ gas laser operating at a power of 1 mW. All spectra were normalized to the intensity of the ~ 1732 cm^{-1} Raman band of PHA.[34]

2.4 Results and Discussion

The extent and rate of biodegradation for neat PCL and neat PHA as well as O-MWCNT/PCL, pristine MWCNT/PHA and O-MWCNT/PHA nanocomposites were

assessed by measuring volumetric biogas and methane production by anaerobic microorganisms.

2.4.1 Biogas and Methane Production from O-MWCNT/PCL PNCs

Biogas and methane measurements were made over the course of 395 d for neat PCL as well as 0.1, 0.5, and 2% w/w O-MWCNT/PCL nanocomposites. After 395 d, anaerobic biodegradation of all O-MWCNT/PCL nanocomposites resulted in cumulative volumes of biogas similar to neat PCL (Figure 2.1A), and all O-MWCNT/PCL nanocomposites reached the theoretical maximum yield for the PCL matrix as estimated using the Buswell equation (Eq. 1). However, while the addition of 0.1–2% w/w O-MWCNTs did not preclude the ultimate biodegradation of the PCL matrix, an O-MWCNT content of 2% w/w elongated the lag phase in biogas production and affected the rate of nanocomposite biodegradation (see Figure 2.1A). This increase in lag phase is indicative of increased substrate recalcitrance and/or bacterial stress induced by toxicants or other inhibitors to bacterial growth.[35-36] The observed attainment of maximum biogas production and elongation of the lag phase were confirmed by repeating the O-MWCNT/PCL nanocomposite biodegradation experiment using a separately obtained microbial culture of anaerobic digester sludge (Figure 6.1).

The effect of CNTs on methanogenetic microorganisms (i.e., methane production) during PNC biodegradation is important to evaluate since it has not, to our knowledge, been previously investigated, and these microorganisms are the most sensitive in an

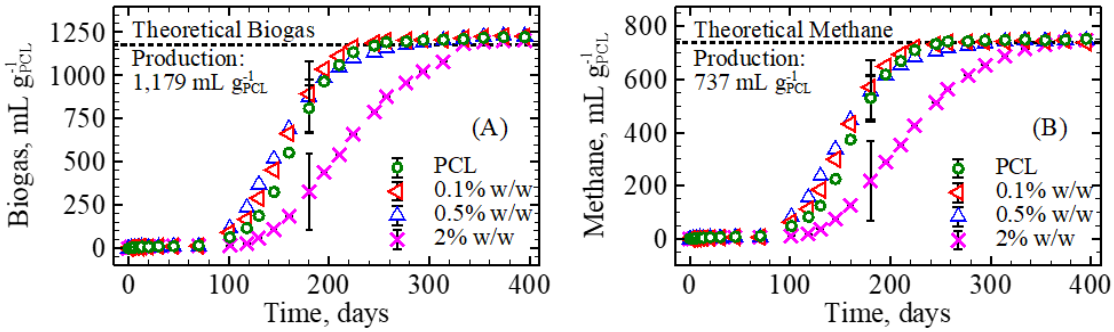

Figure 2.1 (A) Biogas and (B) methane production from the anaerobic biodegradation of PCL and O-MWCNT/PCL nanocomposites of varied CNT loading (0%, 0.1%, 0.5%, 2% w/w). The dashed lines show theoretical biogas and methane production from the PCL matrix of the nanocomposites calculated via the Buswell equation. Each data point represents an average of three replicate samples with SD values shown only for the intermediate timepoints (for clarity) as these feature the highest variation between replicates across the biogas and methane production curves. Plots with full error bars can be found in Figure 6.2.

anaerobic community to contaminants.[29] Figure 2.1B shows that O-MWCNT incorporation into PCL up to 2% w/w did not change the maximum theoretical yield of methane or elongate the lag phase. This suggests that methanogens were either not affected or affected at about the same level as other members of the anaerobic community by CNTs, likely due to an adequate period of acclimation afforded by the slowly degraded polymer matrix (> 200 days for complete biodegradation).

The effect of O-MWCNT loading on the biodegradation rate of O-MWCNT/PCL nanocomposites was quantified by fitting biogas and methane production to four kinetic models including 1st order rate, pseudo-parallel 1st order rate, modified Gompertz, and Logistic. Each model was evaluated for its capacity to accurately predict the observed production of biogas (Figure 2.2, A.1 and B.1) and methane (Figure 2.2, A.2 and B.2) from the nanocomposites. The 1st order rate and pseudo-parallel 1st order rate models failed to

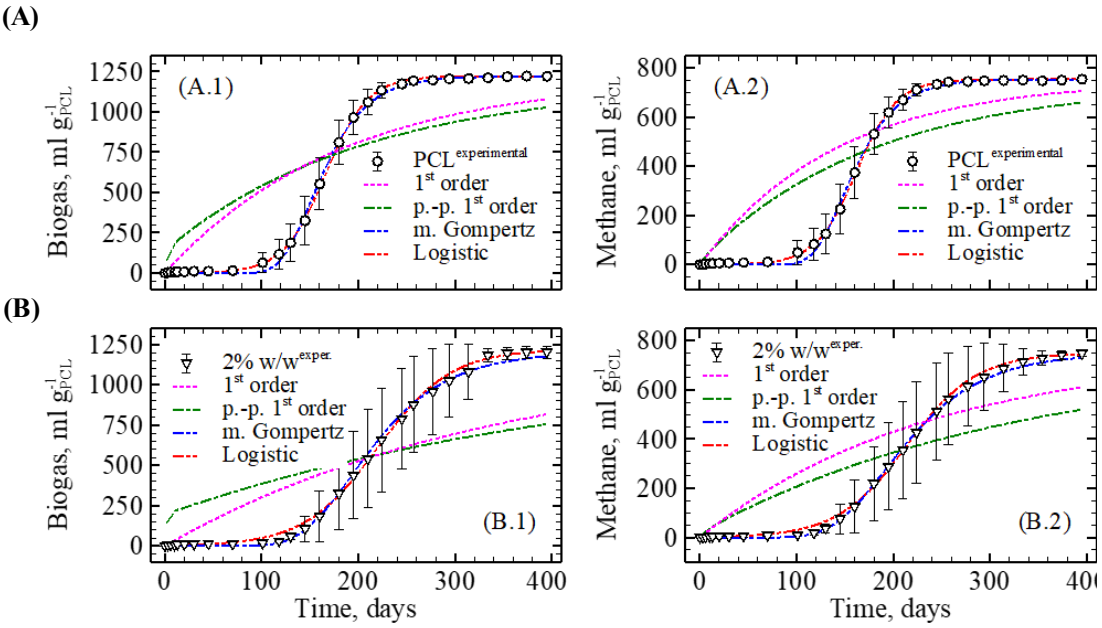

Figure 2.2 Kinetic fits of the experimental biogas (A.1, B.1) and methane (A.2, B.2) production data from (A) neat PCL and (B) 2% w/w O-MWCNT/PCL nanocomposites using 1st order, pseudo-parallel 1st order, modified Gompertz, and Logistic models.

provide accurate predictions of gas production from neat PCL and O-MWCNT/PCL nanocomposites by returning $R^2 < 0.9$ and normalized root-mean-square deviations (NRMSE) of 5-15 (Table 6.1 and Figures 2.2 and 6.3). In contrast, the modified Gompertz and Logistic models were able to accurately describe the anaerobic biodegradation of PNCs (Table 6.1 and Figures 2.2 and 6.3) by returning high R^2 values ($\geq$0.998) and low NRMSE (0.4-0.8) due to their ability to fit non-exponential biogas production data with extended

lag phases. Similar advantages of Gompertz and Logistic models in predicting biodegradation kinetics for recalcitrant biomass[37] or in the presence of inhibition effects[38] have been reported. A particular advantage of the modified Gompertz model lies in its ability to provide physically meaningful values (Table 6.1) for the gas production specific rate constant, k (mL $gPCL^{-1}$ d^{-1}), and the lag phase time constant, λ (d). This model confirmed that the 2% w/w O-MWCNT loading had an inhibitory effect on the rate of PCL matrix biodegradation (~52% decrease in k from 14.3 to 7.4 mL $gPCL^{-1}$ d^{-1}) and an increased lag phase (~17% increase in λ from 120 to 140 d).

Complete mineralization of the PCL matrix into biogas at the end of the experiment for neat PCL and PCL loaded with 0.5% w/w O-MWCNTs was also confirmed by the visual absence of residual PNC in the serum bottle after 355 d (Figure 2.3 A and B). Upon further inspection, small fragments persisted in the 0.5% w/w sample, although complete PCL mineralization still occurred (Figure 2.1), suggesting that these pieces consisted of CNT clusters. Accordingly, CNTs incorporated into PNCs at low loadings are expected to be prone to dispersion in media after polymer degradation. Conversely, the 2% w/w O-MWCNT/PCL nanocomposites retained their circular shape after complete PCL mineralization (Figure 2.3C), suggesting that a CNT mat had formed due to entanglement of the CNTs as seen in previous studies.[19] SEM imaging confirms the formation of a CNT mat; prior to biodegradation, 2% w/w O-MWCNT/PCL possessed a smooth, featureless surface (Figure 2.4A), but after complete PCL loss, a CNT mat characterized by a rough, entangled surface persisted (Figure 2.4B). Thus, beyond a critical CNT loading (2% w/w in this case), CNTs are seemingly able to form three-dimensional mats which are likely to

remain localized in environmental sinks, decreasing the availability of CNTs for subsequent transport and release.

At CNT loadings past a certain threshold, we hypothesize that biofilm formation on the polymer surface is inhibited due to the cytotoxicity of CNTs or the inability to access

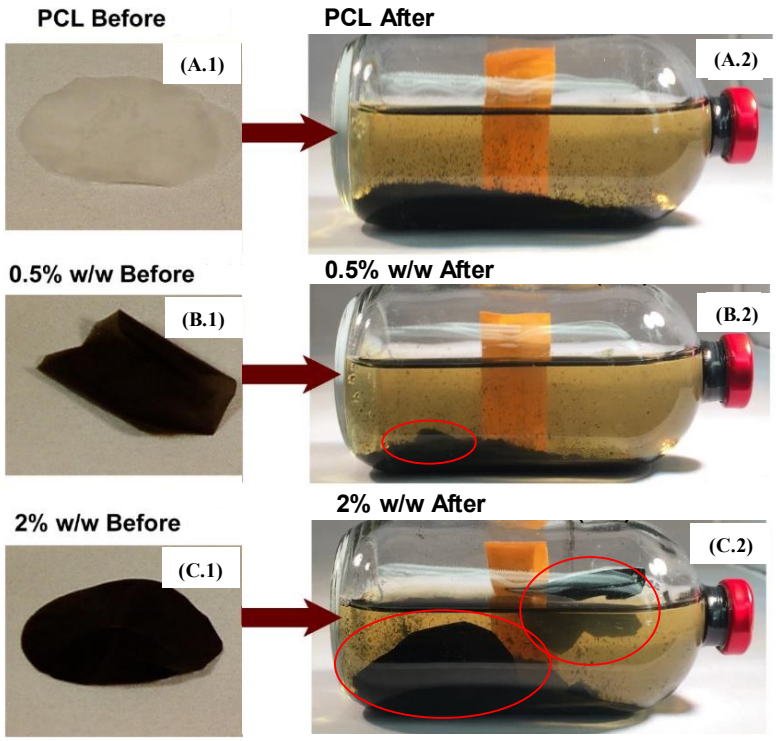

Figure 2.3 O-MWCNT/PCL nanocomposites of (A) neat PCL and O-MWCNT/PCL nanocomposites with CNT loadings of (B) 0.5% w/w and (C) 2% w/w before (left) and after (right) biodegradation in anaerobic mixed culture after 355 d. In every experiment, multiple O-MWCNT/PCL nanocomposites (~30 mm diameter) were initially added to each serum bottle. Black sediment at the bottom of each bottle is solid matter from the anaerobic digester sludge inoculum. In (B), the red circle denotes an example of a residual CNT fragment after complete polymer loss. The red circles in (C) highlight examples of the CNT mat structure persisting in the bottle after full polymer degradation.

underlying polymer through a continuous CNT network, thus delaying the onset of biodegradation (i.e., increasing the lag phase).[19,21] The lack of increased lag phase in biogas production at lower CNT concentrations implies that there is a critical CNT loading which must be reached for inhibitory effects to manifest. It should be noted that the relatively

high CNT loading (i.e., 2% w/w) required to inhibit polymer biodegradation for O-MWCNT/PCL nanocomposites in this study differs from the results described in a previous study for the same PNC using axenic Pseudomonas aeruginosa under aerobic conditions, in which inhibitory effects were observed at O-MWCNT concentrations as low as 0.1% w/w.[21] This difference can be understood by the robustness of a mixed microbial culture, which offers diverse metabolic routes to address obstacles to biodegradation compared to a single microorganism culture which is restricted to fewer metabolic pathways.[39-42]

2.4.2 Biogas and Methane Production from O-MWCNT/PHA PNCs

To assess the effect of polymer type on the CNT loading required for inhibition of PNC biodegradation, biogas and methane production from the O-MWCNT/PCL nanocomposites described in the previous section were compared to biogas and methane evolution from O-MWCNT/PHA nanocomposites. The biogas and methane production plots for neat PHA and O-MWCNT/PHA nanocomposites containing O-MWCNT

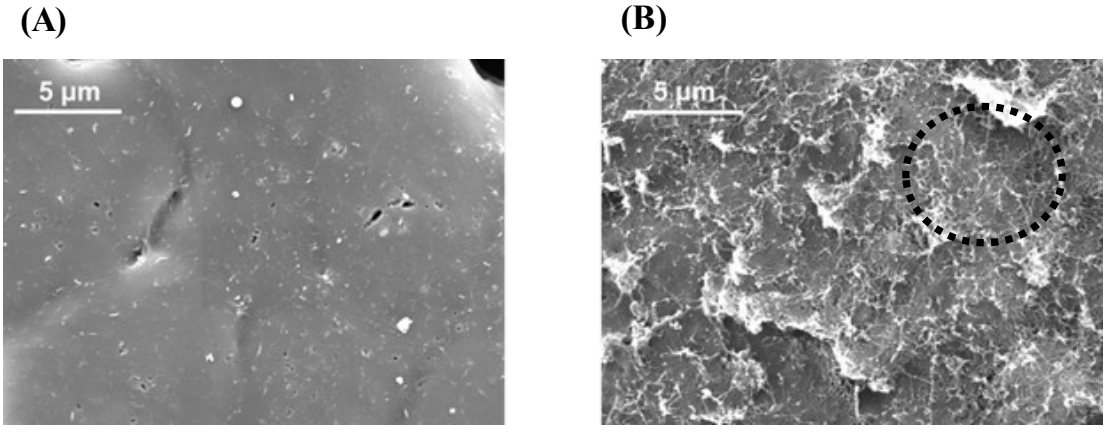

Figure 2.4 SEM images of a 2% w/w O-MWCNT/PCL nanocomposite (A) before and (B) after 355 d of anaerobic biodegradation. (B) The CNT mat (with residual biomass) that persists after the PCL matrix is fully biodegraded. The dotted circle highlights an area with a high concentration of tangled CNTs on the mat surface.

loadings of 0.1, 2, and 5% w/w incubated in the presence of anaerobic microbial consortia are shown in Figure 2.5A. Similar to the O-MWCNT/PCL nanocomposites, the final volumes of biogas and methane produced from O-MWCNT/PHA nanocomposites were both about equal to the theoretical yields and final production from the neat PHA. The attainment of the maximum theoretical biogas and methane yields indicates that the presence of 0.1—5% w/w O-MWCNTs did not impact the ultimate biodegradability of PHA. The small discrepancy observed between the theoretical yield and final observed yield for PHA is likely due to small variations in the complex PHA copolymer structure, an effect which is not accounted for by the Buswell equation (Eq. 1).

In contrast to CNT/PCL nanocomposites, however, there was no effect on the biodegradation rate of CNT/PHA nanocomposites at 2% w/w O-MWCNT. Instead, a loading of 5% w/w O-MWCNTs (compare Figures 2.1A and 2.5A) was required for inhibition to manifest. This increased threshold for inhibition can be understood by the more facile biodegradation of PHA (*i.e.,* more biodegradable) compared to PCL (30 d vs. 250 d), which serves to somewhat offset the cytotoxic effects of the CNTs. Thus, it is apparent that the critical CNT loading required to inhibit polymer biodegradation is increased for a PNC comprised of a readily biodegradable polymer such as PHA compared to a more recalcitrant polymer, such as PCL.

The effect of O-MWCNT loading on the rate of O-MWCNT/PHA nanocomposite biodegradation was quantified through kinetic analysis of biogas and methane production. Again, the modified Gompertz and Logistic models provided superior accuracy in fitting experimental data compared to 1st order and pseudo-parallel 1st order rate models (Figures 2.5, 6.4, 6.5, and Table 6.2). The modified Gompertz model confirmed that biodegradation

of O-MWCNT/PHA nanocomposites with loadings of ≤ 2% w/w O-MWCNTs occurred at the same rate as neat PHA, while 5% w/w O-MWCNT/PHA biodegraded at a nearly three-fold slower rate (62 vs. 18 mL biogas $gPHA^{-1}$ d^{-1}, respectively). Interestingly, the presence of 5% w/w O-MWCNTs did not significantly increase the lag phase in total biogas production from PHA nanocomposites (~5 d for 5% w/w O-MWCNT/PHA vs. ~4 d for neat PHA, Table 6.2), but did lead to a notable elongation of the lag phase in methane production (~24 d for 5% w/w O-MWCNT/PHA vs. ~10 d for neat PHA; Figure 2.5). Thus, the O-MWCNTs affected methanogens more strongly than other members of the anaerobic community, likely because microbes were rapidly exposed to CNTs due to the short lag

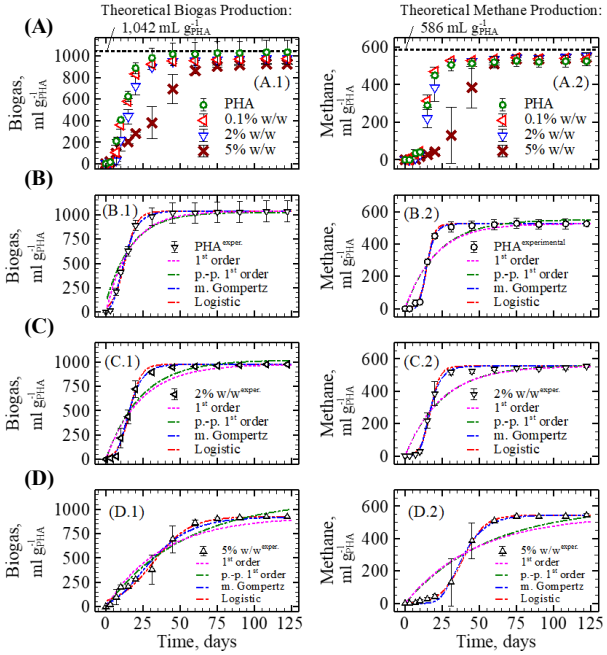

Figure 2.5 Top Row: (A) Biogas (left) and methane (right) production from the biodegradation of neat PHA and O-MWCNT/PHA nanocomposites with 0.1%, 2% and 5% w/w O-MWCNTs. Dotted line represents theoretical maximum biogas and methane production as calculated with the Buswell equation. Each data point represents the average and one standard deviation of gas production from three replicate samples. Bottom three rows display fits of the derived kinetic models to the experimental biogas (left) and methane (right) production data from (B) neat PHA, (C) 2% w/w O-MWCNT/PHA, and (D) 5% w/w O-MWCNT/PHA nanocomposites.

phase for PHA, thus offering decreased time for the more sensitive methanogens to adapt to the cytotoxic CNT surface.

2.4.3 Comparing Biogas and Methane Produced by Pristine and O-MWCNT/PHA PNCs

The impact of CNT oxidation on the biodegradation of CNT/PNCs was evaluated by comparing biogas and methane production from CNT/PHA nanocomposites embedded

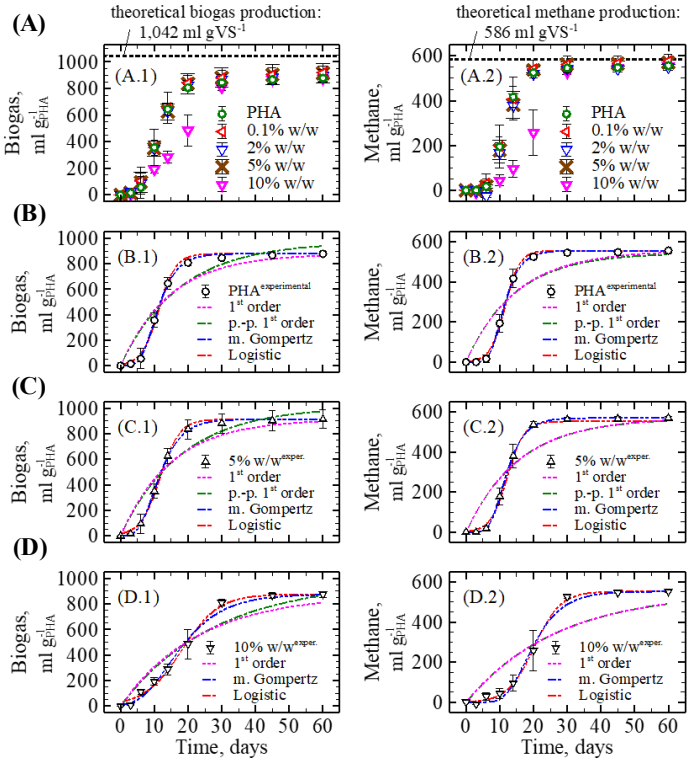

Figure 2.6 Top row: (A) Biogas (left) and methane (right) production from the biodegradation of neat PHA and pristine MWCNT/PHA nanocomposites with 0.1, 2, 5 and 10% w/w pristine MWCNTs. Dotted line represents theoretical maximum biogas and methane production as calculated with the Buswell equation. Each data point represents the average and one standard deviation of gas production from three replicate samples. The bottom three rows display fits of the derived kinetic models to the experimental biogas (left) and methane (right) production data from (B) neat PHA, (C) 5% w/w pristine MWCNT/PHA, and (D) 10% w/w pristine MWCNT/PHA nanocomposites.

with either pristine MWCNTs or O-MWCNTs. For pristine MWCNT with loadings from 0—10% w/w and O-MWCNT loadings from 0—5% w/w, the final biogas and methane yield from the pristine MWCNT/PHA and O-MWCNT/PHA nanocomposites was almost identical to the gas production from neat PHA (Figures 2.5 and 2.6). However, inhibition of biodegradation was observed for nanocomposites with loadings of 10% w/w pristine MWCNTs and 5% w/w O-MWCNTs (Figures 2.5 and 2.6) as quantified by the kinetic constants (Tables 6.2 and 6.3) determined using the modified Gompertz model (Figures 2.5, 2.6, and 6.4-6.7).

The principal reason for the dependence of inhibition threshold on CNT type was ascribed to variations in CNT dispersion within each PNC. Upon visual observation, CNT/PHA nanocomposites with 5% w/w pristine MWCNTs (P-CNTs; Figure 2.7A inset)

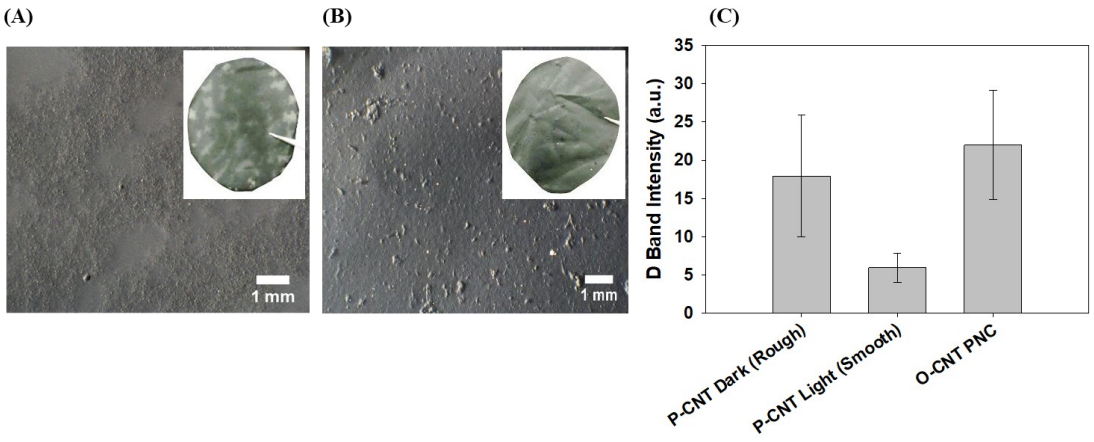

Figure 2.7 A comparison of the CNT dispersion quality in (A) 5% w/w pristine MWCNT/PHA and (B) 5% w/w O-MWCNT/PHA nanocomposites using a stereo microscope. Optical images are shown in the insets. In (C), the average Raman D-band intensity (normalized to the 1732 cm^{-1} PHA band) observed in both the light and dark regions of two different pristine MWCNT/PHA composites as well as two different O-MWCNT/PHA composites. The error bars represent one standard deviation of the D band intensities in five different areas on each sample.

featured mottled dark and light regions, while CNT/PHA nanocomposites with 5% w/w O-MWCNTs displayed a homogeneous surface (Figure 2.7B inset). In stereo microscopy images, these dark areas were characterized by large numbers of CNT bundles (rough areas in Figures 2.7A and 6.8) while light areas (smooth patches in Figures 2.7A and 6.8) were sparse in CNTs. Using Raman microscopy, the rough areas in 5% w/w pristine MWCNT/PHA were confirmed as being CNT-rich (high D-band intensity), while smooth regions possessed lower CNT concentrations (low D-band intensity) as shown in Figures 2.7C and 6.10. In contrast, 5% w/w O-MWCNT/PHA nanocomposites possessed no identifiable CNT bundles in stereo micrographs (Figures 2.7B and 6.11) and a Raman D-band intensity that remained relatively constant across the entire sample surface.

We assert that the pristine MWCNT/PHA nanocomposites required a higher CNT loading to inhibit biodegradation because the poorly dispersed pristine CNTs resulted in areas on the PNC surface which consisted primarily of polymer, thus increasing access and facilitating acclimation of anaerobic microorganisms to PHA. Homogeneously dispersed O-MWCNTs, however, yielded few—if any—areas free of CNTs at a lower loading (*i.e.,* 5% w/w), effectively reducing bacterial access to PHA. While the inherent toxicity of CNTs likely plays a role in their inhibitory effects, both O-MWCNTs and pristine MWCNTs have been shown to exhibit cytotoxicity after incorporation into PNCs, and the difference in cytotoxic effects between these CNT types is therefore expected to be significantly less than the effects caused by the difference in CNT dispersion.[18, 43]

2.4.4 Implications for Biodegradation of CNT/PNCs

In this study, it was determined that the biodegradation kinetics of polymers are impacted by the inclusion of CNTs in anaerobic conditions via tracking polymer

mineralization into biogas. Nanocomposites are likely to end up in anaerobic environments such as landfills and wastewater where anaerobes are particularly relevant in their biodegradation, yet such microbial communities are often overlooked in PNC biodegradation studies.[16-17] Tracking PNC biodegradation via biogas assessment is more accurate than analyses involving mass loss quantification which can introduce error due to residual biomass adhering to the nanocomposite surface. Moreover, the modeling of biodegradation kinetics using the modified Gompertz equation allowed for accurate and quantifiable conclusions to be made in terms of the effects of CNT loading on PNC biodegradation.

Data reported here for pristine MWCNT/PHA nanocomposites in anaerobic mixed culture can be compared to a previous study which assessed the biodegradation rate of the same PNCs by a microbial community under aerobic conditions.[19] Under aerobic mixed culture conditions, pristine MWCNT/PHA nanocomposites (loadings of 0—10% w/w) showed no CNT-dependent inhibition towards biodegradation, which is different from the decreased rate observed at 10% w/w in the present study by an anaerobic community. This difference in behavior can be understood by virtue of the decreased susceptibility of PHA to biodegradation by anaerobic microbes compared to aerobic communities (30 d vs. 7 d, respectively). This supports the overarching conclusion that situations which reduce the rate of neat polymer biodegradation exacerbate the inhibitory effect of CNTs. Thus, when the CNT/PNCs are composed of less biodegradable polymers or when biodegradation occurs in the presence of microbial communities which are relatively inefficient at degrading polymers (*e.g.,* single culture, anaerobic conditions), biodegradation rates will be affected at lower CNT loadings than in situations where PNCs are biodegraded under

conditions which facilitate biodegradation. Furthermore, as seen previously with PNCs biodegraded by *Pseudomonas aeruginosa*, this decrease in biodegradation rate is expected to be exacerbated with increased CNT loading beyond the critical threshold.[21] Similarly, an increased dispersion of CNTs (*e.g.,* due to oxidation) within a polymer matrix also decreases the CNT loading needed to inhibit the rate of polymer biodegradation. In terms of impact on the microbial community, a slower PNC biodegradation process has been shown to equally impact the microbial community while a more rapid biodegradation process featuring a short lag phase affords less acclimation time to microbes, thus disproportionally inhibiting the growth of sensitive methanogen species as was the case here with MWCNT/PHA nanocomposites. These results are valuable for predicting situations (*e.g.,* high CNT loading, recalcitrant polymer) where the inclusion of CNTs into a polymer may render the polymer virtually non-biodegradable. For example, due to the decreased biodegradability of PLA compared to PCL, incorporation of 5% w/w CNTs may effectively render such material inert towards biodegradation for years.[44-46]

Environmental implications regarding CNT release also appear to be dependent on CNT loading. For example, while the polymer matrix of MWCNT/PCL nanocomposites ultimately biodegrades, CNT loadings ≥ 2% w/w result in the formation of a contiguous CNT mat which localizes the CNTs. Conversely, CNT loadings < 2% w/w have been shown to be insufficient to form such a mat. Under these conditions, CNTs in the PNC will fragment and could separate from each other after polymer loss, likely facilitating their subsequent environmental transport and interactions with biota.

2.5 Conclusions

This study is one of the first to address the anaerobic biodegradation of CNT/PNCs, an important route of environmental degradation for such materials. CNT incorporation into PNCs did not prevent complete biodegradation of the polymer matrix but slowed the rate of biodegradation at certain threshold CNT loadings, quantified using the modified Gompertz model. The CNT loading required for such inhibition to manifest was lower under conditions which promoted a slower biodegradation process. Specifically, lower O-MWCNT loadings were required to decrease the biodegradation rate of less biodegradable polymers (PCL) as compared to more rapidly biodegraded polymers (PHA) in the presence of the same anaerobic microbial community. In situations where biodegradation was rapid, the short lag phase caused methanogens to be disproportionately affected by CNT exposure compared to the rest of the microbial community. In addition, the increased dispersibility of O-MWCNTs led to the hindrance of PHA biodegradation at lower loadings (5% w/w) compared to poorly dispersed pristine MWCNTs. At CNT loadings above a certain threshold, the formation of a contiguous CNT mat was observed after polymer loss, while CNTs at loadings below this threshold fragmented. The data presented herein indicates that CNT incorporation into PNCs affects biodegradation kinetics at lower loadings under conditions predisposed to a slower biodegradation process.

2.6 Acknowledgements

This work is dedicated to Dr. Ed Bouwer, who passed away during the preparation of this manuscript. Dr. Ed Bouwer was a respected colleague and mentor to the authors on this manuscript and he will be greatly missed. Authors acknowledge the JHU Raman Scattering Users Center. The authors also acknowledge NSF grants CBET #1236493 and

CBET #1336168 as well as JHU for an Owens Graduate Fellowship awarded to DGG. The manuscript preparation was in part supported by the U.S. DOE under Contract No. DE-AC05-76L01830 at the Pacific Northwest National Laboratory and by the Office of Energy Efficiency and Renewable Energy through the Bioenergy Technologies (BETO) sponsored research at PNNL.

2.7 Appendix 1 Summary

Contains detailed information regarding carbon nanotube polymer nanocomposite (CNT/PNC) preparation. Additionally, biomethane potential (BMP) media preparation and sampling procedure is detailed. Figures report additional data including kinetic model parameters and complete fits for each CNT loading and PNC set. Plots including full error bars for O-MWCNT/PCL samples reported in Figure 2.1 as well as a replicate data set of the same samples are reported. Finally, additional stereo microscopy images and Raman data are reported for 5% w/w pristine MWCNT/PHA and O-MWCNT/PHA PNCs to illustrate the reproducibility of the difference in dispersion offered by each CNT type in the same polymer matrix. Table 6.1: Kinetic parameters for biogas and methane production from O-MWCNT/PCL nanocomposites. Figure 6.1: Biogas production from anaerobic biodegradation of PCL and 2% w/w O-MWCNT/PCL nanocomposites. Figure 6.2: Biogas and methane production from the anaerobic biodegradation of PCL and O-MWCNT/PCL nanocomposites with CNT loadings of 0.1, 0.5, and 2% w/w. Figure 6.3: Experimentally observed vs. model-predicted biogas and methane production for PCL and O-MWCNT/PCL nanocomposites with CNT loadings of 0.1, 0.5, and 2% w/w. Table 6.2: Kinetic parameters for biogas and methane production from O-MWCNT/PHA nanocomposites. Figure 6.4: Biogas and methane production of neat PHA and O-

MWCNT/PHA nanocomposites with 0.1, 2, and 5% w/w CNTs fit to derived kinetic models. Figure 6.5: Experimentally observed vs. model-predicted biogas and methane production for neat PHA and O-MWCNT/PHA nanocomposites with 0.1, 2, and 5% w/w CNT loading. Table 6.3: Kinetic parameters for biogas and methane production from pristine MWCNT/PHA nanocomposites. Figure 6.6: Biogas and methane production from the biodegradation of neat PHA and pristine MWCNT/PHA nanocomposites with 0.1, 2, 5, and 10% w/w pristine MWCNTs fit to derived kinetic models. Figure 6.7: Experimentally observed vs. model-predicted biogas and methane production for neat PHA and pristine MWCNT/PHA nanocomposites loaded with 0.1, 2, 5, and 10% pristine MWCNTs. Figure 6.8: Stereomicroscopy images of 5% w/w pristine MWCNT/PHA nanocomposites. Figure 6.9: Stereomicroscopy images of 5% w/w O-MWCNT/PHA, 5% pristine MWCNT/PHA, and neat PHA films. Figure 6.10: Raman spectra of 5% w/w O-MWCNT/PHA and 5% pristine MWCNT/PHA smooth areas and rough areas. Figure 6.11: Stereomicroscopy images of 5% w/w O-MWCNT/PHA nanocomposites.

2.8 References

1. Ojha, S.; Singh, D.; Sett, A.; Chetia, H.; Kabiraj, D.; Bora, U., Chapter 16 - Nanotechnology in Crop Protection. In *Nanomaterials in Plants, Algae, and Microorganisms*, Tripathi, D. K.; Ahmad, P.; Sharma, S.; Chauhan, D. K.; Dubey, N. K., Eds. Academic Press: 2018; pp 345-391.
2. Costa, S. S.; Miranda, A. L.; de Morais, M. G.; Costa, J. A. V.; Druzian, J. I., Microalgae as source of polyhydroxyalkanoates (PHAs) — A review. *International Journal of Biological Macromolecules* **2019,** *131*, 536-547.
3. Meng, L.; Xie, F.; Zhang, B.; Wang, D. K.; Yu, L., Natural Biopolymer Alloys with Superior Mechanical Properties. *ACS Sustainable Chem. Eng.* **2019,** *7* (2), 2792-2802.
4. Harding, K. G.; Dennis, J. S.; von Blottnitz, H.; Harrison, S. T. L., Environmental analysis of plastic production processes: Comparing petroleum-based polypropylene and polyethylene with biologically-based poly-β-hydroxybutyric acid using life cycle analysis. *Journal of Biotechnology* **2007,** *130* (1), 57-66.
5. Roy, I.; P.M., V., *Polyhydroxyalkanoate (PHA) based blends, composites, and nanocomposites*. Royal Society of Chemistry: 2015; Vol. 30.

6. Lin, J.-H.; Lin, Z.-I.; Pan, Y.-J.; Hsieh, C.-T.; Huang, C.-L.; Lou, C.-W., Thermoplastic polyvinyl alcohol/multiwalled carbon nanotube composites: Preparation, mechanical properties, thermal properties, and electromagnetic shielding effectiveness. *J. Appl. Polym. Sci.* **2016,** *133* (21).
7. Mangeon, C.; Mahouche-Chergui, S.; Versace, D. L.; Guerrouache, M.; Carbonnier, B.; Langlois, V.; Renard, E., Poly(3-hydroxyalkanoate)-grafted carbon nanotube nanofillers as reinforcing agent for PHAs-based electrospun mats. *Reactive and Functional Polymers* **2015,** *89*, 18-23.
8. Gupta, T. K.; Kumar, S., 4 - Fabrication of Carbon Nanotube/Polymer Nanocomposites. In *Carbon Nanotube-Reinforced Polymers*, Rafiee, R., Ed. Elsevier: 2018; pp 61-81.
9. Iqbal, A.; Saeed, A.; Ul-Hamid, A., A review featuring the fundamentals and advancements of polymer/CNT nanocomposite application in aerospace industry. *Polymer Bulletin* **2020**.
10. Skaria, E.; Patel, B. A.; Flint, M. S.; Ng, K. W., Poly(lactic acid)/Carbon Nanotube Composite Microneedle Arrays for Dermal Biosensing. *Analytical Chemistry* **2019,** *91* (7), 4436-4443.
11. Goodwin, D. G.; Xia, Z.; Gordon, T. B.; Gao, C.; Bouwer, E. J.; Fairbrother, D. H., Biofilm development on carbon nanotube/polymer nanocomposites. *Environ. Sci.: Nano* **2016,** *3* (3), 545-558.
12. De Volder, M. F. L.; Tawfick, S. H.; Baughman, R. H.; Hart, A. J., Carbon Nanotubes: Present and Future Commercial Applications. *Science* **2013,** *339* (6119), 535-539.
13. Kingston, C.; Zepp, R.; Andrady, A.; Boverhof, D.; Fehir, R.; Hawkins, D.; Roberts, J.; Sayre, P.; Shelton, B.; Sultan, Y.; Vejins, V.; Wohlleben, W., Release characteristics of selected carbon nanotube polymer composites. *Carbon* **2014,** *68*, 33-57.
14. Kausar, A.; Rafique, I.; Muhammad, B., Review of Applications of Polymer/Carbon Nanotubes and Epoxy/CNT Composites. *Polym. Plast. Technol. Eng.* **2016,** *55* (11), 1167-1191.
15. Kinloch, I. A.; Suhr, J.; Lou, J.; Young, R. J.; Ajayan, P. M., Composites with carbon nanotubes and graphene: An outlook. *Science* **2018,** *362* (6414), 547-553.
16. Gottschalk, F.; Nowack, B., The release of engineered nanomaterials to the environment. *Journal of Environmental Monitoring* **2011,** *13* (5), 1145-1155.
17. Petersen, E. J.; Zhang, L.; Mattison, N. T.; O'Carroll, D. M.; Whelton, A. J.; Uddin, N.; Nguyen, T.; Huang, Q.; Henry, T. B.; Holbrook, R. D.; Chen, K. L., Potential Release Pathways, Environmental Fate, And Ecological Risks of Carbon Nanotubes. *Environ. Sci. Technol.* **2011,** *45* (23), 9837-9856.
18. Goodwin, D. G.; Marsh, K. M.; Sosa, I. B.; Payne, J. B.; Gorham, J. M.; Bouwer, E. J.; Fairbrother, D. H., Interactions of Microorganisms with Polymer Nanocomposite Surfaces Containing Oxidized Carbon Nanotubes. *Environ. Sci. Technol.* **2015,** *49* (9), 5484-5492.
19. Phan, D. C.; Goodwin, D. G.; Frank, B. P.; Bouwer, E. J.; Fairbrother, D. H., Biodegradability of carbon nanotube/polymer nanocomposites under aerobic mixed culture conditions. *Science of The Total Environment* **2018,** *639*, 804-814.

20. Nair, N. R.; Sekhar, V. C.; Nampoothiri, K. M.; Pandey, A., 32 - Biodegradation of Biopolymers. In *Current Developments in Biotechnology and Bioengineering*, Pandey, A.; Negi, S.; Soccol, C. R., Eds. Elsevier: 2017; pp 739-755.
21. Goodwin, D. G.; Boyer, I.; Devahif, T.; Gao, C.; Frank, B. P.; Lu, X.; Kuwama, L.; Gordon, T. B.; Wang, J.; Ranville, J. F.; Bouwer, E. J.; Fairbrother, D. H., Biodegradation of Carbon Nanotube/Polymer Nanocomposites using a Monoculture. *Environ. Sci. Technol.* **2018,** *52* (1), 40-51.
22. Parks, A. N.; Chandler, G. T.; Ho, K. T.; Burgess, R. M.; Ferguson, P. L., Environmental biodegradability of [14C] single-walled carbon nanotubes by Trametes versicolor and natural microbial cultures found in New Bedford Harbor sediment and aerated wastewater treatment plant sludge. *Environmental Toxicology and Chemistry* **2015,** *34* (2), 247-251.
23. Pandey, P.; Mohanty, S.; Nayak, S. K., A Novel Method of Mechanical Oxidation of CNT for Polymer Nanocomposite Application: Evaluation of Mechanical, Dynamic Mechanical, and Rheological Properties. *International Journal of Chemical Engineering* **2014,** *2014*.
24. Bhattacharya, M., Polymer Nanocomposites-A Comparison between Carbon Nanotubes, Graphene, and Clay as Nanofillers. *Materials (Basel)* **2016,** *9* (4), 262.
25. Ghattas, A.-K.; Fischer, F.; Wick, A.; Ternes, T. A., Anaerobic biodegradation of (emerging) organic contaminants in the aquatic environment. *Water Res.* **2017,** *116*, 268-295.
26. Karakashev, D.; Batstone, D. J.; Angelidaki, I., Influence of environmental conditions on methanogenic compositions in anaerobic biogas reactors. *Appl. Environ. Microbiol.* **2005,** *71* (1), 331-338.
27. McDonald, J. E.; Allison, H. E.; McCarthy, A. J., Composition of the Landfill Microbial Community as Determined by Application of Domain- and Group-Specific 16S and 18S rRNA-Targeted Oligonucleotide Probes. *Appl. Environ. Microbiol.* **2010,** *76* (4), 1301-1306.
28. Maintinguer, S. I.; Sakamoto, I. K.; Adorno, M. A. T.; Varesche, M. B. A., Diversity of anaerobic bacteria in sediments from a subtropical reservoir. *Lakes & Reservoirs: Science, Policy and Management for Sustainable Use* **2016,** *21* (4), 351-361.
29. Kugelman, I. J.; Chin, K. K., Toxicity, Synergism, and Antagonism in Anaerobic Waste Treatment Processes. In *Anaerobic Biological Treatment Processes*, AMERICAN CHEMICAL SOCIETY: 1971; Vol. 105, pp 55-90.
30. Chen, Y.; Cheng, J. J.; Creamer, K. S., Inhibition of anaerobic digestion process: A review. *Bioresource Technology* **2008,** *99* (10), 4044-4064.
31. Owen, W. F.; Stuckey, D. C.; Healy, J. B.; Young, L. Y.; McCarty, P. L., Bioassay for Monitoring Biochemical Methane Potential and Anaerobic Toxicity. *Water Res.* **1979,** *13* (6), 485-492.
32. Bohutskyi, P.; Betenbaugh, M. J.; Bouwer, E. J., The effects of alternative pretreatment strategies on anaerobic digestion and methane production from different algal strains. *Bioresource Technology* **2014,** *155*, 366-372.
33. Buswell, A. M.; Mueller, H. F., Mechanism of Methane Fermentation. *Industrial & Engineering Chemistry* **1952,** *44* (3), 550-552.
34. Samek, O.; Obruča, S.; Šiler, M.; Sedláček, P.; Benešová, P.; Kučera, D.; Márova, I.; Ježek, J.; Bernatová, S.; Zemánek, P., Quantitative Raman Spectroscopy Analysis of

Polyhydroxyalkanoates Produced by Cupriavidus necator H16. *Sensors (Basel)* **2016,** *16* (11), 1808.
35. Rolfe, M. D.; Rice, C. J.; Lucchini, S.; Pin, C.; Thompson, A.; Cameron, A. D. S.; Alston, M.; Stringer, M. F.; Betts, R. P.; Baranyi, J.; Peck, M. W.; Hinton, J. C. D., Lag Phase Is a Distinct Growth Phase That Prepares Bacteria for Exponential Growth and Involves Transient Metal Accumulation. *Journal of Bacteriology* **2012,** *194* (3), 686-701.
36. Bertrand, R. L., Lag Phase Is a Dynamic, Organized, Adaptive, and Evolvable Period That Prepares Bacteria for Cell Division. *Journal of Bacteriology* **2019,** *201* (7), e00697-18.
37. Bohutskyi, P.; Phan, D.; Kopachevsky, A. M.; Chow, S.; Bouwer, E. J.; Betenbaugh, M. J., Synergistic co-digestion of wastewater grown algae-bacteria polyculture biomass and cellulose to optimize carbon-to-nitrogen ratio and application of kinetic models to predict anaerobic digestion energy balance. *Bioresource Technology* **2018,** *269*, 210-220.
38. Bohutskyi, P.; Keller, T. A.; Phan, D.; Parris, M. L.; Li, M.; Richardson, L.; Kopachevsky, A. M., Co-digestion of Wastewater-Grown Filamentous Algae With Sewage Sludge Improves Biomethane Production and Energy Balance Compared to Thermal, Chemical, or Thermochemical Pretreatments. *Frontiers in Energy Research* **2019,** *7* (47).
39. Khalid, A.; Arshad, M.; Crowley, D. E., Biodegradation potential of pure and mixed bacterial cultures for removal of 4-nitroaniline from textile dye wastewater. *Water Res.* **2009,** *43* (4), 1110-1116.
40. Ponomarova, O.; Patil, K. R., Metabolic interactions in microbial communities: untangling the Gordian knot. *Current Opinion in Microbiology* **2015,** *27*, 37-44.
41. Hesseltine, C. R., *Applications of Biotechnology to Traditional Fermented Foods*. National Academies Press (US): Washington (DC), 1992; Vol. 6.
42. Hoelzle, R. D.; Virdis, B.; Batstone, D. J., Regulation mechanisms in mixed and pure culture microbial fermentation. *Biotechnology and Bioengineering* **2014,** *111* (11), 2139-2154.
43. Santos, C. M.; Milagros Cui, K.; Ahmed, F.; Tria, M. C. R.; Vergara, R. A. M. V.; de Leon, A. C.; Advincula, R. C.; Rodrigues, D. F., Bactericidal and Anticorrosion Properties in PVK/MWNT Nanocomposite Coatings on Stainless Steel. *Macromolecular Materials and Engineering* **2012,** *297* (8), 807-813.
44. Goldberg, D., A review of the biodegradability and utility of poly(caprolactone). *Journal of environmental polymer degradation* **1995,** *3* (2), 61-67.
45. Vasile, C.; Pamfil, D.; Râpă, M.; Darie-Niţă, R. N.; Mitelut, A. C.; Popa, E. E.; Popescu, P. A.; Draghici, M. C.; Popa, M. E., Study of the soil burial degradation of some PLA/CS biocomposites. *Composites Part B: Engineering* **2018,** *142*, 251-262.
46. Wu, D.; Wu, L.; Zhou, W.; Zhang, M.; Yang, T., Crystallization and biodegradation of polylactide/carbon nanotube composites. *Polymer Engineering & Science* **2010,** *50* (9), 1721-1733.

Chapter 3. Determination of the Effect of Common Silane Treatments on the Biodegradability of Cellulose Nanofibrils

Reproduced from

Frank, B. P.; Durkin, D. P.; Caudill, E. R.; Zhu, L.; White, D. H.; Curry, M. L.; Pedersen, J. A.; Fairbrother, D. H., Impact of Silanization on the Structure, Dispersion Properties, and Biodegradability of Nanocellulose as a Nanocomposite Filler. *ACS Applied Nano Materials* **2018,** *1* (12), 7025-7038.

3.1 Abstract

For nanocellulose to function effectively as a nanofiller in polymers, its interfacial properties are often modified to enhance the dispersion of nanocellulose in the polymer matrix. However, the effect of different surface modification strategies on the persistence of nanocellulose in the environment is unclear. In this study, we have examined the effect of three different hydrophobic silanization reagents on the structure, dispersion properties, and biodegradability of cellulose nanofibrils (CNFs). Specifically, we modified CNFs with hydrophobic alkoxysilanes containing methyl, propyl, or aminopropyl functional groups to form silane-modified CNFs (Si-CNFs). Using a combination of analytical techniques that

included ATR-IR, XPS, and solid state NMR, we demonstrated that silanization coated the CNFs with a nanometer-scale siloxane layer, the extent of which could be controlled by varying the amount of silane added to the CNFs. The stability of Si-CNFs in chloroform-based casting solutions improved compared to untreated CNFs, and scaled with extent and hydrophobicity of the siloxane coating as quantified via a mass recovery settling test. Improvements in stability in casting solutions translated into improved Si-CNF dispersion in solution-blended polyhydroxyalkanoates composites as determined with optical microscopy and SEM. Conversely, the biodegradability of Si-CNFs, assessed by tracking sample mineralization in a mixed microbial culture from an anaerobic sludge digester, was inversely related to both the degree and hydrophobicity of CNF surface modification. As mineralization of nanocellulose is rapid and facile, tracking this property served as a proportional measure of overall biodegradability. In the most extensively silanized samples, no mineralization of Si-CNFs was observed, demonstrating that a < 2 nm thick siloxane coating was sufficiently dense and uniform to prevent microbial access to the easily mineralized nanocellulose substrate. This study highlights the important and contrasting effects that changes to surface chemistry can have on the material and environmentally relevant properties of nanocellulose.

3.2 Introduction

Cellulose is a naturally abundant, biodegradable, and non-toxic covalently-linked homopolymer that consists of 2,000 to 27,000 β(1→4) linked D-glucose residues. Each glucose residue contains three hydroxyl groups which are located on the second, third, and sixth carbons. The cellulose homopolymer exists in four main allomorphs: cellulose I, II, III, and IV. Cellulose I (CI) is the native form present in plants, and of the four is the most

commonly used in the fabrication of polymer composites[1]. Due to the superior mechanical and physical properties offered at the nano-scale, native cellulose is often converted to nanocellulose in the form of cellulose nanocrystals or nanofibrils (CNCs or CNFs, respectively). Both CNCs and CNFs are classified as nanomaterials due to their nano-scale widths, but they differ in their size, shape, and crystallinity.[1-2] Because of the attractive nano-derived properties of CNFs and CNCs, nanocellulose has been utilized for both traditional applications in the paper and textile industries,[3-5] as well as applications in biodegradable packaging,[6] *in vivo* medical devices,[7] and green building materials.[8] While both forms of nanocellulose are used as fillers to structurally reinforce composite materials, research often focuses on CNFs due to the improved mechanical properties afforded by their larger aspect ratio and high degree of fibril entanglement, leading to higher tensile strength and elastic modulus in polymer nanocomposites compared to CNCs.[9-10]

CNFs can be extracted from cellulosic starting material (i.e., plant matter, tunicates) via acid digestion,[11] sonication,[12-14] mechanical milling,[15] or enzyme-assisted methods.[16] The cheap and abundant precursor to CNFs (i.e., cellulose) also makes them attractive compared to other carbon-based nanofillers (e.g., carbon nanotubes (CNTs),[17] carbon fibers,[18] and glass fibers[19]). Unlike other potentially hazardous carbon-based nanofillers,[20-22] once CNFs enter the environment, they typically undergo rapid and complete mineralization[23] as a result of microbial biodegradation to yield biogas, limiting their persistence and environmental impact.[24-25] This combination of beneficial properties make CNFs attractive, environmentally friendly alternatives to synthetic nanofillers in a range of commercial applications.

Due to the limited thermal stability of nanocellulose, which can thermally decompose at temperatures as low as 120 °C, [26-27] polymer nanocomposites containing nanocellulose are often prepared through solvent casting rather than melt mixing. Solvent casting is a technique requiring the formation of a polymer-nanoparticle suspension (i.e., the casting solution), most typically in a volatile organic solvent,[28-29] although aqueous solvent casting systems do exist.[30] The stability of the nanoparticle in the casting solution is an important factor, as the nanofiller's dispersion in the polymer plays a pivotal role in determining the extent to which the desirable attributes of the filler are conferred to the nanocomposite.[31-36] However, CNFs do not disperse well in most organic solvents due to their extensive hydrogen bonding and hydrophilic nature; consequently, solvent casting well-dispersed hydrophobic polymer-CNF nanocomposite materials remains challenging. To improve CNF dispersibility in these types of polymer nanocomposites, nanocellulose has previously been chemically modified to increase its hydrophobicity through covalent functionalization with hydrophobic moieties,[37-38] the grafting of hydrophobic polymers or thiols,[39-40] and physically adsorbing hydrophobic surfactants onto its surface.[41]

While surface modification of CNF enables the production of well-dispersed polymer nanocomposites with improved material properties, the effect of these hydrophobic modifications on the persistence of nanocellulose in the environment (as measured here by its propensity to be mineralized) has received little attention. The implicit assumption appears to be that the facile mineralization of nanocellulose is not significantly impacted by these surface modifications,[39, 42-43] or is unimportant, possibly because ionic functionalizations have been shown to have little effect on its biodegradability.[44] Considering the growth projected for the nanocellulose commercial market,[45-46] an

increasing quantity of modified CNFs can be expected to enter the environment during the production, transportation, use, and disposal of nanocomposite products. Consequently, the effect of common surface modification strategies on the environmental persistence of nanocellulose must be evaluated and understood.

Silanes are frequently used as modification reagents to improve the dispersion and interfacial adhesion between polymers and fillers—including nanocellulose—in composites. The improved dispersion and interfacial properties offered by silanization[37] leads to more efficient transfer of mechanical properties from nanofiller to material. Silanization and silylation[47] of cellulose and nanocellulose has been used to improve the mechanical properties of polymer composites by improving the dispersion of filler in the polymer matrix (shown with optical microscopy[48] and scanning electron microscopy[10, 49-51]), and therefore facilitating the interfacial melding between the filler and polymer.[10, 37, 52-55] For example, Kargarzadeh *et al.*, demonstrated that cellulose nanocrystals modified with *N*-(β-aminoethyl)-γ-aminopropyltrimethoxysilane displayed improved tensile strength and modulus reinforcement of unsaturated polyester resin at 2 wt% compared to unmodified nanocrystals.[53] Similarly, cellulose nanofibers modified with 3-aminopropyl triethoxysilane increased the strain to fracture resistance of poly(lactic acid) by 27% at 0.5 wt% loading, compared to a 18% decrease at the same loading of unmodified fibers.[52] The well-documented capability and utilization of silanized CNFs to improve the properties of polymeric materials motivated us to assess these materials for their biodegradability compared to unmodified CNFs. Specifically, we modified CNFs to different degrees with three common alkoxysilane reagents of varied functionality: methyl trimethoxysilane (MTMS), propyl trimethoxysilane (PTMS), and aminopropyl trimethoxysilane (APTMS).

By virtue of the alkyl character of their R-groups, MTMS, PTMS, and APTMS have been shown to both increase the hydrophobicity of nanocellulose, and improve interfacial adhesion between the nanocellulose and surrounding polymer matrices as a result of improved dispersion.[37, 48]

The principal objectives of the present study were to determine (1) the effect of hydrophobic silanization on the structure of CNFs and their dispersion properties in organic solvents and polymers, and (2) the effect of the same modifications on the mineralization of nanocellulose under anoxic conditions by anaerobic bacteria as a means of assessing their biodegradability. Scanning electron microscopy (SEM), attenuated total reflectance Fourier transform infrared spectroscopy (ATR-FTIR), X-ray photoelectron spectroscopy (XPS), and solid-state ^{13}C- and ^{29}Si-nuclear magnetic resonance spectroscopy (^{13}C-NMR and ^{29}Si-NMR) were used to identify the nature of the Si-CNFs and the ability to control the extent of silanization. The effect of silane modification on CNF stability in organic solvent casting solution was quantitatively assessed by evaluating its suspended mass as a function of settling behavior in chloroform (an organic solvent commonly employed in solvent casting) after silanization. The relation between improved CNF stability in solvent-casting media and dispersion in solution-blended polymer nanocomposite materials was assessed using high impact polystyrene (HIPS) and polyhydroxyalkanoates (PHA) composites. Finally, the effect that the extent and nature of each silane modification had on the biodegradability of nanocellulose was determined using biomethane potential tests[56] to assess the impact silane modification has on the anaerobic biotransformation of CNFs. As nanocellulose is nearly fully mineralized during anaerobic biodegradation,[23] tracking the biogas evolved from a sample is a reliable measure of its overall biodegradability.

3.3 Experimental

3.3.1 Materials Preparation

In this section, principal procedures are outlined, with a more detailed description of materials and methods in the Appendix (Chapter 7). Each chemical was used as received. Freeze-dried cellulose nanofibrils (CNFs) (mechanically milled) were purchased from the University of Maine Process Development Center. CNFs were modified with MTMS, PTMS, or APTMS in ethanol-water (80:20 v/v) following procedures described in the literature.[57] In brief, silane reagents were first hydrolyzed at 0.1, 1, 5, or 10 wt% (with respect to the ethanol solution) for 2 h before CNFs (0.02 g CNF mL_{EtOH}^{-1}) were added. After the solvent was removed, the silane-modified CNFs were annealed under vacuum at 110 °C (to drive condensation reactions), washed with acetone (to remove any unreacted silane reagent), and dried at 60 °C (to remove residual acetone). The final samples were then milled to a powder with a FlackTek Speed Mixer (DAC 150) using 2 mm yttrium-stabilized zirconium milling beads. In this report, it should be understood that "x wt%" of silane modification refers to the proportion of silane added to the reaction mixture (e.g. CNF modified with 5 wt% MTMS refers to the mass of silane reagent added to the functionalization mixture, not with respect to the nanocellulose). Self-condensed siloxane polymers were also prepared in the absence of CNF under the same conditions used for CNF modification. All samples were milled to a similar consistency before evaluating their mineralization or dispersion characteristics.

Throughout this manuscript, Si-CNFs are referred to first by a number that reflects the amount of silane (wt% with respect to the reaction solution) used during CNF modification, followed by: 'Me', 'P', or 'A' referring to methyl-(Me), propyl-(P), and

aminopropyl-(A) trimethoxysilane, respectively. For example, ‘5Me-CNF’ refers to CNFs treated with a reaction solution containing 5 wt% methyl trimethoxysilane. Similarly, self-condensed siloxane polymers are labeled ‘Me-self’, ‘P-self’, and ‘A-self’ for methyl-, propyl-, and aminopropyl- trimethoxysilane self-condensed polymers, respectively.

3.3.2 Materials Characterization

Succinct descriptions of techniques used in the characterization of samples are provided below, while full details of characterization methods are found in the SI. In brief, the morphology of CNFs before and after silane modification was analyzed using scanning electron microscopy (SEM); the functional groups in the unmodified CNF and in each of the Si-CNFs were identified using attenuated total reflectance Fourier transform infrared spectroscopy (ATR-FTIR); the bonding and concentrations of C, O, N, and Si at the surface of the unmodified CNF and Si-CNFs was assessed using X-ray photoelectron spectroscopy (XPS); the carbon structure of the nanocellulose before and after modification and the form of the silane reagents after CNF modification and self-condensation were identified via solid-state ^{13}C- and ^{29}Si- nuclear magnetic resonance spectroscopy (NMR); the amount of Si in the Si-CNFs was quantified with energy dispersive X-ray spectroscopy (EDS); and the dispersion of CNFs in solvent-cast polymer nanocomposites was assessed using optical microscopy (OM), SEM, and EDS.

3.3.3 Supernatant Mass Recovery Tests

The effect that silane modification had on CNF stability in an organic solvent casting solution was investigated via mass recovery analysis performed on the supernatant of chloroform solutions containing unmodified and silane-modified CNFs. In these experiments, CNFs were sonicated in chloroform for 5 h to form a suspension at a

concentration representative of those used in solvent casting syntheses[58] (0.5 mg CNF·$mL_{solvent}^{-1}$). At select time-points (settling times) after the suspension had been formed, 10 mL aliquots of supernatant were removed from the suspension, collected, dried on a 60 °C hotplate, and then weighed to determine the CNF concentration in the supernatant. Triplicate samples of the unmodified CNFs were run to determine the precision of this method. The baseline for detectable suspended concentration was determined through a blank control sample of chloroform run without any nanocellulose, prepared identically to the CNF samples and tracked over 100 h. Results from this study revealed that the baseline level for CNF detection is roughly 7% of the initial CNF concentration. The nonzero concentration value detected is due to contaminant species from sonication (i.e., silica) being present in suspension at low concentrations (< 1 mg·10 mL_{EtOH}^{-1}).

3.3.4 Synthesis of Hydrophobic Solvent Cast Polymer Nanocomposites

To relate changes in the stability of CNFs in chloroform after silanization to their dispersion in a hydrophobic material, polymer nanocomposites were synthesized via a solution casting process where chloroform was used as the solvent. CNFs were suspended in chloroform via sonication at either 9 wt% (with respect to high impact polystyrene polymer) or at the same concentration used in the dispersion studies (5 wt% in polyhydroxyalkanoates) before high impact polystyrene (HIPS) or polyhydroxyalkanoates (PHA) were added at a concentration of 10 mg·$mL_{solvent}^{-1}$, and sonicated for an additional 2 h. The PHA used in these experiments was a co-polymer of poly-3-hydroxybutyrate (P3HB) and poly-4-hydroxybutyrate (P4HB), purchased from Yield10Bioscience (formerly Metabolix Inc., Woburn, MA) Aliquots of this casting solution (5 mL) were

poured in ~40 mm diameter aluminum dishes and dried to evaporate the chloroform, leaving behind a solvent-cast thin film composite of 5 wt% CNF in PHA. This procedure was performed with unmodified CNFs in HIPS and both unmodified CNFs and 5Me-CNFs, the latter used as a representative Si-CNF, in PHA. CNF dispersion in both composites was determined using OM and SEM images of the nanocomposite surfaces. Energy dispersive spectroscopy (EDS) was used to detect the location of unmodified CNF in HIPS after composite synthesis.

3.3.5 Biogas Production Tests

The mineralization of unmodified CNFs and Si-CNFs was assessed using biomethane potential (BMP) tests to track biogas production when the samples were exposed to an anaerobic mixed microbial culture. In brief, a bacterial media was prepared using nutrient and buffers as outlined in Angelidaki, *et al.*[59] The media was heated at 100 °C for 30 min to achieve anoxic conditions before it was inoculated with a culture sourced from anaerobic digester sludge (obtained from Back River Waste Water Treatment Plant, Baltimore, MD) at a concentration of 10% v/v. The BMP media was then adjusted to a pH of 7.2 and kept anoxic via continuous purging with N_2 gas throughout the preparation. CNF samples were combined with the N_2-purged anaerobic bacterial media in septum-sealed bottles (in triplicate) and reacted at mesophilic temperature (35 °C). As CNFs and Si-CNFs underwent mineralization, the evolution of biogas produced a positive pressure within the sealed system which was tracked via volume measurements using a glass syringe. In this way, the volume of biogas measured provided a direct quantification of the pressure increase within the bottles stemming from the evolved biogas. Triplicate samples of blank anaerobic media were also prepared to determine the biogas produced from residual native

organic matter in the sludge. Values from these blanks (typically < 3 mL per time point) were subtracted from each nanocellulose sample to determine the volume of biogas produced due to each CNF alone. Gas composition was also assessed. The rate, magnitude, and change in composition of biogas evolution were determined by measuring the biogas produced at various time points ranging from 3 to 120 days.

Exact sample mass added to each bottle was adjusted to ensure the same amount of biodegradable material (i.e., ~150 mg of nanocellulose) was available in each sample regardless of the silanization. This was accomplished by estimating the overall degree of silanization in each sample based on the atomic % Si determined by EDS (Table 7.1). For example, based on EDS data, 0.1Me-CNF contained approximately one equivalent of silicon-containing reagent for each cellobiose unit (disaccharide composed of two β-glucose residues linked by a β(1→4) bond). As a result, roughly 163 mg of 0.1Me-CNF was added to each bottle based on the assumption that each silicon atom represented the addition of one ($MeSiO_3$) unit to the cellulose structure. In addition to controlling the mass of each sample that went into the bioreactors, the volume of CH_4/CO_2 produced by each sample was benchmarked to the maximum biogas produced by an unmodified CNF control exposed to the same bacterial culture.

3.4 Results

3.4.1 Characterization of CNFs and Si-CNFs

CNF samples were modified with one of three trialkoxysilane reagents (MTMS, PTMS, or APTMS). The amount of silane used in each modification reaction was varied (i.e., 0.1 – 10 wt%) to obtain three series of silane-modified CNFs for characterization. In addition, each silane reagent was self-condensed in the absence of CNF to form siloxane

polymers (Me-self, P-self, A-self) for comparison. Samples were analyzed with a combination of SEM, ATR-FTIR, solid-state ^{13}C- and ^{29}Si-NMR, and XPS/EDS to determine the nature of the silane modification.

The morphology of the unmodified and silane-modified CNFs was characterized with SEM (representative images in Figure 3.1). The identification of cellulose nanofibrils was confirmed via the nanometer-scale widths (101 +/- 17 nm) and micron-scale lengths that were observed.[60] The persistence of these characteristic aspect ratios after silanization indicates that the nanocellulose maintained its nanofibril structure after silane treatment.

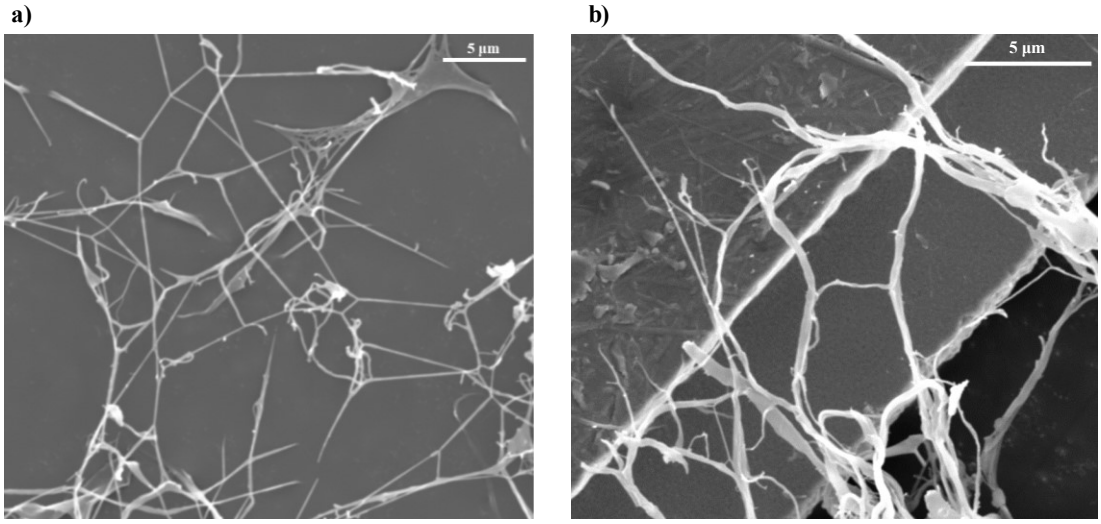

Figure 3.1 SEM images of (a) unmodified cellulose nanofibrils (CNF) and (b) CNFs modified with 10 wt% PTMS (10P-CNF).

Infrared spectra of the 5Me-CNF, 5P-CNF, 5A-CNF, and unmodified CNF powders are presented in Figure 3.2a. For unmodified CNF, the principal peaks for cellulose were observed (i.e., C–O stretching at 1035 cm^{-1}, C–H stretching region at 2900 cm^{-1}, and broad O-H stretching centered at 3350 cm^{-1}).[61] In addition to the characteristic cellulosic peaks, Si-CNFs also displayed new IR peaks which are unique to each respective silane reagent; specifically, Si–CH_3 symmetrical deformation at 766 cm^{-1} and 1270 cm^{-1}

for MTMS-modified CNF;[62-63] methylene stretching peaks at 2880 cm^{-1} and 2950 cm^{-1} for PTMS-modified

CNF;[64-65] and methylene stretching modes at 2920 cm^{-1} and 2860 cm^{-1}, as well as N–H

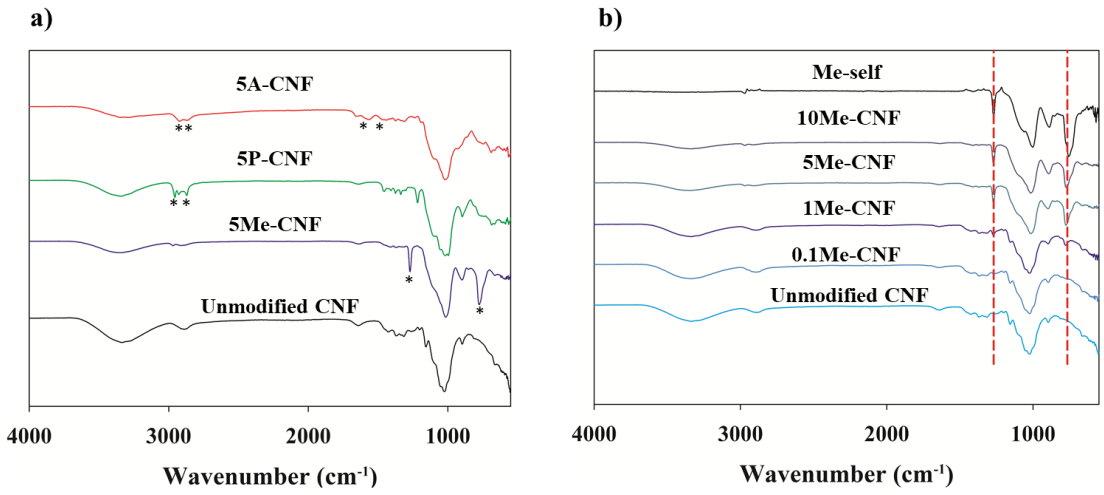

Figure 3.2 ATR-FTIR of (a) cellulose nanofibrils (CNFs) modified with 5 wt% MTMS, PTMS, or APTMS, and (b) CNFs modified with increasing amount of MTMS self-condensate.

scissoring at 1580 cm^{-1} and symmetric deformation of NH_3^+ at 1480 cm^{-1} for APTMS-modified CNF.[66-67] The ATR-FTIR data also revealed that the intensity of each silane peak increases systematically with the degree of silanization. For example, ATR-FTIR data of MTMS-modified CNF in Figure 3.2b show a clear increase of the peaks at 766 cm^{-1} and 1270 cm^{-1} with an increasing degree of silane modification.

XPS was used to characterize the elemental composition and bonding environment of atoms in the near surface region (≲ 2-3 nm) of the unmodified and Si-CNFs (Figures 3.3 and 7.1). Figure 3.3a shows the high-resolution C(1s), O(1s), and Si(2p) photoelectron peaks obtained from CNFs modified with MTMS. The C(1s) envelope of the unmodified

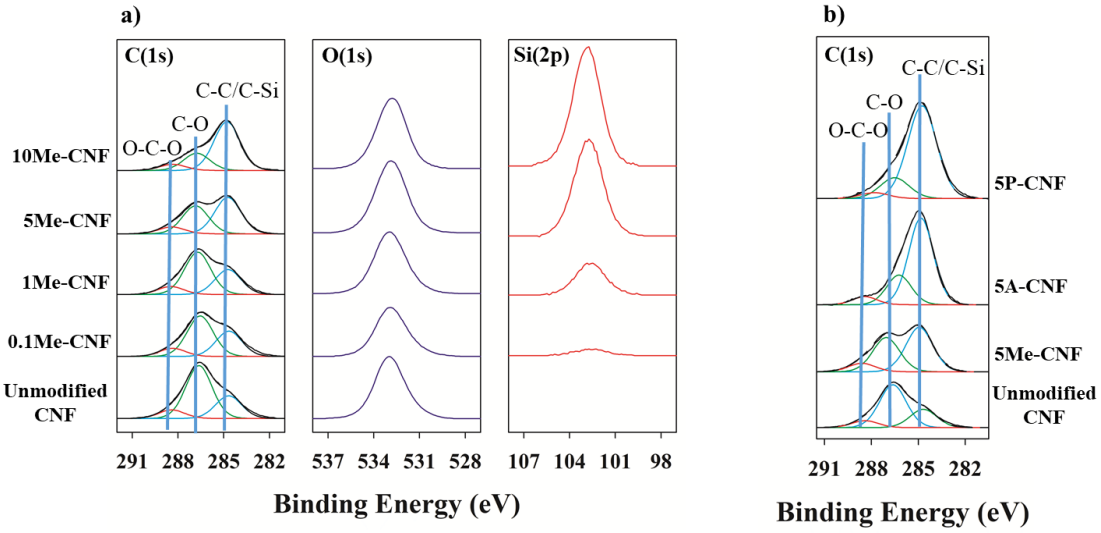

Figure 3.3 XPS of (a) C(1s), O(1s), and Si(2p) regions for cellulose nanofibrils (CNFs) modified with different wt% MTMS, and (b) C(1s) region for CNFs modified with 5 wt% MTMS, PTMS, or APTMS.

CNF is comprised of three components and is consistent with previous measurements of nanocellulose.[68] The envelope consisted of a dominant peak at 286.6 eV due to the presence of C–O bonding, a higher binding energy O–C–O peak at 288.3 eV due to the acetal linkage in nanocellulose, and a peak at 284.8 eV likely due to adventitious carbon. Figure 3.3a shows that the intensity of the photoelectron transition at 284.8 eV (due to C–C or C-Si bonding)[68] in MTMS-modified CNF increased systematically with silane loading due to the introduction of Si–C carbon atoms. In contrast, the C–O and O–C–O peaks decreased in intensity as silanization increased. Additionally, as the degree of silanization increased, the concentration of Si generally increased in both XPS (Figure 3.3a) and EDS (Table 7.1).

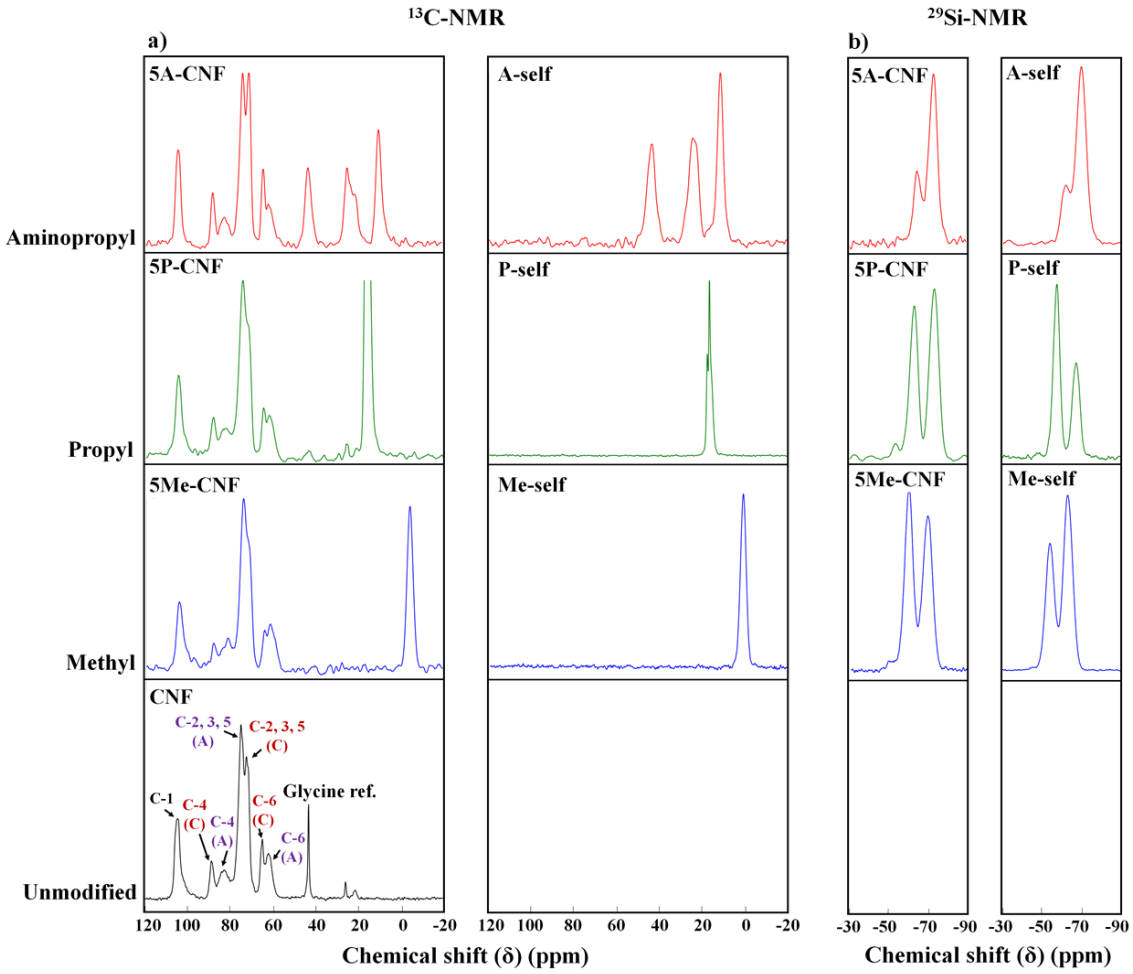

Figure 3.4 Solid-state ^{13}C-NMR spectra (a) of cellulose nanofibrils (CNF) modified with 5 wt% APTMS (5A-CNF), PTMS (5P-CNF), or MTMS (5Me-CNF) compared to self-condensed silane reagents (A-self, P-self, Me-self). In unmodified CNF, characteristic peaks are designated by amorphous ('A', purple), crystalline ('C', dark red), or peaks where the amorphous and crystalline regions are convoluted (black) labels. Shown on the right is solid state ^{29}Si-NMR spectra (b) of Si-CNFs modified with 5 wt% APTMS (5A-CNF), PTMS (5P-CNF), or MTMS (5Me-CNF) compared to self-condensed silane reagents (A-self, P-self, Me-self).

Figure 3.3b compares the C(1s) regions for unmodified CNFs as well as 5Me-, 5P-, and 5A-CNF. Although the C(1s) envelopes contain the same three peaks, the C–C/C–Si peak intensity in 5A-CNF and 5P-CNF is larger than in 5Me-CNF due to the greater number of carbon atoms in the side chain of APTMS and PTMS reagents compared to MTMS. Consistent with expectations, nitrogen was observed only in the APTMS-modified CNFs

(data not shown), and steadily increased in concentration as the amount of APTMS used in modifying the CNFs increased.

To further characterize the nature of the CNFs before and after silanization, solid-state ^{29}Si- and ^{13}C-NMR were performed on the unmodified, 5Me-, 5P-, and 5A-CNFs as well as the self-condensed polymers (Me-self, P-self, and A-self). The ^{13}C-NMR spectrum of untreated nanocellulose with peak assignments is shown in Figure 3.4a along with the spectra of the three self-condensed and three Si-CNF samples. The peaks between 50 and 150 ppm in the CNF-containing spectra reflect carbons C-1 through C-6 (labeled in Figure 7.2) of cellulose in both amorphous and crystalline forms. Peaks corresponding to crystalline and amorphous forms of cellulose in the unmodified CNF spectrum were assigned based on known chemical shifts.[69] In this cellulosic region, the spectra of unmodified CNFs and Si-CNFs were similar, as evinced by the peak shifts in Table 7.2. The peaks between 0 and 50 ppm in the ^{13}C-NMR spectrum arose from the R_1 alkyl side chains (methyl, propyl, and aminopropyl) from the silanization reagents, and are comparable between the self-condensed and Si-CNF spectra. The methylene carbons in the aminopropyl side chain produced peak shifts at 11.7, 24.6 and 43.6 ppm; this reflected the different chemical environments of the three side chain carbons. The methylene and methyl carbons of the propyl side chain produced peak shifts at 15.9 and 16.9 ppm, with a visible shoulder around 17.8 ppm. The methyl side chain produced a large, single peak between 0 and 1 ppm. The ^{29}Si-NMR spectra of both the self-condensates and Si-CNFs is shown in Figure 3.4b with relevant chemical shifts in Table 7.3. The T^i notation used herein indicates that each silicon atom in the silane coupling agents can have three (T) Si–O–R bonds and one bond to a sidechain group (Si–R_1; the R_1 sidechains are methyl, propyl, or aminopropyl

in these experiments). The *i* denotes the number of Si–O–R bonds that bridge to another silicon atom (Si–O–Si).[70] The remaining Si–O–R bonds bridge to either H, CH_3, or cellulose in these experiments. Hence, in addition to the R_1 sidechain, a T^1 silicon atom has one siloxane (Si–O–Si) bridge and two Si–O–R bridges; a T^2 silicon atom has two Si–O–Si bridges and one S–O–R bridge; and a T^3 silicon atom has three Si–O–Si bridges and zero Si–O–R bridges. The T^1 silicon atoms produce ^{29}Si peak shifts between –44 and –49 ppm; T^2 silicon atoms result in peaks around –53 to –57 ppm; and T^3 silicon atoms present peak shifts near –68 ppm.[70-73]

In the Si-CNFs and the self-condensed siloxane polymers (i.e., with no CNF present), the ^{29}Si-NMR showed no chemical shifts near –40 ppm, where T^0 and nonhydrolyzed silicon atoms would be detected.[70, 72, 74] This indicates that the methoxy groups of the trimethoxysilane reagents underwent complete hydrolysis and subsequent self-condensation to produce peak shifts reflecting T^1, T^2, and T^3 silicon atoms.

The ^{29}Si-NMR spectra of the self-condensed and Si-CNF samples are comparable as each are dominated by the presence of T^2 and T^3 silane species (Figure 3.4b). For the self-condensed materials, the more downfield peaks are centered between about –53 and –62 ppm (T^2 forms), and the peaks upfield of this are between approximately –62 and –68 ppm (T^3 forms), with variations in position reflecting the influence of the electron donating character of the R_1 side chains (methyl, propyl, aminopropyl).[75-77] This effect is exhibited by both the self-condensates and the Si-CNFs: the chemical shifts for each type of silicon atom (i.e., T^i designation) are lowest for the aminopropyl trimethoxysilane reagent, followed by the propyl and then the methyl trimethoxysilanes (Table 7.3). For the Si-CNF

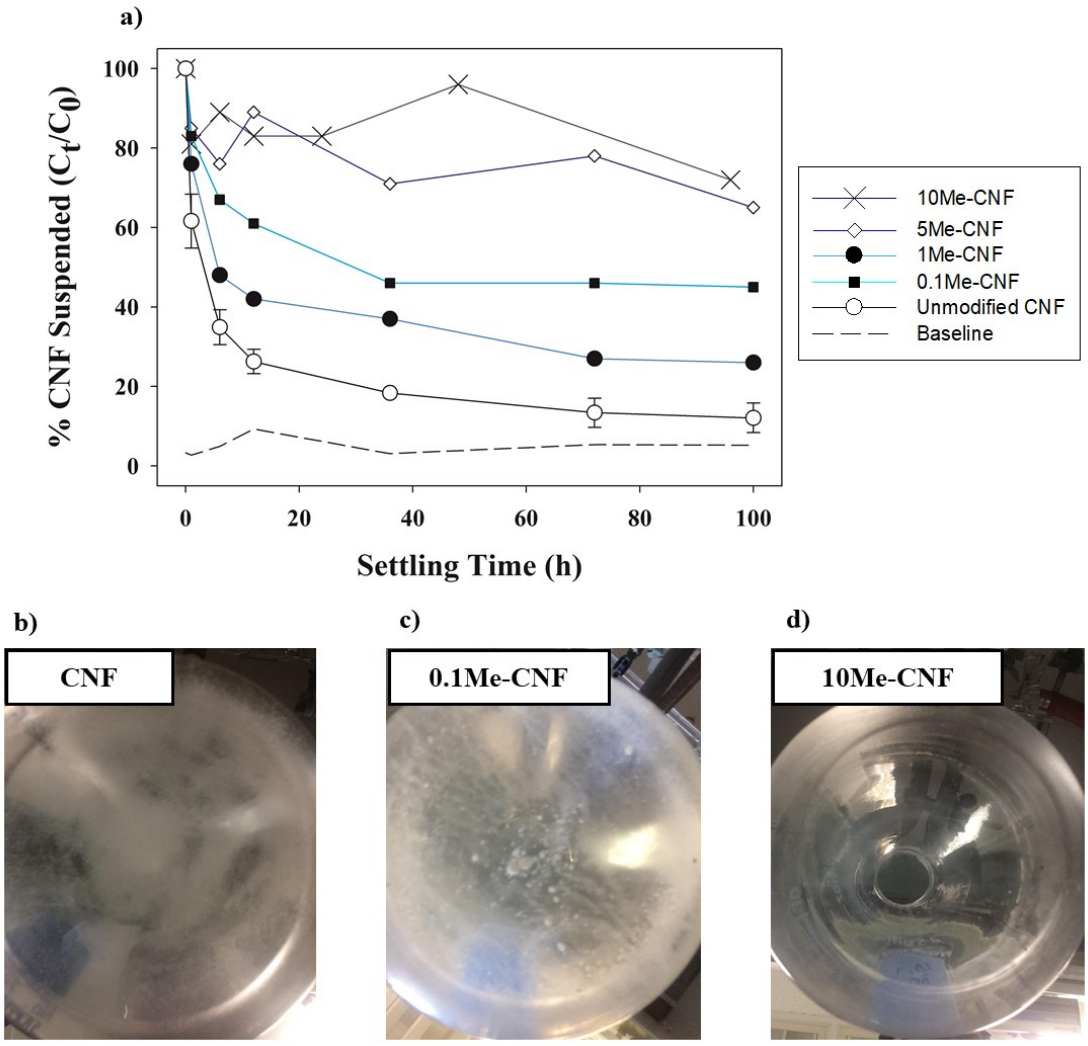

Figure 3.5 Stability of cellulose nanofibrils (CNFs) in chloroform, including (a) mass recovery analysis for CNFs modified with 0.1 (black squares), 1 (black circles), 5 (white diamonds), or 10 (crosses) wt% MTMS compared to unmodified CNFs (white circles). Data are plotted in terms of percent CNF concentration remaining in the supernatant (C_t/C_0) as a function of settling time. The baseline concentration that could be determined via control studies is denoted by the dashed line (see text for details). Also shown are digital images of chloroform solutions containing (b) unmodified CNF, (c) 0.1Me-CNF, and (d) 10Me-CNF after 100 h settling.

materials, the T^2 peaks are between about –59 and –63 ppm, and the T^3 peaks are between approximately –68 and –72 ppm.

A much smaller, but detectable T^1 silicon peak was present (between –44 to –48 ppm) in the spectra of the self-condensates of only the propyl and methyl trimethoxysilanes, and not in those of the aminopropyl self-condensate sample. A smaller T^1 peak was apparent in all Si-CNF spectra, estimated between –44 and –53 ppm. The general observation of T^2 and T^3 peaks dominating the spectra with little T^1 signal is consistent with previous reports for silane-treated cellulose.[72, 78] In summary, the ^{29}Si-NMR spectra are comparable between the self-condensates and silane-treated cellulose samples, although, as expected, the chemical shifts and peak ratios varied.

3.4.2 Stability of Si-CNFs in Solvent Casting Media

Mass recovery analysis was used as a quantitative means to assess the stability of chloroform suspensions made with unmodified CNFs and Si-CNFs. This technique involved dispersing each type of CNF in chloroform and measuring the CNF/Si-CNF concentration remaining in suspension as a function of settling time. Results of mass recovery analyses for CNFs before and after silanization are presented in Figure 3.5 and Figure 7.3.

In each test, the largest decrease in CNF concentration occurred within the first 12 h of settling, followed by a relatively stable suspended concentration for the remaining 88 h. Most of the unmodified CNFs (~70%) sedimented out of suspension during the initial 12 h, which approached the baseline level of detection (Figure 3.5a). As the extent of silanization increased, CNF stability in chloroform generally increased. All of the Si-CNFs were present at a higher concentration in the supernatant after 100 h of settling compared to unmodified CNF. 5Me-CNF and 10Me-CNF were the most stable in chloroform; ~80% of the initial 10Me-CNF concentration remained in suspension after 100 h. In contrast, <

20% of the unmodified CNFs remained in suspension during the same time period. In the unmodified CNF and 0.1Me-CNF (Figure 3.5b and 3.5c), a significant quantity of nanocellulose was observed at the bottom of the flask. The improved stability of 10Me-CNF, in contrast, is demonstrated visually in photographs of representative CNF suspensions after 100 h of settling (shown in Figure 3.5d) via the lack of settled material. The 10Me-CNF solution featured a suspended layer of gel which appeared translucent with no visible particles at the bottom. The presence of 10Me-CNF siloxane in this gel layer was confirmed after 100 h of settling using transmission infrared spectroscopy (data not shown). Furthermore, the hydrophobicity of the silanization strategy (Me, P, or A) appeared to impact CNF stability. Thus, while 5A-CNF displayed improved stability compared to unmodified CNF, it was less stable than CNFs treated with the more hydrophobic reagents (5Me-CNF or 5P-CNF) as shown in Figure 7.3.

3.4.3 Dispersion of Si-CNFs in Hydrophobic Polymer

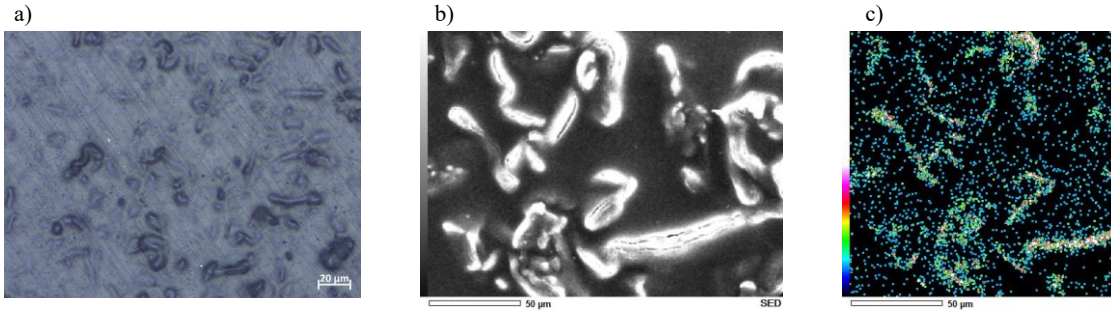

Figure 3.6 a) Optical microscopy images of solvent cast high impact polystyrene (HIPS) nanocomposite filled with 9 wt% cellulose nanofibrils (CNFs). B) Scanning electron microscopy (SEM) images of solvent cast HIPS nanocomposite filled with 9 wt% CNFs. c) Energy dispersive spectroscopy (EDS) O Kα map of solvent cast HIPS nanocomposite filled with 9 wt% CNFs. Black character is oxygen-sparse HIPS polymer and white regions represent high oxygen content from CNFs. EDS map is of the same region shown by SEM in b).

Polymer nanocomposites were prepared through a solution blending of polyhydroxyalkanoates (PHA) or high impact polystyrene (HIPS), hydrophobic polymers—and CNFs in chloroform followed by solvent casting thin films. Unmodified CNFs were solvent cast into high impact polystyrene (HIPS) films and imaged with optical microscopy and SEM/EDS. CNFs were found to homoaggregate into large clusters visible in optical microscopy images shown in Figure 3.6a. Such aggregates were also observed in SEM images as long, bright, fiber-like structures which stood out against the dark HIPS background (Figure 3.6b) and displayed poor interfacial adhesion via the gaps between polymer and fiber. These fibers were confirmed to be CNF via EDS mapping of the O Kα signal intensity across the nanocomposite surface. HIPS lacks oxygen atoms in its molecular structure, and thus yields a dark background in the EDS map in Figure 3.6c.

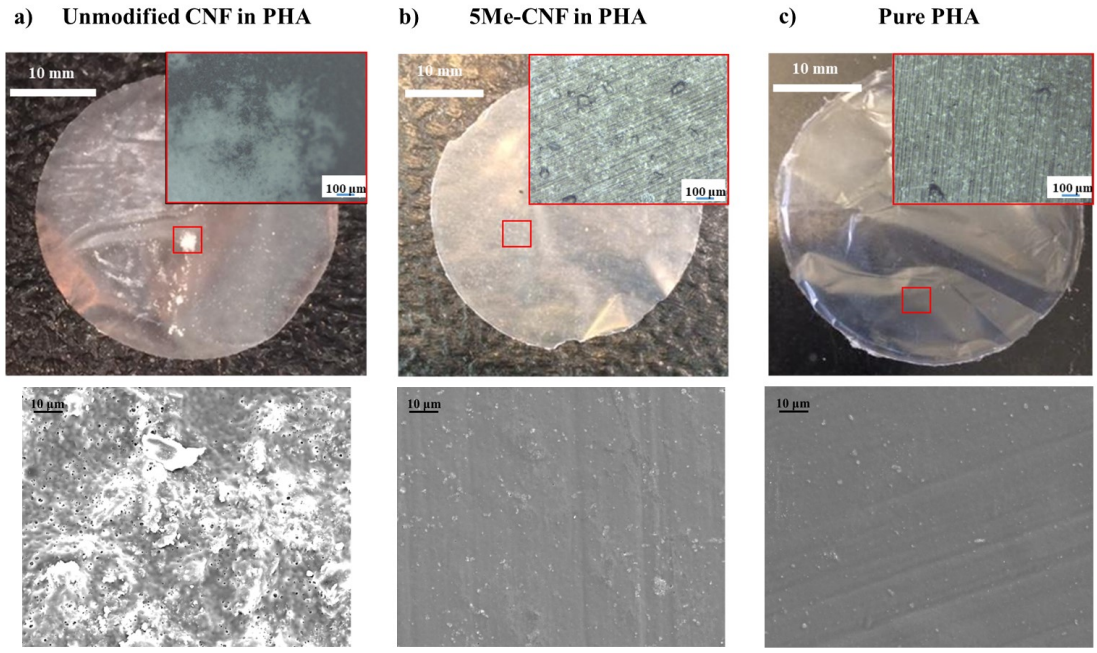

Figure 3.7 (Top) Digital and optical microscopy (OM, inset) images of polyhydroxyalkanoates (PHA) nanocomposites containing (a) unmodified cellulose nanofibrils (CNF), (b) CNFs modified with 5 wt% MTMS (5Me-CNF), and (c) pure PHA. In each digital image, a red box highlights the regions scanned with OM shown in the 1 mm^2 inset images. (Bottom) Comparative SEM images of the nanocomposite surface (10 kV, 1000x) corresponding to each sample.

Conversely, CNF is an oxygen-rich nanomaterial as exhibited in the intense signal (shown as white coloring) in Figure 3.6c. Such aggregation confirms that unmodified CNF struggles to disperse in a commonly used hydrophobic polymer (i.e., HIPS).

Figure 3.7 shows images of representative films containing unmodified CNF and 5Me-CNF nanofillers. Nanocomposites made with unmodified CNF showed extensive aggregation, visible as areas of white patches throughout the film in Figure 3.7a. Optical microscopy of these areas (Figure 7.6a, top inset) confirmed that these aggregates were not seen in neat PHA films (Figure 3.7c). Upon closer inspection with the optical microscope, these aggregates appeared to be white, fluffy particles indicative of poorly dispersed CNF. In contrast, PHA films prepared with 5Me-CNF (Figure 3.7b) displayed no visible white aggregates. These differences are even more apparent in the corresponding SEM images (Fig 3.7 bottom and Fig 7.4). The SEM images of PHA and PHA filled with Si-CNF were flat and largely featureless. In contrast, the PHA loaded with native CNF exhibited a rough surface with many micron sized pores. Closer investigation of the brighter features on the surface revealed the presence of fibril-like features which were distinct and detached (Fig 7.5) from the surrounding polymer matrix. EDS mapping (example shown in Fig 7.6) consistently showed that these structures possessed a higher concentration of oxygen than the surrounding PHA ($C_4O_2H_6$), as would be expected by an oxygen-rich nanocellulose fibril ($C_6O_5H_{10}$). In summary, the OM and SEM images both support the idea that Si-CNFs disperse far more uniformly in hydrophobic PHA polymer than unmodified CNFs. Moreover, in the absence of silanization, the addition of CNFs severely impacts the structural integrity of the hydrophobic polymer matrix.

3.4.4 Biodegradability of Si-CNFs Assessed via Mineralization

While unmodified CNFs completely and rapidly mineralize, the properties of fibrils treated with hydrophobic surface modifiers could differ.[79] Biomethane potential (BMP) tests measure the rate and extent of biogas production as a result of sample mineralization during anaerobic biodegradation, and therefore provide a quantitative method to evaluate how different silane modifications impact the extent and ease of CNF mineralization.[59] The

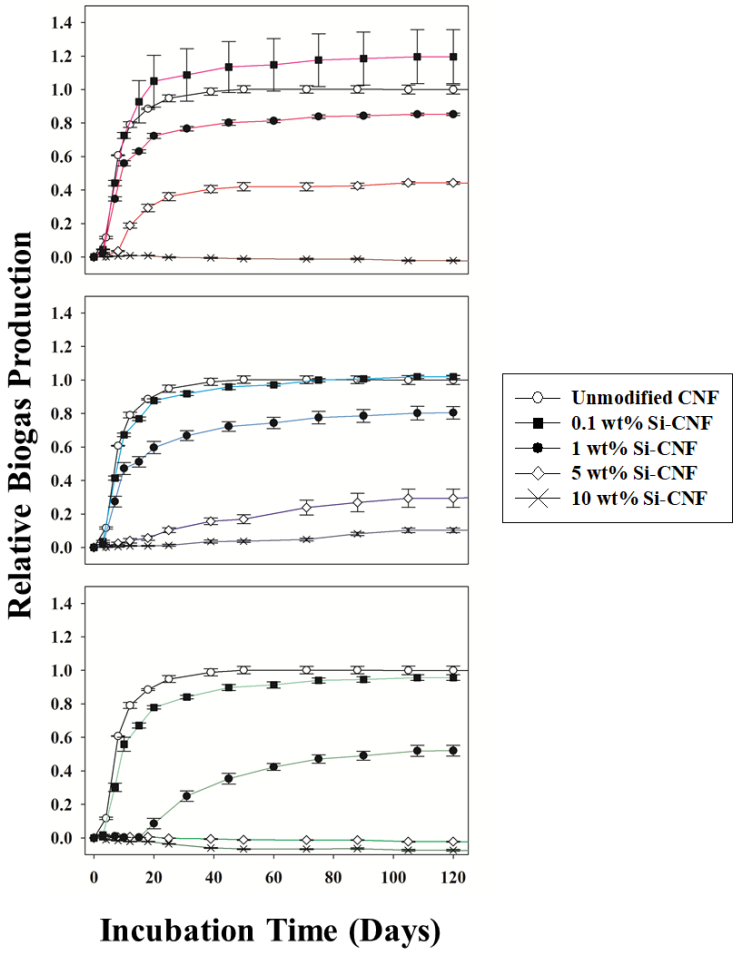

Figure 3.8 Relative biogas production for unmodified cellulose nanofibrils (white circles, CNFs) and CNFs modified with APTMS (top), MTMS (middle), or PTMS (bottom) trimethoxysilane. Each plot displays CNFs modified with 0.1 (black squares), 1 (black circles), 5 (white diamonds), or 10 (crosses) wt% of the respective silane. Values are normalized to the biogas produced from the unmodified CNF sample under the same experimental conditions.

results of BMP tests performed on unmodified and silane-modified CNFs are presented in Figure 3.8 and 3.9. All plots were normalized to the maximum volume produced by the unmodified CNF sample in each set, to account for any differences in bacterial culture obtained from separate visits to the waste water treatment plant. The biogas produced from each Si-CNF relative to unmodified CNFs as a function of inoculation time is shown in Figure 3.8. The biogas production curves typically displayed a sinusoidal shape. These curves provided information on both the rate and extent of each sample's mineralization, the latter expressed by the plateau point in biogas production. For CNFs modified with the lowest amount of silane reagent (i.e., 0.1Me-, 0.1P-, 0.1A-CNF), the extent of mineralization was similar to that for the unmodified CNF, and each Si-CNF completely

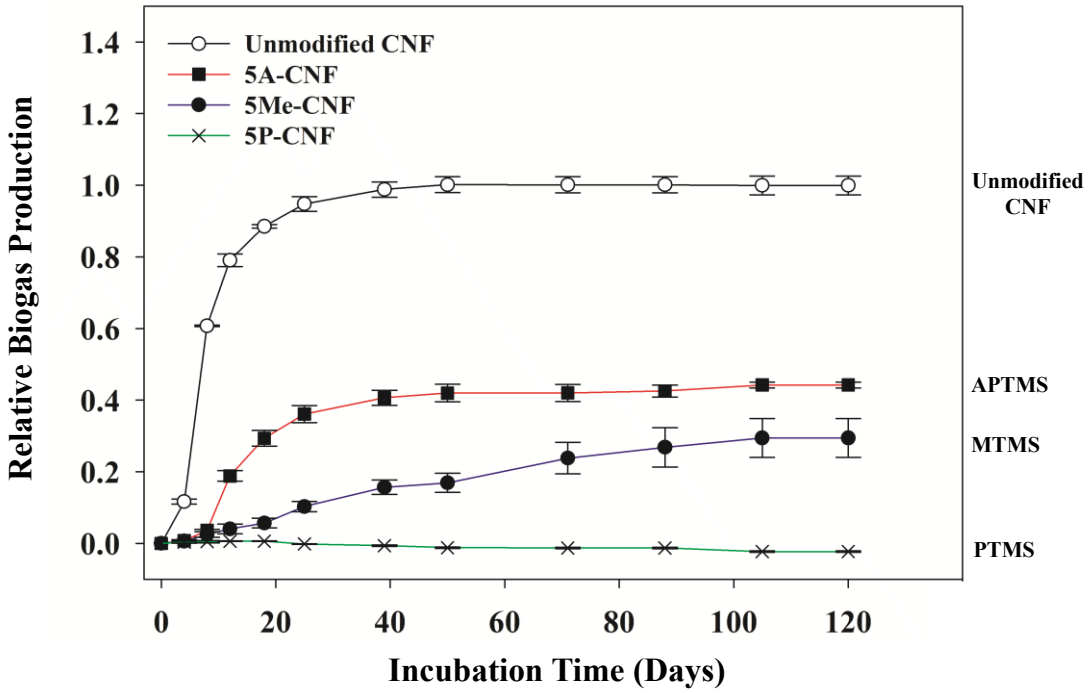

Figure 3.9 Relative biogas production for unmodified cellulose nanofibrils (CNF, white circles) and CNFs modified with 5 wt% ATPMS (squares), MTMS (black circles), or PTMS (crosses) trimethoxysilane. Values are normalized to the biogas produced by an unmodified CNF sample under the same experimental conditions.

mineralized within ~20 d. However, as the extent of silane modification increased beyond this point, the inhibition of biogas production began. This effect was first observed in 1Me-, 1P-, and 1A-CNF as the total volume of biogas produced decreased as compared to the unmodified CNF. For 5Me-CNF, 5P-CNF, and 5A-CNF, a delay in the onset of biogas production was observed along with a further decrease in the total amount of biogas produced. Specifically, 29%, 0%, and 42% of the biogas produced by the unmodified CNF sample was observed for 5Me-CNF, 5P-CNF, and 5A-CNF, respectively. The suppression of biogas production was still more apparent for 10Me-, 10P-, and 10A-CNF, where there was essentially no biogas produced. Separate control studies performed to assess the mineralization of the self-condensed siloxane polymers (Figure 7.7) each yielded no biogas over 80 days of inoculation. Gas chromatography analysis of biogas produced across all samples showed a decrease in N_2 content (used to backfill anaerobic samples at the start of test) as biodegradation proceeded, while the carbon dioxide and methane components grew in intensity (data not shown). This trend was exhibited by all CNF samples as they were mineralized, regardless of the specific silanization. Additionally, the extent and rate of CNF mineralization were impacted by the nature of the silane reagent as shown in Figure 3.9, although this effect was less pronounced than the influence of the extent of silanization. Specifically, for the same amount of added silane (here 5 wt%), the extent and rate of CNF mineralization followed the trend: unmodified CNF > 5A-CNF > 5Me-CNF > 5P-CNF.

3.5 Discussion

3.5.1 Characterization of Si-CNFs

After extensive silane modification, representative SEM images (Figure 3.1b) coupled with ATR and ^{13}C-NMR spectra (Figure 3.2a and 3.4a, respectively) of 5Me-CNF

revealed that the nano-scale fibril structure and bonding of the CNFs was maintained. The ^{13}C-NMR spectra of the unmodified CNFs and the Si-CNFs (Figure 3.4a) additionally demonstrated that the nanocellulose samples contained characteristic peaks of both amorphous and crystalline cellulosic regions before and after treatment with the silane coupling reagents (Table 7.4). Based on averages of all the carbons shown in Table 7.4, it was concluded that the amorphous character of the CNFs was only slightly changed after silanization for each Si-CNF. This is important to establish, as differences in crystallinity are known to affect relative biodegradability between samples[80-81].

Infrared and XPS data demonstrate our ability to control the degree of silanization by tuning the amount of silane added to the reaction mixture. Thus, vibrational features associated with the silane in the ATR-FTIR spectra of MTMS-modified CNFs grew in intensity as more silane was added to the reaction mixture (Figure 3.2b). Additionally, increasing the degree of silanization led to an increase in the Si signal and C–C/C–Si peak intensity measured by XPS (Figure 3.3a), and the Si signal measured by EDS (Table 7.1).

The ATR-FTIR spectra of the Si-CNFs contained peaks associated with both the unmodified CNF and the respective self-condensed siloxane polymer (Figures 3.2a and 7.8). This suggested that the chemical bonding in the silane layer was similar to that of the self-condensed polymer. The solid-state ^{29}Si-NMR experiments supported this interpretation of the ATR-FTIR data, and provided insight into whether the silanes may be solely covalently bound to cellulose, or exist as self-condensed polymers. Specifically, the ^{29}Si-NMR spectra of all Si-CNFs (Figure 3.4b) indicated that considerable self-

condensation of the silane reagents occurred as evidenced by the preponderance of T^2 and T^3 silicon atoms in the samples.

T^3 silanes are unavailable to undergo reaction with nanocellulose while T^1 or T^2 silicon atoms in the Si-CNFs may covalently bond to the nanocellulose through the formation of Si–O–cellulose bonds. Within the T^1 or T^2 peak shifts for the Si-CNFs, we could not directly discern whether the Si-O-R bonds were a Si–O–H bridge or a Si–O–

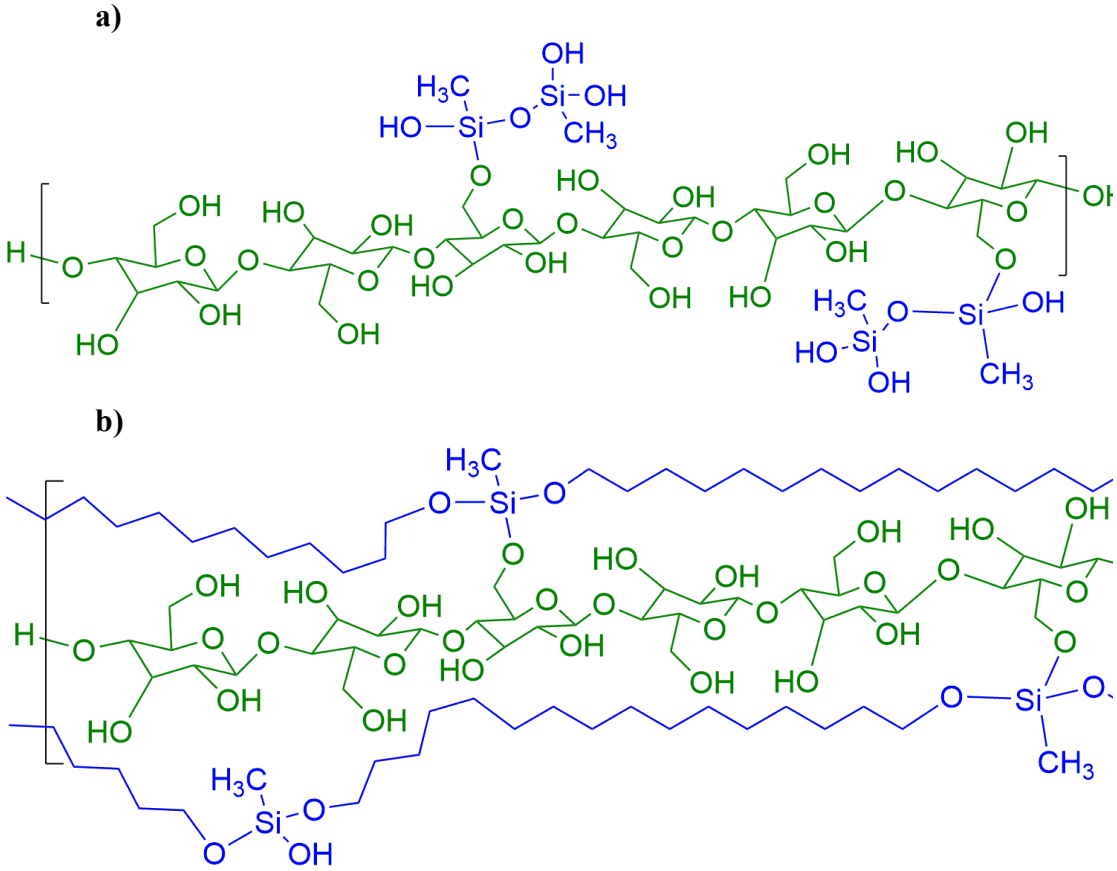

Figure 3.10 Schematics of approximate structures for 0.1Me-CNF (a) and 10Me-CNF (b). For both 0.1Me-CNF and 10Me-CNF, the siloxane coatings (blue) are attached to the CNFs (green) through a small number of covalent bonds. At a low degree of silanization (0.1Me-CNF), a small portion of the CNFs is covered by siloxane. As the degree of silanization increases, the CNFs are coated with siloxane (10Me-CNF). The schematics display a single CNF coated with siloxane to more easily illustrate the silanization, when in reality multiple fibrils were closely associated regardless of the amount of siloxane coating adhered to them. Additionally, in (b), the blue chain around the fibril should be assumed to be repeat $SiO_2(OH)(CH_3)$ siloxane units. Shorthand was used to facilitate interpretation of the schematic.

cellulose bond formed after reaction with an O–H group in the CNFs. However, some degree of covalent bonding between the silane and CNF is likely as the T^1 peaks of the propyl and methyl trimethoxysilane-treated Si-CNFs and T^2 peaks of the propyl trimethoxysilane treated Si-CNFs were broadened relative to those of the corresponding self-condensation products (Table 7.5). Any covalent attachment between the siloxane coating and nanocellulose was sparse, however, as evidenced by the relatively small T^1 peaks in ^{29}Si-spectra, the concomitant lack of significant changes in the crystalline and amorphous regions in ^{13}C-spectra, and the subtle differences in the cellulose region between the spectra of self-condensed, silane-treated, and untreated (^{13}C only) materials. This assertion is consistent with the results of previous NMR investigations of silanized nanocellulose.[82-83] The proposed approximate nature of the silanized CNFs is illustrated in Figure 3.10, where representative MTMS-modified Si-CNFs with relatively low and high coverages of siloxane coating are shown as an example. XPS indicated that as the degree of silanization increased, the fraction of coated CNFs also increased. Thus, in 0.1Me-CNF, only a small portion of the fibrils have a siloxane coating (Figure 3.10a), while the majority of the sample surface is still unmodified CNF. Increased silanization as in 10Me-CNF leads to most, if not all fibrils being coated in siloxane, with minimal nanocellulose exposed (Figure 3.10b). The thickness of this coating in 10Me-CNF was calculated to be ~0.4 nm as determined by the decrease in the cellulosic C–O peak intensity at 286.6 eV between the unmodified CNFs and 10Me-CNF (see Figure 3.3a).[84]

3.5.2 Dispersion Properties of Si-CNFs

The siloxane coated structure of the Si-CNFs described in Figure 3.10 served as the basis to explain their dispersion properties. The instability of unmodified CNF in chloroform is a consequence of the unfavorable intermolecular forces that exist between the hydrophilic surface of the nanocellulose and the hydrophobic solvent compared to the favorable interactions between adjacent nanofibrils. Silanization with MTMS improved the hydrophobicity of CNF, as 0.1Me-, 1Me-, 5Me-, and 10Me-CNF all displayed higher stability in chloroform compared to unmodified CNF. We ascribe this increase in CNF stability to the formation of an extensive and adherent hydrophobic siloxane coating, which led to improved hydrophobic intermolecular interactions between the Si-CNFs and chloroform. The net result was a stable dispersion which manifested as a suspended gel-like layer in solution for 5Me-CNF and 10Me-CNF. In 0.1Me-CNF and 1Me-CNF, the degree of silanization was lessened, which resulted in a smaller fraction of the sample suspended in chloroform due to lacking a sufficient siloxane coating.

Differences in the relative stability of CNFs coated with each type of siloxane can also be rationalized based on differences in the relative hydrophobicity of the coating. The high degree of stability for MTMS- and PTMS-modified CNFs can be attributed to the hydrophobic alkyl chains in the silane R_1-groups. In contrast, the polar terminal amino group in APTMS rendered this siloxane coating more hydrophilic relative to MTMS and PTMS modifications, and therefore less effective at improving the stability of CNF. We note that APTMS-modified CNFs still disperse more effectively than unmodified CNF, most likely due to the hydrophobic nature of both the Si–O linkages and the alkyl R_1 side chain.

The prolonged suspension of Si-CNFs in chloroform—a common solvent used in solvent casting—translated into improved CNF dispersion in polymer nanocomposites synthesized through solution blending with polyhydroxyalkanoates (PHA). The evaporation of solvent during the synthesis of these nanocomposites usually occurred over 1-2 h, which underlined the importance of CNF stability in the casting solution over this time span. In the case of unmodified CNF in the mass recovery tests, only 40% of the initial concentration remained in suspension over the first 2 h of settling in chloroform. Consequently, unmodified CNFs dispersed poorly in HIPS and PHA as evidenced by the formation of aggregated patches of nanocellulose identified visually and with optical and electron microscopies (Figures 3.6 and 3.7).

The improved stability of silane-modified CNFs in chloroform translated into improved Si-CNF dispersion in CNF/PHA nanocomposites. This improvement can be understood when related to the mass recovery analyses of 5Me-CNF in chloroform, which retained 80% of its initial concentration in suspension after the first 2 h, and roughly maintained this concentration for the remainder of the 100 h. The relative uniformity of Si-CNF in PHA compared to unmodified CNF can reasonably be expected to lead to greater improvements in the material properties of PHA as compared to unmodified CNF, as demonstrated by previous studies.[10, 37, 52-55] As shown by these studies, uniform dispersion of nanofiller in polymer nanocomposites is a necessary condition to realize a sufficiently reinforced material. The presented data shows the direct relation between improved stability in solvent casting media and improved dispersion in polymer nanocomposites offered by CNF silanization, marking the materials described in this paper as representative of commercially utilized Si-CNFs.

3.5.3 Mineralization of Si-CNFs

We assessed the impact of silanization on the anaerobic mineralization of nanocellulose using biomethane potential tests to quantify the volume of biogas evolved.[56, 59] Efficient anaerobic mineralization involves a sequence of biodegradation steps which are initiated by the adsorption of a bacterial cell or multiprotein complex of enzymes onto the substrate. Complete conversion of cellulose to biogas requires exposure to a mixed culture of bacteria, as different bacterial species are required for each distinct step of mineralization in the absence of oxygen.[23] To meet this requirement, CNFs were exposed to anaerobic mixed cultures of microorganisms obtained from the digested sludge of a wastewater treatment plant. Here, it is important to make the distinction between whether a sample undergoes complete biodegradation, or mineralization. Complete biodegradation can be thought of as the total loss of sample mass due to bacterial metabolism. This includes both the portion of sample which is mineralized into biogas, and the portion that is broken down into nonvolatile small molecular species or water. In the case of anaerobic biodegradation by a mixed culture, cellulose is expected to be efficiently mineralized into biogas (i.e., carbon dioxide and methane) almost entirely, with little to no nonvolatile species being evolved.[23] Unmodified CNF rapidly mineralizes, as expected,[85] because bacteria and relevant enzymes are able to quickly access and adsorb onto the surface of the CNFs. After the bacteria adsorb, primary biodegradation begins with the enzymatic cleavage of glycosidic linkages in the biopolymer chain to yield cellobiose and glucose molecules.[23, 86] In anoxic environments, the complete biodegradation of these intermediate species can be concluded through mineralization into biogas consisting of methane and carbon dioxide. Due to the near complete conversion of cellulose into biogas, tracking the

mineralization of nanocellulose samples is a reliable measure of their overall biodegradability.

Our data indicated that Si-CNF mineralization was either inhibited or completely ceased compared to unmodified CNF, depending on the degree of silanization as seen in Figure 3.8. These marked and systematic decreases in the rate and extent of CNF mineralization were ascribed to changes in the CNF surface chemistry due to the siloxane coatings. Figure 3.8 shows that as CNFs were increasingly coated with siloxane, the nanocellulose became systematically less susceptible to mineralization. We concluded that this effect occurred at high siloxane loadings because all fibril surfaces were completely and uniformly coated with a siloxane layer (ca. 0.4 nm as determined by XPS), rendering the nanocellulose (i.e., glycosidic linkages) inaccessible to bacteria and enzymes, and therefore non-biodegradable during the 4-month evaluation period. This interpretation also explains the intermediate degree of mineralization of CNFs modified with 1 and 5 wt% silane; in these instances, an incomplete coating of the fibrils with siloxane was achieved, which allowed for mineralization to occur, albeit to a lesser extent than in unmodified CNFs.

In addition to the relationship between the degree of silanization and CNF mineralization, samples treated with 5 wt% silane exhibited noticeable delays in the onset of degradation. In each 5 wt% silanized CNF, a steep rise in biogas production occurred around day 10 or later, while in less silanized samples, this rise took place at day 3. We concluded that for the 5Me-, 5A-, and 5P-CNF samples, the delay in biogas production was a result of hindered bacterial access to the nanocellulose due to a critical level of siloxane coating. This extent of coating disallowed primary biodegradation from proceeding (i.e.,

cleavage of glycosidic linkages) until the uncoated regions were accessed. Once this foothold was established, further mineralization of the primary biodegradation byproducts was enabled, resulting in the typical sinusoidal biogas production displayed in Figure 3.8.

Our data also suggest that the extent of CNF mineralization decreased as more highly hydrophobic silanization reagents were used (Figure 3.9). This trend could possibly be explained through the formation of a superhydrophobic coating on the CNF via the polymerization of PTMS[87] and MTMS.[88] In contrast, APTMS alone cannot impart superhydrophobicity due to its polar amino group, and would require the grafting of other reagents to achieve this effect.[89] As superhydrophobic surfaces have been shown to exhibit decreased bacterial attachment relative to moderately hydrophobic surfaces,[90] we would indeed expect PTMS- and MTMS-coated CNFs to be less prone to mineralization than the moderately hydrophobic APTMS-coated CNFs.

These findings also provide a means to help better understand previous studies involving the biodegradation of composites containing silanized cellulosic materials. Although the number of such studies is limited, composites that contain silanized cellulosic materials are generally less biodegradable than those which contain the unmodified cellulosic materials.[91-94] However, the magnitude of inhibition varies. For example, Way *et al.* indicated that PLA composites filled with silanized wood fibers displayed comparable or slightly improved biodegradation compared to PLA impregnated with the unmodified fibers.[91] Conversely, Jandas *et al.* observed that PLA loaded with silanized banana fibers biodegraded to a lesser degree than PLA loaded with unmodified banana fibers.[92] Results from our studies suggest that these differences are at least in part a reflection of differences in the extent of silanization, which is not typically measured. Furthermore, these previous

studies do not address the fate of the modified nanocellulose filler after polymer degradation, which our data suggests will most likely persist as a result of the silanization.

In summary, our data demonstrate that while silane modification indeed improves the dispersion of nanocellulose in solvent cast polymer composites, it negatively impacts CNF mineralization. The magnitude of both effects scaled with the extent and hydrophobicity of siloxane coating. When completely covered in a siloxane coating, nanocellulose remained stable in solvent casting media over the course of 100 h, which led to an improved dispersion of these Si-CNFs in hydrophobic polymer composites. This is important, as uniform nanofiller dispersion is crucial for efficient transfer of CNF properties to the nanocomposite.[31-33]. While this improved material reinforcement is desired commercially, nanocellulose heavily modified with siloxane coatings is shown to be much more resistant to mineralization relative to the native CNF, thus increasing its environmental persistence. Therefore, in cases where materials featuring an environmentally transient nanofiller is desirable, such as in biomedical materials or products with transient use phases (e.g., packaging materials), nanocellulose extensively modified with silanes should be avoided. Conversely, in applications where non-biodegradable nanofillers are desired (e.g., in pipes or building materials), silane-modified nanocellulose could be used as an inexpensive, low weight nanofiller compared to other carbon-based options (i.e., CNTs, carbon fibers).

To avoid the issue of balancing the dispersion and biodegradability of nanocellulose, one potential solution is to covalently functionalize CNFs with small hydrophobic molecular species (e.g., esters).[38, 95] These molecular functionalization

strategies could improve dispersion of nanocellulose in hydrophobic media without impacting its biodegradability by avoiding the formation of an inhibitory coating.

3.6 Conclusions

Cellulose nanofibrils were modified with three alkoxysilane reagents (MTMS, PTMS, APTMS) to determine the effect of hydrophobic silane modification on the dispersion and mineralization properties of nanocellulose. Silanization of CNFs resulted in the formation of a siloxane coating on the fibrils, the extent of which could be controlled based on the ratio of silane added to CNFs. Silanization did not change the cellulosic structure, crystallinity, or bonding in the CNFs, but improved CNF stability in chloroform by coating the hydrophilic nanocellulose surface with a hydrophobic siloxane layer. Improved stability of silanized CNFs in chloroform translated into improved dispersion of Si-CNFs in a hydrophobic polymer nanocomposite relative to unmodified CNFs, which instead aggregated extensively. Conversely, the extent to which silanized CNFs were mineralized decreased compared to unmodified CNFs, an effect attributable to the blocking of enzymatic cleavage sites by the siloxane coating. Indeed, no mineralization was observed for fully coated CNFs, indicating that such fillers and the materials featuring them would likely persist in the environment for increased periods of time when they are discarded at the end of consumer life. This study demonstrates the ability to control the biodegradability of nanocellulose as a function of its degree of silanization, while also highlighting the inverse relationship between dispersion and biodegradability and thus the need to determine the effect of surface modification strategies on environmentally relevant properties of CNFs in addition to their dispersion properties before commercial use and widespread implementation.

3.7 Acknowledgements

This work was supported by National Science Foundation under the Center for Sustainable Nanotechnology, CHE-1503408. The CSN is part of the Centers for Chemical Innovation Program. J.A.P. acknowledges support from the William A. Rothermel Bascom Professorship. Johns Hopkins would like to thank Chris Krout from the Back River Waste Water Treatment Plant (Baltimore, MD). This study made use of the National Magnetic Resonance Facility at Madison, which is supported by NIH grants P41 GM103399 (NIGMS) and P41GM66326 (NIGMS). Additional equipment was purchased with funds from the University of Wisconsin, the NIH (RR02781, RR08438), the NSF (DMB-8415048, OIA-9977486, BIR-9214394), and the USDA.

3.8 References

1. Moon, R. J.; Martini, A.; Nairn, J.; Simonsen, J.; Youngblood, J., Cellulose Nanomaterials Review: Structure, Properties and Nanocomposites. *Chem. Soc. Rev.* **2011,** *40* (7), 3941-3994.
2. Sacui, I. A.; Nieuwendaal, R. C.; Burnett, D. J.; Stranick, S. J.; Jorfi, M.; Weder, C.; Foster, E. J.; Olsson, R. T.; Gilman, J. W., Comparison of the Properties of Cellulose Nanocrystals and Cellulose Nanofibrils Isolated from Bacteria, Tunicate, and Wood Processed Using Acid, Enzymatic, Mechanical, and Oxidative Methods. *ACS Appl. Mater. Interfaces* **2014,** *6* (9), 6127-6138.
3. Chattopadhyay, D., Synthesis, Characterization and Application of Nano Cellulose for Enhanced Performance of Textiles. *Journal of Textile Science & Engineering* **2016,** *6* (2).
4. He, M.; Cho, B.-U.; Won, J. M., Effect of precipitated calcium carbonate—Cellulose nanofibrils composite filler on paper properties. *Carbohydr. Polym.* **2016,** *136* (Supplement C), 820-825.
5. Wei, H.; Rodriguez, K.; Renneckar, S.; Vikesland, P. J., Environmental Science and Engineering Applications of Nanocellulose-Based Nanocomposites. *Environ. Sci.: Nano* **2014,** *1* (4), 302-316.
6. Azeredo, H. M. C.; Rosa, M. F.; Mattoso, L. H. C., Nanocellulose in Bio-Based Food Packaging Applications. *Ind. Crops. Prod.* **2017,** *97*, 664-671.
7. Lin, N.; Dufresne, A., Nanocellulose in Biomedicine: Current Status and Future Prospect. *Eur. Polym. J.* **2014,** *59*, 302-325.
8. Sun, X.; Wu, Q.; Lee, S.; Qing, Y.; Wu, Y., Cellulose Nanofibers as a Modifier for Rheology, Curing and Mechanical Performance of Oil Well Cement. *Sci. Rep.* **2016,** *6*, 31654.

9. Xu, X.; Liu, F.; Jiang, L.; Zhu, J. Y.; Haagenson, D.; Wiesenborn, D. P., Cellulose Nanocrystals vs. Cellulose Nanofibrils: A Comparative Study on their Microstructures and Effects as Polymer Reinforcing Agents. *ACS Appl. Mater. Interfaces* **2013,** *5* (8), 2999-3009.
10. Lu, J.; Askeland, P.; Drzal, L. T., Surface modification of microfibrillated cellulose for epoxy composite applications. *Polymer* **2008,** *49* (5), 1285-1296.
11. Dufresne, A., *Nanocellulose: From Nature to High Performance Tailored Materials*. Walter de Gruyter: Berlin, Germany, 2012.
12. Hamid, S. B. A.; Zain, S. K.; Das, R.; Centi, G., Synergic Effect of Tungstophosphoric Acid and Sonication for Rapid Synthesis of Crystalline Nanocellulose. *Carbohydr. Polym.* **2016,** *138*, 349-355.
13. Feng, Y.-H.; Cheng, T.-Y.; Yang, W.-G.; Ma, P.-T.; He, H.-Z.; Yin, X.-C.; Yu, X.-X., Characteristics and Environmentally Friendly Extraction of Cellulose Nanofibrils from Sugarcane Bagasse. *Ind. Crops. Prod.* **2018,** *111* (Supplement C), 285-291.
14. Yadav, C.; Saini, A.; Maji, P. K., Energy Efficient Facile Extraction Process of Cellulose Nanofibres and their Dimensional Characterization using Light Scattering Techniques. *Carbohydr. Polym.* **2017,** *165* (Supplement C), 276-284.
15. Phanthong, P.; Karnjanakom, S.; Reubroycharoen, P.; Hao, X.; Abudula, A.; Guan, G., A Facile One-Step Way for Extraction of Nanocellulose with High Yield by Ball Milling with Ionic Liquid. *Cellulose* **2017,** *24* (5), 2083-2093.
16. Henriksson, M.; Henriksson, G.; Berglund, L. A.; Lindström, T., An Environmentally Friendly Method for Enzyme-Assisted Preparation of Microfibrillated Cellulose (MFC) Nanofibers. *Eur. Polym. J.* **2007,** *43* (8), 3434-3441.
17. Carpenter, A. W.; de Lannoy, C. F.; Wiesner, M. R., Cellulose Nanomaterials in Water Treatment Technologies. *Environ. Sci. Technol.* **2015,** *49* (9), 5277-5287.
18. Das, S., Life Cycle Assessment of Carbon Fiber-Reinforced Polymer Composites. *Int. J. Life. Cycle. Assess.* **2011,** *16* (3), 268-282.
19. Akhshik, M.; Panthapulakkal, S.; Tjong, J.; Sain, M., Life Cycle Assessment and Cost Analysis of Hybrid Fiber-Reinforced Engine Beauty Cover in Comparison with Glass Fiber-Reinforced Counterpart. *EIA Review* **2017,** *65* (Supplement C), 111-117.
20. Sarma, S. J.; Bhattacharya, I.; Brar, S. K.; Tyagi, R. D.; Surampalli, R. y., Carbon Nanotube—Bioaccumulation and Recent Advances in Environmental Monitoring. *Crit. Rev. Environ. Sci. Technol.* **2015,** *45* (9), 905-938.
21. Petersen, E. J.; Akkanen, J.; Kukkonen, J. V. K.; Weber, W. J., Biological Uptake and Depuration of Carbon Nanotubes by Daphnia Magna. *Environ. Sci. Technol.* **2009,** *43* (8), 2969-2975.
22. Abbate, C.; Giorgianni, C.; Brecciaroli, R.; Giacobbe, G.; Costa, C.; Cavallari, V.; Albiero, F.; Catania, S.; Tringali, M. A.; Martino, L. B.; Abbate, S., Changes Induced by Exposure of the Human Lung to Glass Fiber–Reinforced Plastic. *Environ. Health Perspect.* **2006,** *114* (11), 1725-1729.
23. Leschine, S. B., Cellulose Degradation in Anaerobic Environments. *Annu. Rev. Microbiol.* **1995,** *49* (1), 399-426.
24. Arvidsson, R.; Nguyen, D.; Svanström, M., Life Cycle Assessment of Cellulose Nanofibrils Production by Mechanical Treatment and Two Different Pretreatment Processes. *Environ. Sci. Technol.* **2015,** *49* (11), 6881-6890.

25. Li, Q.; McGinnis, S.; Sydnor, C.; Wong, A.; Renneckar, S., Nanocellulose Life Cycle Assessment. *ACS Sustainable Chem. Eng.* **2013,** *1* (8), 919-928.
26. Oksman, K.; Etang, J. A.; Mathew, A. P.; Jonoobi, M., Cellulose Nanowhiskers Separated from a Bio-Residue from Wood Bioethanol Production. *Biomass & Bioenergy* **2011,** *35* (1), 146-152.
27. Roman, M.; Winter, W. T., Effect of Sulfate Groups from Sulfuric Acid Hydrolysis on the Thermal Degradation Behavior of Bacterial Cellulose. *Biomacromolecules* **2004,** *5* (5), 1671-1677.
28. Liu, C.-X.; Choi, J.-W., Improved Dispersion of Carbon Nanotubes in Polymers at High Concentrations. *Nanomaterials* **2012,** *2* (4), 329-347.
29. Bhattacharya, M., Polymer Nanocomposites—A Comparison Between Carbon Nanotubes, Graphene, and Clay as Nanofillers. *Materials* **2016,** *9* (4), 262.
30. Kaler, V.; Pandel, U.; Duchaniya, R. K., Development of TiO2/PVA Nanocomposites for Application in Solar Cells. *Materials Today: Proceedings* **2018,** *5* (2, Part 1), 6279-6287.
31. Uddin, M. F.; Sun, C.-T., Effect of Nanoparticle Dispersion on Polymer Matrix and their Fiber Nanocomposites. In *Major Accomplishments in Composite Materials and Sandwich Structures*, Daniel, I. M.; Gdoutos, E. E.; Rajapakse, Y. D. S., Eds. Springer Netherlands: Dordrecht, 2010; pp 693-715.
32. Liu, T.; Phang, I. Y.; Shen, L.; Chow, S. Y.; Zhang, W.-D., Morphology and Mechanical Properties of Multiwalled Carbon Nanotubes Reinforced Nylon-6 Composites. *Macromolecules* **2004,** *37* (19), 7214-7222.
33. Müller, K.; Bugnicourt, E.; Latorre, M.; Jorda, M.; Echegoyen Sanz, Y.; Lagaron, J. M.; Miesbauer, O.; Bianchin, A.; Hankin, S.; Bölz, U.; Pérez, G.; Jesdinszki, M.; Lindner, M.; Scheuerer, Z.; Castelló, S.; Schmid, M., Review on the Processing and Properties of Polymer Nanocomposites and Nanocoatings and their Applications in the Packaging, Automotive and Solar Energy Fields. *Nanomaterials* **2017,** *7* (4), 74.
34. Guzmán de Villoria, R.; Miravete, A., Mechanical Model to Evaluate the Effect of the Dispersion in Nanocomposites. *Acta Materialia* **2007,** *55* (9), 3025-3031.
35. Tessema, A.; Zhao, D.; Moll, J.; Xu, S.; Yang, R.; Li, C.; Kumar, S. K.; Kidane, A., Effect of Filler Loading, Geometry, Dispersion and Temperature on Thermal Conductivity of Polymer Nanocomposites. *Polymer Testing* **2017,** *57*, 101-106.
36. Ferreiro, V.; Schmidt, G.; Han, C.; Karim, A., Dispersion and Nucleating Effects of Clay Fillers in Nanocomposite Polymer Films. In *Polymer Nanocomposites*, American Chemical Society: 2001; Vol. 804, pp 177-191.
37. Nakatani, H.; Iwakura, K.; Miyazaki, K.; Okazaki, N.; Terano, M., Effect of Chemical Structure of Silane Coupling Agent on Interface Adhesion Properties of Syndiotactic Polypropylene/Cellulose Composite. *J. Appl. Polym. Sci.* **2011,** *119* (3), 1732-1741.
38. Espino-Pérez, E.; Domenek, S.; Belgacem, N.; Sillard, C.; Bras, J., Green Process for Chemical Functionalization of Nanocellulose with Carboxylic Acids. *Biomacromolecules* **2014,** *15* (12), 4551-4560.
39. Song, Z.; Xiao, H.; Zhao, Y., Hydrophobic-Modified Nano-Cellulose Fiber/PLA Biodegradable Composites for Lowering Water Vapor Transmission Rate (WVTR) of Paper. *Carbohydr. Polym.* **2014,** *111*, 442-448.

40. Guo, J.; Fang, W.; Welle, A.; Feng, W.; Filpponen, I.; Rojas, O. J.; Levkin, P. A., Superhydrophobic and Slippery Lubricant-Infused Flexible Transparent Nanocellulose Films by Photoinduced Thiol–ene Functionalization. *ACS Appl. Mater. Interfaces* **2016,** *8* (49), 34115-34122.
41. Missoum, K.; Belgacem, M. N.; Bras, J., Nanofibrillated Cellulose Surface Modification: A Review. *Materials* **2013,** *6* (5), 1745-1766.
42. Kalia, S.; Dufresne, A.; Cherian, B. M.; Kaith, B. S.; Averous, L.; Njuguna, J.; Nassiopoulos, E., Cellulose-Based Bio- and Nanocomposites: A Review. *Int. J. Polym. Sci.* **2011,** *2011*.
43. Sair, S.; Oushabi, A.; Kammouni, A.; Tanane, O.; Abboud, Y.; Oudrhiri Hassani, F.; Laachachi, A.; El Bouari, A., Effect of Surface Modification on Morphological, Mechanical and Thermal Conductivity of Hemp Fiber: Characterization of the Interface of Hemp –Polyurethane Composite. *Case Stud. in Therm. Eng.* **2017,** *10*, 550-559.
44. Singh, G. Biodegradation of Nanocellulose and Microbial Community Response: Effect of Surface Modification and Morphology. Virginia Polytechnic Institute and State University, Blacksburg, VA, 2015.
45. Cowie, J.; Bilek, E. M.; Wegner, T. H.; Shatkin, J. A., Market Projections of Cellulose Nanomaterial-Enabled Products--Part 2: Volume Estimates. *TAPPI J.* **2014,** *13* (6), 57-69.
46. Shatkin, J. A.; Wegner, T. H.; Bilek, E. M.; Cowie, J., Market Projections of Cellulose Nanomaterial-Enabled Products- Part 1: Applications. *TAPPI J.* **2014,** *13* (5), 9-16.
47. Barari, B.; Ellingham, T. K.; Ghamhia, I. I.; Pillai, K. M.; El-Hajjar, R.; Turng, L.-S.; Sabo, R., Mechanical Characterization of Scalable Cellulose Nano-fiber Based Composites Made Using Liquid Composite Molding Process. *Composites Part B: Engineering* **2016,** *84*, 277-284.
48. Raquez, J. M.; Murena, Y.; Goffin, A. L.; Habibi, Y.; Ruelle, B.; DeBuyl, F.; Dubois, P., Surface-Modification of Cellulose Nanowhiskers and Their use as Nanoreinforcers into Polylactide: A Sustainably-Integrated Approach. *Compos. Sci. Technol.* **2012,** *72* (5), 544-549.
49. Xu, S. H.; Gu, J.; Luo, Y. F.; Jia, D. M., Effects of Partial Replacement of Silica with Surface Modified Nanocrystalline Cellulose on Properties of Natural Rubber Nanocomposites. *Express Polym. Lett.* **2012,** *6*, 14-25.
50. Montes, S.; Azcune, I.; Cabañero, G.; Grande, H.-J.; Odriozola, I.; Labidi, J., Functionalization of Cellulose Nanocrystals in Choline Lactate Ionic Liquid. *Materials* **2016,** *9* (7), 499.
51. Xiaofei, D.; Xinyu, C.; Linnan, K.; Yongmei, M.; Jingjing, A.; Fosong, W., Combination of Cellulose Nanofibers and Chain-End-Functionalized Polyethylene and their Applications in Nanocomposites. *J. Appl. Polym. Sci.* **2017,** *134* (42), 45387.
52. Robles, E.; Urruzola, I.; Labidi, J.; Serrano, L., Surface-Modified Nano-Cellulose as Reinforcement in Poly(Lactic Acid) to Conform New Composites. *Ind. Crops. Prod.* **2015,** *71*, 44-53.
53. Kargarzadeh, H.; M. Sheltami, R.; Ahmad, I.; Abdullah, I.; Dufresne, A., Cellulose Nanocrystal: A Promising Toughening Agent for Unsaturated Polyester Nanocomposite. *Polymer* **2015,** *56*, 346-357.

54. Pickering, K. L.; Abdalla, A.; Ji, C.; McDonald, A. G.; Franich, R. A., The Effect of Silane Coupling Agents on Radiata Pine Fibre for use in Thermoplastic Matrix Composites. *Compos. Part A Appl. Sci. Manuf.* **2003,** *34* (10), 915-926.
55. Colom, X.; Carrasco, F.; Pagès, P.; Cañavate, J., Effects of Different Treatments on the Interface of HDPE/Lignocellulosic Fiber Composites. *Compos. Sci. Technol.* **2003,** *63* (2), 161-169.
56. Owen, W. F.; Stuckey, D. C.; Healy, J. B.; Young, L. Y.; McCarty, P. L., Bioassay for Monitoring Biochemical Methane Potential and Anaerobic Toxicity. *Water Res.* **1979,** *13* (6), 485-492.
57. Xie, Y.; Hill, C. A. S.; Xiao, Z.; Militz, H.; Mai, C., Silane Coupling Agents used for Natural Fiber/Polymer Composites: A Review. *Compos. Part A Appl. Sci. Manuf.* **2010,** *41* (7), 806-819.
58. Goodwin, D. G.; Boyer, I.; Devahif, T.; Gao, C.; Frank, B. P.; Lu, X.; Kuwama, L.; Gordon, T. B.; Wang, J.; Ranville, J. F.; Bouwer, E. J.; Fairbrother, D. H., Biodegradation of Carbon Nanotube/Polymer Nanocomposites Using a Monoculture. *Environ. Sci. Technol.* **2018,** *52* (1), 40-51.
59. Angelidaki, I.; Sanders, W., Assessment of the Anaerobic Biodegradability of Macropollutants. *Rev. Environ. Sci. Biotechnol.* **2004,** *3* (2), 117-129.
60. Chinga-Carrasco, G., Cellulose Fibres, Nanofibrils and Microfibrils: The Morphological Sequence of MFC Components from a Plant Physiology and Fibre Technology Point of View. *Nanoscale Res. Lett.* **2011,** *6* (1), 417-417.
61. Klemm, D.; Philipp, B.; Heinze, T.; Heinze, U.; Wagenknecht, W., Analytical Methods in Cellulose Chemistry: Section 3.3. In *Comprehensive Cellulose Chemistry*, Wiley-VCH Verlag GmbH & Co. KGaA: 2004; pp 181-195.
62. Ingale, S. V.; Wagh, P. B.; Tripathi, A. K.; Kamble, V. S.; Kumar, R.; Gupta, S. C., Physico-Chemical Properties of Silica Aerogels Prepared from TMOS/MTMS Mixtures. *J. Porous Mater.* **2011,** *18* (5), 567-572.
63. Tanaka, T., The Infrared Spectra of Methoxy-, Methylmethoxy- and Methoxy Endblocked Dimethyl-Polysiloxanes. *Bull. Chem. Soc. Jpn.* **1958,** *31* (6), 762-766.
64. Devouge, S.; Conti, J.; Goldsztein, A.; Gosselin, E.; Brans, A.; Voué, M.; De Coninck, J.; Homblé, F.; Goormaghtigh, E.; Marchand-Brynaert, J., Surface Functionalization of Germanium ATR Devices for Use in FTIR-Biosensors. *J. Colloid Interface Sci.* **2009,** *332* (2), 408-415.
65. Sánchez-Fernández, A.; Peña-Parás, L.; Vidaltamayo, R.; Cué-Sampedro, R.; Mendoza-Martínez, A.; Zomosa-Signoret, V.; Rivas-Estilla, A.; Riojas, P., Synthesization, Characterization, and In Vitro Evaluation of Cytotoxicity of Biomaterials Based on Halloysite Nanotubes. *Materials* **2014,** *7* (12), 7770.
66. Shimizu, I.; Okabayashi, H.; Taga, K.; Nishio, E.; O'Connor, C. J., Diffuse Reflectance Infrared Fourier Transform Spectral Study of the Thermal and Adsorbed-Water Effects of a 3-Aminopropyltriethoxysilane Layer Modified onto the Surface of Silica Gel. *Vib. Spectrosc.* **1997,** *14* (1), 113-123.
67. Saal, K.; Tätte, T.; Tulp, I.; Kink, I.; Kurg, A.; Mäeorg, U.; Rinken, A.; Lõhmus, A., Sol–Gel Films for DNA Microarray Applications. *Mater. Lett.* **2006,** *60* (15), 1833-1838.

68. Johansson, L.-S.; Tammelin, T.; Campbell, J. M.; Setala, H.; Osterberg, M., Experimental Evidence on Medium Driven Cellulose Surface Adaptation Demonstrated Using Nanofibrillated Cellulose. *Soft Matter* **2011,** *7* (22), 10917-10924.
69. Loof, D.; Hiller, M.; Oschkinat, H.; Koschek, K., Quantitative and Qualitative Analysis of Surface Modified Cellulose Utilizing TGA-MS. *Materials* **2016,** *9* (6), 415.
70. Glaser, R. H.; Wilkes, G. L., Structure Property Behavior of Polydimethylsiloxane and Poly(Tetramethylene Oxide) Modified TEOS Based Sol-Gel Materials. *Polymer Bulletin* **1988,** *19* (1), 51-57.
71. Hasegawa, I.; Sakka, S.; Sugahara, Y.; Kuroda, K.; Kato, C., Polymerization of Hydrolysis Products of Methyltriethoxysilane in Aqueous Solutions. *Journal of the Ceramic Society of Japan* **1990,** *98* (1139), 647-652.
72. Salon, M.-C. B.; Gerbaud, G.; Abdelmouleh, M.; Bruzzese, C.; Boufi, S.; Belgacem, M. N., Studies of Interactions Between Silane Coupling Agents and Cellulose Fibers with Liquid and Solid-State NMR. *Magn. Reson. Chem.* **2007,** *45* (6), 473-483.
73. Sindorf, D. W.; Maciel, G. E., Solid-state NMR Studies of the Reactions of Silica Surfaces with Polyfunctional Chloromethylsilanes and Ethoxymethylsilanes. *Journal of the American Chemical Society* **1983,** *105* (12), 3767-3776.
74. Alam, T. M.; Assink, R. A.; Loy, D. A., Hydrolysis and Esterification in Organically Modified Alkoxysilanes: A 29Si NMR Investigation of Methyltrimethoxysilane. *Chemistry of Materials* **1996,** *8* (9), 2366-2374.
75. Henrichs, M. P.; Nicely, V. A., An experimental determination of the local chain conformation of bisphenol A polycarbonate. *Macromolecules* **1990,** *23* (12).
76. Osterholtz, F. D.; Pohl, E. R., Kinetics of the Hydrolysis and Condensation of Organofunctional Alkoxysilanes: A Review. *J. Adhes. Sci. Technol.* **1992,** *6* (1), 127-149.
77. Blum, F. D.; Meesiri, W.; Kang, H.-J.; Gambogi, J. E., Hydrolysis, Adsorption, and Dynamics of Silane Coupling Agents on Silica Surfaces. *J. Adhes. Sci. Technol.* **1991,** *5* (6), 479-496.
78. de Oliveira Taipina, M.; Ferrarezi, M. M. F.; Yoshida, I. V. P.; Gonçalves, M. d. C., Surface Modification of Cotton Nanocrystals with a Silane Agent. *Cellulose* **2013,** *20* (1), 217-226.
79. Pinheiro, I. F.; Ferreira, F. V.; Souza, D. H. S.; Gouveia, R. F.; Lona, L. M. F.; Morales, A. R.; Mei, L. H. I., Mechanical, Rheological and Degradation Properties of PBAT Nanocomposites Reinforced by Functionalized Cellulose Nanocrystals. *Eur. Polym. J.* **2017,** *97* (Supplement C), 356-365.
80. Kint, D.; Muñoz-Guerra, S., A Review on the Potential Biodegradability of Poly(Ethylene Terephthalate). *Polym. Int.* **1999,** *48* (5), 346-352.
81. J., J. M.; L., H. K., The Effect of Crystalline Morphology on the Degradation of Polycaprolactone in a Solution of Phosphate Buffer and Lipase. *Polym. Advan. Technol.* **2008,** *19* (12), 1901-1906.
82. Abdelmouleh, M.; Boufi, S.; ben Salah, A.; Belgacem, M. N.; Gandini, A., Interaction of Silane Coupling Agents with Cellulose. *Langmuir* **2002,** *18* (8), 3203-3208.
83. Zhou, F.; Cheng, G.; Jiang, B., Effect of Silane Treatment on Microstructure of Sisal Fibers. *Appl. Surf. Sci.* **2014,** *292* (Supplement C), 806-812.
84. Jablonski, A.; Zemek, J., Overlayer Thickness Determination by XPS Using the Multiline Approach. *Surface and Interface Analysis* **2009,** *41* (3), 193-204.

85. Singh, G.; Chandoha-Lee, C.; Zhang, W.; Renneckar, S.; Vikesland, P. J.; Pruden, A., Biodegradation of Nanocrystalline Cellulose by Two Environmentally-Relevant Consortia. *Water Res.* **2016,** *104*, 137-146.
86. Lynd, L. R.; Weimer, P. J.; van Zyl, W. H.; Pretorius, I. S., Microbial Cellulose Utilization: Fundamentals and Biotechnology. *Microbiol. Mol. Biol. Rev.* **2002,** *66* (3), 506-577.
87. Ramanathan, R.; Weibel, D. E., Novel Liquid–Solid Adhesion Superhydrophobic Surface Fabricated Using Titanium Dioxide and Trimethoxypropyl Silane. *Appl. Surf. Sci.* **2012,** *258* (20), 7950-7955.
88. Karapanagiotis, I.; Pavlou, A.; Manoudis, P. N.; Aifantis, K. E., Water Repellent ORMOSIL Films for the Protection of Stone and Other Materials. *Mater. Lett.* **2014,** *131* (Supplement C), 276-279.
89. Li, L.; Li, B.; Dong, J.; Zhang, J., Roles of Silanes and Silicones in Forming Superhydrophobic and Superoleophobic Materials. *J. Mater. Chem. A* **2016,** *4* (36), 13677-13725.
90. Yuan, Y.; Hays, M. P.; Hardwidge, P. R.; Kim, J., Surface Characteristics Influencing Bacterial Adhesion to Polymeric Substrates. *RSC Adv.* **2017,** *7* (23), 14254-14261.
91. Way, C.; Dean, K.; Wu, D. Y.; Palombo, E., Biodegradation of Sequentially Surface Treated Lignocellulose Reinforced Polylactic Acid Composites: Carbon Dioxide Evolution and Morphology. *Polym. Degrad. Stab* **2012,** *97* (3), 430-438.
92. P.J., J.; S., M.; S.K., N.; H., S., Effect of Surface Treatments of Banana Fiber on Mechanical, Thermal, and Biodegradability Properties of PLA/Banana Fiber Biocomposites. *Polym. Compos.* **2011,** *32* (11), 1689-1700.
93. Calabia, B.; Ninomiya, F.; Yagi, H.; Oishi, A.; Taguchi, K.; Kunioka, M.; Funabashi, M., Biodegradable Poly(Butylene Succinate) Composites Reinforced by Cotton Fiber with Silane Coupling Agent. *Polymers* **2013,** *5* (1), 128.
94. Kittikorn, T.; Kongsuwan, S.; Malakul, R., Investigation of the durability of sisal fiber/PLA biocomposite through

evaluation of biodegradability by means of microbial growth. *Journal of Metals, Materials and Minerals* **2017,** *27* (2), 23-34.
95. Eyley, S.; Thielemans, W., Surface modification of cellulose nanocrystals. *Nanoscale* **2014,** *6* (14), 7764-7779.

Chapter 4. Biodegradation of Functionalized Nanocellulose is Dictated by Degree of Surface Substitution and Chemical Linkage

To be Submitted to ACS Environmental Science & Technology

Frank, B. P.; Caudill, E. R.; Smith, C. L.; Lankone, R. S.; Carlin, K.; Pedersen, J. A.; Fairbrother, D. H.

4.1 Abstract

Nanocellulose has attracted considerable interest for applications in material science and biomedical engineering due to its natural abundance, physicochemical properties, and ease of mineralization (i.e., complete biodegradation). Covalent functionalization of hydroxyl groups on nanocellulose is frequently required to reduce its aggregation in solvents, but these modification strategies have the potential to alter the biodegradation properties of nanocellulose. Here, cellulose nanofibrils (CNF) functionalized with different esters, carboxylic acids, and ethers exhibited decreased biodegradability when exposed to both anaerobic and aerobic microbial communities, with etherified CNFs exhibiting particular recalcitrance to biodegradation. Importantly, significantly lower levels of functionalization were required to inhibit the biodegradation of nanocellulose than are typically reported for macrocellulose. The decreased biodegradability of functionalized CNF was also found to depend primarily on the degree of substitution at the surface of the material, rather than within the bulk. This dependence

on surface chemistry was attributed not only to the large surface area to volume ratio of nanocellulose and its reduced swelling capacity, but also to the prerequisite step of microbial surface interaction necessary for the biodegradation of cellulose. Results from this study highlight the need to measure the degree of surface substitution to predict the biological transformation and environmental persistence of functionalized nanocellulose.

4.2 Introduction

Nanocellulose, a naturally occurring biopolymer consisting of β-1,4-D-anhydroglucopyranose monomer units,[1] is derived from cellulose following chemical treatment,[2] sonication,[3] mechanical milling,[4] or enzymatic digestion,[5] and possesses mechanical properties comparable to Kevlar and steel.[6] These mechanical properties coupled with the nanoscale width, natural abundance, biodegradability, and biocompatibility of nanocellulose elevate its use in a variety of applications including reinforcing polymer nanocomposites,[1-2] biomedical applications,[7] sensors,[7-8] water treatment,[7] and smart materials.[9-11] Despite its desirable properties, nanocellulose requires hydrophobic surface modification (e.g., coatings, functionalization, surfactant adsorption) to improve dispersion in organic media and reduce hydrogen bond-induced homoaggregation prior to use in material applications.[8, 12-14] Roughly 35 million tons of nanocellulose are produced globally each year, and this number is projected to further increase by 2030.[15-16] Consequently, it is important to understand the effect that surface modification has on the properties of nanocellulose in the environment.

Products featuring cellulosic materials often highlight the biodegradability of cellulose compared to traditional carbon-based options such as carbon nanotubes and

carbon fibers. Biodegradability is a sought-after property because it reduces environmental persistence and impact, particularly when involving complete mineralization into biogas (as opposed to reduction to persistent byproducts).[17-18] While cellulose is readily mineralized in its native form, hydrophobic surface modifications can interfere with the enzymatic degradation pathways of cellulose,[19-21] which are dependent on the surrounding microbial community (i.e., aerobic vs. anerobic).[17, 22-26] In a previous report, we demonstrated that common siloxane coatings applied to the surface of cellulose nanofibrils (CNF) blocked bacterial access to nanocellulose, inhibiting and in some cases preventing its anaerobic mineralization.[12] Covalent functionalization strategies utilizing ether, ester, and urethane linkages avoid the formation of such surface coatings, and have been widely applied to macrocellulose to improve dispersion in organic media and polymers.[27-30] The most commonly used metric to express the extent of covalent functionalization is the overall degree of substitution (DS), representing the average number of cellulosic hydroxyl groups functionalized per anhydroglucose monomer unit (0-3). The overall DS accounts for functionalization in both the surface and bulk regions of the material, and is generally determined using techniques such as elemental analysis[31] or nuclear magnetic resonance spectroscopy.[32-33] For covalently modified cellulose, biodegradability has been found to depend on both DS and type of chemical linkage (i.e., ether,[34-36] ester[19-20, 37]). For example, Wirick et al., demonstrated that as the DS increased, cellulose fibers functionalized with carboxymethyl groups (ether linkage, DS 0.41-1.30) were less degradable by a cellulolytic enzyme complex.[35] A DS-dependent vulnerability to biodegradation was also shown by Rivard et al., for cellulose esterified with acetyl groups, with DS values >1.25 significantly inhibiting biodegradation by anaerobic microbes.[37]

When discussing the biodegradation of modified cellulose, many reports quantify the extent of biodegradation in terms of the evolution of low molecular weight byproducts (e.g., cellobiose, glycolic acid) or use nonrepresentative systems such as model enzymes (e.g., cellulase, esterase) or single microbes as the means to effect biodegradation.[35-36, 38] While the information from these studies is useful in identifying biodegradation trends between different materials, these studies do not capture the complete mineralization of the cellulosic material and/or do not represent the microbial communities encountered in realistic environments.[17-18, 22, 35-36, 38] This is an important distinction to make because while reduction to low molecular weight species is a step in the biodegradation process, such byproducts may be recalcitrant to subsequent mineralization and concentrate in the environment. Failure to discern the ultimate biodegradation of functionalized cellulose has also led to disagreements with respect to the degree of inhibition resulting from chemical functionalization.[19, 21, 34] Additionally, as mineralization of cellulosic materials generally proceeds via the cooperation of a microbial community,[39] more complex systems utilizing environmentally relevant microbes are best suited for discerning the environmental impact of functionalized nanocellulose, rather than model enzymes and a single microbial specie.[17, 22]

Another potentially important factor to consider in the biodegradation of functionalized nanomaterials, such as nanocellulose, is the comparison between the degree of functionalization at the surface ($DS_{surface}$) compared to the overall DS ($DS_{overall}$). This distinction is important as the preliminary step in the biodegradation of a solid phase material involves the adsorption and colonization of microbes at the surface,[40-43] and the biodegradation of cellulosic materials, specifically, requires biofilm formation or the

interaction of highly specific cellulosome complexes with its surface.[23, 44-46] As nanocellulose fibers are composed of numerous cellulose chains woven together into a cord, the chains at the fiber surface are chemically distinct from those within the bulk of the material.[2, 47-48] During chemical functionalization with liquid reagents, the bulk and surface of nanocellulose are both targeted, with the distribution of the modification depending on reaction conditions (e.g. solvent, fiber swelling, and reagent reactivity).[2, 49-50] Alternatively, gas phase reagents selectively target the surface of nanocellulose during functionalization.[51-53] Despite the potential for achieving different levels of surface vs. bulk functionalization, studies of cellulosic materials typically only use bulk sensitive techniques, and thus only quantify $DS_{overall}$.[31, 33, 54-57] The effect of surface substitution is likely to be particularly important for the biodegradation of CNFs compared to macrocellulose due to the large surface area to volume ratio of nanocellulose.[2] Indeed, the environmental properties of carbon nanomaterials such as CNTs,[58-59] carbon dots,[60-62] and graphene[63-64] are often dictated by their surface chemistry.

In this study we compare the influence of surface and bulk functionalization on the mineralization of CNF by aerobic and anaerobic microbial communities. This was accomplished using liquid-phase and gas-phase (surface specific)[51-52] techniques to functionalize nanocellulose with long-chain hydrocarbon esters often used to improve CNF dispersion in polymer nanocomposites.[50, 65] Attenuated total internal reflectance infrared spectroscopy (ATR), solid-state ^{13}C-nuclear magnetic resonance spectroscopy (^{13}C-NMR), and CHN elemental analysis were used to confirm functionalization and determine $DS_{overall}$, while X-ray photoelectron spectroscopy (XPS) was utilized to measure $DS_{surface}$. In addition, CNFs were functionalized with different esters (phenyl, hexyl, dodecyl), ethers

(hexyl, dodecyl), and carboxylic acids (H^+ or Na^+ counterions) to assess the effect of different covalent linkages on its biodegradation under anaerobic and aerobic conditions via biomethane potential (BMP) tests and mass loss, respectively. Kinetic modeling of biogas production under anaerobic conditions enabled quantitative comparisons of the effect of surface and overall functionalization on mineralization rates.

4.3 Experimental

4.3.1 Materials Preparation

Freeze-dried cellulose nanofibrils (CNFs) were purchased from the University of Maine Process Development Center and either used as-received or milled into a powder with a Flack-tek mill (DAC 150, 2800 rpm, 4 min). Ethyl cellulose was purchased from Sigma-Aldrich. Carboxylated CNFs were purchased from the University of Maine Process Development Center as a slurry (1 wt%, 1.5 mmol COOH/g cellulose) of TEMPO oxidized CNFs and dried either as-received (Na^+ counterion) or after washing with dilute HCl (H^+ counterion). CNF esters were prepared by utilizing carboxylic acid reagents as outlined in Espino-Perez et al.,[66] or with acyl chloride reagents. Functionalization with carboxylic acid reagents was performed by first dispersing 200 mg CNFs in 200 mL water via 2 h sonication before adjusting to approximately pH 4 with 4 M HCl. The mixture was then heated to ~140 °C to evaporate water before adding an excess of phenyl acetic acid (phenyl ester CNF), hexanoic acid (hexyl ester CNF), or lauric acid (dodecyl ester CNF, LA-CNF) to form the reaction medium. The sample solutions were stirred with a magnetic stirrer for 14 h, then quenched with ethanol. Functionalized CNF powders were recovered via vacuum filtration and washed with ethanol before drying in a vacuum at 60 °C. Different levels of substitution were achieved based on differences in CNF swelling during reaction.

Esterification reactions using acyl chlorides were carried out by first dispersing 200 mg CNFs in 12 mL of diethyl ether and 0.5 mL of triethylamine in a vented round bottom flask equipped with a magnetic stirrer. After dropwise addition of 1 mL of lauroyl chloride, the samples were gently mixed at room temperature for 6 h. At the end of the reaction time, the samples were quenched with 30 mL of deionized water and recovered by vacuum filtration followed by a dilute HCl (100 mL, pH 5.5) and deionized water (800 mL) wash. All samples were then dried in a vacuum oven at 50°C for 72 h to yield lauroyl chloride esterified CNFs (LC-CNF). Gas-phase esterification was performed by adding ~10 mg of CNF powder to a custom-designed Schlenk line vessel[67] suspended above 1 mL of lauroyl chloride (GP-LC-CNF) or hexanoyl chloride (GP-HC-CNF). The bottom of the vessel was submerged in liquid nitrogen to freeze the reagent, followed by headspace evacuation with a mechanical pump. After sealing the vessel, the reagent was allowed to thaw and vaporize into the headspace of the vessel to react with the CNF powder. The sample was then recovered for characterization and biodegradation. Etherification was performed by dispersing 200 mg of dried CNF in 200 mL of dimethyl sulfoxide (DMSO) via sonication for 3 h. 200 mg K_2CO_3 was then added, and the sample sonicated for an additional 3 h. A 30 mL aliquot of 1-bromohexane (hexyl ether CNF) or 1-bromododecane (dodecyl ether CNF) was then added to the sample before heating to 90 °C and magnetically stirring for 45 m under reflux. The reaction was then quenched with ethanol and the functionalized CNF powder was recovered via vacuum filtration followed by thorough washing with ~1 L of ethanol before being dried in a vacuum oven at 60 °C.

4.3.2 Materials Characterization

4.3.2.1 IR

Attenuated total reflectance infrared spectroscopy (ATR) data of CNF powders were obtained with a Nicolet iS5 spectrometer and an iD5 ATR attachment using a scan range from 4000 cm^{-1} –525 cm^{-1} at 0.964 cm^{-1} resolution.

4.3.2.2 CHN Elemental Analysis

CHN elemental analyses were performed to determine $DS_{overall}$ for functionalized CNFs. Tests were performed on an Exeter Analytical CE440 CHN Analyzer at the Microanalysis Laboratory at University of Illinois at Urbana-Champaign. 2.0 mg to 3.0 mg dried samples were weighed into consumable tin capsules, placed inside an autosampler wheel, and purged with helium. The capsule was then driven into a high temperature (1000°C) furnace and combusted in pure oxygen under static conditions. The resulting combustion products containing carbon dioxide (CO_2), water (H_2O), nitrogen (N_2) and oxides of nitrogen (NO_x) were then passed over copper to scrub excess oxygen and reduce oxides of nitrogen to elemental nitrogen. After scrubbing, the gases entered a mixing volume chamber to ensure a homogeneous mixture at constant temperature and pressure. The mixture then passed through a series of high-precision thermal conductivity detectors to determine the CHN content in two replicates of each sample.

4.3.2.3 Solid-State NMR

Solid-state NMR spectra were collected at the University of Wisconsin-Madison on a Bruker Avance III 500 MHz spectrometer equipped with a 4 mm cross-polarization magic angle spinning (CP-MAS) probe. Cross polarization experiments were performed, where the peak intensity and area depend on both the abundance of the observed nuclei and the number of protons on nearby probed carbon nuclei (within 3-4 Å). ^{13}C spectra were externally referenced using adamantine (upfield peak was set to 38.5 ppm). Spectra were

acquired at 298 K, with a rotational speed of 12 kHz. Other experimental acquisition details are previously reported.[12] All spectra were processed in MestReNova, including baseline correction and manual phase correction. Peaks corresponding to amorphous or crystalline forms of CNF were assigned based on known chemical shifts,[68] and the percentage of crystalline and amorphous character was determined by averaging these respective peak areas.

4.3.2.4 X-ray Photoelectron Spectroscopy

X-ray photoelectron spectra of CNF powders were obtained to determine $DS_{surface}$ using a PHI 5600 XPS equipped with a Mg Kα flood source (1253.6 eV) and a hemispherical energy analyzer. High resolution multiplex scans were collected at ultra-high vacuum (8×10^{-8} torr) using a source power of 300 W, pass energy 23.5 eV, 10 sweeps per spectrum, and 0.025 eV/step. Survey scans were collected from 1200 eV to 0 eV at the same ultra-high vacuum and power but with a pass energy of 187.85 eV, 2 sweeps per spectrum, and 1.6 eV/step. Spectra were analyzed using CASA XPS software.

4.3.3 DS Calculations

4.3.3.1 CHN Analysis

$DS_{overall}$ values for CNF esters and ethers were calculated from the wt % of carbon for each sample (Table 8.1) as compared to unmodified CNF. Based on the carbon content of unmodified CNF (41.3 wt %), any increase in carbon signal was assumed to be caused by functionalization of the cellulosic backbone. For example, to increase the carbon content of unmodified CNF (41.3 wt %) to 53.0 wt % using a dodecyl esterification, roughly 0.45 dodecyl ester groups would need to be added, on average, per glucose monomer unit, corresponding to a $DS_{overall}$ of 0.45.

4.3.3.2 XPS Spectra Analysis

$DS_{surface}$ values for CNF esters and ethers were calculated from the fit C-C component (285.0 eV) in the C(1s) XPS envelope for each sample (Figure 2d, Table 8.2) using CASA XPS software. As the C-C content in unmodified CNF was measured to be ~ 12.3% (due to adventitious carbon), any increase in this component was assumed to be due to functionalization of nanocellulose. For example, to increase the C-C of unmodified CNF (12.3 %) to 47.9 %, roughly 0.43 dodecyl ester groups, on average, would need to be added per glucose monomer, corresponding to a $DS_{surface}$ of 0.43.

4.3.3.3 TEMPO CNF DS

The TEMPO CNF obtained from University of Maine Process Development Center was listed as having 1.5 mmol COOH/g cellulose. Each gram of cellulose features roughly 6.2 mmol of glucose monomer units, which corresponds to 0.243 COOH groups per cellulose unit (1.5 mmol COOH/6.2 mmol cellulose), representing a DS of 0.243.

4.3.4 Biodegradation Tests

4.3.4.1 Biomethane Potential (BMP) Tests

The mineralization of unmodified and functionalized CNFs was assessed using biomethane potential (BMP) tests, adapted with minor modifications from Owen et al.,[69-70] to monitor biogas (i.e., CO_2 and CH_4) production after exposure to an anaerobic microbial community. Microbial media was prepared using nutrients and buffers as previously described[12] and heated at 100 °C for 30 m while sparging with N_2 to achieve anoxic conditions before dosing with anaerobic digestor sludge (10% v/v) obtained from Back River Wastewater Treatment Plant (Baltimore, MD). The BMP media was then adjusted to a pH of ~7 using 20% CO_2 gas and kept anoxic via continuous N_2 sparging.

Duplicate samples of 150 mg (only LA-CNF series) or 100 mg functionalized CNF (difference due to sample availability) were mixed with 100 mL of media in serum bottles (150 mL capacity) and capped with a rubber septum. Samples were then incubated at mesophilic temperature (35 °C) for up to 424 d and biogas production was volumetrically assessed via intermittent headspace measurements with a glass syringe. In each set of samples, unmodified CNF and blank controls (i.e., media in the absence of sample) were digested in triplicate to account for biogas produced by the native material and residual organic matter in the media, respectively. Biogas production was reported as the difference between the volume produced by each sample and the average volume from the blank media for each timepoint. All biogas values were normalized to account for differences in sample mass (comparison between 100 mg and 150 mg CNF Figure 8.1). Due to the ability for each functional group to contribute to biogas production during sample biodegradation (i.e., after cleavage from the CNF backbone), reported values are additionally normalized to the theoretical maximum biogas production from each sample. For example, using the biogas production potential determined for lauric acid (1280 mL/g_{LA}, Figure 8.2a) and unmodified CNF (680 mL/g_{CNF}), a sample esterified with dodecyl ester at a DS of 0.45 (66 wt% cellulose, 34 wt% dodecyl ester) is expected to produce 883 mL/g [(0.66 * 680 mL/g_{CNF}) + (0.34 * 1280 mL/g_{LA})] of biogas if fully mineralized. By normalizing the empirical biogas produced by this sample to the maximum expected value, direct comparisons between samples of different DS (and thus, different contributions of functional groups to biogas production) could be made.

4.3.4.2 Aerobic Biodegradation Tests

Aerobic biodegradation of CNF samples was assessed via determination of mass

loss after exposure to an aerobic microbial community obtained from the primary effluent of the Back River Wastewater Treatment Plant (Baltimore, MD). Triplicate 50 mg samples of each CNF powder were pelletized via centrifugation in conical vials (50 mL, Sarstedt) (Figure 8.3) containing 200 mg/L sodium acetate trihydrate and 10% v/v salt stock (7.18 mM K_2HPO_4, 2.79 mM KH_2PO_4, 0.757 mM $(NH_4)_2SO_4$, 0.0406 mM $MgSO_4 \bullet 7H_2O$), as well as trace elements necessary for bacterial growth. Microbial media was made by adding 10% v/v primary effluent to the vials and shaking at 125 rpm at 28 °C for 60 d. To account for mass loss due to dispersion/dissolution of samples in the media or sampling error, an identical set of CNF samples in abiotic media (i.e., same media without primary effluent) was incubated alongside the microbial samples. After 60 d, residual sample was recovered, washed with MilliQ water (18.2 MΩ*cm, Millipore, USA), and dried in a vacuum oven at 60 °C. Mass loss for each sample was reported as the difference between the average mass lost in bacteria media and the average mass lost in the abiotic media compared to the initial mass (50 mg).

4.3.4.3 Gompertz Modeling

Biogas production rate was quantified using the modified Gompertz kinetic model (Eq. 1)[71]

$$Y_i = Y_m e^{-e^{(\frac{K*e(\lambda - t_i)}{Ym} + 1)}} \quad \text{(Eq. 1)}$$

where Y_m is the experimental ultimate biogas yield (mL/g), K is the specific rate constant (mL g^{-1} d^{-1}), λ is the lag phase time constant (d), and t_i is the total incubation time (d). The Solver optimization tool in Microsoft Excel was used to estimate the model parameters for each sample by minimizing the root mean square deviations (RMSE, Table 8.3), and the

agreement between predicted and empirical values was evaluated by comparing the RMSE and R^2 values.

4.4 Results and Discussion

Cellulose nanofibrils (CNFs) were functionalized with different ester, carboxylic acid, and ether groups (Figure 8.4, 8.5) following literature procedures. Subsequent mineralization by an anaerobic microbial community was assessed by tracking the kinetics of biogas production quantified with modified Gompertz fits (Table 8.3).[71-73] As both the cellulose and functional group can be mineralized (Figure 8.2),[74] biogas production was normalized to the total biogas capable of evolving from complete mineralization of both cellulose and functional group in each sample (see experimental section). Mass loss was used as the metric for aerobic biodegradation, as an open system was required to maintain an oxygenated environment.

Figure 1a shows that unmodified CNFs were completely mineralized by an anaerobic microbial community after 60 d (Figures 1a and 8.6) Amongst the three esterified CNFs, hexyl esterified CNF ($DS_{overall}$: 0.09) exhibited a biodegradation rate (Eq. 1, Table 8.3) comparable to unmodified CNF, while dodecyl ($DS_{overall}$: 0.45) and phenyl ($DS_{overall}$: 0.14) esterified CNFs displayed considerably slower biodegradation rates, although all three esters were ultimately fully mineralized. TEMPO-oxidized CNFs containing carboxylate groups with Na^+ and H^+ (Figure 8.6) counterions ($DS_{overall}$: 0.243) also

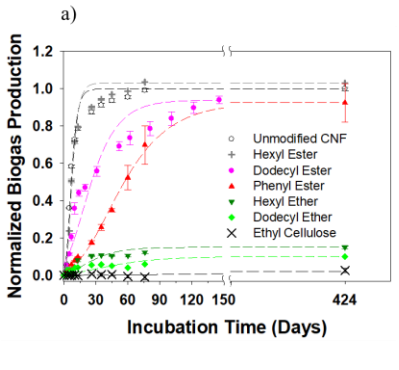

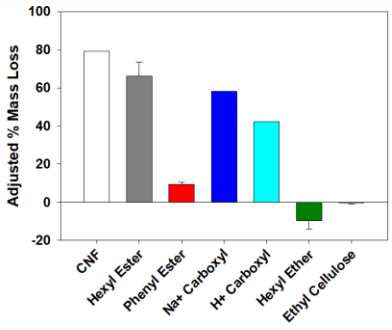

c)

Sample	Anaerobic Biodegradation Compared to CNF (60 d)	Aerobic Biodegradation Compared to CNF (60 d)
Unmodified CNF	1.00	1.00
Hexyl Ester	1.03	0.84
Phenyl Ester	0.55	0.12
Na+ Carboxyl	0.75	0.73
H+ Carboxyl	0.83	0.53
Hexyl Ether	0.11	-0.12
Ethyl Cellulose	0.00	0.00

Figure 4.1 Biodegradation of functionalized cellulose nanofibrils (CNF). a) Normalized biogas production for unmodified CNF, hexyl ester CNF, dodecyl ester CNF, phenyl ester CNF, hexyl ether CNF, dodecyl ether CNF, and ethyl cellulose by an anaerobic microbial community as a function of incubation time (dodecyl ester CNF was not sampled past 146 d). For each sample, values are normalized to the maximum theoretical biogas produced by both cellulose and the added functional group (see experimental section for details). b) Mass loss of (left to right) unmodified CNF (white), hexyl ester CNF (gray), phenyl ester CNF (red), Na^+ Carboxyl CNF (dark blue), H^+ Carboxyl CNF (light blue), hexyl ether CNF (green), and ethyl cellulose (black) after 60 d of exposure to an aerobic microbial community. Values shown represent the difference between microbial and blank samples (see text for details). Error bars represent one standard deviation from duplicate samples. c) Comparison of the relative inhibition of biodegradation for different functionalized CNFs in anaerobic vs. aerobic environments.

biodegraded at markedly slower rates than native CNFs, but ultimately biodegraded to a similar extent. In contrast, etherified nanocellulose was dramatically less susceptible to mineralization even at extremely low $DS_{overall}$ values (hexyl $DS_{overall}$: 0.05 and dodecyl $DS_{overall}$: 0.11); the biodegradation rate of the hexyl and dodecyl etherified CNFs was only 3% and 1% of the rate observed for unmodified CNF, respectively, and only 15% and 10% of each sample biodegraded after 424 d of incubation. This recalcitrance to mineralization agrees with the lack of biogas production from ethyl cellulose, a commercial, non-biodegradable, macrocellulose ether that produced no biogas over 424 d. Incubation of functionalized CNFs for 60 d in an aerobic microbial community found in aerobic

wastewater revealed similar trends of inhibition towards biodegradation (Figure 1b). Thus, unmodified CNFs exhibited 80 % mass loss while hexyl and phenyl CNF esters and carboxylated CNFs all exhibited measurable mass loss, and etherified CNFs were essentially non-biodegradable.

This study is the first to investigate a variety of functionalized nanocellulose in both aerobic and anaerobic environments. CNF functionalization alters biodegradation behavior because it changes the enzymatic degradation process. Previous studies on functionalized cellulose have shown that the enzymatic susceptibility of carboxyl groups and their facilitation of CNF swelling increases their biodegradability.[75-76] Ester groups are prone to enzymatic hydrolysis (assuming a low enough DS), a process which effectively cleaves the functional group from CNF esters to yield a free carboxylic acid while regenerating the biodegradable glucose monomer unit.[20, 74, 77-78] In contrast, ethers are recalcitrant to enzymatic attack/hydrolysis, qualitatively explaining the linkage-dependent biodegradation trends which were observed.[20, 79-80]

Although biodegradation trends between different functionalized CNF were independent of the microbial community (i.e., aerobic vs. anaerobic), the magnitude of inhibition varied (Figure 1c). Specifically, the extent of biodegradation was reduced in aerobic wastewater compared to anaerobic wastewater, likely due to the different microbial populations present. The decreased aerobic biodegradation of functionalized CNF suggests that these materials will be more recalcitrant to biodegradation in aqueous aerobic environments. Thus, it appears that, when possible, functionalized CNF should be disposed of in anaerobic digestors to maximize biodegradation potential.

While complete biodegradation involves conversion to biogas (CH_4 and CO_2), reduction to low molecular weight species is an intermediate step in the biodegradation process and such species would not be detected in the biogas measurements reported here. Degradation to low molecular weight species would, however, still be reflected in the mass differences measured in aerobic biodegradation. Since the biodegradation trends for functionalized CNF were the same in both the biogas and mass loss tests reported here, incomplete biodegradation of functionalized CNFs is not expected to be a significant endpoint compared to their complete mineralization.

During the course of these experiments, it was noted that a CNF ester with relatively high $DS_{overall}$ (dodecyl, $DS_{overall}$ 0.45) biodegraded similarly to a CNF ester with significantly lower $DS_{overall}$ (phenyl, $DS_{overall}$ 0.14) in anaerobic media. Based on existing literature for macrocellulose, a threefold increase in DS would be expected to measurably decrease the biodegradability of CNF despite the difference in ester group. This suggested that traditional overall DS values may not be the best parameter to predict the biodegradability of functionalized nanocellulose. One possible explanation is that the large surface area to volume ratio of nanocellulose causes the surface of functionalized CNFs to take on increased importance as compared to macrocellulose. Under these circumstances, $DS_{surface}$ values may provide a more reliable indicator of biodegradation, though this value is rarely reported. To explore this possibility, a series of esterified CNFs with varying levels of surface and overall substitution were synthesized and characterized (Figure 2).

The $DS_{overall}$ and $DS_{surface}$ values of CNFs functionalized with dodecyl ester groups using liquid phase lauric acid (LA-CNF; Figure 2) or lauroyl chloride (LC-CNF; Figures 8.7, 8.9) were measured and compared. Elemental analysis, the most commonly used

technique to assess $DS_{overall}$ of cellulosic materials, verified an increasing $DS_{overall}$ (Table 8.1). ATR was used to assess the chemical bonding and relative $DS_{overall}$ in esterified CNFs. The unmodified CNF presented in Figure 2a contains the characteristic O-H (3339 cm^{-1}), C-H (2905 cm^{-1}), and C-O (1031 cm^{-1}) stretches of cellulose. An increase in the extent of overall esterification with reaction time is observed by increases in methylene (-CH_2-; 2920 cm^{-1} and 2850 cm^{-1}) and carbonyl (C=O; 1700 cm^{-1}) stretching intensities (LC-CNF ATR

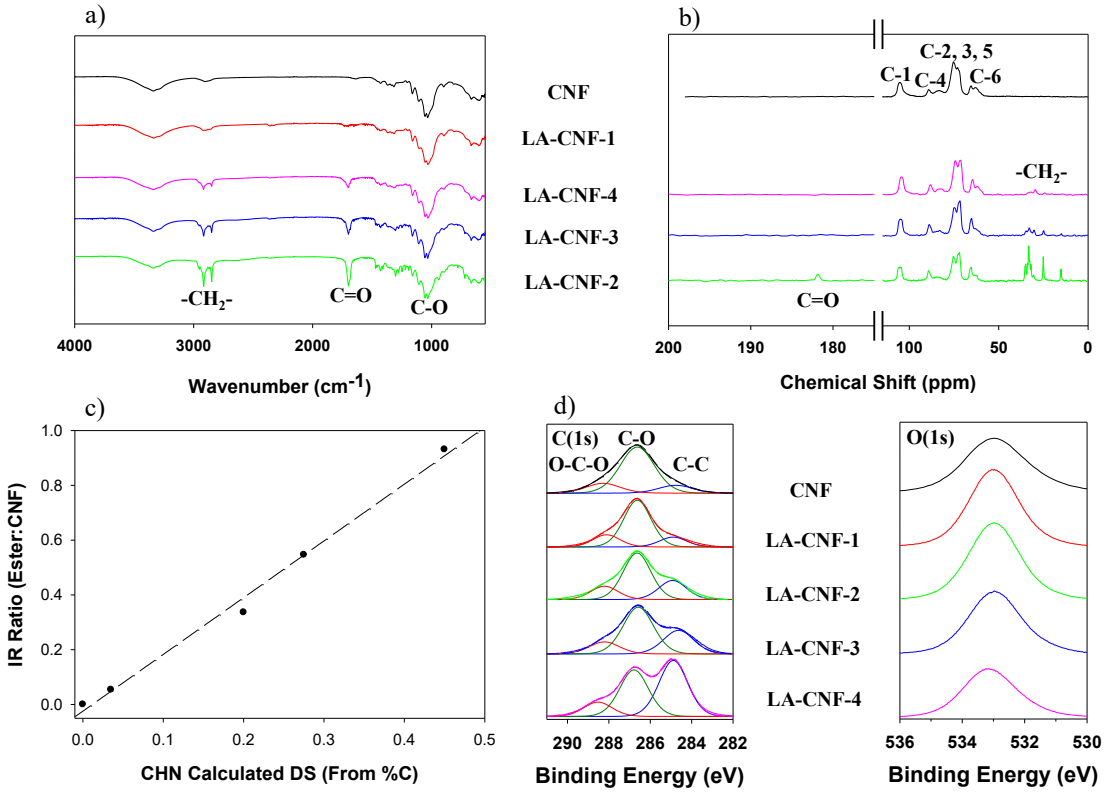

Figure 4.2 Characterization of esterified cellulose nanofibrils (CNF). a) Attenuated total reflectance Fourier transform infrared spectroscopy (ATR) of unmodified CNF (black), and LA-CNF-1 (red), LA-CNF-4 (pink), LA-CNF-3 (blue), and LA-CNF-2 (green) dodecyl ester CNFs. b) Solid-state ^{13}C NMR spectra of unmodified CNFs (black), and LA-CNF-4 (pink), LA-CNF-3 (blue), and LA-CNF-2 (green) dodecyl ester CNFs. c) Relation between ATR-IR peak ratio (C=O:C-O) and overall DS calculated from CHN elemental analysis %C data. d) X-ray photoelectron C(1s) and O(1s) spectra of unmodified CNFs (black) and LA-CNF-1 (red), LA-CNF-2 (green), LA-CNF-3 (blue), and LA-CNF-4 (pink) dodecyl ester CNFs.

Figure 8.7a). Moreover, a linear relationship between the $DS_{overall}$ values from elemental analysis and C=O:C-O IR band ratios was revealed (Figure 2c), suggesting that ATR could be a facile, non-destructive alternative for determining $DS_{overall}$ values of functionalized nanocellulose. Solid-state ^{13}C-NMR qualitatively confirms the increased degree of substitution as shown in Figure 2b. Thus, the ^{13}C-NMR spectrum of unmodified CNF consists of peaks between 50 and 110 ppm of carbons 1-6 of cellulose (C1-C6, labeled in Figure 8.8 and Table 8.4) including amorphous and crystalline features. In addition to these principal cellulose peaks, the spectra of esterified CNF contain ester (180 ppm) and methylene (32, 25, 15 ppm) peaks that increased in intensity with reaction time (LC-CNF spectra Figure 8.7b). NMR spectra reveal a minor increase in crystallinity of the esterified CNF samples compared to the unmodified CNF sample (Table 8.5).[81] XPS was used to determine $DS_{surface}$ values (Figure 2d). The C(1s) region of unmodified CNF contains C-C, C-O, and O-C-O components at 285.0 eV, 286.6 eV, and 288.5 eV, respectively, while the O(1s) region features a single peak centered at 533.2 eV (LC-CNF Figure 8.9). With increased $DS_{surface}$, the C-C component increases in intensity due to the grafting of long alkyl chain ester groups. Importantly, this increase in $DS_{surface}$ was not correlated with the $DS_{overall}$; thus, LA-CNF-2 features the second lowest $DS_{surface}$ (0.10), but the highest $DS_{overall}$ (0.45). In addition to liquid phase esterification, gas phase reactions using lauroyl or hexanoyl chloride were performed in an attempt to restrict functionalization to the CNF surface (Figure 8.10). The XPS spectra in Figure 8.10 confirms that measurable increases in $DS_{surface}$ (Table 8.2) occurred after gas phase functionalization in the absence of substantial bulk functionalization, the latter evidenced by the infrared spectra in Figure 8.11. It should be noted that the increased volatility and reactivity of hexanoyl chloride

enabled higher $DS_{surface}$ values to be obtained compared to lauroyl chloride.

To assess how CNF biodegradability responded to changes in $DS_{surface}$ compared to $DS_{overall}$, LC-CNFs and LA-CNFs were biodegraded by an anaerobic microbial community (Figures 3 and S12). As $DS_{surface}$ increased, Figure 3a shows that the extent and rate of biogas production from LC-CNFs decreased systematically, culminating in LC-CNF-4, where the rate and extent of biodegradation were only 28% and 43% of unmodified CNF, respectively. Notably, this trend of decreased biodegradation did not correlate with the $DS_{overall}$. For example, LC-CNF-3 featured the lowest $DS_{overall}$, and yet was the second most recalcitrant of the LC-CNFs. Increases in the $DS_{surface}$ of LA-CNFs also led to systematic decreases in biodegradation (Figure 3b), analogous to the behavior of the LC-CNFs. Thus, LA-CNF-4, the most surface-functionalized LA-CNF, exhibited 13% and 67% of the rate and extent of biogas production of unmodified CNF, respectively. Again, $DS_{overall}$ did not prove to be a reliable predictor of biodegradability as LA-CNF-2 possessed the highest $DS_{overall}$ value, and yet was almost completely biodegraded (94%), albeit at a slower (29%) rate compared to unmodified CNFs.

It should be noted that although CNFs functionalized with lauroyl chloride (LC-CNF) reached higher $DS_{surface}$ values (max 2.46) than those functionalized with lauric acid (max 0.43), the production of HCl during functionalization with acyl chlorides is known to reduce cellulose chain length and particle size.[50, 82-85] This shortening in chain length increases the overall biodegradability of cellulosic materials by offering more sites/surface area (e.g., chain ends) for the initiation of enzymatic attack.[42, 86-87] In contrast, esterification using carboxylic acids does not produce HCl at the site of functionalization, and thus avoids

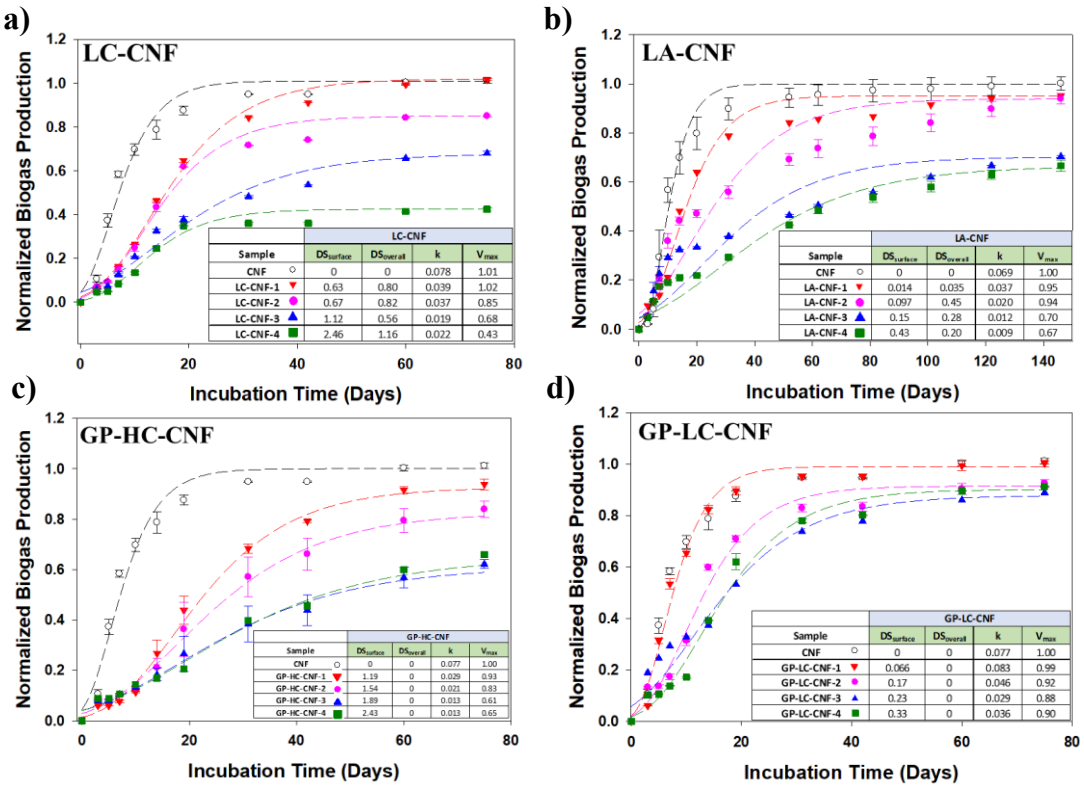

Figure 4.3 Biogas production and modified Gompertz model fits (dotted lines) of cellulose nanofibrils (CNF) esterified using liquid and gas phase methods. Relative biogas production from cellulose nanofibrils esterified using a) liquid phase lauroyl chloride (LC-CNF), b) liquid phase lauric acid (LA-CNF), c) gas phase hexanoyl chloride (GP-HC-CNF), and d) gas phase lauroyl chloride (GP-LC-CF). Biogas volumes are normalized to the maximum theoretical biogas production expected from the combined cellulose and functional group components of each sample. The $DS_{surface}$ and $DS_{overall}$ values as well as normalized maximum biogas volume (V_{max}) and biogas production rate (k) for each sample are provided in the inset of each plot.

damaging the cellulose chain. This explains why LC- CNF samples with higher $DS_{surface}$ values than LA-CNF samples biodegraded more extensively (compare LC-CNF-2 and LA-CNF-4).

Gas phase (GP) functionalization was used to selectively modify the surface of CNFs using hexanoyl chloride (GP-HC-CNF) and lauroyl chloride (GP-LC-CNF). These esterified samples were primarily functionalized at their surface, meaning $DS_{overall}$ was

essentially 0 (Table S1, Figure S11), allowing us to isolate the effect of surface functionalization on the biodegradation of nanocellulose (Figures 3 and S12). Furthermore, the lack of bulk (i.e., overall) functionalization eliminated the need to normalize biogas production to the contribution from the added functional groups. The increased volatility of hexanoyl chloride (HC) enabled a wider range of $DS_{surface}$ values to be achieved (1.19-2.43) compared to lauroyl chloride (LC; 0.07-0.33). The data shown in Figure 3c for the biodegradation of GP-HC-CNF is the clearest indication of the systematic and determinant effect that surface functionalization has on CNF biodegradability. Thus, GP-HC-CNF-1, the least functionalized GP-HC-CNF ($DS_{surface}$ 1.19), displayed a 62% reduction in biogas production rate, although 93% of the sample biodegraded. In contrast, the most surface functionalized GP-HC-CNF (GP-HC-CNF-4; $DS_{surface}$ 2.43) exhibited a biogas production rate of only 17% of the value observed for unmodified CNF, and only 65% of the sample biodegraded. As expected, the lower $DS_{surface}$ values of CNFs functionalized with lauroyl chloride (LC) reduced the magnitude of the inhibition (Figure 3d). Thus, for GP-LC-CNF samples with $DS_{surface}$ values > 0.17, the biogas production rate decreased measurably with the extent of biodegradation reaching approximately 90% of the value expected for unmodified CNFs.

This importance of surface functionalization is consistent with the biodegradation mechanism of cellulosic materials, which is typically initiated at the surface via highly specific microbial interactions. Under anaerobic conditions, cellulose is completely mineralized by cellulolytic microbes, which utilize cellulosomes or multiprotein complexes of enzymes.[23, 26, 39] Cellulosomes are responsible for secreting cellulolytic enzymes and are particularly sensitive to the surface, changing the composition of its

multienzyme complex and of the enzymes secreted based on surface area and structure (e.g., cellulose vs. lignocellulose). The small length of the glucose subunits of cellulose (roughly 0.5 nm)[88] compared to the length of cellulosomes (roughly 18 nm)[89] suggests that the presence of functional groups on the surface of nanocellulose will change the pathway of its enzymatic degradation.[44-45, 90] Specifically, at sites on the surface which have been functionalized, biodegradation will be delayed until these functional groups have been removed and a cellulose substrate recognizable to microbial cellulosomes has been regenerated. For esterified CNFs at relatively low degrees of surface functionalization (e.g., LA-CNF-1, phenyl ester CNF), this effect causes a decrease in biodegradation rate—although ultimately the CNF still fully biodegrades. However, as the degree of surface functionalization increases (e.g., LA-CNF-4, LC-CNF-4), our data indicates that an increasing fraction of the CNFs are recalcitrant to biodegradation, despite the enzymatic susceptibility of ester groups. We ascribe this effect to the presence of high concentrations of ester groups in regions of the surface sufficient to interfere with enzyme regioselectivity, blocking esterases from properly orienting with an individual ester group, and thus impeding the hydrolysis of ester groups.[78] This inability of esterases to biodegrade cellulosic samples with high DS values has also been reported for macrocellulose esters ($DS_{overall}$ 1.8).[19, 37, 78] This dependence of biodegradation behavior on DS is exacerbated when the functional groups are inert to enzymatic hydrolysis, as is the case for etherified CNFs, for which a $DS_{surface}$ of 1.6 and 2.5 was sufficient to eliminate biodegradation of dodecyl and hexyl ether CNF, respectively (See Figure 1 and Table S2).

While $DS_{surface}$ is the primary factor determining the biodegradation of functionalized nanocellulose, the extent of overall CNF functionalization, as measured by

$DS_{overall}$, still plays a role in influencing the extent of biodegradation. For example, CNFs functionalized both at the surface and in the bulk by liquid phase LC exhibited a similar range of $DS_{surface}$ values (0.63-2.46) to CNFs functionalized exclusively at the surface with HC ($DS_{surface}$ 1.19-2.43), but the CNFs functionalized via gas phase HC were less extensively biodegraded (43% gas phase vs. 65% liquid phase). This difference can be attributed to the absence of extensive functionalization in the bulk of the gas phase functionalized CNFs, which allows for an efficient and complete biodegradation process to ensue if, and when, the surface functional groups are removed by hydrolysis. However, it is important to note that $DS_{overall}$ represents a much higher number of cellulose chains than $DS_{surface}$, and yet contributes less to the overall degree of inhibition. Since biogas production reflects the overall biodegradability of the CNF (i.e., surface + bulk biodegradation), this underscores our assertion that the extremely small fraction of CNFs at the surface plays a disproportionate role in determining the overall biodegradability of the nanomaterial.

In contrast to our data, it should be noted that the overall level of functionalization ($DS_{overall}$) is generally a reasonably good predictor for the biodegradation behavior of macrocellulose, although the degree of surface functionalization is rarely reported. In part, this difference between macro and nanocellulose is likely to be a reflection of the comparatively small fraction of cellulose chains at the surface of macrocellulose. Furthermore, the large number of bulk cellulose chains and decreased crystallinity of macrocellulose fibers compared to nanocellulose cause it to swell to a greater degree (~48% swelling vs. ~26%) in aqueous media.[91] Swelling will facilitate enzymatic penetration into the bulk of the fiber network and increase microbial interactions within the

interior of macrocellulose,[2, 91-93] therefore increasing the importance of $DS_{overall}$ in determining its biodegradation compared to nanocellulose.

Thus, the biodegradation of functionalized nanocellulose will be dictated by the extent and chemistry of the functionalized surface after modification. Such microbial interactions are of particular importance, as the future production of functionalized nanocellulose is expected to continue to grow, at which point its release into the environment will be inevitable.[2, 14-16, 94] Thus, the commercial benefit achieved through functionalization of nanocellulose must be carefully weighed against the consequential environmental impact which arises due to hydrophobic modification in order to yield a nanomaterial which is environmentally transient after release.

While sustainability has been identified as an area of focus in the production phase of surface-modified nanocellulose,[51, 66, 95] the end-of-life environmental fate of such nanomaterials has been largely overlooked or assumed to be comparable to unmodified nanocellulose.[1, 96-99] This supposition perhaps arises from the abundant existing literature on macrocellulose which promotes overall DS as the primary indicator of biodegradability, a value which is typically minimized in the functionalization of nanocellulose.[51-52] Results from the present study instead promote the importance of considering the surface chemistry of functionalized nanocellulose, properties which are rarely reported, but reduce the biodegradation of nanocellulose as a function of the degree of surface substitution and the enzymatic recalcitrance of the functional group. Importantly, this resistance to biodegradation manifests as an inability to be mineralized by microbes, a conversion which has been highlighted as the true determinant of environmental biodegradation and sustainability.[17-18]

Indeed, products which utilize surface-functionalized nanocellulose and are marketed as biodegradable (e.g., packaging materials)[96, 100] will in truth feature environmentally persistent nanocellulose. For example, Yu et al., combined surface-esterified nanocellulose with poly(3-hydroxybutyrate-*co*-3-hydroxyvalerate) (PHBV), a biodegradable polymer, to create a strengthened material that was deemed appropriate for use as a biodegradable food packaging material.[96] However, based on our data, the surface-level esterification of nanocellulose used in the reinforcement of PHBV likely would reduce its overall biodegradability, making the nanocomposite material not fully biodegradable. Other applications of hydrophobic nanocellulose, such as its use in flexible displays, will exacerbate this unintended environmental impact if surface chemistry is not properly accounted for.[101-104] For example, Yagyu et al., developed a transparent, flexible nanopaper using acetylated nanocellulose with projected application in electrodes, solar cells, and transistors.[101] The widespread application of such devices that are enabled by hydrophobic nanocellulose presents the potential for adverse environmental impacts due to the demonstrated resistance of such nanomaterials to biodegradation. Thus, it is recommended that synthetic strategies be modulated via analysis of the surface chemistry of functionalized nanocellulose in order to balance the commercial relevance of such materials with their environmental impact.

4.5 Acknowledgements

This work was supported by National Science Foundation under the Center for Sustainable Nanotechnology, CHE-1503408. The CSN is part of the Centers for Chemical Innovation Program. The National Magnetic Resonance Facility at Madison is supported by NIH grants P41 GM103399 (NIGMS) and P41GM66326 (NIGMS). Additional

equipment was purchased with funds from the University of Wisconsin, NIH (RR02781, RR08438), NSF (DMB-8415048, OIA-9977486, BIR-9214394), and USDA. The Bruker AVANCE III 500 NMR spectrometer was supported by a UW2020 grant and a generous gift from Paul J. and Margaret M. Bender. The authors would like to thank Chris Krout from the Back River Wastewater Treatment Plant (Baltimore, MD) for the microbial samples.

4.6 References

1. Kalia, S.; Dufresne, A.; Cherian, B. M.; Kaith, B. S.; Averous, L.; Njuguna, J.; Nassiopoulos, E., Cellulose-Based Bio- and Nanocomposites: A Review. *Int. J. Polym. Sci.* **2011,** *2011*.
2. Dufresne, A., *Nanocellulose: From Nature to High Performance Tailored Materials*. Walter de Gruyter: Berlin, Germany, 2012.
3. Hamid, S. B. A.; Zain, S. K.; Das, R.; Centi, G., Synergic Effect of Tungstophosphoric Acid and Sonication for Rapid Synthesis of Crystalline Nanocellulose. *Carbohydr. Polym.* **2016,** *138*, 349-355.
4. Phanthong, P.; Karnjanakom, S.; Reubroycharoen, P.; Hao, X.; Abudula, A.; Guan, G., A Facile One-Step Way for Extraction of Nanocellulose with High Yield by Ball Milling with Ionic Liquid. *Cellulose* **2017,** *24* (5), 2083-2093.
5. Henriksson, M.; Henriksson, G.; Berglund, L. A.; Lindström, T., An Environmentally Friendly Method for Enzyme-Assisted Preparation of Microfibrillated Cellulose (MFC) Nanofibers. *Eur. Polym. J.* **2007,** *43* (8), 3434-3441.
6. Moon, R. J.; Martini, A.; Nairn, J.; Simonsen, J.; Youngblood, J., Cellulose nanomaterials review: structure, properties and nanocomposites. *Chem. Soc. Rev.* **2011,** *40* (7), 3941-3994.
7. Li, Y.-Y.; Wang, B.; Ma, M.-G.; Wang, B., Review of Recent Development on Preparation, Properties, and Applications of Cellulose-Based Functional Materials. *Int. J. Polym. Sci.* **2018**.
8. Ummartyotin, S.; Manuspiya, H., A critical review on cellulose: From fundamental to an approach on sensor technology. *Renewable and Sustainable Energy Reviews* **2015,** *41*, 402-412.
9. Phanthong, P.; Reubroycharoen, P.; Hao, X.; Xu, G.; Abudula, A.; Guan, G., Nanocellulose: Extraction and application. *Carbon Resources Conversion* **2018,** *1* (1), 32-43.
10. Qiu, X.; Hu, S., "Smart" Materials Based on Cellulose: A Review of the Preparations, Properties, and Applications. *Materials* **2013,** *6* (3), 738-781.
11. Nasseri, R.; Deutschman, C. P.; Han, L.; Pope, M. A.; Tam, K. C., Cellulose nanocrystals in smart and stimuli-responsive materials: a review. *Materials Today Advances* **2020,** *5*, 100055.

12. Frank, B. P.; Durkin, D. P.; Caudill, E. R.; Zhu, L.; White, D. H.; Curry, M. L.; Pedersen, J. A.; Fairbrother, D. H., Impact of Silanization on the Structure, Dispersion Properties, and Biodegradability of Nanocellulose as a Nanocomposite Filler. *ACS Applied Nano Materials* **2018,** *1* (12), 7025-7038.
13. Nakatani, H.; Iwakura, K.; Miyazaki, K.; Okazaki, N.; Terano, M., Effect of Chemical Structure of Silane Coupling Agent on Interface Adhesion Properties of Syndiotactic Polypropylene/Cellulose Composite. *J. Appl. Polym. Sci.* **2011,** *119* (3), 1732-1741.
14. Chin, K.-M.; Sung Ting, S.; Ong, H. L.; Omar, M., Surface functionalized nanocellulose as a veritable inclusionary material in contemporary bioinspired applications: A review. *J. Appl. Polym. Sci.* **2018,** *135* (13), 46065.
15. Brun, V.; Hansen, F.; Turpin, D.; Bennett, K., Cellulose Nanomaterials Research Roadmap. *Agenda 2020 Technology Alliance* **2016**.
16. Madsen, L. D.; Svedberg, E. B., *Materials Research for Manufacturing: An Industrial Perspective of Turning Materials into New Products*. Springer International Publishing: Switzerland, 2016; Vol. 224.
17. Zumstein, M. T.; Narayan, R.; Kohler, H.-P. E.; McNeill, K.; Sander, M., Dos and Do Nots When Assessing the Biodegradation of Plastics. *Environ. Sci. Technol.* **2019,** *53* (17), 9967-9969.
18. Zumstein, M. T.; Schintlmeister, A.; Nelson, T. F.; Baumgartner, R.; Woebken, D.; Wagner, M.; Kohler, H.-P. E.; McNeill, K.; Sander, M., Biodegradation of synthetic polymers in soils: Tracking carbon into CO(2) and microbial biomass. *Sci Adv* **2018,** *4* (7), eaas9024-eaas9024.
19. Puls, J.; Wilson, S. A.; Hölter, D., Degradation of Cellulose Acetate-Based Materials: A Review. *Journal of Polymers and the Environment* **2011,** *19* (1), 152-165.
20. Reese, E. T., Biological Degradation of Cellulose Derivatives. *Industrial & Engineering Chemistry* **1957,** *49* (1), 89-93.
21. Sakai, K.; Yamauchi, T.; Nakasu, F.; Ohe, T., Biodegradation of Cellulose Acetate by Neisseria sicca. *Bioscience, Biotechnology, and Biochemistry* **1996,** *60* (10), 1617-1622.
22. Haider, T. P.; Völker, C.; Kramm, J.; Landfester, K.; Wurm, F. R., Plastics of the Future? The Impact of Biodegradable Polymers on the Environment and on Society. *Angewandte Chemie International Edition* **2019,** *58* (1), 50-62.
23. Leschine, S. B., Cellulose Degradation in Anaerobic Environments. *Annu. Rev. Microbiol.* **1995,** *49* (1), 399-426.
24. Singh, G. Biodegradation of Nanocellulose and Microbial Community Response: Effect of Surface Modification and Morphology. Virginia Polytechnic Institute and State University, Blacksburg, VA, 2015.
25. Singh, G.; Chandoha-Lee, C.; Zhang, W.; Renneckar, S.; Vikesland, P. J.; Pruden, A., Biodegradation of Nanocrystalline Cellulose by Two Environmentally-Relevant Consortia. *Water Res.* **2016,** *104*, 137-146.
26. Pérez, J.; Muñoz-Dorado, J.; de la Rubia, T.; Martínez, J., Biodegradation and biological treatments of cellulose, hemicellulose and lignin: an overview. *International Microbiology* **2002,** *5* (2), 53-63.
27. Ly, B.; Thielemans, W.; Dufresne, A.; Chaussy, D.; Belgacem, M. N., Surface functionalization of cellulose fibres and their incorporation in renewable polymeric matrices. *Compos. Sci. Technol.* **2008,** *68* (15), 3193-3201.

28. Jandura, P.; Kokta, B. V.; Riedl, B., Cellulose Fibers/Polyethylene Hybrid Composites: Effect of Long Chain Organic Acid Cellulose Esters and Organic Peroxide on Rheology and Tensile Properties. *Journal of Reinforced Plastics and Composites* **2001,** *20* (8), 697-717.
29. de Carvalho Oliveira, G.; Filho, G. R.; Vieira, J. G.; De Assunção, R. M. N.; da Silva Meireles, C.; Cerqueira, D. A.; de Oliveira, R. J.; Silva, W. G.; de Castro Motta, L. A., Synthesis and application of methylcellulose extracted from waste newspaper in CPV-ARI Portland cement mortars. *J. Appl. Polym. Sci.* **2010,** *118* (3), 1380-1385.
30. Abushammala, H.; Mao, J., A Review of the Surface Modification of Cellulose and Nanocellulose Using Aliphatic and Aromatic Mono- and Di-Isocyanates. *Molecules* **2019,** *24* (15), 2782.
31. Vaca-Garcia, C.; Borredon, M. E.; Gaseta, A., Determination of the degree of substitution (DS) of mixed cellulose esters by elemental analysis. *Cellulose* **2001,** *8* (3), 225-231.
32. Samaranayake, G.; Glasser, W. G., Cellulose derivatives with low DS. I. A novel acylation system. *Carbohydr. Polym.* **1993,** *22* (1), 1-7.
33. King, A. W. T.; Jalomäki, J.; Granström, M.; Argyropoulos, D. S.; Heikkinen, S.; Kilpeläinen, I., A new method for rapid degree of substitution and purity determination of chloroform-soluble cellulose esters, using 31P NMR. *Anal. Methods* **2010,** *2* (10), 1499-1505.
34. Blanchard, F. A.; Takahashi, I. T.; Alexander, H. C., Biodegradability of [14C]methylcellulose by activated sludge. *Appl. Environ. Microbiol.* **1976,** *32* (4), 557-560.
35. Wirick, M. G., A study of the enzymic degradation of CMC and other cellulose ethers. *Journal of Polymer Science Part A-1: Polymer Chemistry* **1968,** *6* (7), 1965-1974.
36. Wirick, M. G., Aerobic Biodegradation of Carboxymethylcellulose. *Journal (Water Pollution Control Federation)* **1974,** *46* (3), 512-521.
37. Rivard, C. J.; Adney, W. S.; Himmel, M. E.; Mitchell, D. J.; Vinzant, T. B.; Grohmann, K.; Moens, L.; Chum, H., Effects of natural polymer acetylation on the anaerobic bioconversion to methane and carbon dioxide. *Applied Biochemistry and Biotechnology* **1992,** *34* (1), 725-736.
38. Glasser, W. G.; McCartney, B. K.; Samaranayake, G., Cellulose derivatives with a low degree of substitution. 3. The biodegradability of cellulose esters using a simple enzyme assay. *Biotechnology Progress* **1994,** *10* (2), 214-219.
39. Béguin, P.; Aubert, J.-P., The biological degradation of cellulose. *FEMS Microbiology Reviews* **1994,** *13* (1), 25-58.
40. Goodwin, D. G.; Marsh, K. M.; Sosa, I. B.; Payne, J. B.; Gorham, J. M.; Bouwer, E. J.; Fairbrother, D. H., Interactions of Microorganisms with Polymer Nanocomposite Surfaces Containing Oxidized Carbon Nanotubes. *Environ. Sci. Technol.* **2015,** *49* (9), 5484-5492.
41. Zhao, X.; Cornish, K.; Vodovotz, Y., Narrowing the Gap for Bioplastic Use in Food Packaging: An Update. *Environ. Sci. Technol.* **2020**.
42. Chinaglia, S.; Tosin, M.; Degli-Innocenti, F., Biodegradation rate of biodegradable plastics at molecular level. *Polym. Degrad. Stab* **2018,** *147*, 237-244.
43. Tokiwa, Y.; Calabia, B. P.; Ugwu, C. U.; Aiba, S., Biodegradability of plastics. *Int J Mol Sci* **2009,** *10* (9), 3722-3742.

44. Artzi, L.; Bayer, E. A.; Moraïs, S., Cellulosomes: bacterial nanomachines for dismantling plant polysaccharides. *Nature Reviews Microbiology* **2017,** *15* (2), 83-95.
45. Fierobe, H.-P.; Bayer, E. A.; Tardif, C.; Czjzek, M.; Mechaly, A.; Bélaïch, A.; Lamed, R.; Shoham, Y.; Bélaïch, J.-P., Degradation of Cellulose Substrates by Cellulosome Chimeras: Substrate Targeting Versus Proximity Of Enzyme Components. *Journal of Biological Chemistry* **2002,** *277* (51), 49621-49630.
46. Wang, Z.-W.; Lee, S.-H.; Elkins, J. G.; Morrell-Falvey, J. L., Spatial and temporal dynamics of cellulose degradation and biofilm formation by Caldicellulosiruptor obsidiansis and Clostridium thermocellum. *AMB Express* **2011,** *1*, 30-30.
47. Ioelovich, M., Cellulose as a Nanostructured Polymer: A Short Review. *2008* **2008,** *3* (4), 16.
48. Ioelovich, M., Characterization of Various Kinds of Nanocellulose. In *Handbook of Nanocellulose and Cellulose Nanocomposites*, 2017; pp 51-100.
49. Wang, Y.; Wang, X.; Xie, Y.; Zhang, K., Functional nanomaterials through esterification of cellulose: a review of chemistry and application. *Cellulose* **2018,** *25* (7), 3703-3731.
50. Willberg-Keyriläinen, P.; Ropponen, J., Evaluation of esterification routes for long chain cellulose esters. *Heliyon* **2019,** *5* (11), e02898.
51. Berlioz, S.; Molina-Boisseau, S.; Nishiyama, Y.; Heux, L., Gas-Phase Surface Esterification of Cellulose Microfibrils and Whiskers. *Biomacromolecules* **2009,** *10* (8), 2144-2151.
52. Fumagalli, M.; Sanchez, F.; Boisseau, S. M.; Heux, L., Gas-phase esterification of cellulose nanocrystal aerogels for colloidal dispersion in apolar solvents. *Soft Matter* **2013,** *9* (47), 11309-11317.
53. David, G.; Gontard, N.; Guerin, D.; Heux, L.; Lecomte, J.; Molina-Boisseau, S.; Angellier-Coussy, H., Exploring the potential of gas-phase esterification to hydrophobize the surface of micrometric cellulose particles. *Eur. Polym. J.* **2019,** *115*, 138-146.
54. Eyley, S.; Thielemans, W., Surface modification of cellulose nanocrystals. *Nanoscale* **2014,** *6* (14), 7764-7779.
55. Peydecastaing, J.; Vaca-Garcia, C.; Borredon, E., Accurate determination of the degree of substitution of long chain cellulose esters. *Cellulose* **2008,** *16* (2), 289.
56. Söyler, Z.; Meier, M. A. R., Sustainable functionalization of cellulose and starch with diallyl carbonate in ionic liquids. *Green Chem.* **2017,** *19* (16), 3899-3907.
57. Zheng, Y.; Song, J.; Cheng, B.; Fang, X.; Yuan, Y., Preparation and flame retardancy of 3-(hydroxyphenylphosphinyl)-propanoic acid esters of cellulose and their fibers. *Cellulose* **2015,** *22* (1), 229-244.
58. Petersen, E. J.; Zhang, L.; Mattison, N. T.; O'Carroll, D. M.; Whelton, A. J.; Uddin, N.; Nguyen, T.; Huang, Q.; Henry, T. B.; Holbrook, R. D.; Chen, K. L., Potential Release Pathways, Environmental Fate, And Ecological Risks of Carbon Nanotubes. *Environ. Sci. Technol.* **2011,** *45* (23), 9837-9856.
59. Bai, Y.; Wu, F.; Lin, D.; Xing, B., Aqueous stabilization of carbon nanotubes: effects of surface oxidization and solution chemistry. *Environmental Science and Pollution Research* **2014,** *21* (6), 4358-4365.
60. Frank, B. P.; Sigmon, L. R.; Deline, A. R.; Lankone, R. S.; Gallagher, M. J.; Zhi, B.; Haynes, C. L.; Fairbrother, D. H., Photochemical Transformations of Carbon Dots in Aqueous Environments. *Environ. Sci. Technol.* **2020,** *54* (7), 4160-4170.

61. Zhang, B.; Liu, C.-y.; Liu, Y., A Novel One-Step Approach to Synthesize Fluorescent Carbon Nanoparticles. *European Journal of Inorganic Chemistry* **2010,** *2010* (28), 4411-4414.
62. Zhao, P.; Zhu, L., Dispersibility of carbon dots in aqueous and/or organic solvents. *Chemical Communications* **2018,** *54* (43), 5401-5406.
63. Nuncira, J.; Seara, L. M.; Sinisterra, R. D.; Caliman, V.; Silva, G. G., Long-term colloidal stability of graphene oxide aqueous nanofluids. *Fullerenes, Nanotubes and Carbon Nanostructures* **2019**, 1-11.
64. Qi, Y.; Xia, T.; Li, Y.; Duan, L.; Chen, W., Colloidal stability of reduced graphene oxide materials prepared using different reducing agents. *Environ. Sci.: Nano* **2016,** *3* (5), 1062-1071.
65. Willberg-Keyriläinen, P.; Orelma, H.; Ropponen, J., Injection Molding of Thermoplastic Cellulose Esters and Their Compatibility with Poly(Lactic Acid) and Polyethylene. *Materials (Basel)* **2018,** *11* (12), 2358.
66. Espino-Perez, E.; Domenek, S.; Belgacem, N.; Sillard, C.; Bras, J., Green Process for Chemical Functionalization of Nanocellulose with Carboxylic Acids. *Biomacromolecules* **2014,** *15* (12), 4551-4560.
67. Langley, L. A.; Villanueva, D. E.; Fairbrother, D. H., Quantification of Surface Oxides on Carbonaceous Materials. *Chemistry of Materials* **2006,** *18* (1), 169-178.
68. Loof, D.; Hiller, M.; Oschkinat, H.; Koschek, K., Quantitative and Qualitative Analysis of Surface Modified Cellulose Utilizing TGA-MS. *Materials* **2016,** *9* (6), 415.
69. Owen, W. F.; Stuckey, D. C.; Healy, J. B.; Young, L. Y.; McCarty, P. L., Bioassay for Monitoring Biochemical Methane Potential and Anaerobic Toxicity. *Water Res.* **1979,** *13* (6), 485-492.
70. Bohutskyi, P.; Betenbaugh, M. J.; Bouwer, E. J., The effects of alternative pretreatment strategies on anaerobic digestion and methane production from different algal strains. *Bioresource Technology* **2014,** *155*, 366-372.
71. Bohutskyi, P.; Keller, T. A.; Phan, D.; Parris, M. L.; Li, M.; Richardson, L.; Kopachevsky, A. M., Co-digestion of Wastewater-Grown Filamentous Algae With Sewage Sludge Improves Biomethane Production and Energy Balance Compared to Thermal, Chemical, or Thermochemical Pretreatments. *Frontiers in Energy Research* **2019,** *7* (47).
72. Li, P.; Li, W.; Sun, M.; Xu, X.; Zhang, B.; Sun, Y., Evaluation of Biochemical Methane Potential and Kinetics on the Anaerobic Digestion of Vegetable Crop Residues. *Energies* **2019,** *12* (1), 26.
73. Morales, G.; Llorente, I.; Montesinos, E.; Moragrega, C., A model for predicting Xanthomonas arboricola pv. pruni growth as a function of temperature. *PLOS ONE* **2017,** *12* (5), e0177583.
74. Jianlong, W.; Lujun, C.; Hanchang, S.; Yi, Q., Microbial degradation of phthalic acid esters under anaerobic digestion of sludge. *Chemosphere* **2000,** *41* (8), 1245-1248.
75. Homma, I.; Fukuzumi, H.; Saito, T.; Isogai, A., Effects of carboxyl-group counter-ions on biodegradation behaviors of TEMPO-oxidized cellulose fibers and nanofibril films. *Cellulose* **2013,** *20* (5), 2505-2515.
76. Homma, I.; Isogai, T.; Saito, T.; Isogai, A., Degradation of TEMPO-oxidized cellulose fibers and nanofibrils by crude cellulase. *Cellulose* **2013,** *20* (2), 795-805.

77. Liu, S.; Suflita, J. M., Anaerobic biodegradation of methyl esters by Acetobacterium woodii andEubacterium limosum. *Journal of Industrial Microbiology* **1994,** *13* (5), 321-327.
78. Haske-Cornelius, O.; Pellis, A.; Tegl, G.; Wurz, S.; Saake, B.; Ludwig, R.; Sebastian, A.; Nyanhongo, G. S.; Guebitz, G. M., Enzymatic Systems for Cellulose Acetate Degradation. *Catalysts* **2017,** *7* (10), 287.
79. Reese, E. T.; Siu, R. G. H.; Levinson, H. S., The biological degradation of soluble cellulose derivatives and its relationship to the mechanism of cellulose hydrolysis. *Journal of bacteriology* **1950,** *59* (4), 485-497.
80. White, G. F.; Russell, N. J.; Tidswell, E. C., Bacterial scission of ether bonds. *Microbiol Rev* **1996,** *60* (1), 216-232.
81. Lynd, L. R.; Weimer, P. J.; van Zyl, W. H.; Pretorius, I. S., Microbial cellulose utilization: fundamentals and biotechnology. *Microbiol Mol Biol Rev* **2002,** *66* (3), 506-577.
82. Cumpstey, I., Chemical modification of polysaccharides. *ISRN Org Chem* **2013,** *2013*, 417672-417672.
83. Heinze, T.; El Seoud, O. A.; Koschella, A., *Cellulose Derivatives: Synthesis, Structure, and Properties*. Springer International Publishing: Switzerland, 2018.
84. Huang, F.-Y., Thermal Properties and Thermal Degradation of Cellulose Tri-Stearate (CTs). *Polymers* **2012,** *4* (2), 1012-1024.
85. Vaca-Garcia, C.; Thiebaud, S.; Borredon, M. E.; Gozzelino, G., Cellulose esterification with fatty acids and acetic anhydride in lithium chloride/N,N-dimethylacetamide medium. *Journal of the American Oil Chemists' Society* **1998,** *75* (2), 315-319.
86. Okazaki, M.; Moo-Young, M., Kinetics of enzymatic hydrolysis of cellulose: Analytical description of a mechanistic model. *Biotechnology and Bioengineering* **1978,** *20* (5), 637-663.
87. Gaikwad, A., Effect of Particle Size on the Kinetics of Enzymatic Hydrolysis of Microcrystalline Cotton Cellulose: a Modeling and Simulation Study. *Applied Biochemistry and Biotechnology* **2019,** *187* (3), 800-816.
88. Baker, A. A.; Helbert, W.; Sugiyama, J.; Miles, M. J., New Insight into Cellulose Structure by Atomic Force Microscopy Shows the Iα Crystal Phase at Near-Atomic Resolution. *Biophys J* **2000,** *79* (2), 1139-1145.
89. Stern, J.; Moraïs, S.; Lamed, R.; Bayer, E. A., Adaptor Scaffoldins: An Original Strategy for Extended Designer Cellulosomes, Inspired from Nature. *mBio* **2016,** *7* (2), e00083-16.
90. Wang, Y.; Leng, L.; Islam, M. K.; Liu, F.; Lin, C. S. K.; Leu, S.-Y., Substrate-Related Factors Affecting Cellulosome-Induced Hydrolysis for Lignocellulose Valorization. *Int J Mol Sci* **2019,** *20* (13), 3354.
91. Aulin, C.; Ahola, S.; Josefsson, P.; Nishino, T.; Hirose, Y.; Österberg, M.; Wågberg, L., Nanoscale Cellulose Films with Different Crystallinities and Mesostructures—Their Surface Properties and Interaction with Water. *Langmuir* **2009,** *25* (13), 7675-7685.
92. Spence, K. L.; Venditti, R. A.; Rojas, O. J.; Habibi, Y.; Pawlak, J. J., The effect of chemical composition on microfibrillar cellulose films from wood pulps: water interactions and physical properties for packaging applications. *Cellulose* **2010,** *17* (4), 835-848.

93. Ahola, S.; Salmi, J.; Johansson, L. S.; Laine, J.; Österberg, M., Model Films from Native Cellulose Nanofibrils. Preparation, Swelling, and Surface Interactions. *Biomacromolecules* **2008,** *9* (4), 1273-1282.
94. Trache, D.; Tarchoun, A. F.; Derradji, M.; Hamidon, T. S.; Masruchin, N.; Brosse, N.; Hussin, M. H., Nanocellulose: From Fundamentals to Advanced Applications. *Frontiers in Chemistry* **2020,** *8* (392).
95. Wei, L.; Agarwal, U. P.; Hirth, K. C.; Matuana, L. M.; Sabo, R. C.; Stark, N. M., Chemical modification of nanocellulose with canola oil fatty acid methyl ester. *Carbohydr. Polym.* **2017,** *169*, 108-116.
96. Yu, H.; Yan, C.; Yao, J., Fully biodegradable food packaging materials based on functionalized cellulose nanocrystals/poly(3-hydroxybutyrate-co-3-hydroxyvalerate) nanocomposites. *RSC Adv.* **2014,** *4* (104), 59792-59802.
97. Ferreira, F. V.; Pinheiro, I. F.; Gouveia, R. F.; Thim, G. P.; Lona, L. M. F., Functionalized cellulose nanocrystals as reinforcement in biodegradable polymer nanocomposites. *Polym. Compos.* **2018,** *39* (S1), E9-E29.
98. Kargarzadeh, H.; Huang, J.; Lin, N.; Ahmad, I.; Mariano, M.; Dufresne, A.; Thomas, S.; Gałęski, A., Recent developments in nanocellulose-based biodegradable polymers, thermoplastic polymers, and porous nanocomposites. *Progress in Polymer Science* **2018,** *87*, 197-227.
99. Mishra, R. K.; Sabu, A.; Tiwari, S. K., Materials chemistry and the futurist eco-friendly applications of nanocellulose: Status and prospect. *Journal of Saudi Chemical Society* **2018,** *22* (8), 949-978.
100. Rodionova, G.; Lenes, M.; Eriksen, Ø.; Gregersen, Ø., Surface chemical modification of microfibrillated cellulose: improvement of barrier properties for packaging applications. *Cellulose* **2011,** *18* (1), 127-134.
101. Yagyu, H.; Ifuku, S.; Nogi, M., Acetylation of optically transparent cellulose nanopaper for high thermal and moisture resistance in a flexible device substrate. *Flexible and Printed Electronics* **2017,** *2* (1), 014003.
102. Yang, S.; Xie, Q.; Liu, X.; Wu, M.; Wang, S.; Song, X., Acetylation improves thermal stability and transmittance in FOLED substrates based on nanocellulose films. *RSC Adv.* **2018,** *8* (7), 3619-3625.
103. Barhoum, A.; Samyn, P.; Öhlund, T.; Dufresne, A., Review of recent research on flexible multifunctional nanopapers. *Nanoscale* **2017,** *9* (40), 15181-15205.
104. Mertaniemi, H.; Laukkanen, A.; Teirfolk, J.-E.; Ikkala, O.; Ras, R. H. A., Functionalized porous microparticles of nanofibrillated cellulose for biomimetic hierarchically structured superhydrophobic surfaces. *RSC Adv.* **2012,** *2* (7), 2882-2886.

Chapter 5. Photochemical Transformations of Carbon Dots in Aqueous Environments

Reproduced From

Frank, B. P.; Sigmon, L.; Deline, A.; Lankone, R. S.; Gallagher, M.; Zhi, B.; Haynes, C. L.; Fairbrother, D. H., Photochemical Transformations of Carbon Dots in Aqueous Environments. *Environ. Sci. Technol.* **2020**. *54* (7), 4160-4170

5.1 Abstract

The unique physicochemical and luminescent properties of carbon dots (CDs) have motivated research efforts towards their incorporation into commercial products. Increased use of CDs will inevitably lead to their release into the environment where their fate and persistence will be influenced by photochemical transformations, the nature of which is poorly understood. This knowledge gap motivated the present investigation of the effects of direct and indirect photolysis on citric and malic acid-based CDs. Our results indicate that natural sunlight will rapidly and non-destructively photobleach CDs into optically inactive carbon nanoparticles. We demonstrate that after photobleaching, $^{\bullet}$OH exposure degrades CDs in a two-step process that will span several decades in natural waters. The first step, occurring over several years of $^{\bullet}$OH exposure, involves depolymerization of the CD structure, characterized by volatilization of over 60% of nascent carbon atoms and the oxidation of nitrogen atoms into nitro groups. This is followed by a slower oxidation of residual carbon atoms first into carboxylic acids and then volatile carbon species, while

nitrogen atoms are oxidized into nitrate ions. Considered alongside related CD studies, our findings suggest that the environmental behavior of CDs will be strongly influenced by the molecular precursors used in their synthesis.

5.2 Introduction

Carbon dots (CDs) are an emerging class of colloidally stable carbon-based nanomaterials with high fluorescence quantum yields and tunable emission properties.[1] As an environmentally benign alternative to inorganic quantum dots that contain toxic metals, CDs have attracted great interest for their potential in sensing,[2-3] fuel cells,[4-5] drug delivery,[6-7] and bioimaging.[8-9] As a result, the quantity of CDs entering aquatic environments will inevitably increase during the production, use, and disposal of CD-enabled products. While CDs are of similar size to other carbon-based nanomaterials such as fullerenes, they are likely to exhibit different environmental behavior due to the high surface charge imparted by the functional groups (e.g., carboxylic acid, amine, and amide groups) embedded within their structure.[10]

To date, research on the environmental behavior of CDs has largely focused on their colloidal stability,[11-14] transport,[15] and toxicity[16-17] in environmental media. Bayati et al. investigated the effect of ionic strength, pH, and natural organic matter (NOM) on the aggregation of glycerol-based CDs and aminated CDs, finding both species largely stable at the upper bound of environmental ionic strength (i.e., 10 mmol/L NaCl and $CaCl_2$) and across a pH range of 3-11.[12] Li et al. showed that graphene CDs were colloidally stable in solutions of NaCl, KCl, and $MgCl_2$ with an ionic strength of >1000 mM, but were prone to aggregation in solutions containing 1 mM $CaCl_2$.[13] Liu et al. determined that hydrothermally synthesized sodium citrate-based CDs were stable to homoaggregation in

environmentally relevant pH and ionic strength conditions, but this stability could be perturbed by low pH (pH < 3) and high ionic strength conditions (> 30 mM NaCl).[11] The high degree of colloidal stability exhibited by CDs translates into high transport capacity, as exhibited by Kamrani et al., in which citric acid-based CDs readily eluted through quartz media at environmentally relevant conditions and were only partially retained in the column even at extremely high ionic strength and low pH.[15] As a result of their colloidal stability and transport properties, CDs are likely to be present in the water column for significant periods of time. Consequently, their interactions with sunlight are likely to play an important role in determining their fate and persistence in aquatic environments.

The primary photolytic processes acting on CDs in the environment will be direct irradiation by natural sunlight and indirect photolysis via exposure to reactive oxygen species (ROS) of which hydroxyl radicals (•OH) produced by the interaction of sunlight with naturally occurring species (e.g., natural organic matter (NOM) or nitrate/nitrite)[18-20] are typically the most reactive, and as such are often used experimentally to simulate the indirect photolysis of environmental contaminants.[21-25] While the effects of direct and indirect photolysis on other carbon nanomaterials (e.g., CNTs,[26-27] GO,[24, 28] fullerenes[29-30]) have been the subject of significant research, the unique chemical and fluorescent properties of CDs are likely to impart different photochemical behavior. A recent study by Chen et al. identified that CDs synthesized via a hydrothermal route using citric acid and urea rapidly degraded into low molecular weight compounds and could be mineralized to carbon dioxide under both UVB irradiation and natural sunlight exposure.[31] These transformations occurred over the course of 2 h UVB or 8 h natural sunlight exposure and were attributed to processes involving ROS formed by the irradiation of the CDs

themselves, with •OH being the dominant radical species. The rapid photodegradation and mineralization of these CDs suggest they will not persist once they are released into the environment. However, these results cannot necessarily be generalized to all CDs, as an enormous array of precursors and methods (e.g. hydrothermal, isolation from organic waste, thermal decomposition, microwave)[2-3] are currently being used in their synthesis, the effect of which on the chemical, physical, and photochemical properties of CDs remains unknown.

CDs produced from small organic acid molecules, via microwave irradiation, are some of the most widely studied for consumer and research applications due to the low cost and ease of "bottom-up" synthesis.[32] Therefore it is important to develop a mechanistic understanding of their behavior in aquatic environments. In this study, the effects of direct and indirect photolysis on microwave synthesized citric acid-based CDs (CACDs) and malic acid-based CDs (MACDs) were investigated. CDs were exposed to natural sunlight for up to 6 weeks, while the effects of indirect photolysis were simulated by exposing CD solutions to •OH radicals generated by the photolysis of H_2O_2 under UV light. Total carbon analysis (TC), total nitrogen analysis (TN), and ion chromatography (IC) were used to identify the changes in carbon content, nitrogen content, and nitrogen speciation over time. Changes to optical properties were examined using photoluminescence (PL) spectroscopy. The physicochemical transformations of CDs were characterized by a combination of attenuated total reflectance Fourier transform infrared spectroscopy (ATR-FTIR), ^{1}H- and ^{13}C-nuclear magnetic resonance spectroscopy (NMR), and X-ray photoelectron spectroscopy (XPS). Using this suite of analytical techniques, we have identified both the

photochemical transformations and the kinetics of such transformations that these CDs will undergo upon release into natural waters.

5.3 Materials and Methods

Additional details of synthetic procedures, characterization methods, photochemical exposures, and •OH radical quantification are included in the SI. For all suspensions prepared, the initial concentration of CDs was first determined via the recorded mass of dry CD powder added to a known volume of water.

5.3.1 Materials

All chemicals were purchased from Sigma-Aldrich and used without further purification. Milli-Q® water (18.2 Ω, Millipore, USA) was used to prepare all aqueous solutions.

5.3.2 Synthesis of CDs

CDs were prepared using a bottom-up microwave-assisted pyrolysis method as described by Zhi et al.[33] Two types of CDs were synthesized, using ethylene diamine (EDA) and either citric or malic acid as precursors to form CACDs and MACDs, respectively.

5.3.3 Characterization of CDs

CDs were characterized initially and after exposure to the effects of direct and indirect photolysis using a combination of TC, TN, IC, charged aerosol detection (CAD), ATR-FTIR, XPS, ^{1}H- and ^{13}C-NMR, and PL. Transmission electron microscopy (TEM) and UV-Vis spectroscopy were used to further characterize the as-synthesized CDs.

5.3.4 *Exposure to Natural Sunlight*

Solar irradiation experiments were conducted by adding suspensions of CDs in Milli-Q water to borosilicate glass test-tubes (16 mm outer diameter x 125 mm, Corning, USA).

Sample test-tubes were sealed with PTFE-lined caps, and placed outside on a rooftop in Baltimore, MD (39° 19' W, 76° 37' N). Equivalent dark controls were prepared by wrapping glass test-tubes in aluminum foil, and CD-free controls were prepared identically without CDs. At time points ranging from 0 to 6 weeks, samples and controls were retrieved sacrificially for analysis. Unless otherwise specified, natural sunlight exposures were performed under ambient conditions with no sparging of the samples. Therefore, dissolved oxygen levels should be representative of those encountered in natural waters.

5.3.5 *Exposure to 254nm Irradiation*

254nm irradiation experiments were performed on 100 mg/L CACD and MACD solutions in quartz test tubes. Samples and aluminum foil-wrapped dark controls were exposed to 254nm light emitted by 16 lamps (RPR 100, Southern New England Ultraviolet Company, Branford, CT, $1.5x10^{17}$ photons/s) for 0-14 days. Samples were quantified for CD concentration before and after irradiation using TOC and CAD measurements.

5.3.6 *Exposure to •OH Radicals*

Suspensions of MACDs and CACDs were prepared and added to quartz test tubes, sealed with an aluminum foil cap, and vented via a syringe tip. Samples were exposed to •OH radicals generated by the photolysis of H_2O_2 in a photochemical reactor equipped with 16 low pressure mercury lamps emitting 300 nm light (RPR 100, Southern New England Ultraviolet Company, Branford, CT, approx. 1.5×10^{17} photons/s). •OH exposure studies performed for TC, TN, ATR-FTIR, and XPS were all carried out at concentrations at or below 350 mg/L CD. ^{13}C-NMR experiments required a higher CD concentration (1.7×10^{4} mg/L) to achieve reasonable signal-to-noise ratio.

5.3.7 Determination of ˙OH Radical Dose

The total dose of ˙OH generated by the photodegradation of H_2O_2 as well as the equivalent environmental exposure time in natural surface waters (Table 9.1) were determined using methods described by Lankone et al.[34] Briefly, the steady-state ˙OH concentration in solution generated during the photolysis of H_2O_2 was determined via monitoring the rate of salicylic acid (i.e., a probe molecule) decomposition from an initial concentration of 0.07 mM. With this methodology, the steady-state concentration of ˙OH with CDs present in solution could be determined with a standard error of less than 10%. Duration of ˙OH exposure was also recorded, enabling a molar*time ˙OH dose to be determined. This dose (M*min) was then related to an equivalent duration of exposure to ˙OH in the natural environment, wherein the steady-state concentration ranges between 10^{-15}-10^{-17} M.[19, 24, 35] For example, a ˙OH concentration of 10^{-15} M, results in a monthly ˙OH dose of 10^{-15} M * 2.2×10^4 min/month = 2.2×10^{-11} $\frac{M*min}{month}$. Importantly, control studies found that CD concentrations used in this study (≤ 319 mg/L) had no effect on the steady-state ˙OH concentration (Figure 9.1).

5.3.8 CD Settling Tests

Suspensions of CACDs (15 mg/L) were allowed to settle for 1 week in either MilliQ water or a mixture of NaCl, KCl, and $CaCl_2$ (4 mM Ca^{+2}, 13 mM Cl^-, 0.3 mM Na^+, 5 mM K^+) at pH 7 or 8. Supernatant was analyzed for suspended CDs using PL.

5.4 Results and Discussion

5.4.1 Initial CD Characterization

The as-synthesized CACDs were characterized by an emission peak at 480 nm and an absorbance below 400 nm, with a peak centered at 350 nm (Figure 9.2a). As-synthesized

MACDs emitted most strongly at 470 nm with a broad absorbance below 400 nm and a weak peak around 350 nm (Figure 9.2b). TEM images (Figure 9.2c and 9.2d) of the as-synthesized CACDs and MACDs reveal spherical nanoparticles with sub-10 nm diameters. ATR-FTIR of CACDs and MACDs (Figure 9.3a and 9.3b) both exhibited broad IR features at 3280 cm^{-1}, 3085 cm^{-1}, and 2927 cm^{-1} corresponding to N-H, O-H, and C-H stretching modes, respectively.[36-37] For CACDs, features at 1700 cm^{-1} (carboxyl) and 1646 cm^{-1} (amide) are attributed to carbonyl (C=O) stretches,[38-39] while the feature at 1547 cm^{-1} is indicative of an N-H bend in an amide group (O=C-NH);[37, 40] MACDs share the same carbonyl bands, however the N-H bend occurs at 1527 cm^{-1}.[37, 40-41] The C (1s) envelope of the native CDs, as measured by XPS, contained contributions from C-C and C-H species centered at 285 eV, with a higher binding energy shoulder at ~ 288 eV due to the presence of more oxidized carbon atoms (e.g. amide and carboxyl groups; Figure 9.4 and 9.5). It should be noted that due to their small size (i.e., diameters < 10 nm), XPS spectra reflect the entire CD nanoparticle with respect to composition and chemical bonding environment.

5.4.2 Effects of Direct Photolysis

Upon entering aquatic environments, CDs will immediately experience the effects of direct photolysis due to their absorbance within the solar power distribution reaching the earth's surface (Figure 9.6a). Photoluminescence (PL) spectroscopy was used to monitor the fluorescent properties of CDs after exposure to sunlight and artificial indoor light, while changes in composition and chemical bonding were evaluated using a combination of TC/TN, XPS, ATR-FTIR, and ^{1}H-NMR.

CACDs exposed to natural sunlight experienced rapid photobleaching, as their fluorescence disappeared after 12 h of irradiation, observed both spectroscopically (Figure 5.1a, 9.7) and visually (Figure 9.8). This low photostability is in stark contrast to the persistence of fluorescence (Figure 9.9a) observed under artificial laboratory lighting. This difference in photostability is attributed to the differences in overlap between the absorbance spectrum of the CDs and the respective emission spectra from natural sunlight (solar irradiance, Figure 9.6a) and fluorescent bulbs (Figure 9.9b). Thus, it is likely that the

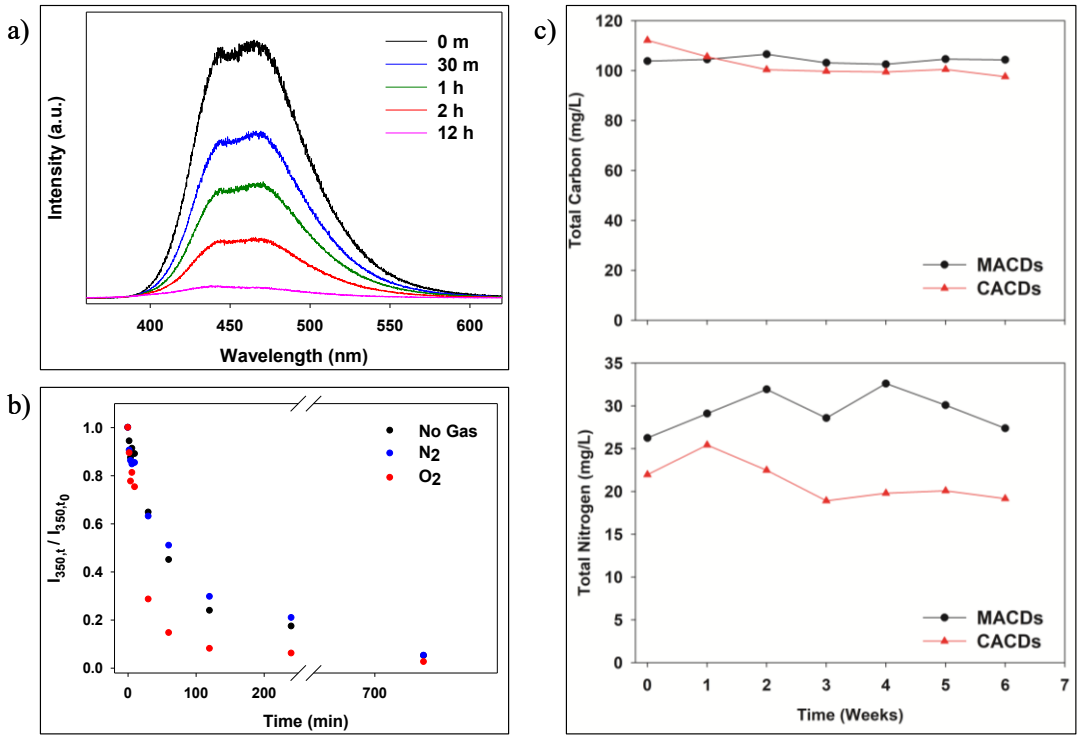

Figure 5.1 Effect of natural sunlight on CDs. a) Emission profiles of CACDs after exposure to 0 min (black), 30 min. (blue), 1 hr. (green), 2 hr. (red), and 12 hr. (pink) of natural sunlight. b) Emission of CACDs at 350 nm (black) compared to emission of CACDs after sparging with N_2 (blue) or O_2 (red) gas as a function of exposure to natural sunlight. c) Total carbon (top) and total nitrogen (bottom) concentration of CACDs (red triangles) and MACDs (black circles) after exposure to 0-6 weeks of natural sunlight in non-sparged water.

< 400 nm component of natural sunlight drives photobleaching of CDs in the environment. The loss of fluorescence induced by exposure to sunlight was also found to be more rapid in solutions initially saturated with O_2, but unaffected in solutions sparged with N_2 (Figure 5.1b). This behavior indicates that photobleaching in natural sunlight likely involves reactions with ROS formed via the presence of dissolved oxygen in solution.

Despite the rapid loss of fluorescence in CD solutions (i.e., < 12 h), exposure of up to 6 weeks of sunlight had no observable effect on the carbon or nitrogen content as

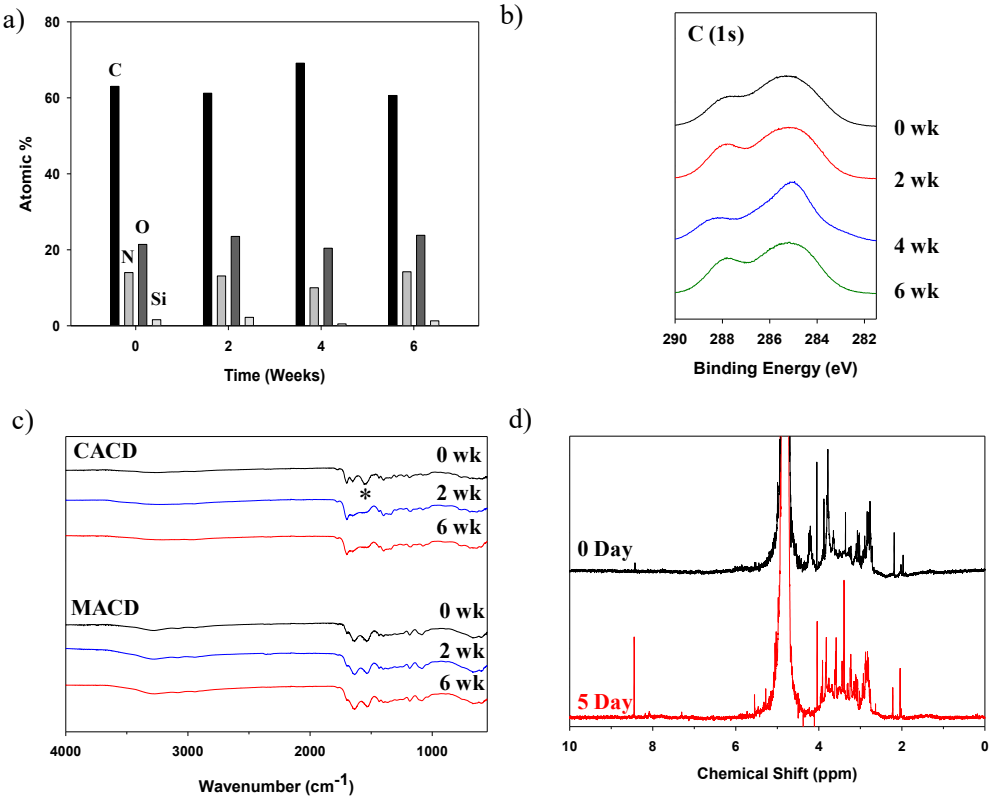

Figure 5.2 Effect of natural sunlight on CD structure. a) Atomic composition of lyophilized CACDs after natural sunlight exposure for 0-6 wk as determined with XPS. b) XPS C (1s) regions of lyophilized parent CACDs after 0 (black), 2 (red), 4 (blue), and 6 (green) weeks of natural sunlight exposure. (c) ATR-FTIR spectra of CACDs (top) and MACDs (bottom) exposed to natural sunlight for 0, 2, and 6 weeks, with (*) indicating the N-H bend at 1547 cm^{-1}. (d) ^{1}H-NMR spectra of CACDs (black) and CACDs exposed to 5 days of natural sunlight (red).

exhibited by TC and TN (Figure 5.1c). Similarly, XPS data revealed that the composition within the CACDs (Figure 5.2a) and MACDs (Figure 9.10) as well as the chemical bonding environment within both CACDs (Figures 5.2b, 9.4) and MACDs (Figure 9.5) also remained constant over the course of the 6-week exposure. ATR-FTIR spectra of CACDs and MACDs (Figure 5.2c) were largely unchanged after 6 weeks of exposure to sunlight, though for CACDs, loss of intensity at 1547 cm^{-1} was observed during the first two weeks of outdoor exposure, suggesting photobleaching could be driven through proton abstraction from the amide groups initially present in the CD structure, though not extensively enough to meaningfully change the CD composition.

^{1}H-NMR spectra of CACDs acquired before and after photobleaching also indicated only minor chemical changes to proton bonding environments (Figure 5.2d). As-synthesized CACDs featured clusters of ^{1}H-NMR peaks in several diagnostic regions: 1.8 ppm to 2.5 ppm, 2.5 ppm to 4.5 ppm, and at 8.4 ppm, indicative of protons in the α- or β-position to carbonyl or amide groups,[42-44] protons bound to or in the α-position to oxidized carbon species (i.e., alcohol, ether, ester, carbonyl),[42, 45] and non-exchangeable amide protons[46-48] respectively. In contrast, no carboxylic acid protons were observed due to exchange of these acidic protons in the (D_2O) solvent. The photobleached CACDs exhibited a largely similar ^{1}H-NMR spectrum to the parent CACDs. The only changes observed were the loss of peak intensity at 4.2 ppm and the increase in intensity of the peak at 8.4 ppm, likely indicating some degradation of the amide groups initially present in the CDs.

Collectively, these findings indicate that the principle effect of natural sunlight on organic acid-based CDs immediately after entering an aquatic environment is rapid (i.e., <

12 h) photobleaching (Figure 5.1a) in a process modulated by the relative level of dissolved oxygen therein (Figure 5.1b). While the initial rate of photobleaching may vary to some degree dependent on the concentration of dissolved oxygen available to generate ROS, the complete photobleaching of CDs is expected to occur in all aqueous environments, irrespective of dissolved oxygen content (Figure 5.1b). Findings also indicate that the CD structure and composition will remain largely unchanged during photobleaching, supported by mass-recovery studies which demonstrated that 101.4 % +/- 2.1 % of CD mass is recovered after 21 d of natural sunlight exposure (see Chapter 9 for details).

Interestingly, these findings contrast with a study published by Chen et al., in which it was reported that citric acid/urea CDs were rapidly volatilized in totality after 8 h of natural sunlight exposure due to extensive structural decomposition driven by CD-produced $^{\bullet}OH$.[31] We posit one possibility for the contrasting photochemical behavior observed between these studies is that the different structural features present in the two different types of CDs, arising by virtue of the different precursors used (e.g., urea features a carbonyl group which EDA lacks), strongly regulate the persistence of CD photoactivity, the overall phototransformation pathway, and resultant kinetics of sunlight driven degradation. While we did not observe degradation or volatilization for CDs exposed to sunlight in the present study, the photobleaching and comparatively small changes that did occur to the CDs indeed could arise from similar reactions between CD-generated ROS and the CDs themselves[31] (e.g., $^{\bullet}OH$-driven proton abstraction)[49] as suggested by the increase in photobleaching rate with increased dissolved oxygen content.

Importantly, because as-synthesized CDs remained colloidally stable in the presence of divalent cations known to destabilize other nanomaterials (Figure 9.11), the

lack of significant changes to the physicochemical properties of CDs after photobleaching suggests that they will remain colloidally stable in natural environments after irradiation by natural sunlight. Specifically, spectroscopic measurements (i.e., XPS, ATR-FTIR) of the photobleached CDs indicate the retention of negatively charged oxygen-containing functional groups (i.e., carboxyl, hydroxyl) which are responsible for the electrostatic repulsion between CDs, an effect which is responsible for the colloidal stability of carbon dots[50-54] as well as other carbon nanomaterials (CNTs,[55-57] graphene[58-60]) in aqueous environments. Structural degradation of CDs by direct photolysis was only observed under 254 nm irradiation analogous to that used in wastewater treatment plants, as quantified using TOC and CAD (Figure 9.12), but this wavelength of light does not reach the surface of the Earth.[61-63] Consequently, photobleached CDs can be expected to remain stable for long periods in the water column where they will be subject to reactions with ROS (primarily $^{\bullet}OH$) generated by the irradiation of common constituents of natural water (NOM, NO_3^-).[18-20]

5.4.3 Effects of Indirect Photolysis

To assess the effects of indirect photolysis on CDs, CACD and MACD suspensions were exposed to $^{\bullet}OH$ produced via 300 nm irradiation of H_2O_2. 300 nm irradiation of CDs in the absence of H_2O_2 photobleached CDs without any measurable structural changes. A previous analytical study enabled us to determine the Molar × time dose of $^{\bullet}OH$ generated during H_2O_2 photolysis (Table 9.1), permitting comparison to the equivalent dose of $^{\bullet}OH$ CDs would experience in the natural environment. The kinetics of CD photodegradation by $^{\bullet}OH$ was assessed using TC and TN, while reaction products were identified through a combination of IC, ATR-FTIR, ^{13}C-NMR, and XPS.

TC data indicated that during •OH exposure, both CACDs and MACDs reacted in two well defined temporal stages. First, ~ 60% of carbon atoms initially present in both CD types were lost after a 1.4×10^{-9} M*min exposure to •OH (Figure 5.3a). Following this rapid and extensive loss of carbon atoms, the residual carbon-containing species were significantly less susceptible to further •OH-mediated degradation during the second stage of the reaction as the •OH dose increased beyond 1.4×10^{-9} M*min •OH. At an •OH dose of

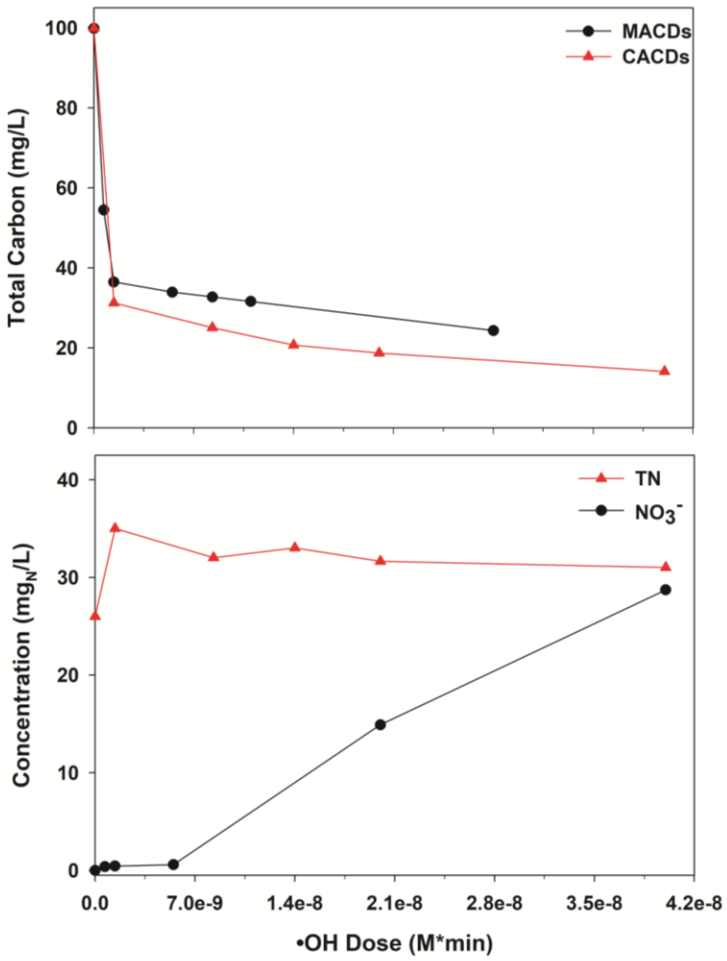

Figure 5.3 Degradation of CDs by •OH. (a) Total carbon concentration of MACD (black) and CACD (red) as a function of •OH dose. (b) Total nitrogen (red) and nitrate concentration (black) of CACD solution in terms of mg/L nitrogen as a function of •OH dose.

2.8×10^{-8} M*min, the carbon content only decreased by an additional 10% for MACDs, while a dose of 4.0×10^{-8} M*min •OH only decreased the carbon content by 15% for CACDs.

Complementary TN analysis (Figure 5.3b) revealed that the total nitrogen content was relatively insensitive to •OH exposure (•OH doses of 4.0×10^{-8} M*min), in marked contrast to the considerable loss of carbon (compare Figures 5.3a and 5.3b). Although the total nitrogen content remained essentially constant during •OH exposure, nitrogen speciation evolved. Specifically, the production of nitrate was observed for •OH doses in excess of 5.5×10^{-9} M*min (Figure 5.3b) and increased steadily until all CD nitrogen atoms were converted into nitrate ions. The constant TN content coupled with the steady increase

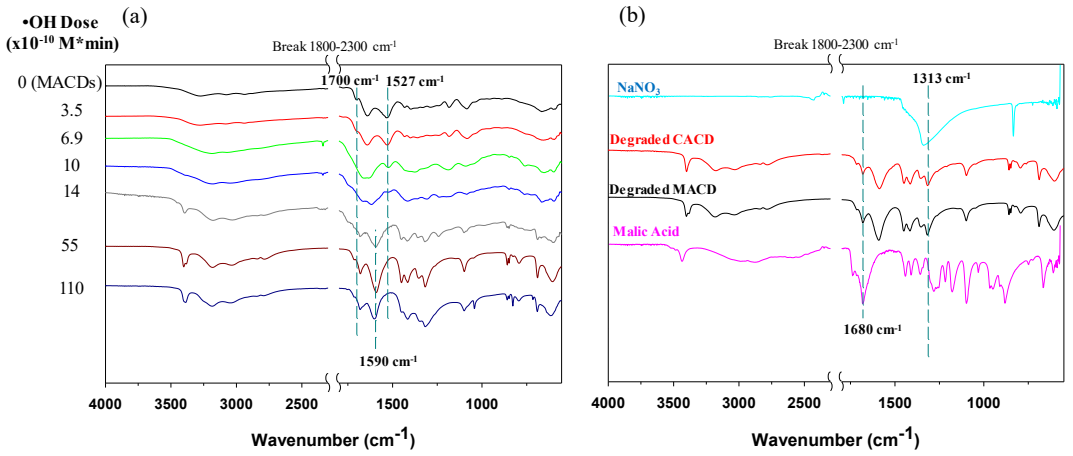

Figure 5.4 ATR-FTIR of lyophilized MACDs after exposure to different •OH doses. (a) MACDs (black) after exposure to 3.5×10^{-10} M*min (red), 6.9×10^{-10} M*min (light green), 1.0×10^{-9} M*min (blue), 1.4×10^{-9} M*min (grey), 5.5×10^{-9} M*min (dark red), and 1.1×10^{-8} M*min (dark blue) •OH. Insufficient masses of photoproducts were recovered for CDs reacted with •OH doses > 1.1×10^{-8} M*min, precluding ATR-FTIR analysis. Dotted lines mark carboxyl C=O (stretch, 1700 cm^{-1}), N-H (bend, 1527 cm^{-1}), and nitro (stretch, 1590 cm^{-1}) modes. (b) Degradation products of CACDs (red) and MACDs (black) after exposure to 5.5×10^{-9} M*min •OH shown in comparison to malic acid (MA, pink) and sodium nitrate (blue). Dotted lines mark carboxyl C=O (stretch, 1680 cm^{-1}) and nitrate ν_3 (stretch, 1313 cm^{-1}) modes.

in nitrate concentration in solution indicates that over time the •OH-driven degradation of CDs will produce nitrate ions.

ATR-FTIR spectra shown in Figure 5.4a provide spectroscopic evidence of two distinct phases in the reaction of MACDs with •OH. The first phase of degradation was initiated upon exposure to an •OH dose of 6.9×10^{-10} M*min, which resulted in a decrease in intensity of the amide N-H bending mode at 1527 cm^{-1}, and a red-shift of the (carboxylic) C=O stretch to 1680 cm^{-1} indicative of a change in the chemical bonding environment in the MACDs. The simultaneous diminishment and transformation of these features indicates that •OH-mediated decomposition of CDs involves a cleavage of the amide moieties initially present in the CD backbone. After •OH exposure increased from 6.9×10^{-10} M*min to 1.4×10^{-9} M*min, the amide groups initially present in the CDs had been oxidized into nitro groups(i.e., NO_2), as evidenced by the simultaneous loss of the O=C-NH bend at 1527 cm^{-1} and the appearance of the ν_4/ν_1 stretches of nitro groups at 1590 cm^{-1} and 1414 cm^{-1}, respectively.[64] Additionally, the appearance of peaks at ~ 3400 cm^{-1} and 1100 cm^{-1} indicate the formation of hydroxyl groups in the photoproducts[38, 65] whose sharpness and peak positions are very similar to the hydroxyl features present in malic acid (Figure 5.4b). By a •OH dose of 1.4×10^{-9} M*min, the previous carbonyl feature at 1700 cm^{-1} had shifted and is now centered on 1680 cm^{-1} , indicating that the carbonyl species are now in a more highly hydrogen-bound chemical environment (i.e., small carboxylic acids, such as malic acid). As the •OH dose increases, new bands at 1313 cm^{-1}/831 cm^{-1} also emerge which can be assigned to and the ν_3 stretch (E')/ν_2 bend (A_2'') of nitrate ions.[66] Collectively, the formation of these oxidized nitrogen groups and the similarity of degraded CD spectra to malic acid strongly suggests that CDs were depolymerized in the presence

of •OH through the cleavage of their initial amide bonds to form nitro groups and malic acid photofragments.

The second phase of degradation shown by ATR-FTIR was observed for •OH doses beyond 1.4×10^{-9} M*min, and is defined as being the period of exposure during which the spectra remained relatively unchanged with increasing •OH dose, aside from an increase in nitrate and nitro peak intensities. ATR-FTIR spectra observed for the solid phase (i.e., lyophilized) species produced by MACDs exposed to •OH doses in excess of 5.5×10^{-9} M*min continued to exhibit peaks similar to those of sodium nitrate and the solid malic acid precursor (Figure 5.4b, common peaks: free O-H at 3400 cm^{-1}, carboxy C=O at 1680 cm^{-1}, and O-H deformation at 1100 cm^{-1}). Furthermore, Figure 5.4b demonstrates sustained

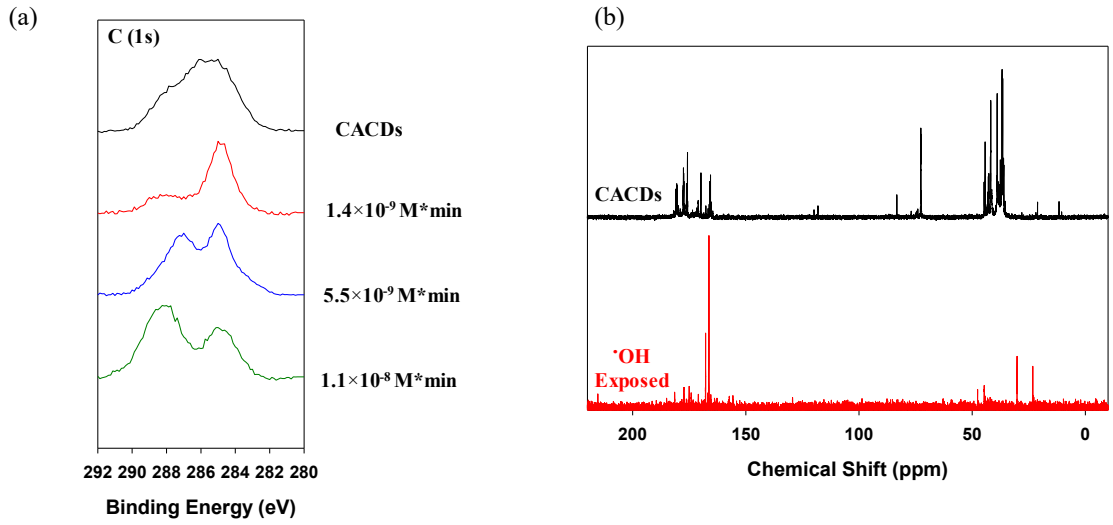

Figure 5.5 a) C (1s) region of lyophilized CACDs (black) after exposure to a dose of 1.4×10^{-9} M*min (red), 5.5×10^{-9} M*min (blue), and 1.1×10^{-8} M*min (green) •OH. Insufficient masses of photoproducts were recovered for CDs reacted with •OH doses > 1.1×10^{-8} M*min, precluding XPS analysis. b) ^{13}C-NMR of photobleached CACDs in D_2O before (black) and after (red) exposure to 5.7×10^{-8} M*min •OH. At the significantly higher CD concentration required for NMR (1.7×10^{4} mg/L), this •OH dose leads to the loss of 60% of carbon from solution as determined with TC.

exposure of both MACDs and CACDs to •OH in excess of 5.5×10^{-10} M*min resulted in the formation of near identical photoproducts as suggested by the similarity of their spectra. It should be noted that XPS and ATR-FTIR analysis was not possible for •OH doses above 1.1×10^{-8} M*min, as the mass loss due to volatilization of carbon (as shown by TC) precluded sufficient sample recovery.

XPS spectra of CACDs exposed to •OH also indicate a two-phase degradation process. During the first period of degradation, •OH exposure up to 1.4×10^{-9} M*min •OH resulted in a loss of higher binding energy features (i.e., carbonyl carbon), and the C (1s) region was dominated by the C-C/C-H species at 285 eV with only a small shoulder at 288 eV (Figure 5.5a). The CDs then entered the second phase of •OH exposure from doses of 5.5×10^{-9} M*min to $1.1*10^{-8}$ M*min, at which point the carbonyl feature reemerged in the C (1s) region at 288 eV. XPS analysis also revealed that exposure to •OH produced an overall decrease in the carbon content and a small increase in the nitrogen content of the non-volatile photoproducts (Figure 9.13). Specifically, CACDs were initially composed of 55% carbon and 15% nitrogen, but exposure to $1.1*10^{-8}$ M*min •OH led to products that contained 35% carbon and 20% nitrogen. This enrichment of nitrogen with increasing •OH exposure as measured by XPS is qualitatively consistent with the trends observed by TC/TN in that it further indicates that carbon was lost and volatilized from the CDs, while nitrogen atoms remain associated with the CD photoproduct.

The ^{13}C-NMR of CACDs exposed to •OH also indicated extensive degradation to the CDs. Photobleached CACDs (Figure 5.5b) prior to •OH exposure contained various carbon functional groups including carboxylic acids/amides (160-180 ppm)[67], alcohols/ethers (70-90 ppm),[68-69] and both substituted (i.e., branched) and primary alkane

carbons centered around 30-50 ppm and 10-30 ppm, respectively.[70-71] After a •OH dose sufficient to cause a loss of 60% TC, ^{13}C-NMR was performed again to assess the CDs nearing the end of the first phase of degradation (see Figure 5.3). The resultant ^{13}C-NMR indicates that the CDs degraded through the loss of substituted/branched alkane groups (30 ppm to 50 ppm). This suggests that the crosslinked network initially present in the CDs was degraded during •OH exposure. Interestingly, the growth of one peak around 165 ppm, likely a carboxyl species, agrees with the increase in such species as shown with ATR-FTIR and XPS spectra.

To contextualize these results in terms of the equivalent environmental •OH exposure, we applied a methodology developed by Lankone et al. which allowed the integrated •OH dose to be benchmarked to the maximum •OH dose a sample would experience during one month of exposure in sunlit waters (10^{-15} M * 2.2×10^{4} min/month = 2.2×10^{-11} $\frac{M*min}{month}$). For example, exposure to a solution of H_2O_2 at an initial concentration of 100 mM, as it is photolyzed for 4 hours results in CD exposure of 1.4×10^{-9} M*min; this dose corresponds to an equivalent environmental exposure of approximately 64 months ($\frac{1.4*10^{-9}M*min}{2.2*10^{-11}\frac{M*min}{month}}$). In this study, relations to environmental timescale were done under the assumption that CDs consistently experience the maximum •OH dose (i.e., 10^{-15} M) in the environment, though calculations based on the full range of $[•OH]_{ss}$ are reported in Chapter 9 (Table 9.1). Using these calculations and assuming an environmental steady state •OH concentration of 10^{-15} M, we can discuss CD photodegradation by indirect photolysis in terms of the equivalent environmental timescale.

The two-step degradation process first observed with TC and TN data (Figure 5.3a and 5.3b) can now be interpreted to indicate that the period of initial CD degradation in the presence of •OH occurs over approximately 64 +/- 5 months of indirect photolysis in sunlit waters. During this time, as indicated by ATR-FTIR and XPS, the CDs are depolymerized via the cleavage of amide groups, resulting in the formation of nitro groups and carboxylic acid species. Additionally, TC indicates that 60% of carbon atoms are lost from solution, most likely as volatile species, similar to the reactions of •OH with GO which evolve CO_2 as an end product.[24] We note the rate of loss of the amide feature at 1527 cm^{-1} closely corresponds to the rate at which the initial carbon volatilization occurs (compare TC and ATR-FTIR data in Figures 5.3a and 5.4a, respectively), suggesting that the first step in the degradation of CDs by •OH is hydrogen abstraction from N-H and/or C-H groups,[49, 72-73] leading to the degradation of amide linkages. Additional evidence of this depolymerization is seen in ^{13}C-NMR data via the loss of C=C (120 ppm) and substituted/branched alkane character (30-50 ppm), representing the degradation of crosslinked character within the CDs, resulting in the primary alkane signature which persists in the resultant photoproducts (10-30 ppm) which are also carboxylated as seen in both ATR-FTIR (1680 cm^{-1}; Figure 5.4a) and ^{13}C-NMR (165 ppm; Figure 5.5b). The redshift of the carboxyl C=O stretch coupled with the persistence of primary alkanes seen in ^{13}C-NMR provides evidence for the evolution of low molecular weight carboxylic acids after depolymerization which are less sterically hindered than in the parent CD, thus able to participate in more extensive hydrogen bonding.[38]

In contrast to the significant loss/volatilization of carbon atoms, the TN and ATR-FTIR data reveal that during the first 64 +/- 5 months of environmental exposure, there is

little to no change in the total nitrogen content, although the nitrogen species initially present in the CDs have been converted/oxidized into nitro groups by •OH. This oxidation occurs over the same •OH dose as the loss in amide character in ATR-FTIR (1646 cm^{-1}), suggesting that nitrogen atoms involved in amide linkages in the parent CDs are oxidized into nitro groups after cleavage during indirect photolysis.

Following the initial •OH-mediated depolymerization of the CD structure, the second phase of indirect photolysis is observed for cumulative •OH doses in excess of approximately $1.4*10^{-9}$ M*min, or beyond the first 64 +/- 5 months of environmental exposure, and is characterized by a much slower decrease in carbon content. During this phase, residual carbon atoms are further oxidized by •OH, leading to a significant increase in the concentration of highly oxidized photoproducts structurally similar to the dicarboxylic acids used in the original CD synthesis (e.g. malic acid as shown with ATR-FTIR in Figure 5.4b), and related carboxylic acids (e.g. glutaric acid, Figure 9.14). The formation of carboxylated carbon species is consistent with the increase in concentration of the C(1s) shoulder above 286 eV in XPS. Because both CACDs and MACDs generated photoproducts with similar spectroscopic signatures, this degradation pathway is likely generalizable to CDs synthesized from EDA and carboxylic acid precursors.

When the changes in composition and structure are considered together, our results indicate that during this second stage of indirect photolysis, residual carbon atoms are oxidized by •OH to carboxyl groups which then serve as precursors for the formation of volatile species[73] such as CO_2[24] or acetone.[74] Continued •OH-mediated oxidation of previously formed nitro groups leads to the evolution of nitrate ions[75] as indicated by the IC and ATR-FTIR data (Figures 5.3b and 5.4a). Thus, extrapolation of these trends to

sustained (maximum) •OH exposure in the natural environment, in excess of the 43 years of equivalent exposure simulated in laboratory studies, indicates CDs would eventually degrade such that all carbon atoms will be volatilized while nitrogen atoms are stoichiometrically converted into nitrate ions.

The reason for the two distinct temporal regimes of carbon loss, however, remains somewhat unclear. One possible explanation is that the more recalcitrant carbon atoms seen in the second phase of the process are associated with fragments containing carbon-nitrogen bonds residual from reactions of •OH with the parent CDs. This interpretation is supported by IC data which clearly shows that the formation of nitrate ions from the CDs requires a dose of •OH in excess of 5.5×10^{-9} M*min. The evolution of nitrate ions from nitro groups requires C-N bond cleavage, a limiting prerequisite step in the volatilization of these carbon atoms compared to those in other bonding environments.

5.5 Environmental Implications

Due to their highly charged surface and small size, CDs are colloidally stable in the water column at which point microbial interactions only play a minor role in their degradation (Figure 9.15).[11-14] Thus, the effects of both direct and indirect photolysis will play an important role in determining the fate and persistence of CDs in aquatic environments. In contrast to their photostability under illumination in laboratory settings (i.e., under fluorescent lighting), the citric and malic acid-based CDs investigated in this study will rapidly photobleach after only a few hours of direct photolysis by natural sunlight, likely precluding the use of these particular CDs as sensors in outdoor settings. Once the CACDs and MACDs have photobleached, the resultant carbon nanoparticles exhibit similar physicochemical properties to the parent CDs, suggesting a high degree of

colloidal stability. Consequently, these photobleached CDs will persist for extended periods of time in the environment while being difficult to monitor or track due their poor light scattering properties and lack of fluorescent signature.

Ultimately, photobleached CDs will be degraded by indirect photolysis via reactions with ROS, primarily $^{\bullet}OH$ produced by exposure of NOM and other constituents of water (e.g., metal ions, nitrate, dissolved oxygen) to natural sunlight.[20] Based on the relation to environmental timescale which was used (assuming exposure to the maximum environmental $[^{\bullet}OH]_{ss}$),[34] the first stage of this indirect photolysis will occur over the course of approximately 5-6 years of environmental exposure in sunlit waters, resulting in depolymerization of the CD via cleavage of its amide bonds and the oxidation of a majority of the carbon atoms in the CDs into volatile carbon species (e.g., CO_2 and acetone). Over the same time span, nitrogen atoms will be oxidized into nitro groups bound to fragments of the parent CDs. Environmental exposure of the residual photoproducts will lead to the formation of carboxylic acid species similar to the organic acids used in the CD synthesis (e.g. malic acid). These carboxylic acids will serve as precursors to the production of volatile carbon species, a process which will continue until all carbon atoms in the CDs are ultimately mineralized (timespan of several decades based on TC trend). In contrast, nitrogen atoms in the CDs will be stoichiometrically oxidized from nitro groups into nitrate ions as indicated by IC data (half-life roughly 75 years). Given the projected lifetime and colloidal stability of photobleached CDs and their photoproducts throughout this prolonged photodegradation process, future studies identifying the environmental impact of these various intermediate species will be prudent.

A comparison of the results from this study with previous studies highlights the diversity of photochemical transformations experienced by carbon-based nanomaterials in the environment. For example, GO rapidly photofragments in natural sunlight as a result of the reactivity of the highly strained epoxide groups that exist on its surface, leading to the formation of reduced graphene oxide species (rGO) and the evolution of CO_2.[28] Conversely, oxidized carbon nanotubes (CNTs) do not fragment upon exposure to sunlight or ROS, but rather undergo photodecarboxylation, causing them to lose surface charge which leads to sedimentation.[26] Aggregates of fullerenes are prone to ROS-driven degradation by sunlight, leading to disaggregation, the formation of dissolved organic species, and eventual mineralization.[29] However, under simulated sunlight[30] and UVA light conditions,[76] fullerenes showed a higher level of resistance to mineralization, only exhibiting surface oxidation. These observations clearly indicate that the structure and physicochemical properties of carbon nanomaterials play a determinant role in regulating their photochemical reactions in the environment. With this in mind, it is not unreasonable that the photochemical transformations of CDs will be sensitive to their chemical structure and composition.

Although the phototransformations of the microwave-synthesized CACDs and MACDs using ethylene diamine outlined in this study parallel one another and were structurally stable for 6 weeks in natural sunlight, it has been reported that CACDs synthesized via a hydrothermal route using urea are completely mineralized in sunlight after less than one day at concentrations similar to the ones used in the present study (50 mg/L).[31] Thus, the intrinsic chemical and physical characteristics of CDs imparted via their precursors appear to dictate their photostability. As such, it will be important to identify

the different phototransformations of CDs synthesized with a wide variety of precursors and synthetic pathways. Additionally, a detailed understanding of the mechanisms and influential factors which dictate CD photobleaching will be needed to improve photostability if CDs are to be used as environmental sensors and tracers in outdoor settings.

5.6 Acknowledgements

This work was supported by National Science Foundation under the Center for Sustainable Nanotechnology, CHE-1503408.The CSN is part of the Centers for Chemical Innovation

Program. LRS is supported by the National Science Foundation Graduate Research Fellowship Program under Grant No. DGE-1746891. The authors would like to thank Steven Chow for assistance with ion chromatography measurements, the Materials Characterization Facility at Johns Hopkins University, and the U.S. Department of Energy (DOE)/NREL/ALLIANCE for the solar irradiance data as well as Casey Smith for assistance with figures. TEM characterization was carried out in the Characterization Facility, University of Minnesota, which receives partial support from the MRSEC program (DMR-1420013).

5.7 Appendix 4 Summary

Chapter 9 highlights detailed calculation of $^{\bullet}OH$ dose and relation to environmental timescale (Table 9.1, Figure 9.1) and experimental procedures for CD synthesis and characterization (PL, UV-Vis, TEM, ATR-FTIR, XPS, TC, TN, IC, ^{1}H- and ^{13}C-NMR; Figures 9.2, 9.3, 9.4, 9.5). CD absorption compared to solar emission spectrum (Figure 9.6) and emission spectrum of fluorescent bulbs (Figure 9.9), effects of photobleaching after

exposure to natural sunlight (Figure 9.7, 9.8, 9.10) along with stability studies of CDs in the presence of divalent cations (Figure 9.11). Figure outlining the loss of CD from solution under 254 nm irradiation as quantified with TOC and CAD (Figure 9.12). Additional figures illustrating change in XPS composition of CDs after •OH exposure (Figure 9.13) are included and ATR-FTIR comparing degraded MACDs to glutaric acid (Figure 9.14).

5.8 References

1. Yan, F.; Sun, Z.; Zhang, H.; Sun, X.; Jiang, Y.; Bai, Z., The fluorescence mechanism of carbon dots, and methods for tuning their emission color: a review. *Microchimica Acta* **2019,** *186* (8), 583.
2. Liu, M. L.; Chen, B. B.; Li, C. M.; Huang, C. Z., Carbon dots: synthesis, formation mechanism, fluorescence origin and sensing applications. *Green Chem.* **2019,** *21* (3), 449-471.
3. Huang, S.; Li, W.; Han, P.; Zhou, X.; Cheng, J.; Wen, H.; Xue, W., Carbon quantum dots: synthesis, properties, and sensing applications as a potential clinical analytical method. *Anal. Methods* **2019,** *11* (17), 2240-2258.
4. Zhang, Z.; Zhang, J.; Chen, N.; Qu, L., Graphene quantum dots: an emerging material for energy-related applications and beyond. *Energ. Environ. Sci.* **2012,** *5* (10), 8869-8890.
5. Fei, H.; Ye, R.; Ye, G.; Gong, Y.; Peng, Z.; Fan, X.; Samuel, E. L. G.; Ajayan, P. M.; Tour, J. M., Boron- and nitrogen-doped graphene quantum dots/graphene hybrid nanoplatelets as efficient electrocatalysts for oxygen reduction. *ACS Nano* **2014,** *8* (10), 10837-10843.
6. Hettiarachchi, S. D.; Graham, R. M.; Mintz, K. J.; Zhou, Y.; Vanni, S.; Peng, Z.; Leblanc, R. M., Triple conjugated carbon dots as a nano-drug delivery model for glioblastoma brain tumors. *Nanoscale* **2019,** *11* (13), 6192-6205.
7. Zhang, Z.; Lei, Y.; Yang, X.; Shi, N.; Geng, L.; Wang, S.; Zhang, J.; Shi, S., High drug-loading system of hollow carbon dots–doxorubicin: preparation, in vitro release and pH-targeted research. *J. Mater. Chem. B* **2019,** *7* (13), 2130-2137.
8. Zhi, B.; Cui, Y.; Wang, S.; Frank, B. P.; Williams, D. N.; Brown, R. P.; Melby, E. S.; Hamers, R. J.; Rosenzweig, Z.; Fairbrother, D. H.; Orr, G.; Haynes, C. L., Malic acid carbon dots: from super-resolution live-cell imaging to highly efficient separation. *ACS Nano* **2018,** *12* (6), 5741-5752.
9. Boakye-Yiadom, K. O.; Kesse, S.; Opoku-Damoah, Y.; Filli, M. S.; Aquib, M.; Joelle, M. M. B.; Farooq, M. A.; Mavlyanova, R.; Raza, F.; Bavi, R.; Wang, B., Carbon dots: Applications in bioimaging and theranostics. *Int. J. Pharm.* **2019,** *564*, 308-317.
10. Sciortino, A.; Cannizzo, A.; Messina, F., Carbon nanodots: a review—from the current understanding of the fundamental photophysics to the full control of the optical response. *C — Journal of Carbon Research* **2018,** *4* (4), 67.

11. Liu, X.; Li, J.; Huang, Y.; Wang, X.; Zhang, X.; Wang, X., Adsorption, aggregation, and deposition behaviors of carbon dots on minerals. *Environ. Sci. Technol.* **2017,** *51* (11), 6156-6164.
12. Bayati, M.; Dai, J.; Zambrana, A.; Rees, C.; Fidalgo de Cortalezzi, M., Effect of water chemistry on the aggregation and photoluminescence behavior of carbon dots. *J. Environ. Sci.* **2018,** *65*, 223-235.
13. Li, Q.; Chen, B.; Xing, B., Aggregation kinetics and self-assembly mechanisms of graphene quantum dots in aqueous solutions: cooperative effects of pH and electrolytes. *Environ. Sci. Technol.* **2017,** *51* (3), 1364-1376.
14. Dager, A.; Uchida, T.; Maekawa, T.; Tachibana, M., Synthesis and characterization of mono-disperse carbon quantum dots from fennel seeds: photoluminescence analysis using machine learning. *Sci. Rep.* **2019,** *9* (1), 14004.
15. Kamrani, S.; Rezaei, M.; Kord, M.; Baalousha, M., Transport and retention of carbon dots (CDs) in saturated and unsaturated porous media: role of ionic strength, pH, and collector grain size. *Water Res.* **2018,** *133*, 338-347.
16. Havrdova, M.; Hola, K.; Skopalik, J.; Tomankova, K.; Petr, M.; Cepe, K.; Polakova, K.; Tucek, J.; Bourlinos, A. B.; Zboril, R., Toxicity of carbon dots – effect of surface functionalization on the cell viability, reactive oxygen species generation and cell cycle. *Carbon* **2016,** *99*, 238-248.
17. Tabish, T. A.; Scotton, C. J.; Ferguson, D. C. J.; Lin, L.; Veen, A. v. d.; Lowry, S.; Ali, M.; Jabeen, F.; Ali, M.; Winyard, P. G.; Zhang, S., Biocompatibility and toxicity of graphene quantum dots for potential application in photodynamic therapy. *Nanomedicine* **2018,** *13* (15), 1923-1937.
18. Zepp, R. G.; Hoigne, J.; Bader, H., Nitrate-induced photooxidation of trace organic chemicals in water. *Environ. Sci. Technol.* **1987,** *21* (5), 443-450.
19. Page, S. E.; Logan, J. R.; Cory, R. M.; McNeill, K., Evidence for dissolved organic matter as the primary source and sink of photochemically produced hydroxyl radical in arctic surface waters. *Environ. Sci. Proc. Imp.* **2014,** *16* (4), 807-822.
20. Gligorovski, S.; Strekowski, R.; Barbati, S.; Vione, D., Environmental implications of hydroxyl radicals (•OH). *Chem. Rev.* **2015,** *115* (24), 13051-13092.
21. Miller, P. L.; Chin, Y.-P., Indirect Photolysis Promoted by Natural and Engineered Wetland Water Constituents: Processes Leading to Alachlor Degradation. *Environ. Sci. Technol.* **2005,** *39* (12), 4454-4462.
22. Lam, M. W.; Mabury, S. A., Photodegradation of the pharmaceuticals atorvastatin, carbamazepine, levofloxacin, and sulfamethoxazole in natural waters. *Aquatic Sciences* **2005,** *67* (2), 177-188.
23. Vione, D.; Maddigapu, P. R.; De Laurentiis, E.; Minella, M.; Pazzi, M.; Maurino, V.; Minero, C.; Kouras, S.; Richard, C., Modelling the photochemical fate of ibuprofen in surface waters. *Water Res.* **2011,** *45* (20), 6725-6736.
24. Hou, W.-C.; Henderson, W. M.; Chowdhury, I.; Goodwin, D. G.; Chang, X.; Martin, S.; Fairbrother, D. H.; Bouchard, D.; Zepp, R. G., The contribution of indirect photolysis to the degradation of graphene oxide in sunlight. *Carbon* **2016,** *110*, 426-437.
25. Zepp, R. G.; Faust, B. C.; Hoigne, J., Hydroxyl radical formation in aqueous reactions (pH 3-8) of iron(II) with hydrogen peroxide: the photo-Fenton reaction. *Environ. Sci. Technol.* **1992,** *26* (2), 313-319.

26. Chen, C.-Y.; Jafvert, C. T., Photoreactivity of carboxylated single-walled carbon nanotubes in sunlight: reactive oxygen species production in water. *Environ. Sci. Technol.* **2010,** *44* (17), 6674-6679.
27. Hou, W.-C.; BeigzadehMilani, S.; Jafvert, C. T.; Zepp, R. G., Photoreactivity of unfunctionalized single-wall carbon nanotubes involving hydroxyl radical: chiral dependency and surface coating effect. *Environ. Sci. Technol.* **2014,** *48* (7), 3875-3882.
28. Hou, W.-C.; Chowdhury, I.; Goodwin, D. G.; Henderson, W. M.; Fairbrother, D. H.; Bouchard, D.; Zepp, R. G., Photochemical transformation of graphene oxide in sunlight. *Environ. Sci. Technol.* **2015,** *49* (6), 3435-3443.
29. Hou, W.-C.; Jafvert, C. T., Photochemical transformation of aqueous C60 clusters in sunlight. *Environ. Sci. Technol.* **2009,** *43* (2), 362-367.
30. Sanchís, J.; Aminot, Y.; Abad, E.; Jha, A. N.; Readman, J. W.; Farré, M., Transformation of C60 fullerene aggregates suspended and weathered under realistic environmental conditions. *Carbon* **2018,** *128*, 54-62.
31. Chen, X.; Fang, G.; Liu, C.; Dionysiou, D. D.; Wang, X.; Zhu, C.; Wang, Y.; Gao, J.; Zhou, D., Cotransformation of carbon dots and contaminant under light in aqueous solutions: a mechanistic study. *Environ. Sci. Technol.* **2019,** *53* (11), 6235-6244.
32. de Medeiros, T. V.; Manioudakis, J.; Noun, F.; Macairan, J.-R.; Victoria, F.; Naccache, R., Microwave-assisted synthesis of carbon dots and their applications. *J. Mater. Chem. C* **2019,** *7* (24), 7175-7195.
33. Zhi, B.; Gallagher, M. J.; Frank, B. P.; Lyons, T. Y.; Qiu, T. A.; Da, J.; Mensch, A. C.; Hamers, R. J.; Rosenzweig, Z.; Fairbrother, D. H.; Haynes, C. L., Investigation of Phosphorous Doping Effects on Polymeric Carbon Dots: Fluorescence, Photostability, and Environmental Impact. *Carbon* **2018,** *129*, 438-449.
34. Lankone, R. S.; Barclay, M.; Deline, A. R.; Fairbrother, D. H., Quantifying hydroxyl radical concentrations and total dose via principle component analysis of UV-Vis Spectroscopy. *Anal. Methods* **Submitted**.
35. Haag, W. R.; Hoigné, J., Photo-sensitized oxidation in natural water via .OH radicals. *Chemosphere* **1985,** *14* (11), 1659-1671.
36. Schneider, J.; Reckmeier, C. J.; Xiong, Y.; von Seckendorff, M.; Susha, A. S.; Kasák, P.; Rogach, A. L., Molecular fluorescence in citric acid-based carbon dots. *J. Phys. Chem. C* **2017,** *121* (3), 2014-2022.
37. Yuan, H.; Yu, J.; Feng, S.; Gong, Y., Highly photoluminescent pH-independent nitrogen-doped carbon dots for sensitive and selective sensing of p-nitrophenol. *RSC Adv.* **2016,** *6* (18), 15192-15200.
38. Max, J.-J.; Chapados, C., Infrared spectroscopy of aqueous carboxylic acids: malic acid. *J. Phys. Chem. A* **2002,** *106* (27), 6452-6461.
39. Dousseau, F.; Pezolet, M., Determination of the secondary structure content of proteins in aqueous solutions from their amide I and amide II infrared bands. Comparison between classical and partial least-squares methods. *Biochemistry* **1990,** *29* (37), 8771-8779.
40. Liu, W.; Li, C.; Ren, Y.; Sun, X.; Pan, W.; Li, Y.; Wang, J.; Wang, W., Carbon dots: surface engineering and applications. *J. Mater. Chem. B* **2016,** *4* (35), 5772-5788.
41. Colthup, N. B., Spectra-structure correlations in the infra-red region. *J. Opt. Soc. Am.* **1950,** *40* (6), 397-400.

42. Wishart, D. S.; Case, D. A., [1] - Use of Chemical Shifts in Macromolecular Structure Determination. In *Methods in Enzymology*, James, T. L.; Dötsch, V.; Schmitz, U., Eds. Academic Press: 2002; Vol. 338, pp 3-34.
43. Fouda, A. S.; Elmorsi, M. A.; Shaban, S. M.; Fayed, T.; Azazy, O., Evaluation of N-(3-(dimethyl hexadecyl ammonio)propyl) palmitamide bromide as cationic surfactant corrosion inhibitor for API N80 steel in acidic environment. *Egypt. J. Pet.* **2018,** *27* (4), 683-694.
44. Shaban, S. M., N-(3-(Dimethyl benzyl ammonio)propyl)alkanamide chloride derivatives as corrosion inhibitors for mild steel in 1 M HCl solution: experimental and theoretical investigation. *RSC Adv.* **2016,** *6* (46), 39784-39800.
45. Szilágyi, L.; Jardetzky, O., α-Proton chemical shifts and secondary structure in proteins. *Journal of Magnetic Resonance (1969)* **1989,** *83* (3), 441-449.
46. Blundell, C. D.; DeAngelis, P. L.; Day, A. J.; Almond, A., Use of 15N-NMR to resolve molecular details in isotopically-enriched carbohydrates: sequence-specific observations in hyaluronan oligomers up to decasaccharides. *Glycobiology* **2004,** *14* (11), 999-1009.
47. Blundell, Charles D.; Deangelis, Paul L.; Almond, A., Hyaluronan: the absence of amide–carboxylate hydrogen bonds and the chain conformation in aqueous solution are incompatible with stable secondary and tertiary structure models. *Biochem J.* **2006,** *396* (3), 487-498.
48. Hill, S. A.; Benito-Alifonso, D.; Davis, S. A.; Morgan, D. J.; Berry, M.; Galan, M. C., Practical three-minute synthesis of acid-coated fluorescent carbon dots with tuneable core structure. *Sci. Rep.* **2018,** *8* (1), 12234.
49. Stadtman, E. R., Oxidation of free amino acid and amino acid residues in proteins by radiolysis and by metal-catalyzed reactions. *Annu. Rev. Biochem.* **1993,** *62* (1), 797-821.
50. Zhao, P.; Zhu, L., Dispersibility of carbon dots in aqueous and/or organic solvents. *Chemical Communications* **2018,** *54* (43), 5401-5406.
51. Zhang, B.; Liu, C.-y.; Liu, Y., A Novel One-Step Approach to Synthesize Fluorescent Carbon Nanoparticles. *European Journal of Inorganic Chemistry* **2010,** *2010* (28), 4411-4414.
52. Xu, M.; Xu, S.; Yang, Z.; Shu, M.; He, G.; Huang, D.; Zhang, L.; Li, L.; Cui, D.; Zhang, Y., Hydrophilic and blue fluorescent N-doped carbon dots from tartaric acid and various alkylol amines under microwave irradiation. *Nanoscale* **2015,** *7* (38), 15915-15923.
53. Wang, W.; Damm, C.; Walter, J.; Nacken, T. J.; Peukert, W., Photobleaching and stabilization of carbon nanodots produced by solvothermal synthesis. *Physical Chemistry Chemical Physics* **2016,** *18* (1), 466-475.
54. Fiuza, T.; Gomide, G.; Campos, A. F. C.; Messina, F.; Depeyrot, J., On the Colloidal Stability of Nitrogen-Rich Carbon Nanodots Aqueous Dispersions. *C — Journal of Carbon Research* **2019,** *5* (4), 74.
55. Smith, B.; Wepasnick, K.; Schrote, K. E.; Cho, H.-H.; Ball, W. P.; Fairbrother, D. H., Influence of Surface Oxides on the Colloidal Stability of Multi-Walled Carbon Nanotubes: A Structure−Property Relationship. *Langmuir* **2009,** *25* (17), 9767-9776.
56. Zhang, L.; Wang, M.; Fang, J.; Yang, K.; Lin, D., The effect of oxidation on physicochemical properties and aqueous stabilization of multiwalled carbon nanotubes:

comparison of multiple analysis methods. *Science China Chemistry* **2016,** *59* (11), 1498-1507.
57. Bai, Y.; Wu, F.; Lin, D.; Xing, B., Aqueous stabilization of carbon nanotubes: effects of surface oxidization and solution chemistry. *Environmental Science and Pollution Research* **2014,** *21* (6), 4358-4365.
58. Hadadian, M.; Goharshadi, E. K.; Youssefi, A., Electrical conductivity, thermal conductivity, and rheological properties of graphene oxide-based nanofluids. *Journal of Nanoparticle Research* **2014,** *16* (12), 2788.
59. Nuncira, J.; Seara, L. M.; Sinisterra, R. D.; Caliman, V.; Silva, G. G., Long-term colloidal stability of graphene oxide aqueous nanofluids. *Fullerenes, Nanotubes and Carbon Nanostructures* **2019**, 1-11.
60. Qi, Y.; Xia, T.; Li, Y.; Duan, L.; Chen, W., Colloidal stability of reduced graphene oxide materials prepared using different reducing agents. *Environ. Sci.: Nano* **2016,** *3* (5), 1062-1071.
61. Bitter, J. L.; Yang, J.; Beigzadeh Milani, S.; Jafvert, C. T.; Fairbrother, D. H., Transformations of oxidized multiwalled carbon nanotubes exposed to UVC (254 nm) irradiation. *Environ. Sci.: Nano* **2014,** *1* (4), 324-337.
62. Gilmore, K. R.; Luong, H. V., Improved Method for Measuring Total Dissolved Solids. *Analytical Letters* **2016,** *49* (11), 1772-1782.
63. Leckner, B., The spectral distribution of solar radiation at the earth's surface—elements of a model. *Solar Energy* **1978,** *20* (2), 143-150.
64. Iogansen, A. V.; Litovchenko, G. D., The characteristic bands of the stretching vibrations of the nitro group in infrared absorption. *J. Appl. Spectrosc.* **1965,** *3* (6), 404-411.
65. Barańska, H.; Kuduk-Jaworska, J.; Szostak, R.; Romaniewska, A., Vibrational spectra of racemic and enantiomeric malic acids. *J. Raman Spectrosc.* **2003,** *34* (1), 68-76.
66. Brooker, M. H.; Irish, D. E., Vibrational frequency assignments of isotopically different forms of nitrate ion in ionic nitrate crystals. *Can. J. Chem.* **1970,** *48* (8), 1198-1201.
67. Howarth, O. W.; Lilley, D. M. J., Carbon-13-NMR of peptides and proteins. *Prog. Nucl. Mag. Res. Sp.* **1978,** *12* (1), 1-40.
68. Katsuraya, K.; Hatanaka, K.; Matsuzaki, K.; Amiya, S., Assignment of finely resolved 13C NMR spectra of poly(vinyl alcohol). *Polymer* **2001,** *42* (24), 9855-9858.
69. Ding, S.; Hong, Y.-W.; Chen, C.-Y.; Chang, N.-C., One and two dimensional 1H and 13C high resolution NMR investigation of lariat ethers and their alkali metal ionic complexes: A more tangible evidence for the presence of less common C–H···O hydrogen bonds. *Biophys. Chem.* **2006,** *121* (2), 75-83.
70. Gilbert, A.; Yamada, K.; Yoshida, N., Exploration of intramolecular 13C isotope distribution in long chain n-alkanes (C11–C31) using isotopic 13C NMR. *Org. Geochem.* **2013,** *62*, 56-61.
71. Ritter, W.; Hull, W.; Cantow, H. J., Determination of the most stable conformers of branched alkanes by 13C-NMR spectroscopy at very low temperatures. *Tetrahedron Lett.* **1978,** *19* (34), 3093-3096.
72. Doan, H. Q.; Davis, A. C.; Francisco, J. S., Primary steps in the reaction of OH radicals with peptide systems: perspective from a study of model amides. *J. Phys. Chem. A* **2010,** *114* (16), 5342-5357.

73. Vel Leitner, N. K.; Berger, P.; Legube, B., Oxidation of amino groups by hydroxyl radicals in relation to the oxidation degree of the α-carbon. *Environ. Sci. Technol.* **2002,** *36* (14), 3083-3089.
74. Quici, N.; Morgada, M. E.; Gettar, R. T.; Bolte, M.; Litter, M. I., Photocatalytic degradation of citric acid under different conditions: TiO2 heterogeneous photocatalysis against homogeneous photolytic processes promoted by Fe(III) and H2O2. *Appl. Catal. B-Environ.* **2007,** *71* (3), 117-124.
75. Pelizzetti, E.; Minero, C.; Piccinini, P.; Vincenti, M., Phototransformations of nitrogen containing organic compounds over irradiated semiconductor metal oxides: Nitrobenzene and Atrazine over TiO2 and ZnO. *Coordin. Chem. Rev.* **1993,** *125* (1), 183-193.
76. Hwang, Y. S.; Li, Q., Characterizing photochemical transformation of aqueous nC60 under environmentally relevant conditions. *Environ. Sci. Technol.* **2010,** *44* (8), 3008-3013.

Chapter 6. Appendix 1—Influence of Polymer Type and Carbon Nanotube Properties on Carbon Nanotube/Polymer Nanocomposite Biodegradation

Reproduced from

Frank, B.P.; Goodwin, D.G., Jr.; Bohutskyi, P.; Lu, X.; Kuwama, L.; Bouwer, E. J.; Fairbrother, D. H., Influence of Polymer Type and Carbon Nanotube Properties on Carbon Nanotube/Polymer Nanocomposite Biodegradation. *Science of the Total Environment*. **Submitted 2020**.

6.1 Appendix Summary

The Appendix contains detailed information regarding carbon nanotube polymer nanocomposite (CNT/PNC) preparation. Additionally, biomethane potential (BMP) media preparation and sampling procedure is detailed. Figures report additional data including kinetic model parameters and complete fits for each CNT loading and PNC set. Plots including full error bars for O-MWCNT/PCL samples reported in Figure 2.1 as well as a replicate data set of the same samples are reported. Finally, additional stereo microscopy images and Raman data are reported for 5 % w/w MWCNT/PHA and O-MWCNT/PHA PNCs to illustrate the reproducibility of the difference in dispersion offered by each CNT type in the same polymer matrix.

6.2 O-MWCNT Preparation

Pristine MWCNTs were oxidized by adding 1 g of MWCNTs (Nanocyl NC7000, outer diameter 9.5 nm, 1.5 μm length, 90% purity) to 0.3 M HNO_3 and refluxing for 5 h at 110 °C. The resulting O-MWCNTs were washed with deionized water continuously until

the pH of the filtrate reached 7 and then dried in an oven (Forced Convection Oven, Felisa Ovens, Zapopan, Jalisco, Mexico) overnight at 80 °C. The O-MWCNTs had an oxygen content of 4.1% as determined by X-ray photoelectron spectroscopy (XPS) (PHI 5600 XPS, 58.7 eV pass energy, 0.125 eV/step, Mg Kα X-rays) and quantitative analysis in CasaXPS software (Teignmouth, UK).

6.3 O- MWCNT/PCL Nanocomposite Preparation

O-MWCNT/PCL nanocomposites were prepared by adding 16 mg of ethyl cellulose (EC) (48.0 - 49.5% (w/w) ethoxyl basis, Lot # BCBG4792V, Sigma-Aldrich) and a particular mass of CNTs to a 50 mL Erlenmeyer flask containing 40 mL of dichloromethane (DCM, >99.8%, Sigma-Aldrich). EC was used for CNT stabilization in DCM. O-MWCNTs in EC were sonicated in an ice water bath for 1 h to optimize dispersion quality. To prepare casting suspensions, 400 mg of poly-ε-caprolactone (PCL) was then added to each CNT suspension and sonicated for an additional 3 h. During all steps of sonication, the ice water bath was replenished every 1 h to minimize solvent volatilization and improve dispersion quality. A solvent resistant, disposable syringe was then used to distribute the PCL and CNT/PCL nanocomposite casting suspensions in 5 mL aliquots to aluminum dishes (44 mm diameter, 12.5 mm height, Fisherbrand, VWR, Radnor, PA). PCL and CNT/PCL nanocomposite coupons formed after solvent evaporation at room temperature overnight. The next day, PCL and CNT/PCL nanocomposites were soaked in a deionized water bath to help separate the coupons from their aluminum dishes. PCL and CNT/PCL nanocomposites were then trimmed around their outer edges to a uniform shape and size (~30 mm in diameter) with a mass of 27 ± 3 mg. O-MWCNT/PCL nanocomposites coupons with 0.1, 0.5, and 2 % w/w O-MWCNTs were prepared and all contained 5% w/w

EC. Neat PCL films containing 5% w/w EC without CNT fillers were also prepared as controls. All steps of sonication during preparation of the CNT/PCL casting solution used a Branson 1510 ultrasonicator bath containing ice water. CNT suspensions were also capped tightly to prevent solvent volatilization. As shown in our previous study, thermogravimetric analysis revealed that this solvent casting method of CNT/PCL nanocomposite preparation did not trap any measurable amount of solvent in the PCL.[1] The crystallinity of the polymer, a property that can affect biodegradation, has also been shown to remain constant with increasing CNT loading in PCL with the CNT loadings used in this study.[1]

6.4 O-MWCNT/PHA and Pristine MWCNT/PHA Nanocomposite Preparation

Both oxidized and pristine MWCNTs were prepared with PHA. The same O-MWCNTs used with PCL were also used with PHA. The pristine MWCNTs used were from NanoLab Inc. (PD15L5-20, Lot # 20130820, outer diameter 15 ± 5 nm, length 5-20 μm). The metal contents for both batches of CNTs were measured previously using X-ray photoelectron spectroscopy: both CNT types had below 0.1% w/w Fe and O-MWCNTs had 0.8% Al. To prepare each PHA nanocomposite a particular mass of O-MWCNTs or pristine MWCNTs and 80 mg EC were added to 160 mL chloroform (CHCl3, HPLC grade, ≥99.9%, Sigma-Aldrich). A CNT suspension stabilized by EC was then produced by sonication using a Branson 1510 ultrasonicator bath operating at 70 watts for 3 h. During this process, the suspension was capped tightly to prevent solvent volatilization. After the CNT/EC suspension was prepared, 1600 mg of polyhydroxyalkanoates (PHA, 95-100%, Metabolix Inc., Cambridge, MA), a copolymer of poly-3-hydroxybutyrate (P3HB) and

poly-4-hydroxybutyrate (P4HB), was added and the mixture was sonicated for an additional 2 h to produce a casting suspension. A pre-determined volume of this casting suspension, discussed further in Phan et al., was then poured into aluminum dishes (44 mm diameter, 12.5 mm height, Fisherbrand) and allowed to sit overnight to enable the solvent to evaporate. The MWCNT/PHA nanocomposites generated in this way were then peeled from the aluminum dishes and consistently trimmed around the edges to have similar physical dimensions (~30 mm diameter); the CNT/PNC masses were 31.1 ± 2.1 mg. CNT/PHA nanocomposites were prepared with O-MWCNT and pristine MWCNT loadings of 0.5, 1, 2, 5, and 10 (pristine only) % w/w and all coupons contained 5% w/w EC. Neat PHA (containing 5% w/w EC), without CNTs fillers, were also prepared as controls. As shown in our previous study with thermogravimetric analysis, this method of CNT/PHA nanocomposite preparation did not trap any measurable amount of solvent in the PHA and CNT/PHA nanocomposite coupons. The crystallinity was also shown to not change considerably with increasing CNT loading in PHA.[2]

6.5 BMP Media Preparation

Digested anaerobic sludge used in BMP tests was collected at the Back River Wastewater Treatment Plant, (Baltimore, MD) from the running digester outlet and was used as inoculum. Media was prepared following the recipe outlined in Owen et al, with minor modifications.[3] The inoculum to substrate (*i.e.,* inoculum to neat polymer or polymer matrix of CNT/polymer nanocomposite) ratio (ISR) utilized was approximately 1:1 on a volatile solids (VS) basis. The polymer or CNT/PNC substrate organic loads use were about 1.5 g VS L^{-1} for PHA and nearly 3 g VS L^{-1} for PCL (due to its slow biodegradability). The PCL and CNT/PCL samples were biodegraded with a different

batch of freshly collected anaerobic sludge inoculum than the PHA and CNT/PHA samples, however, due to the high stability of the microbial community in the digester at the BRWWTP and the dramatically different biodegradation profiles of the two polymers (years vs. months, respectively), any slight differences in PNC biodegradation profiles due to variations in culture are expected to be comparatively minimal.

6.6 Measuring Biogas Production and Composition

Samples containing PNCs and 100 mL of defined anaerobic medium and inoculum were incubated in three biological replicates at 35 ± 0.5 °C until biogas production plateaued. For neat PHA and CNT/PHA PNCs, six carefully weighed PNC coupons were added into each 150 mL serum bottle to reach a final polymer mass of approximately 150 mg, while for neat PCL and CNT/PCL PNCs 10-12 samples (± 3 mg in mass variation per coupon among all sets) were used to reach approximately 300 mg of polymer. The difference in sample mass used between PHA and PCL replicates was due to differences in sample availability; however, biogas and methane production was normalized to the mass added to each bottle to account for this difference. Biogas readings were collected every 1-3 d during periods of high biogas production (≤ 10 d) and every 10-20 d for periods of low biogas production (> 10 d). All biogas volumetric readings were made after samples were equilibrated to room temperature. Glass, gastight syringes (5-50 mL depending on evolved gas volume) lubricated with deionized water and equipped with 20-gauge needles were used for gas volume measurements. After the volumetric reading and equilibration of the BMP serum bottle headspace to atmospheric pressure, 250 µL of gas phase was sampled using a Hamilton SampleLock syringe, and assayed for CH_4 and CO_2 content using a Shimadzu GC-8A gas chromatograph equipped with a Hayes Q 80/100 column and

a thermal conductivity detector (TCD). An injection temperature of 130 °C, a column with a current of 80 mA, and helium as a carrier gas at a pressure of 2 bar were used. Analytical standard grade N_2, CO_2, and CH_4 gases (Supelco >98% purity), each injected into the GC at 50, 150, and 250 μL, were used to calibrate the GC-TCD prior to sample gas composition measurements. Every biogas measurement represents an average of three biological replicates and one standard deviation.

6.7 Biogas and Methane Production from O-MWCNT/PCL PNC

Figures in this section report kinetic model parameters (first order, pseudo first order, Gompertz, and Logistic models) and complete fits for O-MWCNT/PCL nanocomposite biogas and methane production for O-MWCNT loadings of 0, 0.1, 0.5, and 2% w/w. Also reported is the plot from Figure 2.1 with complete error bars reported as well as a plot of biogas production from a replicate data set of neat PCL and 2% w/w O-MWCNT/PCL nanocomposites.

Table 6.1 Kinetic parameters for biogas and methane production from O-MWCNT/PCL nanocomposites. The model used to describe the results is bolded.

Sample	1st-order rate model			Pseudo-parallel 1st-order rate model					**Modified Gompertz model**				Logistic model			
	$k\times10^3$ (d^{-1})	NRMSE	R^2	k_1 (d^{-1})	$k_2\times10^3$ (d^{-1})	P_{biodeg}	NRMSE	R^2	k (mL*g*VS^{-1}*d^{-1})	λ (d)	NRMSE	R^2	k	b	NRMSE	R^2
Biogas Production																
PCL	5.5	8.28	0.856	0.31	4.9	0.119	15.4	0.843	14.3	120	0.575	0.999	0.046	2060	0.405	1.000
0.1 % CNT	5.8	9.41	0.874	0.55	5.3	0.129	17.2	0.862	14.1	110	0.559	0.999	0.045	1167	0.378	1.000
0.5 % CNT	5.9	11.5	0.899	0.45	5.3	0.119	20.9	0.888	11.3	97.6	0.520	1.000	0.036	267	0.842	0.999
2% CNT	2.9	5.93	0.841	0.56	2.1	0.167	15.7	0.804	7.39	140	0.561	0.999	0.026	333	0.560	0.998
Methane Production																
PCL	7.0	10.7	0.834	0.14	5.6	0.024	10.4	0.856	9.1	118	0.574	0.999	0.048	2326	0.394	1.000
0.1 % CNT	5.3	13.2	0.885	0.12	4.9	0.005	12.9	0.889	9.2	110	0.562	0.999	0.047	1343	0.362	1.000
0.5 % CNT	6.4	14.6	0.896	0.11	6.1	0.006	14.4	0.899	7.2	96.5	0.520	1.000	0.037	273	1.366	0.999
2% CNT	4.3	10.8	0.807	0.13	3	0.026	10.3	0.837	5.04	137	0.558	1.000	0.028	386	0.925	0.999

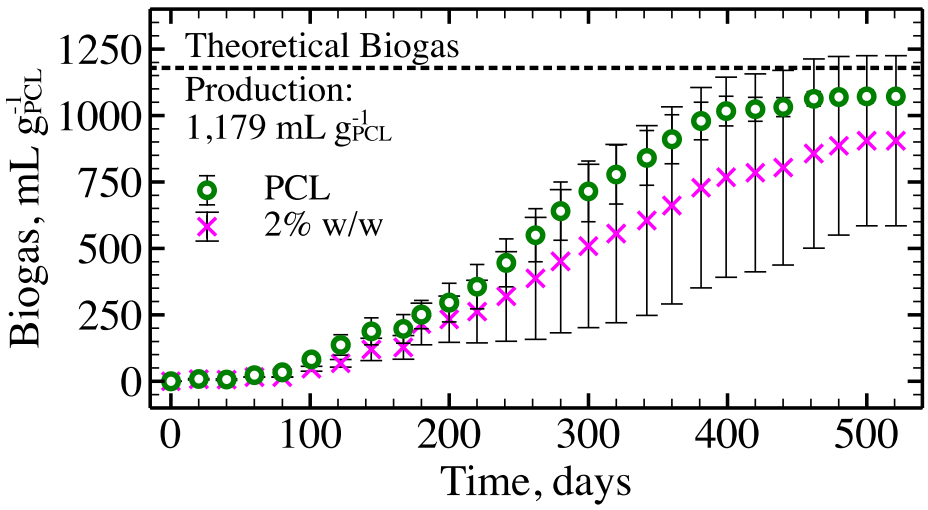

Figure 6.1 Biogas production from anaerobic biodegradation of PCL and 2% w/w O-MWCNT/PCL nanocomposite. Each data point represents an average of three replicate specimens with one standard deviation.

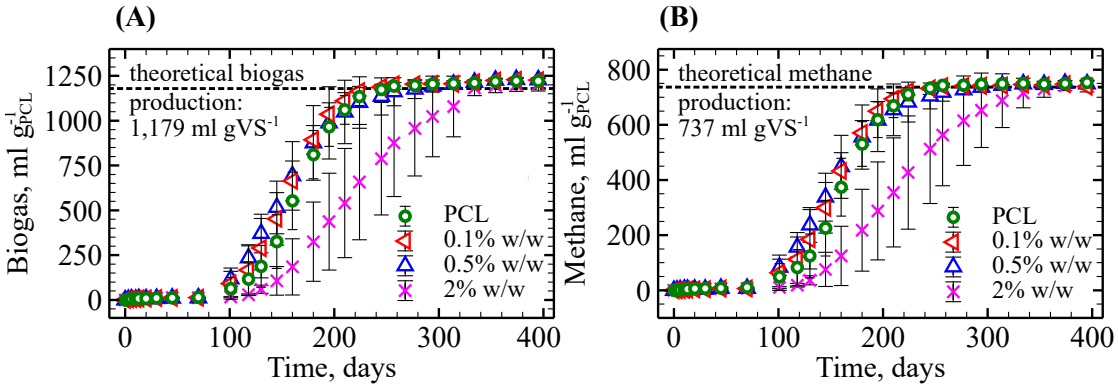

Figure 6.2 (A) Biogas and (B) methane production from the anaerobic biodegradation of PCL and O-MWCNT/PCL nanocomposites of varied CNT loading (0.1%, 0.5%, 2% w/w). The dashed lines show theoretical biogas and methane production from the PCL matrix of the nanocomposites calculated via the Buswell equation. Each data point represents an average of three replicate specimens with one standard deviation.

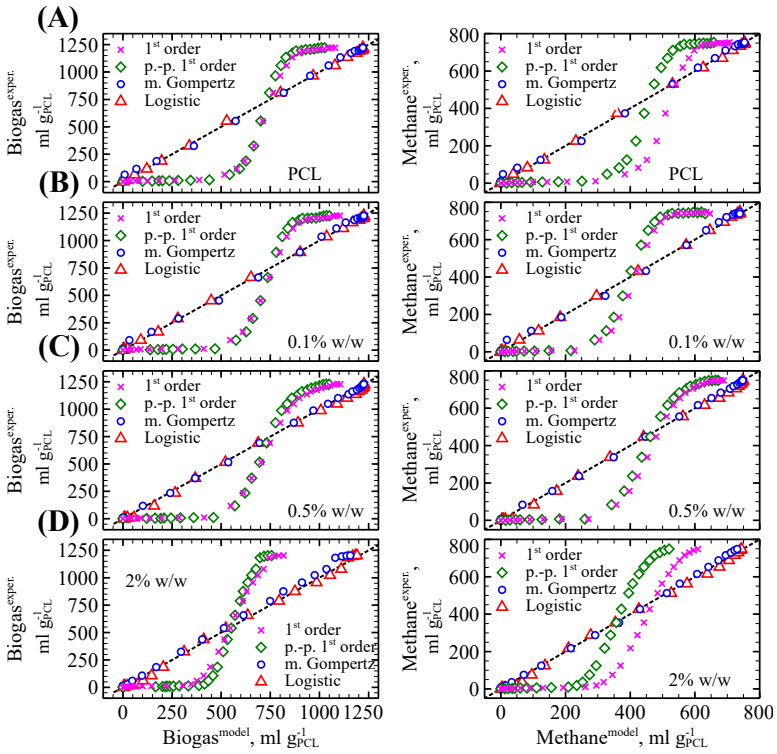

Figure 6.3 Experimentally observed vs. model-predicted biogas (left) and methane (right) production for (A) PCL, and PCL loaded with (B) 0.1% w/w O-MWCNTs, (C) 0.5% w/w O-MWCNTs, and (D) 2% w/w O-MWCNTs

6.8 Biogas and Methane Production from O-MWCNT/PHA PNCs

Figures in this section report additional data including kinetic modeling parameters (first order, pseudo first order, Gompertz, and Logistic models) and complete fits for O-MWCNT/PHA biogas and methane production for O-MWCNT loadings of 0, 0.1, 2, and 5% w/w.

Table 6.2 Kinetic parameters for biogas and methane production from O-MWCNT/PHA nanocomposites. The model used to describe the results is bolded.

Sample	1st-order rate model			Pseudo-parallel 1st-order rate model					**Modified Gompertz model**				Logistic model			
	$k\times10^3$ (d^{-1})	NRMSE	R^2	k_1 (d^{-1})	$k_2\times10^3$ (d^{-1})	P_{biodeg}	NRMSE	R^2	k ($mL*g*VS^{-1}*d^{-1}$)	λ (d)	NRMSE	R^2	k	b	NRMSE	R^2
O-MWCNT/PHA, Biogas Production																
PHA	0.062	2.77	0.968	0.062	0	0.990	2.78	0.968	62.5	3.88	0.50	0.998	0.25	23.6	1.19	0.994
0.1 % CNT	0.058	3.66	0.955	0.055	0	0.964	3.58	0.952	64.7	5.17	0.19	0.997	0.27	36.6	1.14	0.994
0.5 % CNT	0.046	3.44	0.951	0.043	0	0.981	3.32	0.947	57.4	6.94	0.37	0.998	0.26	59.5	0.75	0.996
5% CNT	0.026	0.80	0.971	0.021	0	0.990	0.70	0.974	18.4	4.75	0.43	0.988	0.083	14.5	0.84	0.990
O-MWCNT/PHA, Methane Production																
PHA	0.050	59.9	0.915	0.046	0	0.940	57.9	0.910	52.7	9.50	0.38	0.998	0.41	406	3.79	0.997
0.1 % CNT	0.052	101	0.910	0.047	0	0.966	97.3	0.904	57.8	9.53	0.38	0.999	0.44	583	4.71	0.998
0.5 % CNT	0.041	112	0.927	0.038	0	0.993	108	0.922	40.0	9.76	0.370	0.999	0.31	204	12.2	0.996
5% CNT	0.021	42.7	0.924	0.019	0	0.990	41.3	0.928	19.1	23.6	0.59	0.998	0.14	210	5.18	1.000

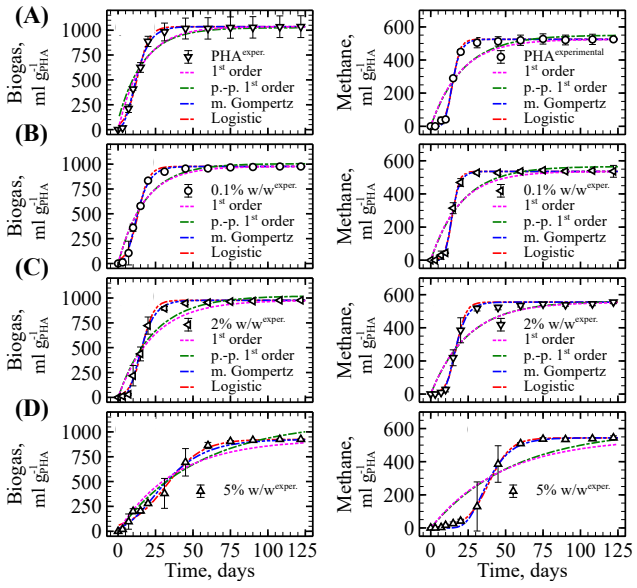

Figure 6.4 Biogas (left) and methane (right) production from the biodegradation of (A) neat PHA and O-MWCNT/PHA nanocomposites with (B) 0.1, (C) 2, and (D) 5% w/w O-MWCNTs fit to derived kinetic models. Dotted line represents theoretical maximum biogas and methane production as calculated with the Buswell equation. Each data point represents the average and one standard deviation of gas production from three replicate

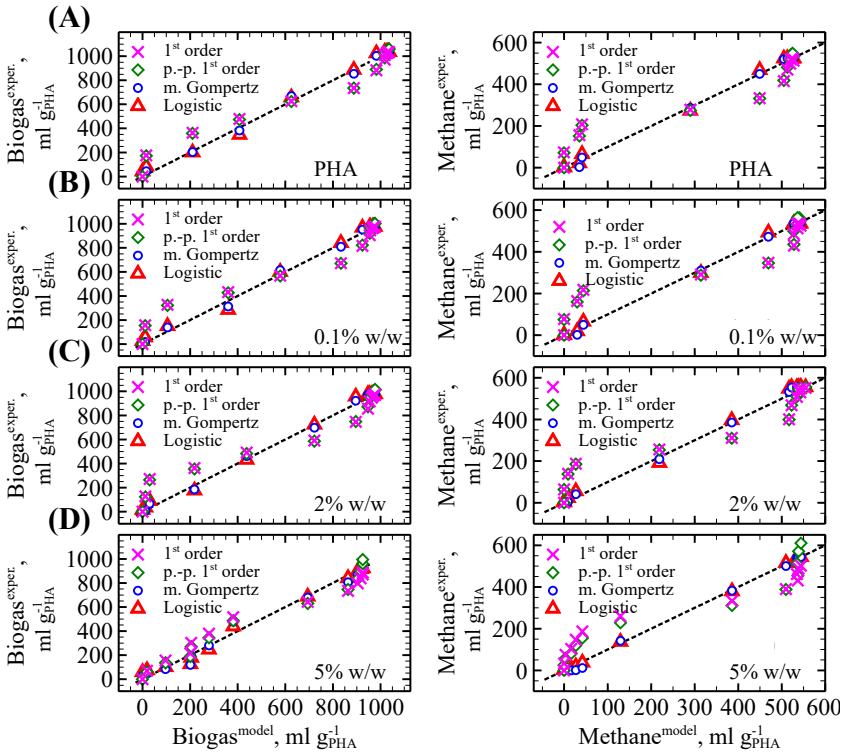

Figure 6.5 Experimentally observed vs. model-predicted biogas (left) and methane (right) production for (A) PHA, and PHA loaded with (B) 0.1% w/w O-MWCNTs, (C) 2% w/w O-MWCNTs, and (D) 5% w/w O-MWCNTs fit to derived models.

6.9 Biogas and Methane Production from Pristine and O-MWCNT/PHA PNCs

Figures in this section report additional data including kinetic model parameters (first order, pseudo first order, Gompertz, and Logistic models) and complete fits for biogas and methane production from pristine MWCNT/PHA nanocomposites with CNT loadings of 0, 0.1, 2, 5, 10% w/w. Also reported are replicate stereo microscopy images and Raman data for 5 % w/w pristine MWCNT/PHA and O-MWCNT/PHA PNCs to illustrate the reproducibility of the difference in dispersion offered by each CNT type in the same polymer matrix, as well as comparison of 5% w/w pristine MWCNT/PHA and O-

MWCNT/PHA PNCs stereo microscopy images to pure PHA.

Table 6.3 Kinetic parameters for biogas and methane production from pristine MWCNT/PHA nanocomposites. The model used to describe the results is bolded.

Sample	1st-order rate model			Pseudo-parallel 1st-order rate model					**Modified Gompertz model**				Logistic model			
	$k\times10^3$ (d^{-1})	NRMSE	R^2	k_1 (d^{-1})	$k_2\times10^3$ (d^{-1})	P_{biodeg}	NRMSE	R^2	k ($mL*g*VS^{-1}*d^{-1}$)	λ (d)	NRMSE	R^2	k	b	NRMSE	R^2
MWCNT/PHA, Biogas Production																
PHA	0.069	3.71	0.927	0.057	0	0.93	3.46	0.921	84.9	5.83	0.27	0.999	0.40	91.4	0.44	0.997
0.1 % CNT	0.068	3.50	0.939	0.057	0	0.97	3.27	0.933	77.5	5.20	0.11	0.999	0.36	59.8	0.62	0.998
0.5 % CNT	0.068	2.36	0.936	0.056	0	0.95	2.19	0.930	77.1	5.43	0.22	1.000	0.36	63.4	0.29	0.998
5% CNT	0.067	3.38	0.940	0.055	0	0.97	3.13	0.934	75.5	5.38	0.12	1.000	0.35	57.0	0.61	0.998
10% CNT	0.043	5.65	0.954	0.036	0	0.94	5.31	0.960	37.3	5.60	0.93	0.992	0.18	27.6	2.57	0.995
MWCNT/PHA, Methane Production																
PHA	0.067	1018	0.908	0.07	0	0.93	1028	0.908	63.9	6.92	0.2	1	0.47	219	101	0.998
0.1 % CNT	0.068	52.1	0.918	0.067	0	0.97	50.8	0.918	58	6.54	0.13	1	0.41	135	6.8	0.999
0.5 % CNT	0.062	20.3	0.895	0.061	0	0.95	20.2	0.894	62.8	7.51	0.550	0.998	0.47	325	1.9	0.994
5% CNT	0.064	64.8	0.914	0.064	0	0.97	64.9	0.914	57.6	6.93	0.46	1.000	0.41	156	8.4	0.998
10% CNT	0.037	2.72	0.903	0.037	0	0.94	2.73	0.903	34.2	11.6	0.52	0.993	0.26	191	0.6	0.998

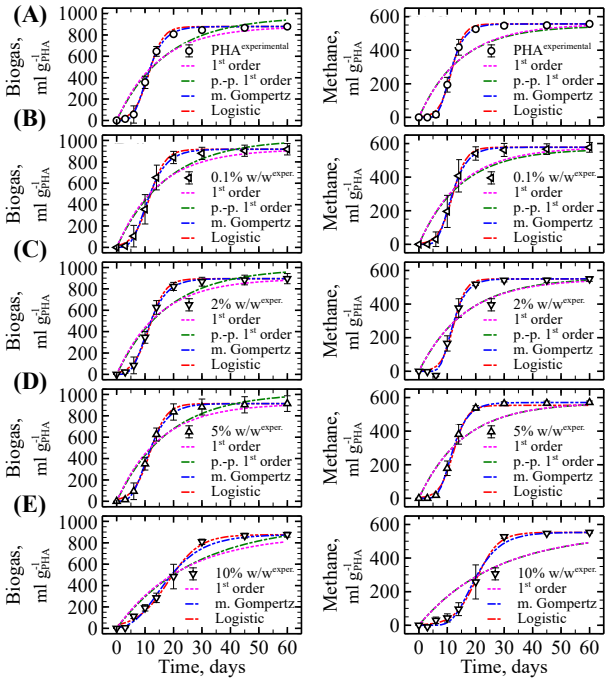

Figure 6.6 Biogas (left) and methane (right) production from the biodegradation of (A) neat PHA and pristine MWCNT/PHA nanocomposites with (B) 0.1, (C) 2, (D) 5 and (E) 10% w/w pristine MWCNTs fit to derived kinetic models. Dotted line represents theoretical maximum biogas and methane production as calculated with the Buswell equation. Each data point represents the average and one standard deviation of gas production from three replicate samples.

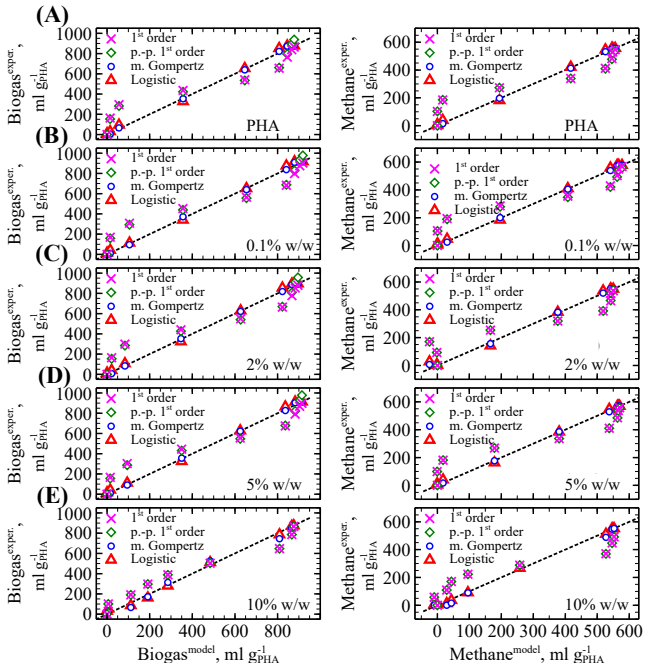

Figure 6.7 Experimentally observed vs. model-predicted biogas (left) and methane (right) production (A) PHA, and PHA loaded with (B) 0.1% w/w, (C) 2% w/w, (D) 5% w/w, and (E) 10% w/w pristine MWCNTs.

Figure 6.8 Replicate stereo microscopy images of 5% w/w pristine MWCNT/PHA nanocomposite coupons for assessment of CNT dispersion quality. (A) and (B) are different areas of one specimen while (C) is one area from a separate specimen.

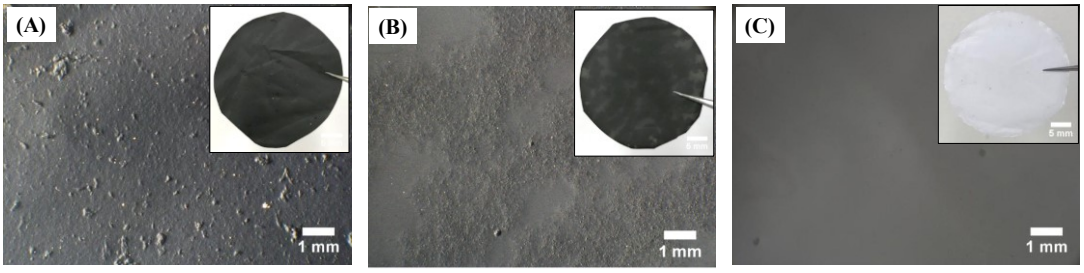

Figure 6.9 A comparison of the CNT dispersion quality in (A) 5% w/w O-MWCNT/PHA and (B) 5% w/w pristine MWCNT/PHA nanocomposites using a stereo microscope. (C) A stereo microscope image of neat PHA is also shown as a control. Optical images are shown in the insets.

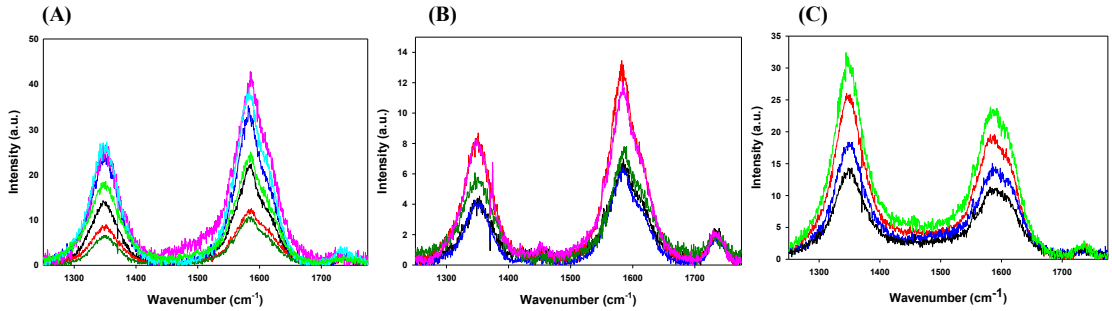

Figure 6.10 Raman spectra of defective (D) and graphitic (G) bands for replicate areas of CNT/PHA polymer nanocomposites (each in duplicate) normalized to the PHA band at 1735 cm^{-1}. Plots include (A) 5% w/w pristine MWCNT/PHA composite (rough area), (B) 5% w/w pristine MWCNT/PHA composite (smooth area), and a (C) 5% w/w O-MWCNT/PHA composite.

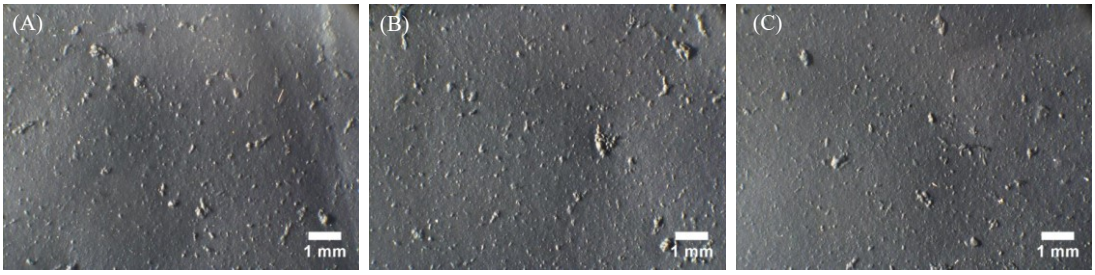

Figure 6.11 Replicate stereo microscopy images of 5% w/w O-MWCNT/PHA nanocomposites for assessment of CNT dispersion quality. (A) and (B) are different areas of one specimen while (C) is one area from a separate specimen.

6.10 References

1. Goodwin, D. G.; Boyer, I.; Devahif, T.; Gao, C.; Frank, B. P.; Lu, X.; Kuwama, L.; Gordon, T. B.; Wang, J.; Ranville, J. F.; Bouwer, E. J.; Fairbrother, D. H., Biodegradation of Carbon Nanotube/Polymer Nanocomposites using a Monoculture. *Environ. Sci. Technol.* **2018,** *52* (1), 40-51.

2. Phan, D. C.; Goodwin, D. G.; Frank, B. P.; Bouwer, E. J.; Fairbrother, D. H., Biodegradability of carbon nanotube/polymer nanocomposites under aerobic mixed culture conditions. *Science of The Total Environment* **2018,** *639*, 804-814.

3. Owen, W. F.; Stuckey, D. C.; Healy, J. B.; Young, L. Y.; McCarty, P. L., Bioassay for Monitoring Biochemical Methane Potential and Anaerobic Toxicity. *Water Res.* **1979,** *13* (6), 485-492.

Chapter 7. Appendix 2—Impact of Silanization on the Structure, Dispersion Properties, and Biodegradability of Nanocellulose as a Nanocomposite Filler

Reproduced from

Frank, B. P.; Durkin, D. P.; Caudill, E. R.; Zhu, L.; White, D. H.; Curry, M. L.; Pedersen, J. A.; Fairbrother, D. H., Impact of Silanization on the Structure, Dispersion Properties, and Biodegradability of Nanocellulose as a Nanocomposite Filler. *ACS Applied Nano Materials* **2018,** *1* (12), 7025-7038.

7.1 Materials

Freeze-dried cellulose nanofibrils (CNFs) were purchased from the University of Maine Process Development Center. CNFs were obtained from bleached mixed northern softwood Kraft pulp with a high percentage of black spruce. The CNF was produced using mechanical refining to reduce the size of the fibers to nanoscale. Aminopropyl trimethoxysilane (APTMS, 97%, Sigma-Aldrich), methyl trimethoxysilane (MTMS, >98%, Sigma-Aldrich), and propyl trimethoxysilane (PTMS, 97%, Sigma-Aldrich) modification reagents were used as received. Acetic acid used to acidify the silanization solution was purchased from PHARMCO (ACS Reagent Grade, Glacial Acetic Acid). Ethanol was purchased from PHARMCO (200 proof, general use HPLC-UV Reagent

Grade). Chloroform was purchased from Fisher Scientific (HPLC Grade, hydrocarbon stabilized). Anaerobic digester sludge was provided by Back River Waste Water Treatment Plant (Baltimore, MD). Aqueous solutions made from ultrapure water (18.2 MΩ·cm at 25 °C) produced by a Millipore system (Direct-Q 3 UV, Millipore, USA).

7.2 Biomethane Potential Tests

To sample biogas produced from each sample, a syringe was then inserted into the headspace of the bottles, with volume measurements obtained via reading the volume in the syringe once the pressure within the syringe had equilibrated with atmospheric pressure. Biogas composition of each sample was determined by injecting 250 µL of biogas from the headspace of the septum sealed bottles into a Shimadzu GC-8A gas chromatograph (GC) equipped with a thermal conductivity detector. The GC was operated at an injection temperature of 130 °C and a column temperature of 45 °C, using helium at 2 $kg \cdot cm^{-2}$ as a mobile phase.

7.3 Materials Characterization

Scanning electron microscopy images of CNF and Si-CNF were obtained using a JEOL-IT100 SEM with a Tungsten filament operated at 10 kV. Composite images were obtained at 20 kV. All samples were Au-sputter coated for 1 min to prevent charging. The SEM was equipped with an integrated EDS system which was used to obtain bulk elemental characterization data and maps. As-received unmodified CNF was sonicated into water at high concentration to make a slurry. This slurry was then frozen and lyophilized to yield a foamy solid. After sputter coating this solid with gold, SEM imaging revealed that the foam consisted of resolvable individual cellulose nanofibrils. 10P-CNF (chosen as a reperesentative Si-CNF) was sonicated in dichloromethane to produce a suspension of

nanoparticle. A TEM grid was dipped into the suspension, then dried before introduction into the SEM. Imaging revealed that individual Si-CNFs were discernable against the TEM grid background. Lyophilization of the Si-CNF samples was not possible, as the highly hydrophobic material now failed to disperse well in water, and so water could not infiltrate the CNF network to occupy hydrogen bonding sites.

Attenuated total reflectance infrared spectroscopy data were collected using a Nicolet iS10 spectrometer using a scan range from 4000-525 cm^{-1} with 32 scans at 4 cm^{-1} resolution.

X-ray photoelectron spectroscopy (XPS) data were obtained using a PHI 5600 instrument equipped with a Mg Kα flood source (1253.6 eV) and a hemispherical energy analyzer. Scans were taken at a source power of 300 W, with a pass energy of 58.7 eV, 10 sweeps, and 0.125 eV/step. Samples were attached as powder to double-sided copper adhesive tape which was attached to an iron XPS sample stage. Spectra were analyzed using CASA XPS software.

Solid-state NMR experiments were conducted with a 11.75 T standard bore magnet on a Bruker Advance III 500 MHz spectrometer. The instrument was equipped with a 4 mm $^{1}H(X)$ cross-polarization magic angle spinning probe. Unless otherwise noted, spectra were externally referenced using adamantine for ^{13}C spectra or 3-(trimethylsilyl)-1-propanesulfonic acid sodium (TSS) salt for ^{29}Si spectra. The adamantine peak in the ^{13}C spectrum was set to 38.47 ppm, and that for TSS in the ^{29}Si spectrum was set to 1.46 ppm. Spectra for the nanocellulose and silane self-condensates were collected at 12 kHz spinning speed. All spectra were acquired at 298 K. The ^{13}C and ^{29}Si spectra were obtained by ^{13}C and ^{29}Si cross-polarization (CP) sequence, respectively, with a 27.2 ms acquisition time,

13.3 µs dwell time, and 100 kHz ^{1}H radio frequency (RF) decoupling power. The ^{13}C spectra were obtained under 44.5 kHz ^{13}C RF power with 1 ms contact time and 1300 scans with recycle delay of 4 s. The ^{29}Si spectra were obtained under 31.25 kHz 29Si RF power with 3 ms contact time and 10240 scans with recycle delay of 5 s. ^{29}Si-NMR spectra and ^{13}C-NMR spectra were processed using polynomial fit baseline correction and exponential line broadening.

Optical microscopy images were obtained using a Zeiss Axioscope.A1 equipped with an Axiocam 105 color camera. Images displayed an area of 1 mm^2 of the nanocomposite surface.

7.4 Figures

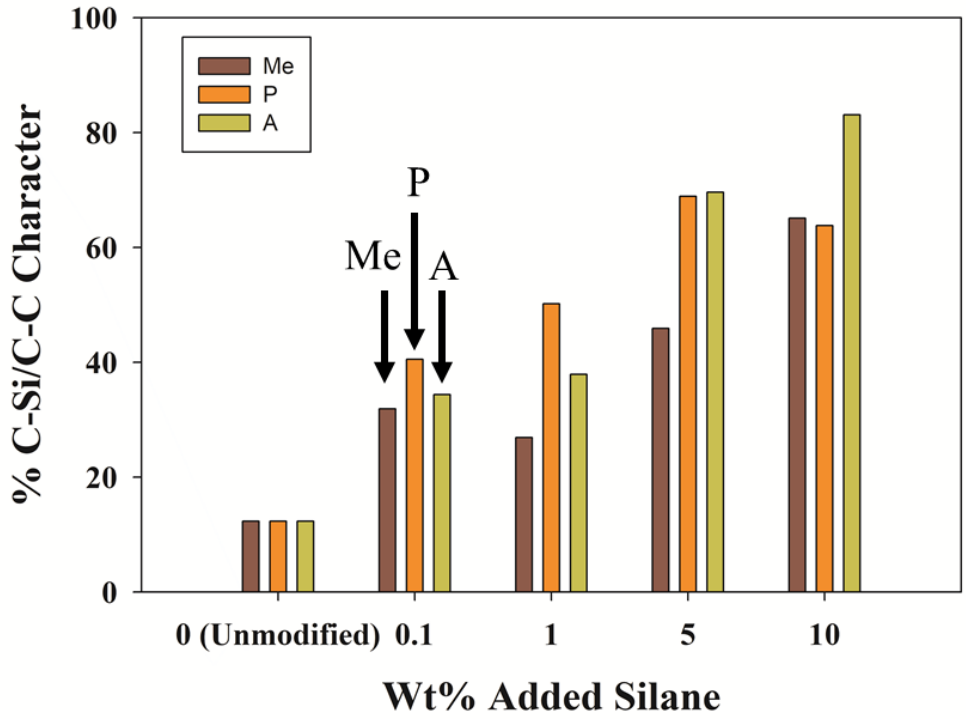

Figure 7.1 X-ray photoelectron spectroscopy (XPS) ratios of the C-C/C-Si character in the C(1s) regions for methyl- (Me, left), propyl- (P, middle), and aminopropyl- (A, right) trimethoxysilane modified cellulose nanofibrils (CNFs) at 0 through 10 wt%.

Table 7.1 Atomic % of silicon determined using energy dispersive X-ray spectroscopy (EDS) analysis of silane modified cellulose nanofibrils (Si-CNF). Values for Si-CNFs modified with methyl-, propyl-, and aminopropyl- trimethoxysilane (MTMS, PTMS, APTMS, respectively) are shown.

	MTMS	PTMS	APTMS
0.1 wt% Si-CNF	0.5	1.4	1.8
1 wt% Si-CNF	4.7	8.9	4.7
5 wt% Si-CNF	14.1	19.9	15.4
10 wt% Si-CNF	14.7	21.8	10.7

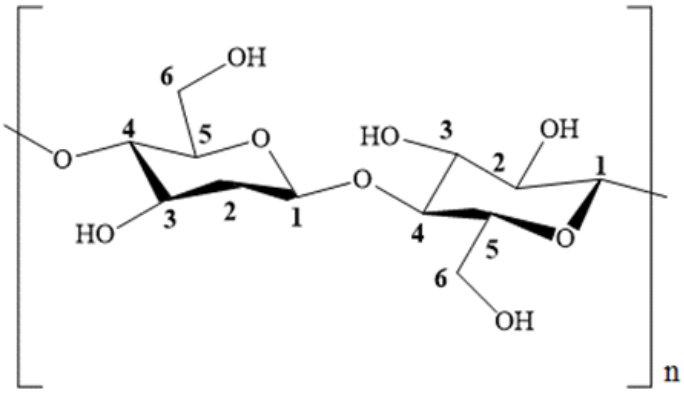

Figure 7.2 C-1 though C-6 labeled in cellobiose repeat unit

Table 7.2 Assignment of ^{13}C-NMR chemical shifts (δ_{13C}) for untreated (CNF) and silane-treated nanocellulose (5A-CNF, 5P-CNF, 5Me-CNF).*

	δ_{13C} (ppm)						
	C-1	**C-4 (C)**	**C-4 (A)**	**C-2,3,5 (C)**	**C-2,3,5 (A)**	**C-6 (C)**	**C-6 (A)**
CNF	104.9 102.4†	89.0	83.6 81.1†	72.8 71.8†	75.2 75.5†	65.4	62.7
5A-CNF	105.2	89.0	83.5 82.1†	72.1	75.0	65.4	63.1
5P-CNF	105.2 102.4†	89.0	84.6† 83.3	72.8	75.2	65.6	63.0
5Me-CNF	104.9 101.1†	88.8	84.1† 82.0	72.3	74.8	65.0	62.3

* Crystalline (C) and amorphous (A) forms are designated.
† Indicates a shoulder.

Table 7.3 Assignments of ^{29}Si-NMR chemical shifts (δ_{29Si}) for silanization reagent self-condensates (A-self, P-self, and Me-self) and silane-treated nanocellulose (5A-CNF, 5P-CNF, and 5Me-CNF).*

	δ_{29Si} (ppm)						
	Self-condensed				Silane-treated nanocellulose		
	T^1	T^2	T^3		T^1	T^2	T^3
A-self	n/a	–59.9	–68.2	**5A-CNF**	–53.3	–63.1	–71.6
P-self	–47.6	–57.5	–67.2	**5P-CNF**	–51.6	–61.4	–71.6
Me-self	–44.1	–52.8	–61.7	**5Me-CNF**	–48.5	–59.1	–68.3

* Peak shifts are designated by their T^i described in the body of the text.

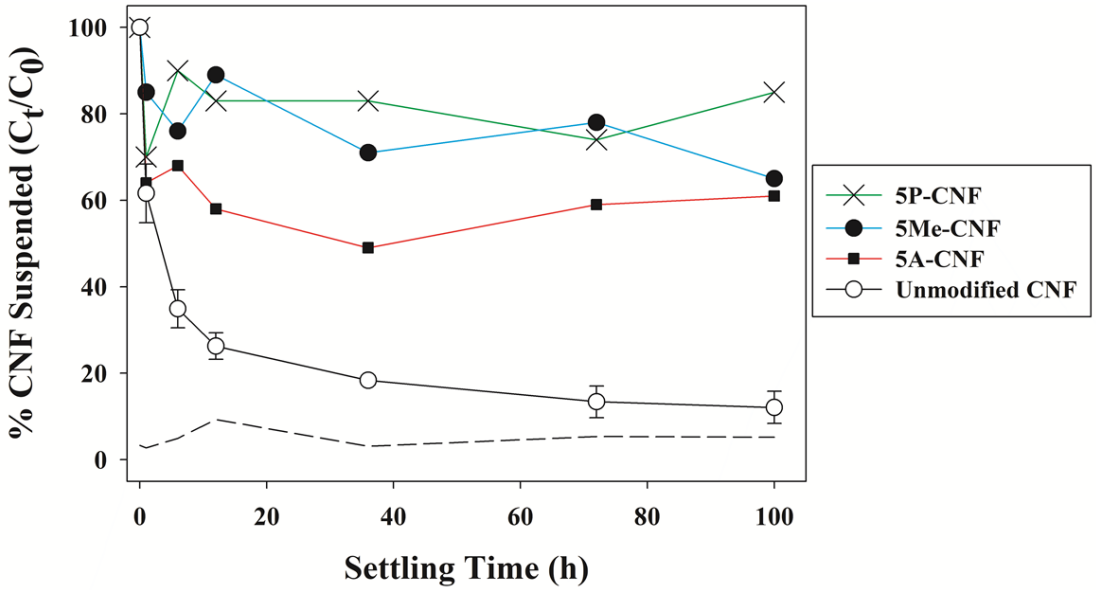

Figure 7.3 Mass recovery analysis of cellulose nanofibrils (CNF, white circles) modified with 5 wt% methyl- (black circles), propyl- (crosses), or aminopropyl- (squares) trimethoxysilane. Data are plotted in terms of percent CNF concentration remaining in the supernatant (C_t/C_0). Baseline detectable concentration denoted by dashed line.

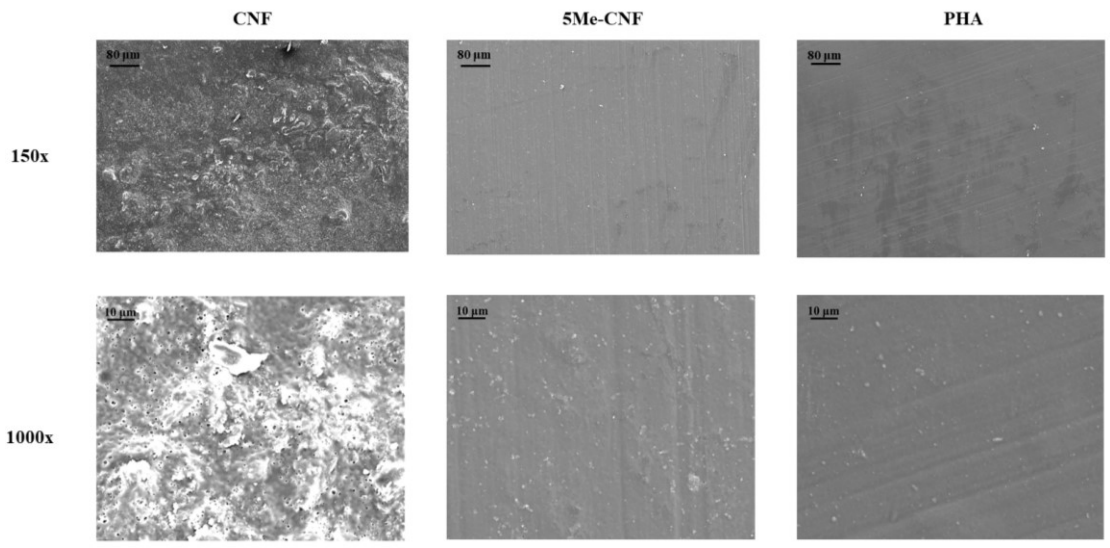

Figure 7.4 Scanning electron microscopy (SEM) images of polyhydroxyalkanoates (PHA) filled with unmodified cellulose nanofibrils (CNF, left), CNFs modified with 5 wt% methyl trimethoxysilane (5Me-CNF, center), and no nanofiller (right) at 150x (top) and 1000x (bottom) magnification.

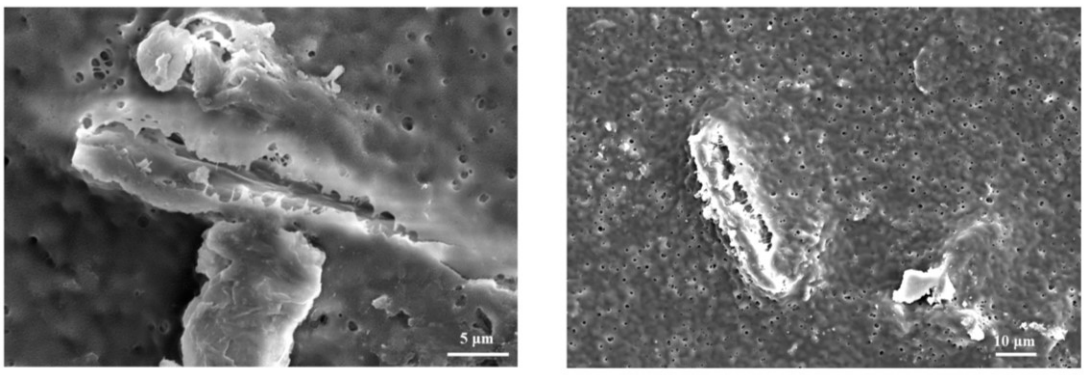

Figure 7.5 Scanning electron microscopy (SEM) of polyhydroxyalkanoates (PHA) filled with 5 wt% unmodified cellulose nanofibrils (CNFs). Images highlight regions of tearing in the polymer matrix due to the large CNF aggregates.

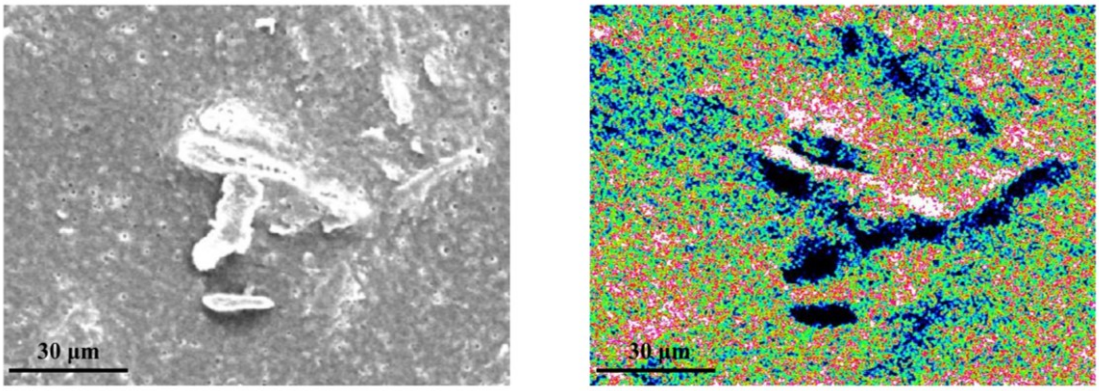

Figure 7.6 Scanning electron microscopy (SEM, left), and energy dispersive X-ray spectroscopy (EDS, right) oxygen map of an aggregate of unmodified cellulose nanofibrils (CNFs) in polyhydroxyalkanoates (PHA). White regions in the EDS map correspond to areas of high oxygen concentration.

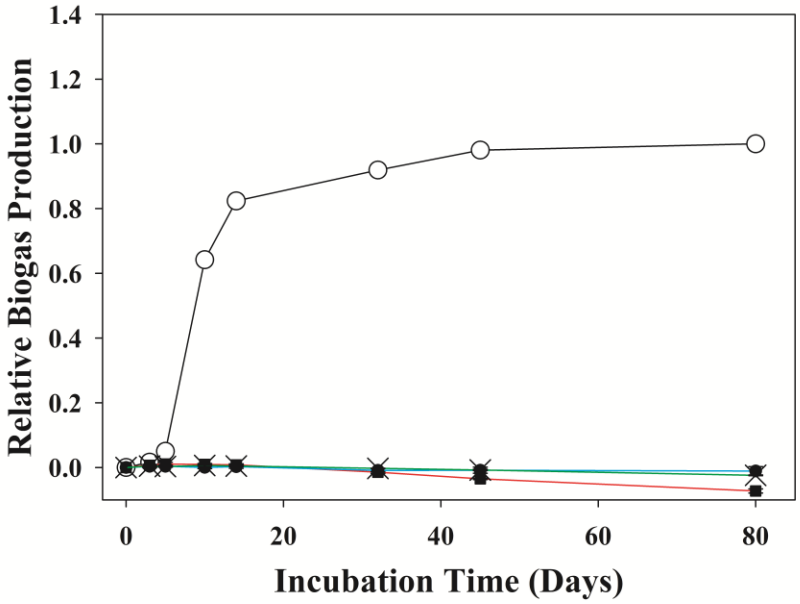

Figure 7.7 Relative biogas production for cellulose nanofibrils (CNF, white circles) and self-condensed methyl- (Me-self, black circles), propyl- (P-self, crosses), or aminopropyl- (A-self, squares) trimethoxysilane. Values are normalized for maximum biogas produced by unmodified CNF sample.

Table 7.4 ^{13}C composition of crystalline (C) and amorphous (A) regions of untreated (CNF) and silane-treated nanocellulose (5A-CNF, 5P-CNF, 5Me-CNF) based on peak integration of C-4, C-2,3,5, and C-6 peaks.

	^{13}C Composition (%)							
	C-4		C-2,3,5		C-6		Average C	Average A
	C	A	C	A	C	A		
CNF	37	63	44	57	42	58	41 ± 3.3	60 ± 3.3
5A-CNF	53	48	50	50	56	44	53 ± 2.8	47 ± 2.8
5P-CNF	42	58	42	58	44	57	42 ± 1.0	58 ± 1.0
5Me-CNF	28	72	30	70	35	66	31 ± 3.4	69 ± 3.4

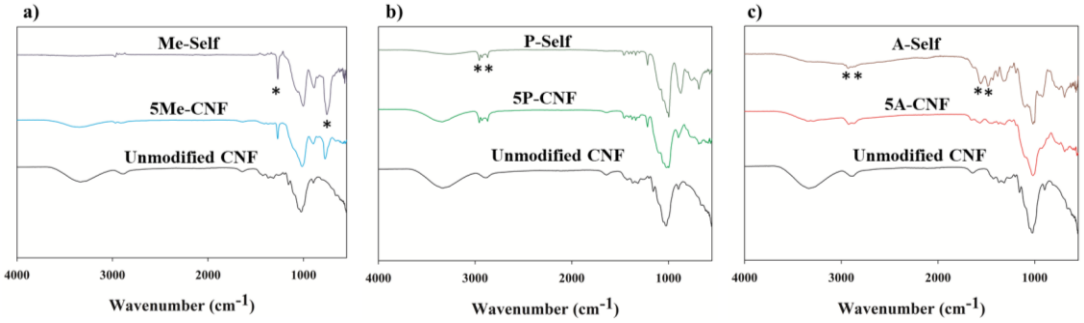

Figure 7.8 Attenuated total reflectance Fourier transform infrared spectroscopy of self-condensed silanes (top plots) compared to respective 5 wt% silane modified cellulose nanofibrils (middle plots) and unmodified cellulose nanofibrils (CNF, bottom plots). Plots are methyl- (a), propyl- (b), and aminopropyl- (c) trimethoxysilane modified. Characteristic silane peaks are denoted by an *.

Table 7.5 Peak width in Hz of self-condensed (A-self, P-self, and Me-self) and silane-treated nanocellulose (5A-CNF, 5P-CNF, and 5Me-CNF) from solid-state ^{29}Si-NMR experiments.

^{29}Si peak widths (Hz)							
	Self-condensed				Silane-treated CNF		
	T^1	T^2	T^3		T^1	T^2	T^3
A-self	n/a	507	539	**5A-CNF**	218	387	520
P-self	165	330	410	**5P-CNF**	361	498	559
Me-self	129	537	559	**5Me-CNF**	217	504	584

Chapter 8. Appendix 3—Biodegradation of Functionalized Nanocellulose is Dictated by Degree of Surface Substitution and Chemical Linkage

8.1 Figures

Table 8.1 Elemental analysis composition and calculated $DS_{overall}$ for cellulose nanofibrils (CNFs) functionalized with different ether and ester groups.

Sample	%C	%H	%N	%O	$DS_{overall}$
Cellulose Nanofibrils	41.26	6.07	0	52.67	0
Hexyl Ester CNF	42.80	6.30	0	50.90	0.09
Phenyl Ester CNF	44.75	5.86	0	49.39	0.14
Dodecyl Ether CNF	45.41	6.85	0.11	47.63	0.11
Hexyl Ether CNF	42.18	5.84	0.05	51.93	0.05
GP-HC-CNF-1	-	-	-	-	0
GP-HC-CNF-2	-	-	-	-	0
GP-HC-CNF-3	43.60	5.96	0.13	50.31	0.14
GP-HC-CNF-4	-	-	-	-	0
GP-LC-CNF-1	-	-	-	-	0
GP-LC-CNF-2	-	-	-	-	0
GP-LC-CNF-3	41.75	5.93	0.14	52.18	0.013
GP-LC-CNF-4	-	-	-	-	0
LC-CNF-1	58.45	9.31	0.55	31.69	0.80
LC-CNF-2	58.69	9.18	0.47	31.66	0.82
LC-CNF-3	55.26	8.51	0.36	35.87	0.56
LC-CNF-4	61.96	9.66	0.70	27.68	1.16
LA-CNF-1	42.56	6.27	0.08	51.09	0.035
LA-CNF-2	53.04	8.15	0.10	38.71	0.45
LA-CNF-3	49.47	7.42	0.08	43.03	0.28
LA-CNF-4	47.33	6.99	0.95	44.73	0.20

Table 8.2 X-ray photoelectron spectra %C-C component values (calculated using peak-fitting in CASAXPS software) and calculated $DS_{surface}$ for cellulose nanofibrils (CNFs) functionalized with different ether and ester groups

Sample	%C-C	$DS_{surface}$
Cellulose Nanofibrils	12.3	0
Hexyl Ester CNF	14.2	0.03
Phenyl Ester CNF	25.1	0.17
Dodecyl Ether CNF	30.2	0.16
Hexyl Ether CNF	25.2	0.25
GP-HC-CNF-1	53.1	1.19
GP-HC-CNF-2	58.7	1.54
GP-HC-CNF-3	63.2	1.89
GP-HC-CNF-4	68.4	2.43
GP-LC-CNF-1	20.7	0.066
GP-LC-CNF-2	30.8	0.165
GP-LC-CNF-3	35.8	0.227
GP-LC-CNF-4	42.7	0.33
LC-CNF-1	56.3	0.63
LC-CNF-2	57.8	0.67
LC-CNF-3	68.7	1.12
LC-CNF-4	82.3	2.46
LA-CNF-1	14.28	0.014
LA-CNF-2	24.17	0.097
LA-CNF-3	28.79	0.15
LA-CNF-4	47.9	0.43

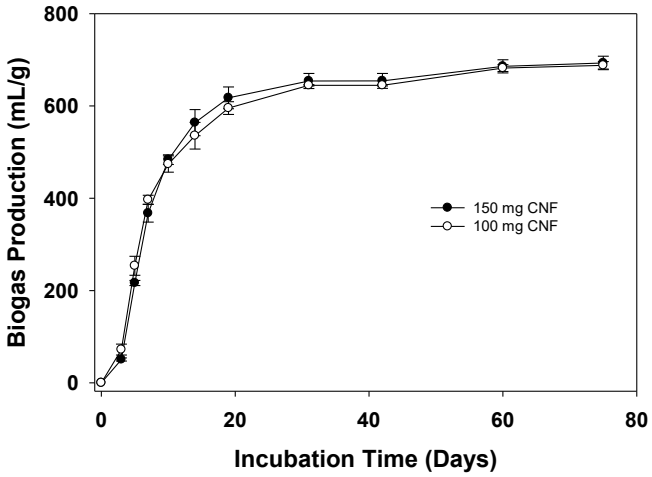

Figure 8.1 Biogas production during mineralization of 150 mg (black circles) and 100 mg (white circles) cellulose nanofibrils (CNF) by an anaerobic microbial community. Biogas production was normalized for mass loading. Error bars represent one standard deviation from the average of triplicate samples.

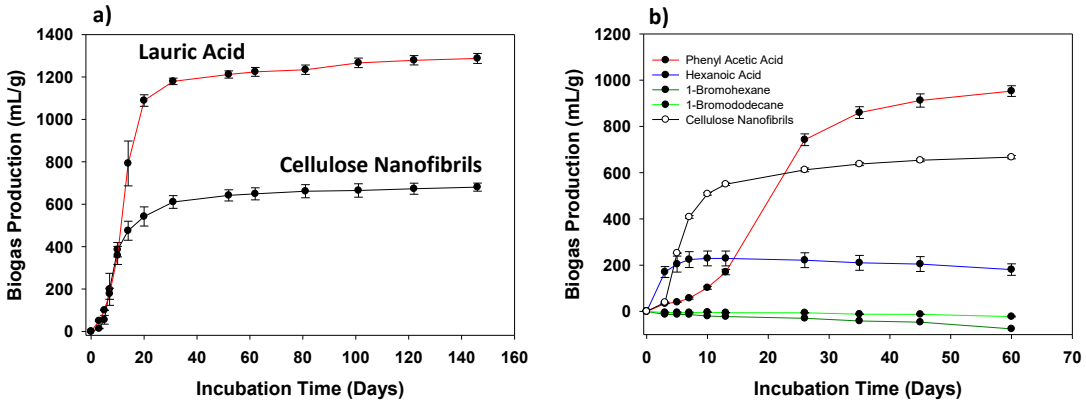

Figure 8.2 a) Biogas production during mineralization of lauric acid (red) and cellulose nanofibrils (black) by an anaerobic microbial community. Error bars represent one standard deviation from the average of triplicate samples. b) Biogas production during mineralization of phenyl acetic acid (red), hexanoic acid (blue), 1-bromohexane (dark green), 1-Bromododecane (light green), and cellulose nanofibrils. Error bars represent one standard deviation from the average of triplicate samples.

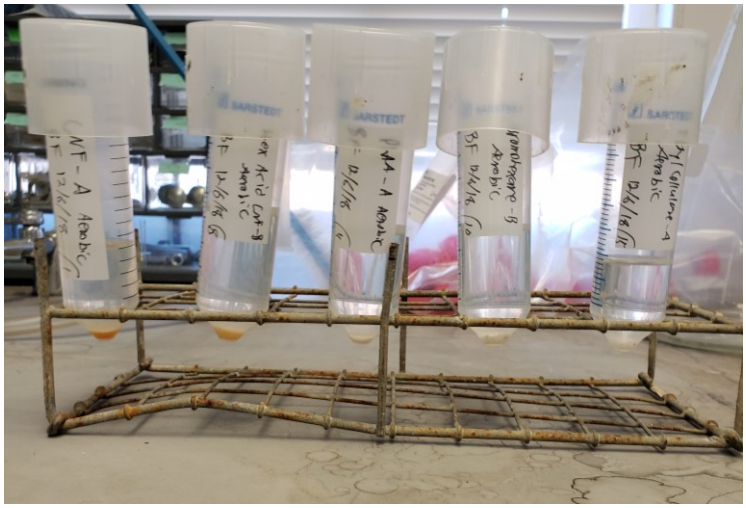

Figure 8.3 Digital images of functionalized cellulose nanofibrils after 60 d of exposure to an aerobic microbial community in 50 mL conical vials.

Table 8.3 Gompertz model statistics and parameters for functionalized cellulose nanofibrils (CNFs). Parameters include root mean squared error (RMSE), normalized root mean square error (NRMSE), coefficient of determination (R^2), Maximum Normalized Biogas production, biogas production rate (k), and lag phase (l).

Sample	RMSE	NRMSE	R^2	Max Normalized Biogas	k	l
CNF	0.058	0.250	0.977	1.01	0.078	0.680
LC-CNF-1	0.028	0.080	0.995	1.02	0.039	3.014
LC-CNF-2	0.037	0.086	0.989	0.85	0.037	2.824
LC-CNF-3	0.037	0.181	0.976	0.680	0.019	0.000
LC-CNF-4	0.020	0.254	0.980	0.425	0.022	2.958
LA-CNF-1	0.052	0.138	0.986	0.951	0.0366	2.7034
LA-CNF-2	0.095	0.289	0.937	0.939	0.020	0.000
LA-CNF-3	0.092	0.312	0.897	0.703	0.0120	0.0000
LA-CNF-4	0.048	0.251	0.968	0.666	0.009	0.000
GP-HC-CNF-1	0.022	0.172	0.996	0.927	0.028605	5.18512
GP-HC-CNF-2	0.021	0.127	0.995	0.829	0.020836	3.20093
GP-HC-CNF-3	0.021	0.079	0.990	0.614	0.012562	0
GP-HC-CNF-4	0.024	0.123	0.988	0.652	0.012575	0.490277
GP-LC-CNF-1	0.045	0.410	0.987	0.991	0.083278	1.567631
GP-LC-CNF-2	0.043	0.163	0.986	0.915	0.046283	2.431703
GP-LC-CNF-3	0.052	0.191	0.975	0.879	0.02929	0
GP-LC-CNF-4	0.040	0.201	0.987	0.902	0.036069	3.393186
Hexyl Ester CNF	0.056	0.236	0.986	1.030	0.095382	2.32292
Phenyl Ester CNF	0.018	0.202	0.996	0.925	0.011017	10.79035
Na^+ Carboxyl CNF	0.018	0.043	0.997	0.853	0.015817	2.418212
Ethyl Cellulose	0.005	1.486	0.636	0.027	5.74E-05	0.579426
H^+ Carboxyl CNF	0.062	0.224	0.964	0.867	0.020046	0
Hexyl Ether CNF	0.021	2.047	0.865	0.151	0.003117	0.730345
Dodecyl Ether CNF	0.020	0.494	0.664	0.101	0.001171	0
Dodecyl Ester CNF	0.061	0.294	0.955	0.786	0.025815	0

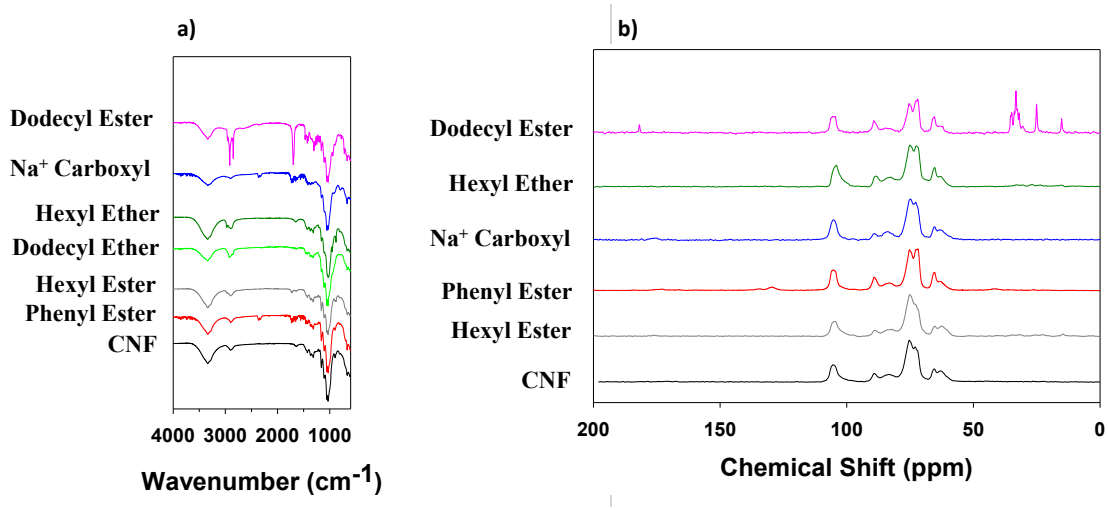

Figure 8.4 a) Attenuated total reflectance infrared spectroscopy (ATR-IR) and b) ^{13}C-NMR of cellulose nanofibrils (black) functionalized with dodecyl (pink), hexyl (grey), and phenyl (red) esters as well as hexyl (dark green) and dodecyl (light green) ethers and carboxylic acid (blue).

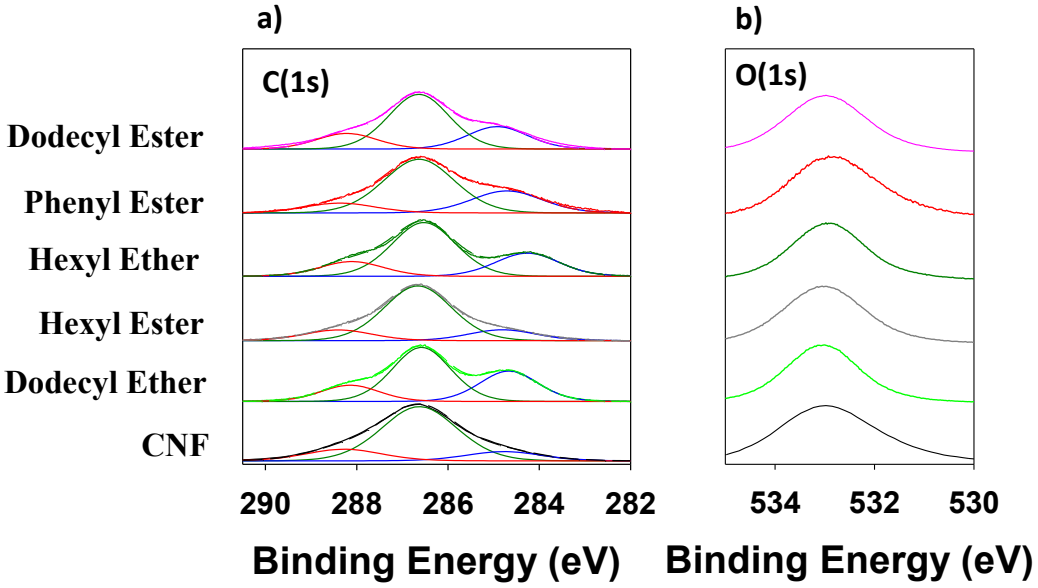

Figure 8.5 X-ray photoelectron spectroscopy a) C(1s) with component peak fitting and b) O(1s) regions of cellulose nanofibrils (CNFs) and CNFs functionalized with dodecyl (pink), phenyl (red), and hexyl (grey) esters and dodecyl (light green) and hexyl (dark green) ethers.

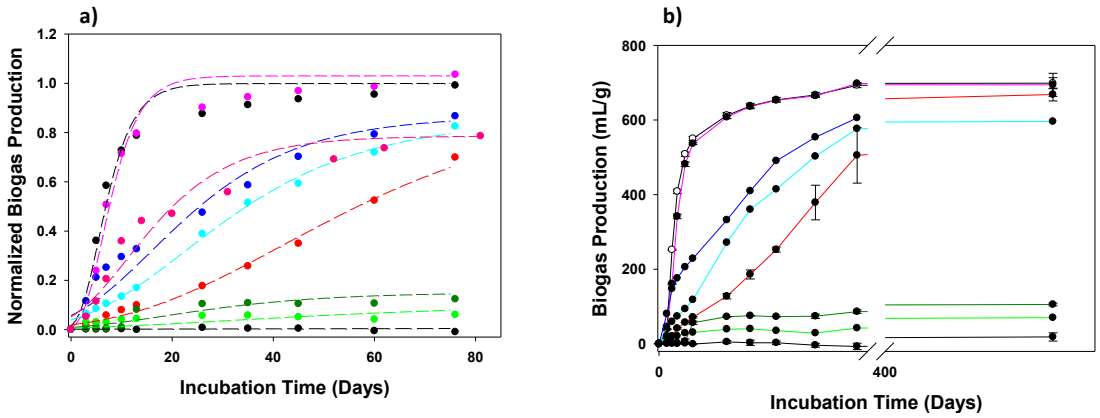

Figure 8.6 a) Normalized and b) unnormalized biogas production from the mineralization of cellulose nanofibrils (CNFs) and CNFs functionalized with hexyl ester (pink), dodecyl ester (magenta), carboxylic acid with Na^+ (dark blue) and H^+ (light blue) counterions, phenyl ester (red), hexyl ether (dark green), and dodecyl ether (light green) as well as commercial ethyl macrocellulose (black).

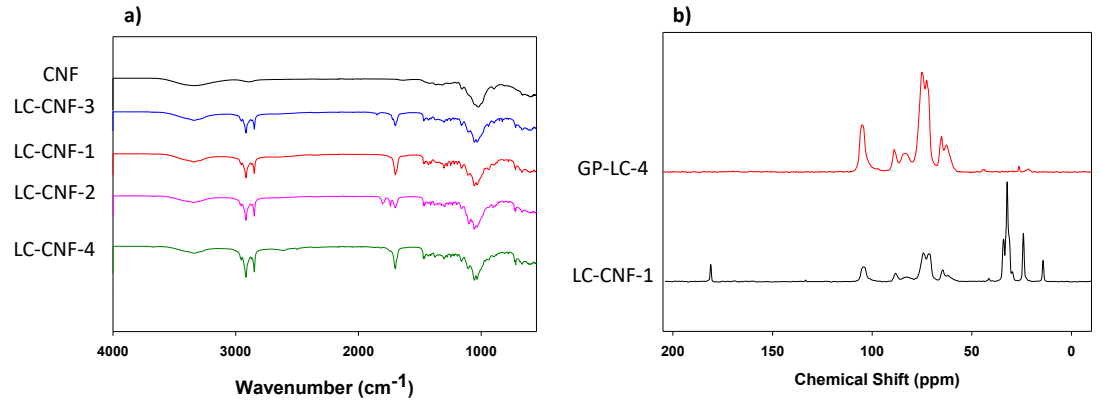

Figure 8.7 a) Attenuated total internal reflectance infrared spectroscopy of cellulose nanofibrils (CNF) esterified with lauroyl chloride. b) ^{13}C-NMR of cellulose nanofibrils functionalized with either gas phase (red) or liquid phase (black) lauroyl chloride.

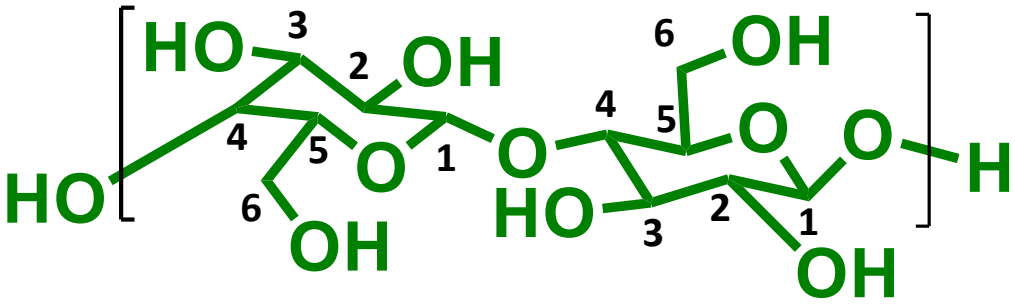

Figure 8.8 Nanocellulose repeat unit (cellobiose) with carbon 1-6 labeled for each glucose subunit.

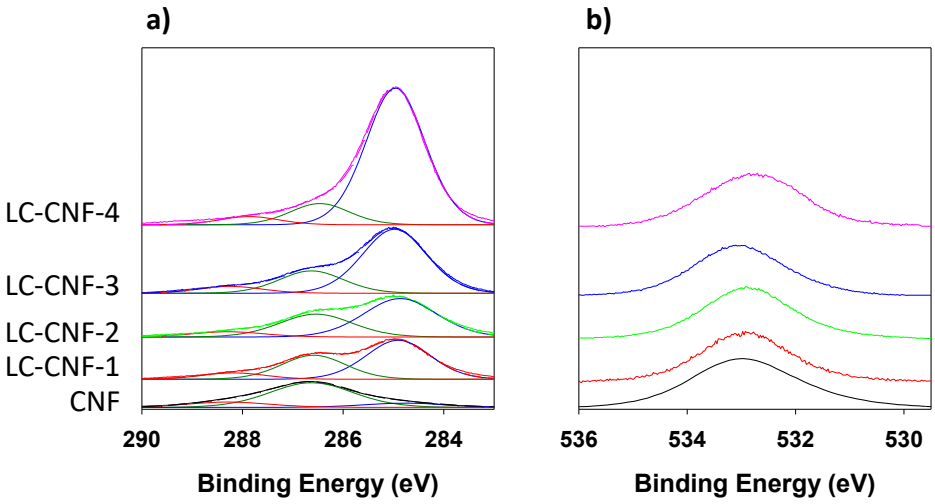

Figure 8.9 X-ray photoelectron a) fitted C(1s) and b) O(1s) regions of cellulose nanofibrils (CNF) esterified with lauroyl chloride.

Table 8.4 Assignment of ^{13}C-NMR chemical shifts (δ_{13C}) for untreated and functionalized cellulose nanofibril (CNF) samples.

	δ_{13C} (ppm)									
	CO	aromatic C	C1	C4 (C)	C4 (A)	C2,3,5 (C)	C2,3,5 (A)	C6 (C)	C6 (A)	aliphatic C
CNF	n/a	n/a	105.4 102.5†	89.3	83.5 82.3†	73.0 72.0†	75.3 74.6†	65.5	63.0 61.5†	n/a
Phenyl Ester CNF	172.7 174.7†	134.5 129.5	105.3 101.9†	89.1	83.0 84.1†	72.6 71.9	75.2 74.6†	65.4	63.4 62.8†	41.3, 42.2†
Hexyl Ester CNF	176.0	n/a	104.7 97.7†	88.9	82.2 83.6†	72.9	75.1	65.2	62.5 60.0†	34.6, 31.7, 25.9, 22.9, 14.4
Na^+ Carboxyl CNF	175.7 177.6†	n/a	105.3	89.0 87.5†	83.8 81.4†	72.7 71.6†	74.9 74.5†	65.2	63.1 59.0†	n/a
LA-CNF-3	181.6	n/a	105.2	88.7	83.1	72.0	74.7	65.2	62.4	34.7†, 32.7, 30.0, 24.6, 14.7
LA-CNF-2	181.9	n/a	105.2	89.0	83.7 81.4†	72.0	75.1	65.5	63.3 60.8†	35.5†, 35.0, 33.1, 32.0†, 30.5, 25.0, 23.4†, 22.3†, 16.5†, 15.1
Hexyl Ether	n/a	n/a	104.2 100.5†	88.6	82.7	72.1	75.0	65.4	62.7	32.8, 31.0, 30.4, 27.5†, 26.8, 23.6, 15.3
LA-CNF-4	181.2	n/a	104.6 100.8†	88.6	83.4 82.0	71.2 72.1†	74.7 73.7†	64.6 65.3†	62.5, 61.2†, 59.6†	34.1, 33.2†, 32.4, 31.3†, 29.9, 25.4†, 24.3, 22.7†, 14.4, 12.2, 10.6
GP-LC-4	n/a	n/a	105.1 102.4†	89.0	83.6 82.4†	72.7 71.9†	75.1 74.5†	65.2 66.0†	62.7 60.9†	44.5, 43.7, 26.3†, 23.2, 21.8, 20.5†
LC-CNF-1	181.0	n/a	104.4 101.2†	88.3	83.1 80.0†	71.7 71.2	74.3 73.6†	64.6 65.4†	62.1 61.3†	41.5, 34.2, 32.3, 31.4†, 29.6, 24.2, 14.3

* Crystalline (C) and amorphous (A) forms are designated.
† Indicates a shoulder.

Table 8.5 Composition of cellulose nanofibrils carbon atom 1-6 in terms of % crystalline and % amorphous character before and after functionalization with a variety of ether, ester, and carboxyl groups.

	^{13}C Composition (%)									
	C-4		C-2,3,5		C-6		Average C		Average A	
	C	A	C	A	C	A	Avg	St Dev	Avg	St Dev
CNF	38	62	39	61	40	60	39	1.0	61	1.0
Phenyl Ester CNF	48	52	48	52	49	51	49	0.6	52	0.8
Hexyl Ester CNF	31	69	32	68	35	65	33	2.1	67	2.1
Na^+ Carboxyl CNF	39	61	41	59	40	60	40	1.0	60	1.0
Hexyl Ether CNF	43	57	44	56	45	55	44	1.2	56	1.2
LA-CNF-2	58	42	56	44	60	40	58	1.5	42	1.5
LA-CNF-3	56	44	55	45	57	43	56	1.1	44	1.1
LA-CNF-4	50	50	51	49	52	48	51	0.9	49	0.9
GP-LC-CNF-4	43	57	42	58	43	57	43	0.8	57	0.8
LC-CNF-1	51	49	50	50	51	49	51	1.0	49	1.0

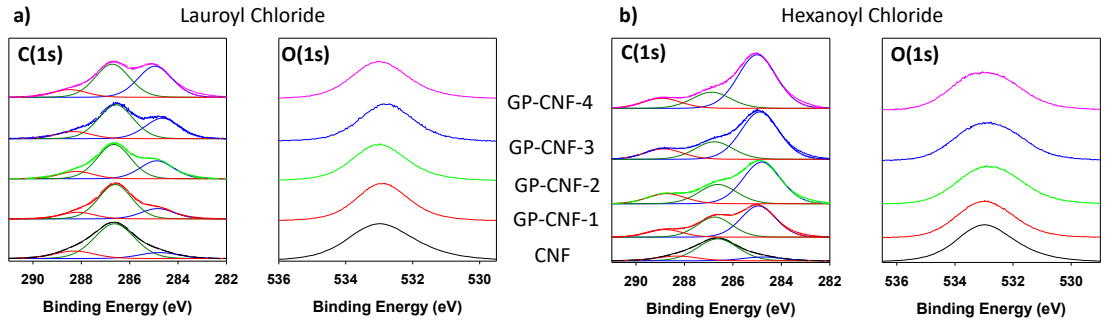

Figure 8.10 X-ray photoelectron fit C(1s) and O(1s) regions for cellulose nanofibrils (CNFs) functionalized with gas phase a) lauroyl chloride and b) hexanoyl chloride

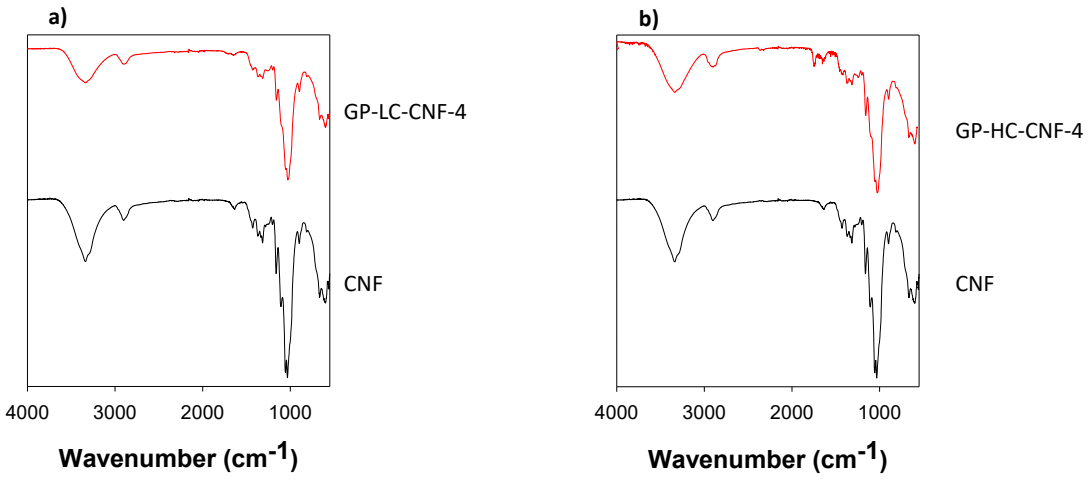

Figure 8.11 Attenuated total reflectance infrared spectra of cellulose nanofibrils (CNFs) esterified with gas phase a) lauroyl chloride and b) hexanoyl chloride

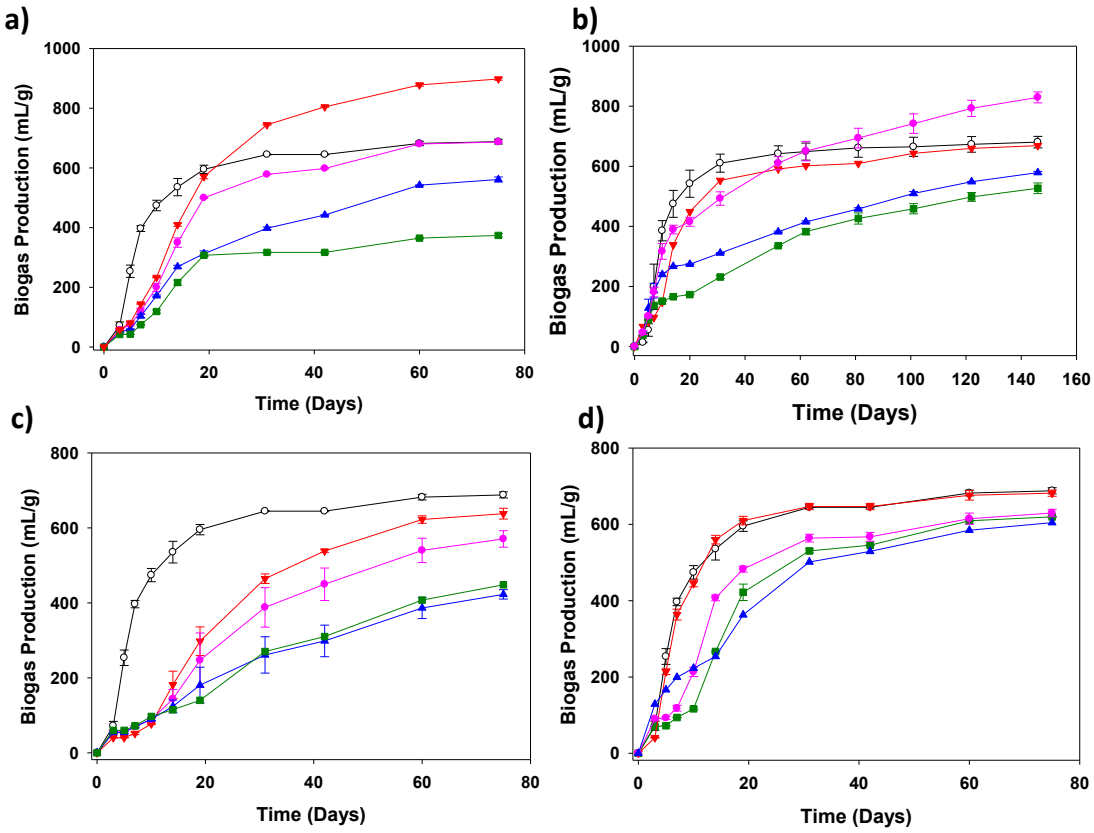

Figure 8.12 Unnormalized biogas production of cellulose nanofibrils (white circles) functionalized with a) liquid phase lauroyl chloride, b) liquid phase lauric acid, c) gas phase hexanoyl chloride, and d) gas phase lauroyl chloride during mineralization by an anaerobic microbial community. In each plot, increasing degree of surface substitution follows the order: red down triangles, pink circles, blue up triangles, green squares. Error bars represent one standard deviation of the average from duplicate samples.

Chapter 9. Appendix 4—Photochemical Transformations of Carbon Dots in Aqueous Environments

Reproduced From

Frank, B. P.; Sigmon, L.; Deline, A.; Lankone, R. S.; Gallagher, M.; Zhi, B.; Haynes, C. L.; Fairbrother, D. H., Photochemical Transformations of Carbon Dots in Aqueous Environments. *Environ. Sci. Technol.* **2020**. *54* (7), 4160-4170

9.1 Synthesis of CDs

Carbon dots (CDs) were synthesized via bottom up microwave-assisted pyrolysis adapted from a previously reported method.[1] 2 mL of a 4 M citric or malic acid solution and 540 μL of ethylenediamine were combined in a beaker, allowed to react (exothermic), and subsequently cooled at room temperature for 30 min. The mixture was then heated in a microwave oven at 700 W for 2 min. Approximately 10 mL of deionized water was added to the resultant solid and the mixture was magnetically stirred for 30 min, or until it completely dissolved. Dialysis tubing (0.1-1.0 kDa pore size) was prepared by soaking in deionized water for 30 min, before adding the dissolved CDs and dialyzing against deionized water for 24 h. The solution was transferred to an oven and dried at 40 °C until all water was evaporated and a red-brown solid remained.

9.2 Characterization of CDs

Transmission Electron Microscopy (TEM): TEM images of CACDs and MACDs were obtained using a FEI Tecnai F30 TEM with a 300 kV electron beam.

UV-Visible Spectroscopy (UV-Vis): UV-visible extinction spectra were measured from 200 to 800 nm using a Thermo Scientific Evolution 220 UV-Visible spectrometer (Waltham, MA). CDs were analyzed at 15 mg/L.

Photoluminescence (PL) Tests: Fluorescence (PL) spectra were obtained using a Thermo Scientific Lumina fluorescence spectrometer (Waltham, MA). An excitation wavelength of 350 nm was used and emission spectra were recorded from 360 to 650 nm with a 0.1 nm interval, a photomultiplier tube voltage of 700 V, and a 20 ms integration time. Excitation and emission slit widths of 2.5 nm were used for CACD solutions and slit widths of 5 nm were used for MACD solutions. To avoid interference from inner filter effects, all CD solutions used in PL spectroscopy had absorbances of ≤ 0.1 at the characteristic peak at approximately 350 nm. CDs were analyzed at 15 mg/L.

Total carbon (TC)/Total Nitrogen (TN)/Ion Chromatography (IC)/Charged Aerosol Detection analysis: Solutions of 100 mg/L CACDs and MACDs were exposed to natural sunlight or $^{\bullet}OH$. Test tubes wrapped in aluminum foil to prevent light exposure were used as dark controls, and Milli-Q water samples were used as blank controls. CD samples were diluted with Milli-Q water after photolysis to a volume of 20 or 40 mL for TC analysis. Diluted samples were filtered through a 0.20 μm PES syringe filter into acid-washed TC vials before injection into a Shimadzu TOC-L total organic carbon analyzer equipped with a Shimadzu TNM-L total nitrogen measuring unit and an ASI-L Shimadzu auto sampler (Kyoto, Japan). TC and TN signals were converted into CD concentrations (mg/L) via reference to calibration curves prepared with CDs. For TN, the CD concentration was converted into mg N/L using a standard of sodium nitrate solution as a reference. For IC, filtered samples prepared for TC/TN analysis were transferred into 0.5 mL vials and

analyzed with no further sample pre-treatment using Dionex ICS-2100 system (Thermo Fisher, Waltham, MA) equipped with an AS18 ion exchange column. Samples were run using a 67 mA suppressor current and 30 mM KOH eluent flow at a rate of 1 mL/min. A nitrate calibration curve was prepared from a combined seven anion standard (Thermo Fisher, Waltham, MA).

254 nm Irradiation

Total Organic Carbon (TOC)

Citric acid carbon dots (CACDs) and malic acid carbon dots (MACDs) were suspended at 100 ppm in HPLC-grade water and added in 10 mL aliquots to a 15 mL quartz test tube. Samples were irradiated by 254 nm light for a range of exposures before being diluted with 10 mL HPLC-grade water to achieve necessary volume for TOC. These diluted samples were then filtered through a 0.20 μm PES syringe filter into cleaned TOC vials. Each carbon dot solution was sampled 3 times, with the furthest outlier being removed as determined by the TOC software. TOC signal was approximately translated into concentration of carbon dots (ppm) via reference to a calibration curve made with each carbon dot type (i.e., malic or citric acid).

Charged Aerosol Detection (CAD)

Samples prepared for TOC analysis were also measured using CAD. The advantages of using CAD include high precision, low required sample volume, and rapid data acquisition. In addition, CAD is a measurement of the total dissolved solids (TDS) in a solution, not solely carbon-containing species. In this way, CAD serves as a more direct quantification of the carbon dots or degradation products left in solution, as it takes into account dissolved

nitrogen species even if they lack carbon content. Thus, the calibration curve for MACD and CACD is directly a reference to the remaining carbon dot or degradation products in solution, not just species which contain carbon as in the TOC measurement. Samples for CAD were taken directly from TOC samples after TC and NPOC analysis. These samples (already filtered through 0.20 μm PES syringe filter for TOC) were then injected into a Waters 515 HPLC Pump with a 1 mL/min flow rate using 70% degassed methanol as a mobile phase. The pump injected samples into a Dionex Corona Veo Charged Aerosol Detector in duplicate to confirm precision in reference to a calibration curve made using MACD or CACD.

Attenuated Total Reflectance Infrared (ATR-FTIR) spectra: Solutions of CACDs and MACDs were exposed to natural sunlight (at 2000 mg/L) or •OH (at 350 mg/L) and lyophilized (LabConco FreeZone 2.5 Plus, 2.5L, Kansas City, MO) into powders. ATR-FTIR of lyophilized CD samples were obtained using a Nicolet iS5 (Thermo Fisher, Waltham, MA) spectrometer with an iD5 ATR attachment using a scan range from 4000-525 cm^{-1} with 64 scans at 0.964 cm^{-1} resolution.

X-ray Photoelectron Spectroscopy (XPS): Solutions of CACDs and MACDs were exposed to natural sunlight (at 2000 mg/L) or •OH (at 350 mg/L) and lyophilized into powders. XPS of lyophilized CDs were obtained using a PHI (Chanhassen, MN) 5600 XPS equipped with a Mg Kα flood source (1253.6 eV) and a hemispherical energy analyzer. High-resolution multiplex scans were collected at ultra-high vacuum (8×10^{-8} torr) with a source power of 300 W, a pass energy of 29.35 eV, 10 sweeps per spectrum, and 0.125 eV/step. Survey scans (1200-0 eV binding energy) were collected at the same ultra-high vacuum with a

pass energy of 58.7 eV, 2 sweeps per spectrum, and 1.0 eV/step. Spectra were analyzed using CASA XPS software.

NMR: For ^{1}H-NMR analysis, 600 µL of a 5 mg/mL solution of CACDs was exposed to natural sunlight and analyzed in a NMR tube using a 400 MHz NMR (Bruker UltraShield, Billerica, MA). For ^{13}C-NMR, 600 µL of a 1.7×10^{4} mg/L solution of photobleached CACDs exposed to $^{\bullet}$OH was analyzed using the same spectrometer, run for 100 scans and 160 loops. Due to the higher concentration of CDs needed for NMR (1.7×10^{4} mg/L vs. 350 mg/L for ATR-FTIR/XPS data), a higher $^{\bullet}$OH dose was required to drop the TC in solution to 40% of the initial concentration, allowing for the direct comparison between the XPS/ATR-FTIR and NMR of the CDs. This amount of carbon loss required a $^{\bullet}$OH dose of 5.7×10^{-8} M*min and corresponded to the point in the carbon loss profile at the end of the first phase of degradation by $^{\bullet}$OH (see Figure 5.3).

9.3 Natural Sunlight Exposures

Photobleaching: CACD and MACD solutions with concentrations of 15 mg/L were prepared; solutions wrapped in aluminum foil to prevent light exposure were used as dark controls. Samples were exposed to natural sunlight and at time intervals of 0 min, 30 min, 1 h, 2 h, and 12 h, two irradiated CD samples (light replicates) and a single dark control were removed. After removal, undiluted samples were analyzed using UV-vis and PL spectroscopy.

Photobleaching Images: CACD and MACD solutions with concentrations of 100 mg/L were prepared and exposed to natural sunlight for 0, 30 min, and 1, 4, 8, 12, 24, and 48 h. After exposure, samples were analyzed with UV-Vis and PL spectroscopy and images were taken under indoor or 350 nm light.

Photobleaching in Lab Light: CACD and MACD solutions with concentrations of 100 mg/L were prepared and exposed to laboratory fluorescent lighting (emission spectrum in Figure 9.9b) for 10 days. After exposure, samples were analyzed with PL spectroscopy.

Effect of O_2 and N_2 Sparging: CACD and MACD solutions with concentrations of 15 mg/L were prepared and either left untreated or were treated by bubbling with N_2 or O_2 for 15 minutes. Samples wrapped in aluminum foil to prevent light exposure were used as dark controls. Samples were exposed to natural sunlight at time intervals of 2 min, 4 min, 6 min, 10 min, 30 min, 1 h, 2 h, 4 h, 6 h, and 24 h. For each time interval, two irradiated CD samples (light replicates) and a single dark control were removed. After exposure, undiluted samples were analyzed using UV-visible and PL spectroscopy.

Aggregation/Settling Test: CACD and MACD solutions with CD concentrations of 15 mg/L were prepared and the pH was adjusted to 7 or 8 using 1M HCl or 4M NaOH. For each type of CD at each pH, four samples containing 8 mL each of CD solution were prepared. One irradiated sample and one dark sample had NaCl, KCl, and $CaCl_2$ added to produce final salt concentrations of 15 mg/L NaCl, 400 mg/L KCl, and 400 mg/L $CaCl_2$ (4 mM Ca^{+2}, 13 mM Cl^-, 0.3 mM Na^+, 5 mM K^+). Blanks containing Milli-Q water with or without salts were also prepared. All samples were analyzed after 1 week of settling using PL spectroscopy.

TC and TN: Solutions of 100 mg/L CACDs and MACDs were exposed to natural sunlight for 0, 1, 2, 3, 4, 5, and 6 weeks. Samples were analyzed for TC and TN. Samples wrapped in aluminum foil were used as dark controls and Milli-Q water was used for blank controls.

ATR-FTIR and XPS: Solutions of 2000 mg/L CACDs and MACDs were exposed to natural sunlight for 2, 4, and 6 weeks and lyophilized (LabConco FreeZone 2.5 Plus, 2.5L, Kansas City, MO) into powders. ATR-FTIR and XPS were run on the recovered CD powder from each time point.

^{1}H-NMR: A 900 µL sample of CACDs at 5 mg/mL in D_2O was exposed to natural sunlight alongside an identical sample wrapped in aluminum foil to serve as a dark control. After 5 d of exposure, samples were retrieved from the roof and immediately transferred into an NMR tube for analysis.

Mass Recovery Experiments: A known mass of CACDs (~15 mg) was added to 6 mL of DI water and exposed in triplicate to natural sunlight for 21 d on a rooftop. Controls included an identical triplicate set of tubes wrapped in aluminum foil to serve as dark controls, and triplicate vials of pure DI water to serve as blanks. After 21 d of irradiation, the samples were lyophilized in pre-weighed centrifuge tubes and weighed using an analytical balance to determine the % recovery of CDs after natural sunlight exposure. It was determined that CACDs exposed to sunlight for 21 d yielded 101.4 % +/- 2.1 % recovery, comparable to the dark control samples which were recovered at 95.8 % +/- 3.5 %, while, as expected, no mass was recovered from the blank controls. pH of these solutions was measured to be ~7 using litmus paper both before and after 21 days of exposure to natural sunlight.

9.4 Exposure to ˙OH Radicals

CD solutions at 100 mg/L were placed into a Rayonet reactor and irradiated with 300 nm UV light (16 bulbs, RPR-300). Samples were dosed daily with 100 mM H_2O_2. UV-Vis was used to measure the loss of H_2O_2 over time and ensure that each dose of H_2O_2 was fully reacted before the next H_2O_2 dose was added.

TC/TN/IC: 10 mL samples at 100 mg/L CACD and MACD were removed from the Rayonet after ˙OH doses up to 4.0×10^{-8} M*min and 2.8×10^{-8} M*min, respectively. Samples wrapped in aluminum foil were used as dark controls and Milli-Q water was used as a blank control. Samples were analyzed using TC, TN, and IC.

ATR-FTIR and XPS: Samples for spectroscopic analysis were prepared at 350 mg/L CACDs or MACDs and exposed to ˙OH doses up to 1.1×10^{-8} M*min before being lyophilized and compared to the unexposed parent CDs. Samples were analyzed using ATR-FTIR and XPS.

^{13}C-NMR: CD samples for ^{13}C-NMR were first photobleached at 1.7×10^{4} mg/L and then reacted with an ˙OH dose of 5.7×10^{-8} M*min ˙OH. A ^{13}C-NMR was then prepared at 1.7×10^{4} mg/L CACD/L D_2O solution.

9.5 Quantification of ˙OH Radical Dose

Procedures used here have been reported in greater detail by Lankone et al.,[2] In brief, salicylic acid (SA) was used at 0.07 mM as a probe molecule that could be quantified using UV-Vis spectroscopy. In the presence of ˙OH radicals, SA reacts to form 2,3-dihydroxybenzoic acid and 2,5-dihydroxybenzoic acid. Under irradiance with 300 nm light (in absence of ˙OH radicals), SA is photostable and decreases in concentration by less than

4% over the 30 s necessary to perform the outlined measurements. To enable deconvolution of SA from the two product species (2,3-dihydroxybenzoic acid and 2,5-dihydroxybenzoic acid), reference solutions of each compound at a known concentration were prepared. UV-Vis spectra were collected of these reference solutions and later used to determine the concentration of SA during •OH exposure in solutions containing a mixture of SA, 2,3-dihydroxybenzoic acid and 2,5-dihydroxybenzoic acid. Since the rate constant for the reaction of SA with •OH radicals is known ($5x10^9$ M^{-1} s^{-1}), measuring the rate of SA degradation enabled the steady state •OH concentration to be determined for a given dose of H_2O_2. Crucially, CD exposure to H_2O_2 in the present study was performed in the absence of SA, necessitating a correction factor be applied to the •OH radical concentration measured with SA (from Lankone et al.) to determine the actual •OH radical concentration present in solutions used to photolyze CDs in these experiments. As part of the present study, we evaluated the $[OH]_{ss}$ in the presence of CDs to show that for the concentrations used (1 - 319 mg/L), the presence of CDs did not have an impact on $[•OH]_{ss}$ (Figure 9.1).

H_2O_2 concentration in the quartz vessels was tracked over time using UV-Vis spectroscopy, which, along with knowledge of the $[•OH]_{ss}$ throughout the decomposition of H_2O_2, allowed for the dose of •OH radicals for each experiment to be determined. Moreover, this dose could also be related to the timescale in the environment which would deliver the equivalent •OH dose. For example, a single 100 mM dose of H_2O_2 results in an average steady state •OH radical concentration of 5.79×10^{-12} M*min for a total exposure time of approximately 8 h. Environmental $[•OH]_{ss}$ values in surface waters have been reported on the order of 10^{-15}-10^{-17} M.[3-5] In a given month, then (assuming a maximum exposure to •OH at 10^{-15} M), we can estimate the dose of •OH radicals delivered in the

natural environment is the product of 10^{-15} M and 21,600 min (i.e., minutes in a 30 day month, assuming 12 h of sunlight per day). Therefore, cumulative exposure to $^{\bullet}OH$ from a single 100 mM H_2O_2 dose across its degradation period (i.e., 8 hours of 300 nm irradiation) can be estimated to be roughly 129 months of environmental $^{\bullet}OH$ exposure. Table 9.1 summarizes the relationship between H_2O_2 dose and environmental timescale.

9.6 BMP Media Preparation

CDs were biodegraded using biomethane potential tests (BMP). Digested anaerobic sludge used in BMP tests was collected at the Back River Wastewater Treatment Plant, (Baltimore, MD) from the running digester outlet and was used as inoculum. Media was prepared following the recipe outlined in Owen et al, with minor modifications.[6] The CD samples were biodegraded over 130 d.

9.7 Measuring Biogas Production and Composition

Samples containing 150 mg of CDs and 100 mL of defined anaerobic medium and inoculum were incubated in three biological replicates at 35 ± 0.5 °C until biogas production plateaued. Biogas and methane production were normalized to the mass added to each bottle to account for this difference. Glass, gastight syringes (5-50 mL depending on evolved gas volume) lubricated with deionized water and equipped with 20-gauge needles were used for gas volume measurements. After the volumetric reading and equilibration of the BMP serum bottle headspace to atmospheric pressure, 250 µL of gas phase was sampled using a Hamilton SampleLock syringe, and assayed for CH_4 and CO_2 content using a Shimadzu GC-8A gas chromatograph equipped with a Hayes Q 80/100 column and a thermal conductivity detector (TCD). An injection temperature of 130 °C, a column with a current of 80 mA, and helium as a carrier gas at a pressure of 2 bar were

used. Analytical standard grade N_2, CO_2, and CH_4 gases (Supelco >98% purity), each injected into the GC at 50, 150, and 250 µL, were used to calibrate the GC-TCD prior to sample gas composition measurements.

9.8 Figures

Table 9.1 Relationship between initial H_2O_2 concentration and photolysis time to $^{\bullet}OH$ dose. The range of environmental timescale for equivalent $^{\bullet}OH$ exposure in natural surface waters is also indicated, with the minimum and maximum values determined assuming a steady state $^{\bullet}OH$ concentration of 10^{-15} M and 10^{-17} M, respectively. Hydrogen peroxide doses beyond (2x) 100 mM yielded a linear increase in both hydroxyl radical dose and equivalent environmental exposure.

Total H_2O_2 Dose (mM)	Photolysis Time (min)	$^{\bullet}OH$ Dose (M*min)	Minimum Environmental Timescale (Months)	Maximum Environmental Timescale (Months)
25	60	3.5E-10	16	1606
50	120	6.9E-10	32	3211
75	180	1.0E-09	48	4817
100	240	1.4E-09	64	6422
(2x) 100	960	5.5E-09	257	25689
(3x) 100	1440	8.3E-09	385	38533
(4x) 100	1920	1.1E-08	514	51378

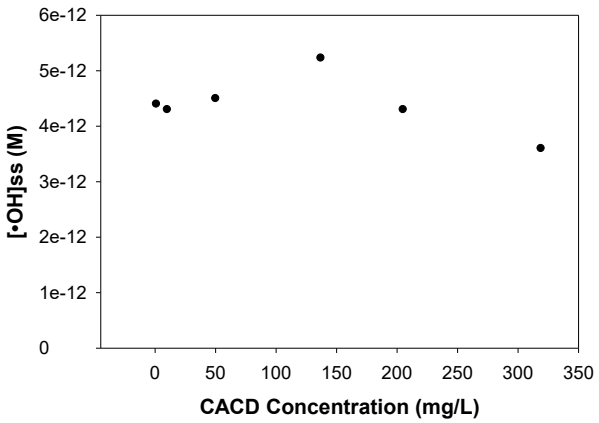

Figure 9.1 Steady state concentration of •OH ([•OH]$_{ss}$) generated by photolysis of 100 mM H_2O_2 in the presence of 1-319 mg/L photobleached CACDs.

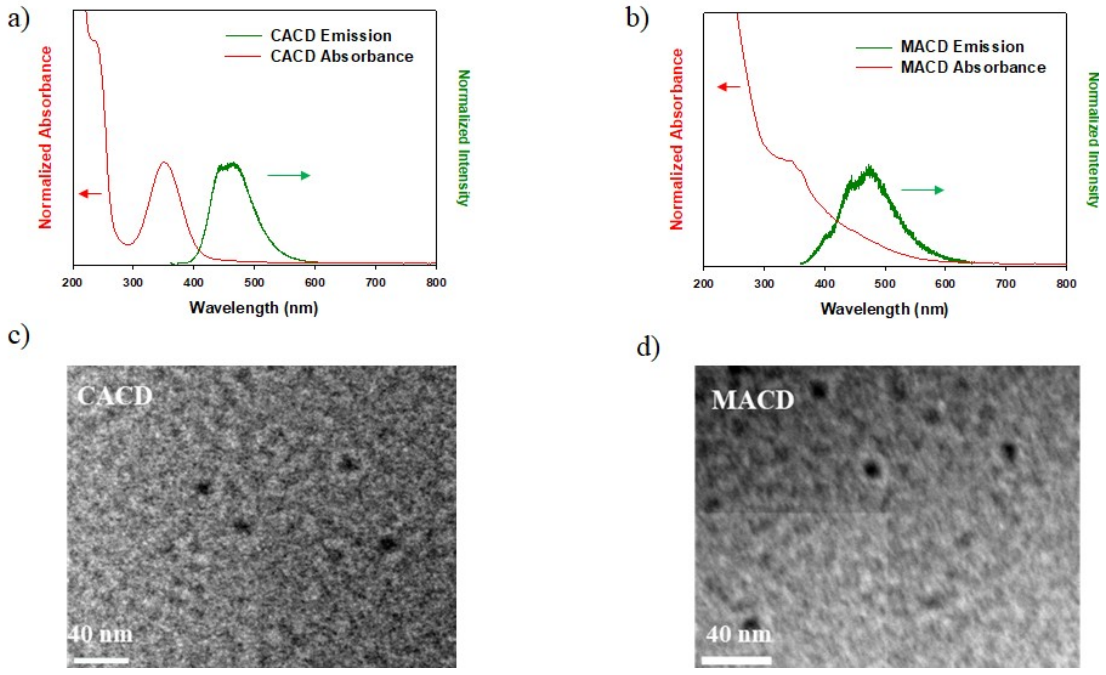

Figure 9.2 Characterization of parent CDs. Emission and absorption profiles of CACDs (a) and MACDs (b). Transmission electron microscopy of CACDs (c) and MACDs (d).

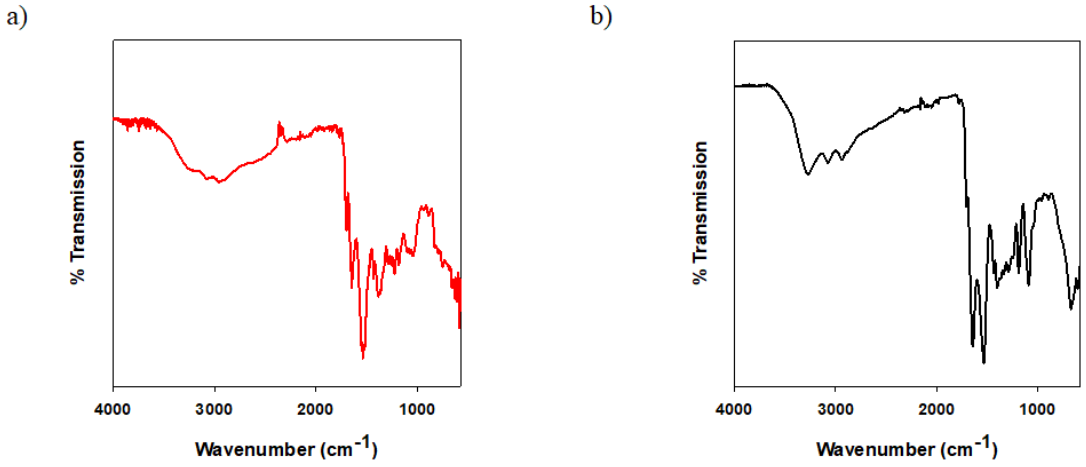

Figure 9.3 ATR-FTIR spectra of lyophilized as-synthesized CACDs (a) and MACDs (b).

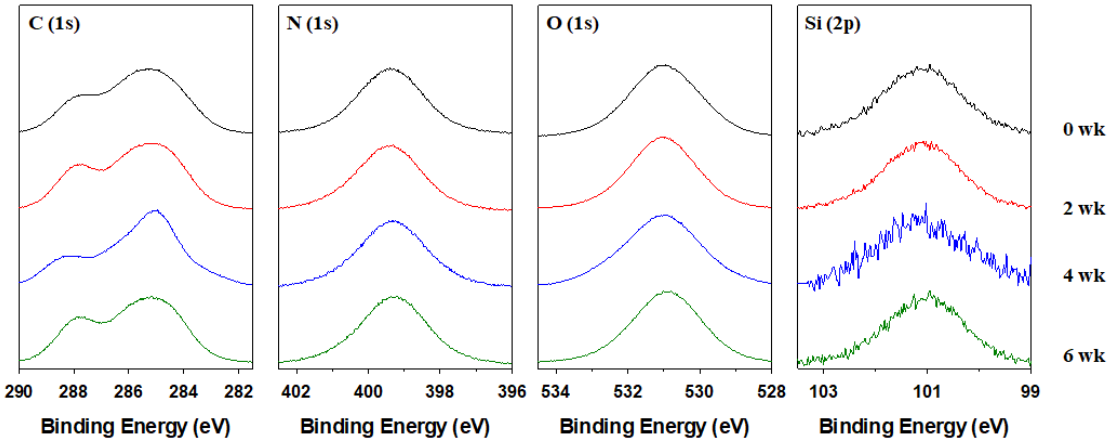

Figure 9.4 Normalized C (1s), N (1s), O (1s), and Si (2p) XPS regions of lyophilized CACDs after exposure to 0 (black), 2 (red), 4 (blue), and 6 (green) weeks of natural sunlight. Silicon is from SiO_2, residual from CD synthesis.

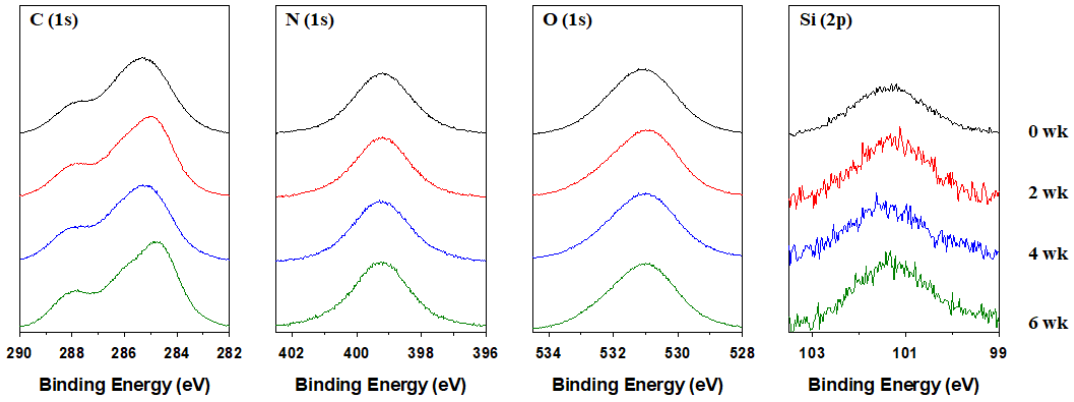

Figure 9.5 Normalized C (1s), N (1s), O (1s), and Si (2p) XPS regions of lyophilized MACDs after exposure to 0 (black), 2 (red), 4 (blue), and 6 (green) weeks of natural sunlight. Silicon is from SiO_2, residual from CD synthesis.

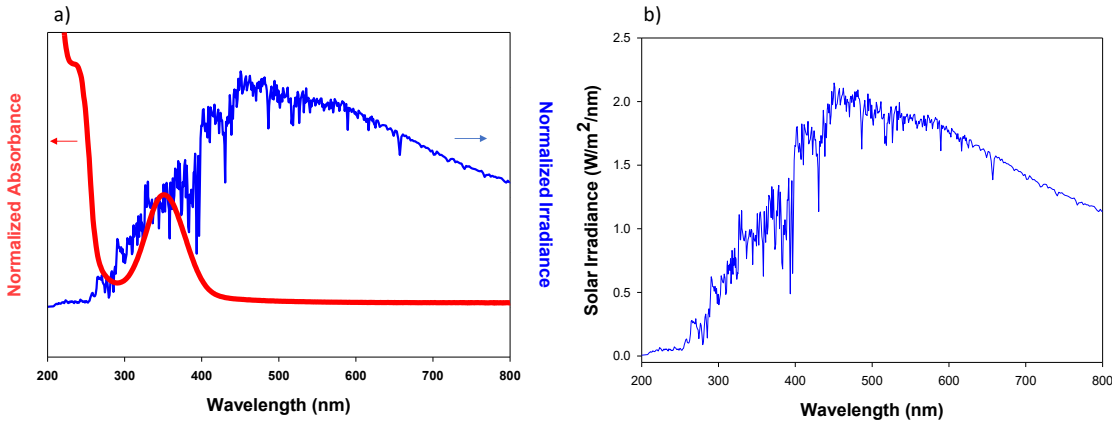

Figure 9.6 a) Absorption profile of CACDs (red) overlaid with the solar irradiance spectrum (blue, obtained from https://www.nrel.gov/grid/solar-resource/spectra-astm-e490.html). b) Solar irradiance spectrum with units.

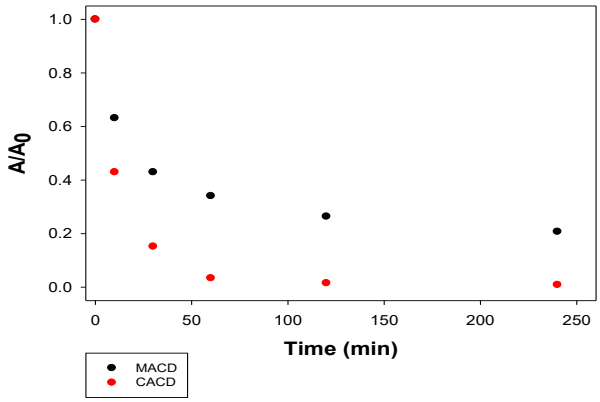

Figure 9.7 Photobleaching rates of 15 mg/L CACDs (red) or MACDs (black) after 240 min of natural sunlight exposure as measured by photoluminescence spectroscopy (PL). Fluorescence is shown in terms of the area of the emission curve at each time point normalized to the initial emission at t=0.

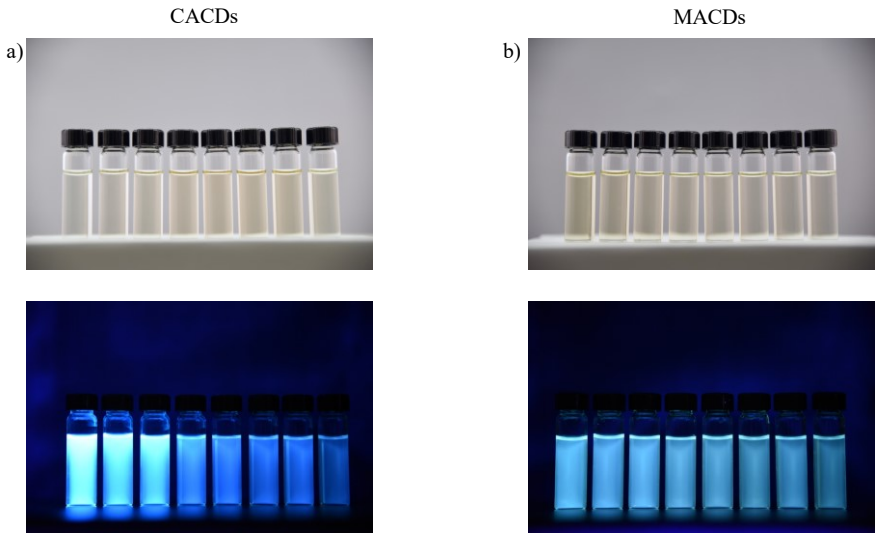

Figure 9.8 Photographs of 100 mg/L solutions of CACDs (a) and MACDs (b) after exposure to 0, 0.5, 1, 4, 8, 12, 24, or 48 hr (left to right) of sunlight. Samples are shown post-exposure under either lab light (top) or 350 nm light (bottom).

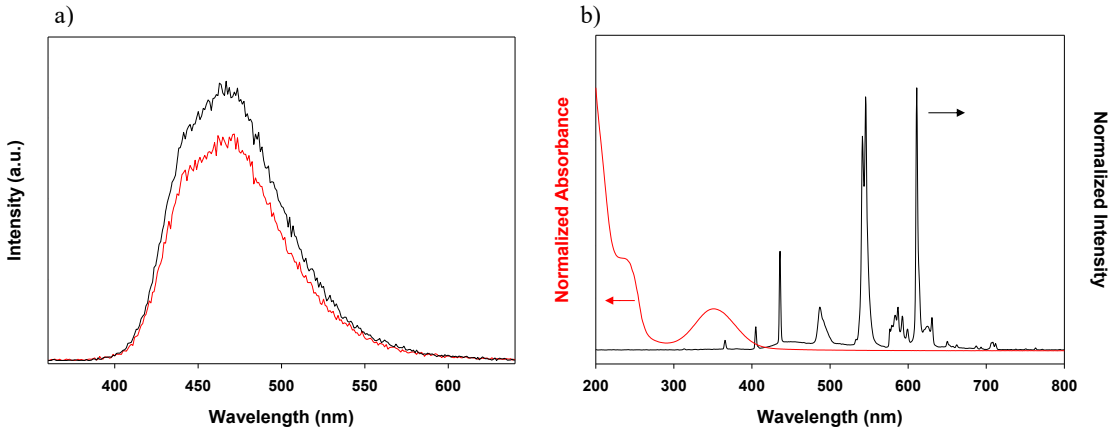

Figure 9.9 a) Photoluminescence spectra of CACDs before (black) and after (red) 10 days of laboratory fluorescent light exposure. b) Absorption profile of CACDs (red) overlaid with the emission spectrum of fluorescent indoor bulbs (black). CD concentration matched that used in natural sunlight exposures (i.e., 100 mg/L).

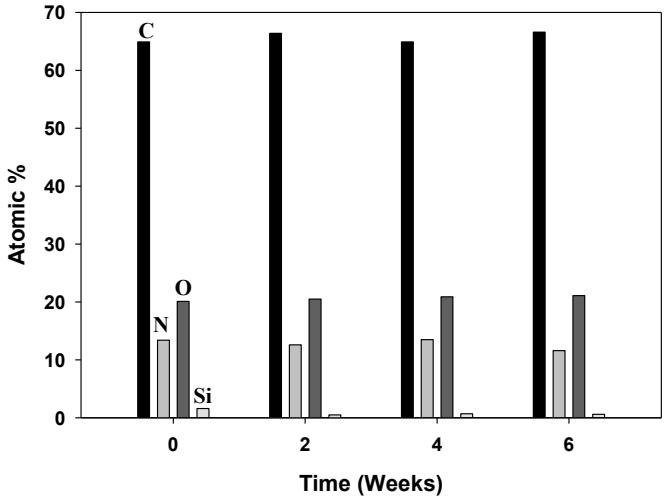

Figure 9.10 Atomic composition of lyophilized MACDs exposed to 0-6 weeks of natural sunlight as determined by XPS.

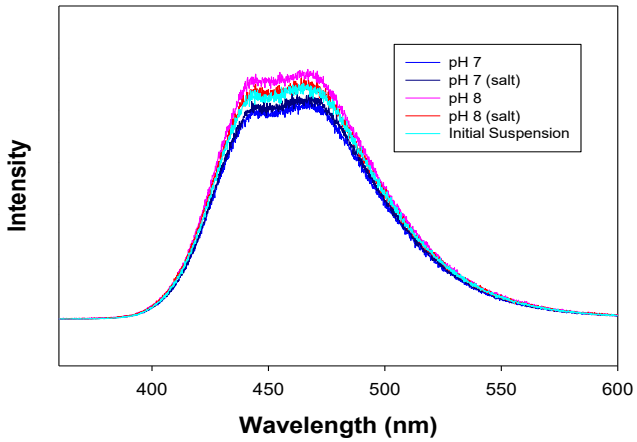

Figure 9.11 Photoluminescence spectroscopy of 15 mg/L CACD fluorescence before and after 1 week of settling at pH 7 or 8 in pure water or in a mixture of 15 mg/L NaCl, 400 mg/L KCl, and 400 mg/L $CaCl_2$ (4 mM Ca^{+2}, 13 mM Cl^-, 0.3 mM Na^+, 5 mM K^+).

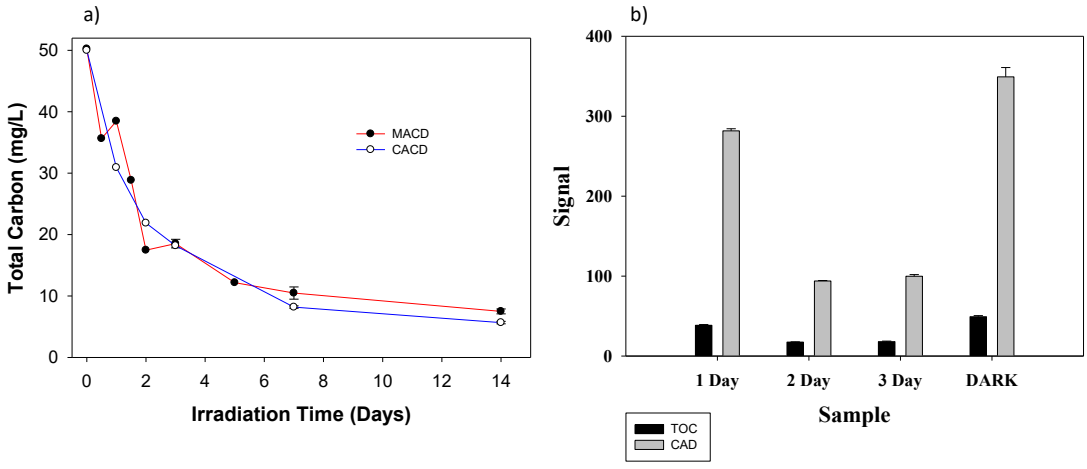

Figure 9.12 a) Total carbon of MACD (red) and CACD (blue) solutions during 14 d exposure to 254 nm light. b) Comparison of total carbon and total dissolved carbon of CACDs after 3 d exposure to 254 nm light. Total carbon and total dissolved solids were measured by TOC and CAD, respectively.

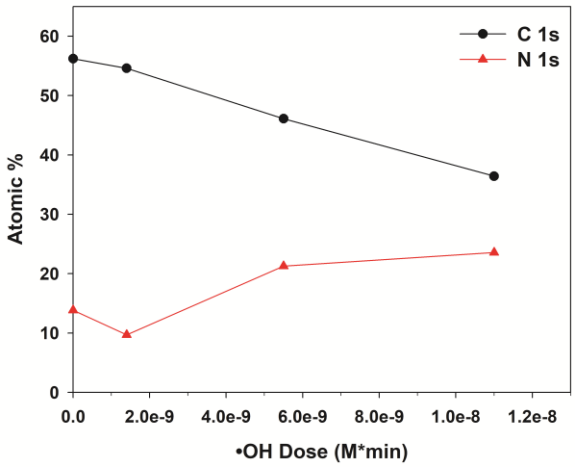

Figure 9.13 Atomic % of carbon (black) and nitrogen (red) in lyophilized CACDs after exposure to a dose of 0-1.1×10^{-8} M*min •OH as determined with XPS.

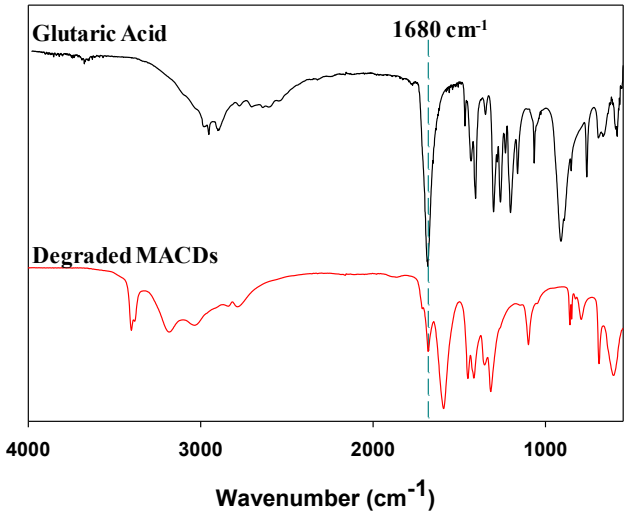

Figure 9.14 ATR-FTIR spectrum of glutaric acid (black) compared to lyophilized MACDs exposed to 5.5×10^{-9} M*min •OH (red). Dotted line at 1680 cm^{-1} marks the C=O stretch of a carboxylic acid group.

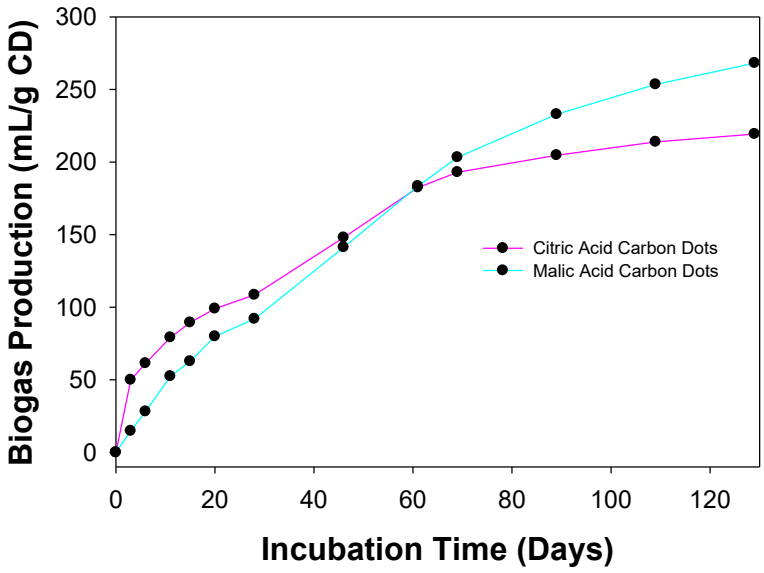

Figure 9.15 Biodegradation of CACD and MACD by an anaerobic microbial community over 130 d assessed via biogas production. Biogas evolution was normalized to the mass of CD sample.

9.9 References

1. Zhi, B.; Gallagher, M. J.; Frank, B. P.; Lyons, T. Y.; Qiu, T. A.; Da, J.; Mensch, A. C.; Hamers, R. J.; Rosenzweig, Z.; Fairbrother, D. H.; Haynes, C. L., Investigation of Phosphorous Doping Effects on Polymeric Carbon Dots: Fluorescence, Photostability, and Environmental Impact. *Carbon* **2018,** *129*, 438-449.

2. Lankone, R. S.; Barclay, M.; Deline, A. R.; Fairbrother, D. H., Quantifying hydroxyl radical concentrations and total dose via principle component analysis of UV-Vis Spectroscopy. *Anal. Methods* **Submitted**.

3. Hou, W.-C.; Henderson, W. M.; Chowdhury, I.; Goodwin, D. G.; Chang, X.; Martin, S.; Fairbrother, D. H.; Bouchard, D.; Zepp, R. G., The contribution of indirect photolysis to the degradation of graphene oxide in sunlight. *Carbon* **2016,** *110*, 426-437.

4. Haag, W. R.; Hoigné, J., Photo-sensitized oxidation in natural water via .OH radicals. *Chemosphere* **1985,** *14* (11), 1659-1671.
5. Page, S. E.; Logan, J. R.; Cory, R. M.; McNeill, K., Evidence for dissolved organic matter as the primary source and sink of photochemically produced hydroxyl radical in arctic surface waters. *Environ. Sci. Proc. Imp.* **2014,** *16* (4), 807-822.
6. Owen, W. F.; Stuckey, D. C.; Healy, J. B.; Young, L. Y.; McCarty, P. L., Bioassay for Monitoring Biochemical Methane Potential and Anaerobic Toxicity. *Water Res.* **1979,** *13* (6), 485-492.

Chapter 10. Curriculum Vitae

Benjamin P. Frank, Ph.D.

6112 Bellinham Ct., Apt. 512, Baltimore, MD 21210

Phone: 215-266-1016 | Email: benjaminphillipfrank@gmail.com

Summary

Ph.D. chemist (May 2020 defense) with a strong work ethic who is adept in the characterization, functionalization, and bio-/photo-degradation of thin film polymer nanocomposites, cellulosic materials, and nanoparticles. Experienced in a wide range of experimental techniques including XPS, FTIR, and SEM/EDS and interpreting and presenting data to both technical and non-technical audiences. Has 3 years of experience managing day-to-day operations of a multi-user central analytical facility including instrument maintenance, operation, and supporting data collection/analysis. Well-versed in planning, conducting, and managing productive scientific research and writing in a highly collaborative, multi-institutional, and team-focused environment, as evidenced by authorship on 15 papers and 24 presentations.

Education

Ph.D. Chemistry—Johns Hopkins University **Aug 2014—May 2020**

- Thesis: "Environmental Transformations of Next-Generation Carbon Nanomaterials"
- GPA: 3.72/4.00
- Coursework: Materials & Surface Chemistry, Intermediate Quantum Chemistry, Chemical Kinetics, Methods in Time-Resolved Spectroscopy, Responsible Conduct of Research, Experimental Methods in Physical Chemistry, Research Laboratory Safety, Physical and Chemical Processes II, Micro/Nano-Structured Materials and Devices, Chemical and Biological Properties of Materials

M.A. Chemistry—Johns Hopkins University **Aug 2014—Oct 2016**

B.S. Chemistry (Cum Laude)—University of Pittsburgh Aug 2010—Apr 2014

- GPA: 3.41/4.00
- Honors
- Concentration in Biological Sciences
- Coursework: General Chemistry I & II, Analytic Geometry & Calculus II, Foundations of Biology (Lecture and Lab) I & II, Organic Chemistry (Lecture and Lab) I & II, Introduction to Physics I & II, Introduction to Laboratory Physics, Analytic Geometry and Calculus III, Introduction to Analytical Chemistry (Lecture and Lab), Instrumental Analysis (Lecture and Lab), Physical Chemistry I & II, Physical Chemistry Lab I, Chemical Biology, Ecology

Research Experience

Ph.D. Candidate, Johns Hopkins University (Baltimore, MD) Aug 2014—Present

Supervisor: Dr. D. Howard Fairbrother, Professor, Department of Chemistry

1. Influence of Polymer Type and Carbon Nanotube Properties on Carbon Nanotube/Polymer Nanocomposite Biodegradation
    - Determined that the environmental biodegradation of polymer nanocomposite thin films is slowed when loaded with carbon nanotubes (CNTs), and this effect occurs at lower CNT loadings under conditions (polymer, microbe, CNT type) which promote a slow biodegradation process
    - Created carbon nanotube polymer composites via solution blending, and characterized materials using both surface and bulk sensitive techniques
    - Quantified biodegradation by tracking biogas production and assessing biogas composition via gas chromatography
2. Impact of Chemical Modification on the Biodegradation of Nanocellulose
    - Discovered that hydrophobic coatings (siloxane resins) improve the dispersion of nanocellulose in organic media and polymer as a function of extent and hydrophobicity of the coating, but biodegradability of coated nanocellulose is decreased
    - Utilized anaerobic and aerobic microbial cultures to biodegrade various nanoparticles, polymers, and reagents as a means to understand the environmental impact of next-generation nano-enabled products
    - Showed for the first time that covalent modifications inhibit the biodegradation of nanocellulose as a function of the degree of surface substitution rather than the overall degree of substitution
    - Used XPS, NMR (in collaboration with Pedersen group, University of Wisconsin), and FTIR to characterize various surface modifications of

cellulosic materials in order to understand the impact of such treatments on biodegradation and dispersion in hydrophobic media
    - Characterization of nanoparticles both native and functionalized, polymers, and precursor compounds using a variety of spectroscopic techniques including XPS, ATR-FTIR, SEM/EDS, NMR, and Uv-Vis
    - Development of protocols for the preparation of nanocellulose functionalized with a variety of ether, ester, and carboxylic acid groups
    - Lead contributor to project within NSF-funded Center for Sustainable Nanotechnology (CSN) focused on designing sustainable nanocellulose for material reinforcement
3. Environmental Transformations of Carbon Dots
    - Mechanistically explained the photolytic degradation process of carbon nanodots by analyzing subtle spectroscopic changes (XPS and FTIR)
    - Determined that carbon dots will primarily degrade via interactions with reactive oxygen species in the environment, leading to conversion of carbon to CO_2 and nitrogen to nitrate ions
    - Compared findings to established systems via extensive literature searching to determine that the environmental transformations of carbon dots are sensitive to the precursors used in their synthesis
4. Management Experience and Teamwork
    - Training and supervising the research activities of two post-doctoral researchers, one masters student, five undergraduates, and three visiting international students as well as several Ph.D. candidate graduate students
    - Working effectively in a multi-disciplinary lab on projects with chemists, biologists, material scientists, and environmental engineers
    - Highly experienced in productively conducting work remotely and over video calls due to working in a highly collaborative research center involving more than 10 different groups spatially dispersed across the United States
    - Maintaining an updated and detailed laboratory notebook
    - Experienced in effective literature searching as a means to address obstacles to research via coordination with research advisor
    - Maintenance of laboratory space and instrumentation and promoting a team environment via effective communication and interpersonal skills
5. Communication and Writing Experience
    - Experience presenting work at five different national conferences and nineteen different research meetings for the Center for Sustainable Nanotechnology including presentations to an external review panel and a review panel assembled by NSF

- Meticulously edited fifteen different manuscripts (four first-author to date) throughout the peer review process
- Played a key role in researching, writing, and assembling a large review paper involving the effect of surface oxidation on the environmental properties of carbon nanotubes
- Writing annual research updates for the Center for Sustainable Nanotechnology and Johns Hopkins University
- Led Center for Sustainable Nanotechnology Professional Development Committee for two years, including organizing a student-selected external speaker series
- Presented research to a audiences with a range of experience both in person and virtually including scientists of different disciplines

Surface Characterization Lab, Johns Hopkins University Jan 2017—Present

- Managed the JHU surface characterization facility at JHU for 3 years including day-to-day maintenance and upkeep of ultra-high vacuum instrumentation and components
- Collected, interpreted, and presented data for users with a variety of projects involving thin films, coatings/resins, inks, metal complexes, ligands, silica, nanoparticles, papers, polymers, and semiconductor materials

STEM Formulations Intern, FMC Corporation (Ewing, NJ) May 2013—Aug 2013

- Developed a cost-saving method of formulating Clomazone CS herbicide by reducing curing time (estimated to save $500k annually compared to previous method)
- Characterized formulations for viscosity (rheology), herbicide release, and particle size

New Technologies Intern, Particle Sciences (Bethlehem, PA) Summer 2011 & 2012

- Developed drug-eluting medical devices using melt-mixing and injection molding techniques under Good Manufacturing Practice (GMP) and testing drug release and material hardness

Undergraduate Researcher, University of Pittsburgh Fall 2012-Spring 2014

Supervisors: Dr. Mark Rebeiz, Associate Professor, Department of Biological Sciences;

Dr. Geoffrey Hutchison, Associate Professor, Department of Chemistry

- Used AFM to determine chain length dictates spontaneity of SAM assembly for piezoelectric molecules
- Researched the evolutionary pathways of *Drosophila melanogaster* via inspection of their growth plates and DNA

Teaching Experience

Teaching Assistant, Johns Hopkins University, Department of Chemistry

- TA for General Chemistry I & II Lecture and Lab
    - Led and graded experiments involving titrations, spectroscopy, indicators, catalysts
- Head TA for Physical Chemistry Lab
    - Led and graded experiments and lab reports involving bomb calorimetry, SEM, AFM, and STM

Skills

- Experienced with X-ray photoelectron spectroscopy (XPS), Fourier transform infrared spectroscopy (FTIR), attenuated total reflectance-Fourier transform infrared spectroscopy (ATR-FTIR), Raman spectroscopy, transmission/scanning electron microscopy (TEM/SEM), energy dispersive X-ray spectroscopy (EDX/EDS), UV-Vis-NIR spectroscopy, viscosity testing (rheometry), porosity/surface area measurements (BET), Mass spectrometry (MS), tensile testing, UV-Vis spectroscopy, gas chromatography (GC), thermogravimetric analysis (TGA), differential scanning calorimetry (DSC), total organic carbon analysis (TOC), nuclear magnetic resonance spectroscopy (NMR), and atomic force microscopy (AFM), ion chromatography (IC) on a variety of samples including thin films, polymer nanocomposites, coatings, resins, inks, cellulosic materials (e.g., paper), and nanoparticles
- Statistical data analysis/processing and kinetic modeling using SigmaPlot, Microsoft Office, CASA XPS, and AugerScan as well as experience with ChemDraw and Endnote software
- Experienced in assessing structural changes of materials via interpretation of spectroscopic data especially with XPS (including peak fitting) and FTIR
- Ability to work in a collaborative environment and adapt to rapidly changing project goals and needs by offering mentorship, teamwork, flexibility, and coordination within a team
- Experienced in day-to-day laboratory tasks and instrumentation including handling microbial media, sterile technique, wet chemistry, gas phase chemistry, titration, chemical functionalization, centrifugation, gas tanks/lines, serial dilutions, colorimetric tests, analytical balance, waste disposal, preparing nanocomposites, preparing and assessing colloidal suspensions, chemical derivatization, pH probe, milling samples, suspension tests

Activities

Co-Organizer of Gordon Research Seminar **2019**

Member of the American Chemical Society	**2016-Present**
Member of the Center for Sustainable Nanotechnology (CSN)	**2015-Present**
Member of the CSN Professional Development Committee	**2015-Present**
Chair of the CSN Professional Development Committee	**2016-2018**
Member of the CSN Student Board	**2015-Present**

Awards

2019 Shepherd Memorial Travel Award ($400 value for conference travel)

Publications (15 total)

1. **Frank, B. P**.; Sigmon, L. R.; Deline, A. R.; Lankone, R. S.; Gallagher, M. J.; Zhi, B.; Haynes, C. L.; Fairbrother, D. H., Photochemical Transformations of Carbon Dots in Aqueous Environments. *Environ. Sci. Technol.* 2020, *54* (7), 4160-4170.
2. **Frank, B. P.**; Caudill, E. R.; Smith, C.; Lankone, R. S.; Carlin, K.; Pedersen, J. A.; Fairbrother, D. H., Biodegradation of Functionalized Nanocellulose is Dictated by Degree of Surface Substitution and Chemical Linkage. *Environmental Science & Technology Letters* In Preparation.
3. **Frank, B. P.**; Goodwin, D. G. J.; Bohutskyi, P.; Lu, X.; Kuwama, L.; Bouwer, E. J.; Fairbrother, D. H., Influence of Polymer Type and Carbon Nanotube Properties on Carbon Nanotube/Polymer Nanocomposite Biodegradation. *Science of The Total Environment* Submitted.
4. Deline, A. R.; **Frank, B. P.**; Smith, C.; Wallace, A.; Sigmon, L. R.; Durkin, D. P.; Goodwin, D. G., Jr.; Gallagher, M. J.; Fairbrother, D. H., Influence of Oxygen-Containing Functional Groups on the Environmental Properties, Transformations, and Toxicity of Carbon Nanotubes. *Chem. Rev.* Submitted.
5. Zhi, B.; Yao, X.; Wu, M.; Mensch, A. C.; Cui, Y.; Deng, J.; Duchimaza-Heredia, J. J.; Trerayapiwat, K.; Niehaus, T.; Nishimoto, Y.; **Frank, B. P.**; Zhang, Y.; Lewis, R. E.; Hamers, R. J.; Fairbrother, D. H.; Orr, G.; Murphy, C. J.; Cui, Q.; Haynes, C. L., Multicolor Polymeric Carbon Dots: Synthesis, Separation, and Polyamide-Supported Molecular Fluorescence. *JACS* Submitted.
6. Duraj-Thatte, A. M.; Manjula-Basavanna, A.; Courchesne, N. m.-M. D.; Cannici, G.; Sánchez-Ferrer, A.; **Frank, B. P.**; Van 't Hag, L.; Fairbrother, D. H.; Mezzenga, R.; Joshi, N. S., Aqua-Processable, Biodegradable and Coatable AquaPlastic from Engineered Microbial Biofilms *Nat. Nanotechnol.* Submitted.
7. Cheng, Y.; Smith, K. J.; Arinze, E. S.; Dziatko, R. A.; Gao, T.; **Frank, B. P.**; Thon, S. M.; Bragg, A. E., Size- and Surface-Dependent Photoresponses of Solution-Processed Aluminum Nanoparticles. *ACS Photonics* 2020.

8. Durkin, D. P.; **Frank, B. P.**; Haverhals, L. M.; Howard Fairbrother, D.; De Long, H. C.; Trulove, P. C., Engineering Lignocellulose Fibers with Higher Thermal Stability through Natural Fiber Welding. *Macromolecular Materials and Engineering* 2019, *304* (6), 1900042.
9. Alzate-Sánchez, D. M.; Ling, Y.; Li, C.; **Frank, B. P.**; Bleher, R.; Fairbrother, D. H.; Helbling, D. E.; Dichtel, W. R., β-Cyclodextrin Polymers on Microcrystalline Cellulose as a Granular Media for Organic Micropollutant Removal from Water. *ACS Appl. Mater. Interfaces* 2019, *11* (8), 8089-8096.
10. **Frank, B. P.**; Durkin, D. P.; Caudill, E. R.; Zhu, L.; White, D. H.; Curry, M. L.; Pedersen, J. A.; Fairbrother, D. H., Impact of Silanization on the Structure, Dispersion Properties, and Biodegradability of Nanocellulose as a Nanocomposite Filler. *ACS Applied Nano Materials* 2018, *1* (12), 7025-7038.
11. Zhi, B.; Gallagher, M. J.; **Frank, B. P.**; Lyons, T. Y.; Qiu, T. A.; Da, J.; Mensch, A. C.; Hamers, R. J.; Rosenzweig, Z.; Fairbrother, D. H.; Haynes, C. L., Investigation of Phosphorous Doping Effects on Polymeric Carbon Dots: Fluorescence, Photostability, and Environmental Impact. *Carbon* 2018, *129*, 438-449.
12. Phan, D. C.; Goodwin, D. G.; **Frank, B. P.**; Bouwer, E. J.; Fairbrother, D. H., Biodegradability of Carbon Nanotube/Polymer Nanocomposites Under Aerobic Mixed Culture Conditions. *Science of The Total Environment* 2018, *639*, 804-814.
13. Zhi, B.; Cui, Y.; Wang, S.; **Frank, B. P.**; Williams, D. N.; Brown, R. P.; Melby, E. S.; Hamers, R. J.; Rosenzweig, Z.; Fairbrother, D. H.; Orr, G.; Haynes, C. L., Malic Acid Carbon Dots: From Super-resolution Live-Cell Imaging to Highly Efficient Separation. *ACS Nano* 2018, *12* (6), 5741-5752.
14. Goodwin, D. G.; Boyer, I.; Devahif, T.; Gao, C.; **Frank, B. P.**; Lu, X.; Kuwama, L.; Gordon, T. B.; Wang, J.; Ranville, J. F.; Bouwer, E. J.; Fairbrother, D. H., Biodegradation of Carbon Nanotube/Polymer Nanocomposites using a Monoculture. *Environ. Sci. Technol.* 2018, *52* (1), 40-51.
15. Durkin, D. P.; Gallagher, M. J.; **Frank, B. P.**; Knowlton, E. D.; Trulove, P. C.; Fairbrother, D. H.; Fox, D. M., Phosphorus-Functionalized Multi-Wall Carbon Nanotubes as Flame-Retardant Additives for Polystyrene and Poly (methyl methacrylate). *Journal of Thermal Analysis and Calorimetry* 2017, *130* (2), 735-753.

Presentations as Presenting Author (24 total)

1. Effect of Chemical Modification on the Biodegradability of Cellulose Nanofibrils; Developing Nanocellulose to be an Environmentally Sustainable Structural Reinforcement Agent in Polymer Nanocomposites; Assessing the Effect of Nanocellulose Functionalization on Its Use as a Biodegradable Reinforcement Agent (Selected presentations from Center for Sustainable Nanotechnology biannual research conferences and weekly meetings 2015—2020 various locations—Oral & Poster, **19 total**)
2. Evaluating Hydrophobic Coatings and Covalent Functionalization of Nanocellulose for Use as a Biodegradable Nanocomposite Filler (TechConnect, 2019 Boston, MA—Poster)

3. Effect of Chemical Functionalization on the Dispersion Properties and Biodegradability of Nanocellulose (Environmental Nanotechnology GRC & GRS 2019, Newry, ME—Poster)
4. Effect of Chemical Modification on the Dispersion and Biodegradation of Nanocellulose (Sustainable Nanotechnology Organization Conference 2018, Washington, D.C.—Oral)
5. Impact of Silanization on the Structure, Dispersion Properties, and Biodegradability of Nanocellulose (ACS National Conference 2018, New Orleans, LA—Oral)
6. Silane Modification of Nanocellulose and Its Effect on Function and Environmental Impact (Environmental Nanotechnology GRC & GRS 2017, Stowe, VT—Poster)